The Lamb Shift Experiment in Muonic Hydrogen

Dissertation

submitted to the Physics Faculty

of the Ludwig–Maximilians–University Munich

by

Aldo Sady Antognini

from Bellinzona, Switzerland

Munich, November 2005

1st Referee	:	Prof. Dr. Theodor W. Hänsch
2nd Referee	:	Prof. Dr. Dietrich Habs
Date of the Oral Examination	:	December 21, 2005

Even if
I don't think,
I am.

Itsuo Tsuda

Je suis où je ne pense pas,
je pense où je ne suis pas.

Jacques Lacan

A mia mamma e mio papà
con tanto amore

Abstract

The subject of this thesis is the muonic hydrogen (μ^-p) Lamb shift experiment being performed at the Paul Scherrer Institute, Switzerland. Its goal is to measure the $2S-2P$ energy difference in μp atoms by laser spectroscopy and to deduce the proton root–mean–square (rms) charge radius $r_{\rm p}$ with 10^{-3} precision, an order of magnitude better than presently known. This would make it possible to test bound–state quantum electrodynamics (QED) in hydrogen at the relative accuracy level of 10^{-7}, and will lead to an improvement in the determination of the Rydberg constant by more than a factor of seven. Moreover it will represent a benchmark for QCD theories.

The experiment is based on the measurement of the energy difference between the $2S^{\rm F=1}_{1/2}$ and $2P^{\rm F=2}_{3/2}$ levels in μp atoms to a precision of 30 ppm, using a pulsed laser tunable at wavelengths around 6 μm. Negative muons from a unique low–energy muon beam are stopped at a rate of 70 s^{-1} in 0.6 hPa of H_2 gas. Highly excited μp atoms are formed, and most of them promptly deexcite to the ground state within $\sim$100 ns. However, there is a roughly 1% probability that long–lived $\mu{\rm p}_{2S}$ atoms with a lifetime of 1.3 μs are formed.

An incoming muon triggers a pulsed, multi–stage laser system which delivers 0.2 mJ per pulse at $\lambda \simeq 6$ μm with 55 s^{-1} repetition rate. It consists of two XeCl excimer lasers followed by dye lasers which pump an oscillator–amplifier frequency–controlled Ti:Sa laser. Its 6 ns long pulse at 708 nm is then frequency shifted to 6 μm via third Stokes production in a Raman cell filled with hydrogen. The laser pulse has a delay of about 1.5 μs with respect to the prompt muon cascade.

If the laser is on resonance, it induces $2S-2P$ transitions. The subsequent deexcitation to the $1S$ state emits a 1.9 keV K_α x ray which is detected by large area avalanche photodiodes. The resonance frequency, and hence the Lamb shift and $r_{\rm p}$, are determined by measuring the intensity of these x rays as a function of the laser wavelength.

A search for the $2S-2P$ resonance line was performed in November 2003 when a broad range of laser frequencies was scanned (49.7409 − 49.8757 THz), corresponding to proton radii between 0.844 and 0.905 fm. The result of the data analysis is that no significant $2S-2P$ resonance was observed. The negative result is with high probability due to the low statistics and not to an incorrect search region.

The first part of this thesis reports on the present status of the Lamb shift theory in μp. Following, there is a detailed description of the apparatus and analysis of the data. An estimate of the present and future laser–induced event rates are given, together with a study of the present and future background. In the Appendices are discussed: the energy levels in H, the proton radius definition, the relevance of this experiment, the $2S$ state population and lifetime, and the spectroscopic properties of the $2S-2P$ transition.

Contents

Abstract i

Contents ii

List of Tables vi

List of Figures vii

1 Overview of the muonic hydrogen Lamb shift experiment 1

2 Present status of the $2S - 2P$ Lamb shift in muonic hydrogen 7
2.1 Vacuum polarization . . . 8
2.2 Finite nuclear size . . . 11
2.3 Relativistic recoil corrections . . . 12
2.4 Fine and hyperfine structure . . . 14
2.5 The $\Delta E(2P_{3/2}^{\mathrm{F}=2} - 2S_{1/2}^{\mathrm{F}=1})$ energy splitting . . . 14

3 Muon beam, target, and electronics 17
3.1 Low–energy muon beam . . . 17
3.1.1 Cyclotron trap . . . 18
3.1.2 Muon extraction channel . . . 22
3.1.3 The 5 T solenoid with the muon detector . . . 23
3.2 Gas target . . . 26
3.2.1 Detectors for the 1.9 keV energy x rays: the LAAPDs . . . 27
3.2.2 Electron detectors . . . 30
3.2.3 Anti–coincidence detector . . . 30
3.2.4 Intermezzo about foils . . . 31
3.3 Electronics of the data acquisition system . . . 33

4 The laser system 35
4.1 Excimer lasers . . . 37
4.2 Dye lasers . . . 40
4.3 Continuous wave Ti:Sa laser . . . 42
4.3.1 Wavelength control . . . 43
4.3.2 Frequency stabilization . . . 44
4.4 Pulsed Ti:Sa oscillator and amplifier . . . 44

4.4.1 Oscillator . . . 44
4.4.2 Injection seeding . . . 45
4.4.3 Chirp in the Ti:Sa oscillator . . . 46
4.4.4 Ti:Sa amplifier . . . 50
4.5 Raman cell . . . 51
4.6 $Q_{01}(1)$ Stokes–shift in H_2 . . . 55
4.7 Water absorption . . . 56
4.8 Frequency calibration of the 6 μm light . . . 57
4.9 FP calibration and stability . . . 59
4.10 Summary of the frequency control of our laser system . . . 62
4.11 The 6 μm multipass cavity . . . 64
4.12 Summary . . . 68

5 Measurements **71**
5.1 Analysis of the waveform digitizer signals . . . 71
5.2 Event classification . . . 73
5.2.1 Signal versus particle identification . . . 73
5.2.2 Event construction . . . 73
5.3 X-ray and electron energy spectra: K_α energy cut and delayed electron cut 74
5.4 Second–muon cut . . . 77
5.5 Electron time spectrum . . . 78
5.6 Time calibration and resolution . . . 81
5.7 LAAPDs x-ray efficiency . . . 83
5.7.1 Detector efficiency ε_x . . . 83
5.7.2 Total efficiency η_x . . . 85

6 Search for the $2S-2P$ resonance **87**
6.1 "Laser ON" and "Laser OFF" data . . . 87
6.2 2 keV x-ray energy and time spectra . . . 87
6.3 Resonance line . . . 91
6.4 Problems during 2003–run . . . 92
6.5 Event and background rate in 2003 beam time . . . 95

7 Future improvements of the apparatus **97**
7.1 Thin–disk laser . . . 97
7.2 Future event rate . . . 101
7.3 Background rate . . . 102
7.4 Possible background reduction . . . 103
7.5 Measuring time and search of the resonance . . . 104
7.6 Future extension of the experiment . . . 106

A Theory of hydrogen energy levels **107**
A.1 Bohr energy levels . . . 107
A.2 Dirac energy levels . . . 108
A.3 The Lamb shift . . . 109
A.4 Radiative corrections . . . 112
A.5 Perturbative and all–order approaches to the self–energy . . . 113
A.6 One–loop self–energy . . . 115
A.7 Two–loop self–energy . . . 115
A.8 Finite nuclear size and nuclear structure corrections . . . 118
A.9 Summary . . . 121

B Bound–state QED test and extraction of Rydberg constant **123**
B.1 Bound–state QED test . . . 124
B.2 Rydberg constant . . . 125
B.3 Lamb shift and R_∞ uncertainty related to α and m/M . . . 126
B.3.1 Lamb shift uncertainty caused by α . . . 126
B.3.2 Uncertainty of R_∞ caused by the uncertainty of m/M . . . 126

C Electron–proton scattering experiments **129**
C.1 Elastic scattering cross sections . . . 129
C.2 Measurements and extraction of the nuclear structure . . . 131
C.3 Structure functions . . . 132

D Proton radius **135**
D.1 Proton radius in scattering experiments . . . 135
D.2 Proton radius in atomic hydrogen . . . 136
D.3 Problems related to the definition of the proton radius . . . 136

E $2S-2P$ transition probability **137**
E.1 $2S-2P$ transition probabilities and matrix elements . . . 137
E.2 $2S-2P$ linewidth . . . 139
E.3 Laser intensity . . . 141
E.4 Two–level system . . . 141
E.5 Summary . . . 143

F $2S-2P$ transition systematics **145**
F.1 Doppler broadening . . . 145
F.2 Zeeman effect . . . 145
F.2.1 Linear versus quadratic Zeeman effect . . . 146
F.2.2 Orbital and spin magnetic moments . . . 146
F.2.3 Zeeman effect of the hyperfine levels . . . 147
F.2.4 Anomalous Zeeman effect versus Breit–Rabi solution . . . 148
F.3 Collisional shift and broadening . . . 149
F.3.1 Model . . . 149

F.3.2 $2S - 2P$ energy shift . . . 150
F.3.3 Electric field and interatomic potential . . . 151
F.3.4 Numerical results . . . 152

G Population and lifetime of the $2S$ state **155**
G.1 Muonic hydrogen formation and cascade processes . . . 155
G.2 Population of the $2S$ state . . . 158
G.3 Long and short–lived $2S$ components . . . 159
G.4 Lifetime of the $2S$ long–lived state . . . 161

H Background of the $2S - 2P$ resonance **163**
H.1 Background from muon transfer to carbon . . . 164
H.2 Uncorrelated background . . . 169
H.3 Total background . . . 172

References **175**

Acknowledgements **185**

List of Tables

2.1 Uehling and Källen–Sabry contributions for different wave–functions 9
2.2 Summary of all contributions to the $\Delta E(2P^{F=2}_{3/2} - 2S^{F=1}_{1/2})$ energy difference 15

4.1 Requirements on the laser system 35

5.1 Energies and measured relative yields of the μp K-series 77

7.1 Summary of the various background contributions expected in the laser time window for the future experiment 103

A.1 Theoretical expectation of the $1S$ and $2S$ Lamb shifts in hydrogen 111

E.1 Matrix elements for the various $2S - 2P$ transitions 139
E.2 Spectroscopic properties of the $2S^{F=1}_{1/2} - 2P^{F=2}_{3/2}$ transition 143

F.1 Zeeman shift in a 5 T magnetic field 148

G.1 Processes involved in the deexcitation of μp after its formation 156

H.1 Energies and yields of radiative transitions after muon transfer from a μp to a μC atom 164
H.2 Summary of the various contributions to the background in the laser time window for 2003–run 172

List of Figures

1.1 Characteristic energy and size of exotic atoms. 3
1.2 Simple sketch of the muon cascade in hydrogen and principle of the experiment. 4

2.1 Energy levels in hydrogen and muonic hydrogen 8
2.2 Vacuum polarization insertion in the photon propagator 9
2.3 Higher order finite nuclear size corrections to μp energy levels 10
2.4 Double and triple vacuum polarization, and Källen–Sabry corrections . . . 10
2.5 Light–by–light corrections 10
2.6 Other radiative corrections to muonic hydrogen energy levels 11

3.1 Lay–out of the muon beam 18
3.2 Photo of the PSI πE5 area 19
3.3 Principle of the axial extraction of the muons from the CT 20
3.4 Number of "useful" extracted and detected muons as function of the HV on the foil placed in the CT 22
3.5 Schematic view of the apparatus mounted inside the 5 T axial solenoid . . . 24
3.6 Muon kinetic energy between the CT trap and the hydrogen gas target . . . 25
3.7 Schematic view of the target assembly 26
3.8 Picture of the open target for the beam time 2002 27
3.9 Schematic view of an LAAPD with its electric field distribution 28
3.10 Measured energy spectrum when the LAAPD is irradiated by a ^{55}Fe source 29
3.11 Energy spectrum of the α particles from Th of the dielectric coating of the 6 μm cavity mirrors 32

4.1 Schematic view of the laser system 36
4.2 Principle arrangement of the excimer lasers electronics 38
4.3 Schematic view of the Bethune and transversely pumped dye cell 40
4.4 Efficiencies and lifetimes of several dye solutions 41
4.5 Schematic view of the Ti:Sa continuous wave laser 43
4.6 Schematic view of the pulsed Ti:Sa oscillator 45
4.7 Oscillator output pulse 46
4.8 Simulated oscillator frequency shift versus time 48
4.9 Measurement of the frequency shift in Ti:Sa oscillator 49
4.10 Simplified representation of the sequential Raman scattering 51
4.11 Measured quantum efficiency for production of first, second and third Stokes 54

4.12 Measurements of the Raman conversion efficiency for third Stokes 55
4.13 Water absorption coefficient as a function of the frequency 57
4.14 Wavelength calibration of the 6 μm light by scanning a water line 58
4.15 Schematic view of the apparatus used to calibrate the FP with Rb lines . . 60
4.16 Measurement of the Fabry–Perot drift at 780 nm 61
4.17 Frequency control of our 6 μm laser source 63
4.18 Sketch of the 6 μm multipass cavity 64
4.19 Off–axis coupling into the 6 μm cavity 65
4.20 Monitoring system for the 6 μm cavity 65
4.21 Simulated light intensity distribution inside the 6 μm multipass cavity . . . 66
4.22 Time distributions of the light escaping the cavity 67

5.1 Examples of typical WFD spectra 72
5.2 LAAPD electron energy spectrum 74
5.3 Demonstration of the DELE cut effectiveness 75
5.4 X-ray energy spectrum with DELE cut fit with several x-ray peaks 76
5.5 Demonstration of the *second muon* cut effectiveness for delayed x rays . . . 78
5.6 2D spectrum of time t_e and energy E_e of the signals detected in the electron paddles 79
5.7 Time spectrum of electron paddle signals 80
5.8 Time spectrum of the time differences $t_e - t_x$ for the *xe* event class 81
5.9 Timing of the V_2 signal as a function of run number 83
5.10 LAAPDs x-rays detection efficiency as a function of the x-ray energy 85

6.1 X-ray energy spectrum from the *xe* event class 88
6.2 Time spectrum of 2 keV x rays 89
6.3 An example of a "shifted" 2 keV time spectrum 90
6.4 Result of the search for the $2S - 2P$ resonance line 92
6.5 Simulated examples of the resonance search for a signal rate of 0.5 h^{-1}, a signal to background ratio of 1, and a measuring time per point of 7 h . . . 93
6.6 Detection loss for laser–induced x rays due to μp_{2S} drift 94

7.1 Principle of the thin–disk laser 98
7.2 Optical pump design for the thin–disk laser with 16 pump beam passes . . 99
7.3 Schematic representation of the Q-switched laser resonator 99
7.4 Measured output energy of the thin–disk Q-switched Yb:YAG laser as a function of the repetition rate 100
7.5 Simulated examples of the resonance search for a signal rate of 15 h^{-1}, a background rate of 8 h^{-1}, and a measuring time per point of 2 hours 105
7.6 Simulated examples of the resonance search for a signal rate of 15 h^{-1}, a background rate of 8 h^{-1}, and a measuring time per point of 5 hours 105

A.1 Self–energy graph for a free and a bound electron 112
A.2 Expansion of the bound self–energy in terms of Coulomb fields 112

A.3 The Feynman diagrams contributing to the two–loop QED energy 114
A.4 Diagrammatic representation of the M terms 116
A.5 Diagrammatic representation of the P terms 117
A.6 Diagrammatic representation of the F terms 117
A.7 B_{60} term for hydrogenic atoms as a function of the nuclear charge Z 118
A.8 Finite nuclear size contributions to the Lamb shift 120
A.9 Radiative corrections of order $\alpha(Z\alpha)^5 m\langle r_{\rm p}^2\rangle m_r^3$ to the finite size effect . . . 121

C.1 Diagrams contributing to elastic $e-$p scattering 130
C.2 Internal and external Bremsstrahlung 131

E.1 Calculated $2S-2P$ resonance curve 142
E.2 $2S-2P$ transition probability as a function of the laser fluence 143

F.1 Interaction potentials between the μp atom and hydrogen molecule 151
F.2 Collisional shift and broadening 153

G.1 Cascade in μp, and the rate of the various deexcitation processes 157
G.2 $\mu{\rm p}_{2S}$ initial population ε_{2S} *vs* pressure from x–ray measurements 159
G.3 Fraction of $\mu{\rm p}_{2S}$ atoms which are slowed below 0.31 eV as a function of their initial kinetic energy and measured initial kinetic energy distribution . 160

H.1 X-ray energy spectra at various delayed times 165
H.2 Fitted background parameters compared with $\mu{\rm C}_{4\to3}$ line intensity 167
H.3 Simulation of the time spectrum of μC x rays from muon transfer to the polypropylene foils, for different reflection probabilities 168
H.4 2 keV–background due to muon transfer from μp to C–atoms 169
H.5 Measured 2 keV–background x-ray time spectrum 173

Chapter 1

Overview of the muonic hydrogen Lamb shift experiment

The goal and the principle of the muonic hydrogen Lamb shift experiment being performed at the Paul Scherrer Institute (Switzerland) are described in this Chapter. Muonic hydrogen (μ^-p) is a two–body Coulomb bound system formed by a negative muon and a proton. The goal of this experiment is to measure the energy difference $\Delta E(2P_{3/2}^{\mathrm{F}=2} - 2S_{1/2}^{\mathrm{F}=1})$ by laser spectroscopy to a precision of 30 ppm and to deduce the root–mean–square (rms) proton charge radius r_{p} with 10^{-3} relative accuracy. The rms charge radius is defined by $r_{\mathrm{p}}^2 = \int d\mathbf{r}\, r^2 \rho(\mathbf{r})$ where $\rho(\mathbf{r})$ is the proton charge distribution (cf. Appendix D). The extraction of the proton radius from the measured transition frequency in muonic hydrogen is given by the relation (cf. Chapter 2)

$$\Delta E(2P_{3/2}^{\mathrm{F}=2} - 2S_{1/2}^{\mathrm{F}=1}) = 209.968(5) - 5.2248 \cdot r_{\mathrm{p}}^2 + 0.0347 \cdot r_{\mathrm{p}}^3 \ \ [\mathrm{meV}] \qquad (1.1)$$

where r_{p} is expressed in fm. In terms of frequency this energy splitting is about 50 THz, corresponding to a wavelength of about 6 μm. The main contribution in Eq. (1.1) is given by vacuum polarization effects calculable in the framework of bound–state quantum electrodynamics (QED). The $2S$ hyperfine splitting is 23 meV, the $2P$ fine and hyperfine splittings are a few meV, *i.e.,* much smaller than $\Delta E(2P_{3/2}^{\mathrm{F}=2} - 2S_{1/2}^{\mathrm{F}=1})$. Nevertheless these splittings are large compared to the natural linewidth of the $2S - 2P$ transition which is essentially given by the $2P$ lifetime ($\hbar\Gamma_{2P} = 0.077$ meV). The six allowed $2S - 2P$ transitions are therefore well separated. The particular transition (Eq. (1.1)) chosen for this experiment is the one with the largest matrix element. The relative contribution of the proton size to the $2S - 2P$ energy splitting is 1.8%. Therefore already a measurement of the corresponding transition frequency ($\sim$ 50 THz) with a moderate accuracy of 1.5 GHz, which corresponds to about $\sim$ 10% of the naturalline width, leads to a improvement of an order of magnitude in the determination of the r_{p} value compared to the present value extracted from the Lamb shift in "electronic" hydrogen and electron–proton scattering experiments.

This radius is being recognized as a basic property of the simplest nucleus, the proton, and treated in the recently published 2002–CODATA [1] adjustment as a fundamental physical constant. The most precise and reliable value of r_{p} is derived from spectroscopic data on hydrogen and deuterium due to a significant reduction of the uncertainty of the relevant bound–state QED theory in the last few years [2–4]. This is achieved by comparing the measured $1S$ Lamb shift (2×10^{-6} relative accuracy [1, 5]) with the theoretical value which has a relative accuracy of 5×10^{-7} when terms related to r_{p} are not considered.

The rms–radius, extracted from these spectroscopic data using a least square adjustment method, is $r_{\rm p} = 0.8736(77)$ fm which has the largest weight on the current CODATA value of $r_{\rm p} = 0.8750(68)$ fm [1]. This value is mainly limited by the experimental uncertainty of the $1S$ Lamb shift. It also relies on the assumption that the related bound–state QED calculations are correct which is justified at the level of the present experimental accuracy. However, when the experimental uncertainty will be reduced by measuring, *e.g.,* the $1S-3S$ transition frequency, the theoretical uncertainty related to the two–loop self–energy may be the limiting factor in the extraction of the $r_{\rm p}$ value.

Knowledge of $r_{\rm p}$ which does not depend on bound–state QED calculations comes from electron–proton scattering experiments which have a long history. A recent reevaluation of all available scattering data yields a value of $r_{\rm p} = 0.895(18)$ fm [6]. The resulting uncertainty in $r_{\rm p}$ is as large as 2%, mainly associated with normalization and fitting procedures.

A precise knowledge of $r_{\rm p}$ from the μp Lamb shift experiment would make it possible to test bound–state QED in hydrogen on the level of the quoted experimental and theoretical uncertainties. A comparison of the predicted (using the $r_{\rm p}$ value from μp spectroscopy or electron scattering) with the measured H($1S$) Lamb shift leads to a bound–state QED test, whereas a subtraction of the predicted $1S$ Lamb shift from the measured $1S-2S$ transition frequency in hydrogen [7] leads to a better determination of the Rydberg constant R_∞ (cf. Appendix B). The 2% uncertainty of the $r_{\rm p}$ value extracted from scattering experiments limits the bound–state QED test to a relative accuracy of 7×10^{-6}. If $r_{\rm p}$ will become known with 10^{-3} relative accuracy from μp spectroscopy, bound–state QED calculations can be tested with a relative accuracy of 2×10^{-6}, limited by the experimental uncertainty in hydrogen spectroscopy. A value of 3×10^{-7} may be reached in future when an increased accuracy of other transition frequencies in hydrogen or other atomic systems reduces the Rydberg constant uncertainty by a factor of ten. In contrast, the rms radius extracted from μp spectroscopy can be combined with the measured $1S-2S$ transition frequency in hydrogen to reduce the uncertainty of R_∞ by a factor of six [8] if bound–state QED calculations are assumed to be correct.

To sum up, μp spectroscopy offers the possibility to determine $r_{\rm p}$ with 10^{-3} precision which would lead to a test of bound–state QED and to an improved determination of the Rydberg constant. Interest in the $r_{\rm p}$ value comes also from the QCD community, since it would serve as an important benchmark for effective field and lattice theory calculations ($r_{\rm p} = 0.88(3)$ fm [9]).

Muonic hydrogen is an exotic atom. An exotic atom is an atom with an electron replaced by a heavy negative particle such as a muon μ^- with mass $207\,m_e$ (muonic atom), a pion π^- with mass $273\,m_e$ (pionic atom), a kaon K^- with mass $966\,m_e$ (kaonic atom), or an antiproton $\bar{p}$ with mass $1836\,m_e$ (antiprotonic atom). The common feature of these particles is that they are much more massive than the electron. The atomic binding energy is proportional to the reduced mass of the system and thus increases with increasing orbiting particle mass. The characteristic energy and size of exotic atoms lie in the energy gap between atomic and nuclear physics as shown in Fig. 1.1, and offer the possibility to study and measure a variety of basic physical phenomena and quantities related to atomic or nuclear physics such as the proton radius, the pion mass, strong interaction scattering lengths and so on. The orbits of the μ^- in muonic hydrogen lie 186 times closer to the nucleus compared to the electron orbits in hydrogen since

$$\langle r^{\rm orbit}\rangle \simeq \frac{\hbar}{Z\alpha\, m_r c}\, n^2\,, \tag{1.2}$$

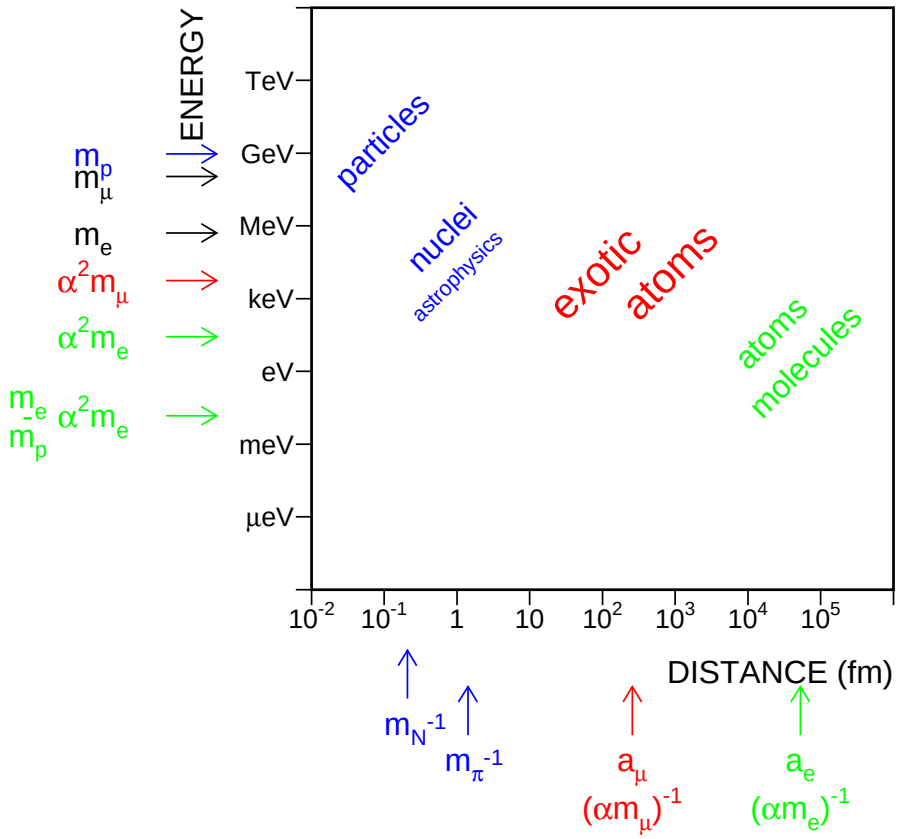

Figure 1.1: Characteristic energy and size of exotic atoms. a_μ and a_e are the ground state Bohr radii of muonic and "normal" hydrogen, respectively (Courtesy of V. Markushin).

where $\langle r^{\rm orbit}\rangle$ is the characteristic distance of the orbiting particle, m_r the reduced mass of the system, $\hbar$ the Planck constant, c the speed of light, Z the nuclear charge, and n the principal quantum number. Hence exotic atoms are much more sensitive to the nuclear structure than normal atoms. The leading finite size effect is proportional to the square of the wave function at the nucleus position and depends therefore on the mass of the orbiting particle as

$$\Delta E_{\rm finite\ size}(nl) = \frac{2(Z\alpha)^4 c^4}{3\hbar^2 n^3}\, m_r^3\, r_{\rm p}^2\, \delta_{l0}\,, \tag{1.3}$$

where l is the orbital quantum number. The nuclear structure effects scale with the reduced mass of the system as $m_r^3 r_{\rm p}^2$. Thus the relative contribution of the proton size to the Lamb shift in muonic hydrogen is rather large (1.8×10^{-2}), much more than the corresponding value of 1.4×10^{-4} for normal hydrogen.

The principle of the μp Lamb shift experiment is summarized in the following. Very low–energy (few keV) negative muons from an specifically designed muon beam at the Paul Scherrer Institute are stopped in 0.6 hPa of hydrogen gas at a rate of 70 s^{-1}. After μ^- atomic capture, μp atoms in highly excited states are formed, and most of them deexcite ("muonic cascade") to the ground state within 100 ns, with emission of Lyman–series x rays such as K_α, K_β, and so on (see Fig. 1.2 (left)). About $\sim 1\%$ of the μp atoms form long–lived μp_{2S} atoms with a lifetime of 1.3 μs at 0.6 hPa [10, 11]. A short laser pulse with a wavelength around 6 μm is sent into a mirror cavity and illuminates the muon stop

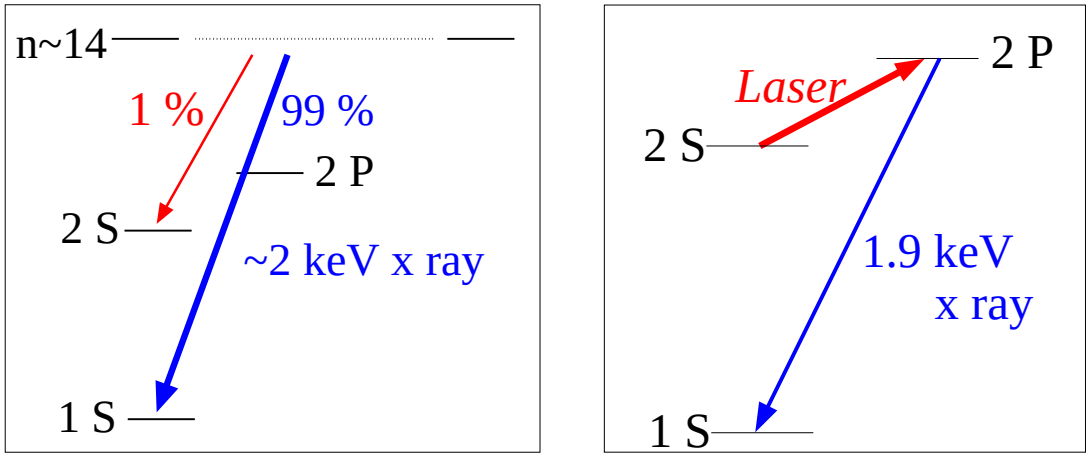

Figure 1.2: (Left): A very simple sketch of the muon cascade in hydrogen. The muon is captured in an highly excited state ($n \sim 14$). With $\sim 99\%$ probabilty the muon deexcites down to the ground state causing the emission of a 2 keV x ray. About 1% of the stopped muons end in a long–lived μp_{2S} state having the lifetime of about 1.3 μs at 0.6 hPa H_2 gas pressure. (Right): Basic idea of the μp_{2S} Lamb shift experiment. A short laser pulse drives the $2S - 2P$ transition. When a μp atom is excited to the $2P$ state it immediately decays ($2P$ lifetime $\sim 10^{-11}$ s^{-1}) to the ground state emitting a 1.9 keV K_α x ray.

volume in order to drive the $2S - 2P$ transition. The laser system is triggered by the muons entering the apparatus, and the light pulse has a delay of ~ 1.5 μs relative to the muons stop. A shorter delay of a few hundreds ns would be optimal, but the present value is limited by the time needed by the laser system to produce the light pulse after it has been triggered. When on resonance, the laser induces the transition to the $2P$ state. The $2P$ state decays with a lifetime of 8.5 ps to the ground state emitting a 1.9 keV K_α x ray (see Fig. 1.2 (right)). These x rays are detected with large area avalanche photodiodes (LAAPDs) placed above and below the muon stop volume. To ensure that the K_α x rays originate from a muonic atom the detection of the muon decay electron is also required, *i.e.,* the detection of the electron originated by the muon decay $\mu^- \rightarrow e^- \nu_\mu \bar{\nu}_e$ (the muon lifetime is 2.2 μs). This reduces the background at times when the laser induces the transition by an order of magnitude.

The signature of a laser–induced $2S - 2P$ transition is therefore the detection of a K_α x ray in time coincidence with the light of the laser illuminating the stop volume, followed by an electron from muon decay. The resonance frequency, and hence the Lamb shift and the proton charge radius, is determined by measuring the rate of laser–induced x rays as a function of the laser frequency.

The $2S$ lifetime is limited essentially by two processes: muon decay and collisional $2S$ quenching [10, 12, 13], and this puts particular requirements on both the muon beam and the laser system. Single muons entering the apparatus at random times trigger the pulsed laser and the data acquisition system. The laser has to have therefore a short response time, *i.e.,* a short delay time between muon trigger and laser pulse, so that a good amount of μp_{2S} atoms are still available when the laser pulse illuminates the target volume. This short delay is the most severe requirement for the laser system. No pre–synchronization of the laser with the muon is possible since muons enter the apparatus at random times. Such a pre–synchronization is possible at a pulsed muon beam available at other accelerator facilities. This would eliminate the problem related to the delay of the

laser system but would considerably worsen the background since it prevents the correct pairing of x rays and electrons. Moreover those sources have much lower integral muon intensities and are therefore not suitable for this experiment which has to be performed at low gas pressure.

Since the fastest laser delay achievable with our system was $\sim$ 1.5 μs, we had to reduce the target gas pressure to 0.6 hPa (at room temperature), to have a $2S$ lifetime of the order of the laser delay. Such a low gas pressure makes it difficult to stop muons efficiently in a small volume which can be illuminated by the laser light with sufficiently high intensity. A new low–energy negative–muon beamline was developed at PSI which yields an order of magnitude more muon stops in a small low–density (hPa) gas volume than a conventional muon beam. Even with this dedicated muon beam the longitudinal stop distribution is $\sim$ 20 cm. To prevent the low–energy muon beam to blow up due to multiple scattering in the low hydrogen gas pressure, the target is placed in a strong axial magnetic field (5 Tesla). The magnetic field limits the choice of x-ray detectors, and the size of the superconducting coils required to generate this magnetic field limits the volume of the target and detectors. Fortunately the strong magnetic field does not affect in a remarkable way the $2S - 2P$ transition frequency in muonic hydrogen (cf. Appendix F).

The Lamb shift measurement requires a complex laser system which provides typically 0.2 mJ pulse energy tunable at 6 μm wavelength with a short delay time. Such a system is not commercially available and thus a home–made multistage laser system has been developed (cf. Chapter 4). The pulse delivered by the laser system is confined inside a new type of multipass cavity which provides the large illumination volume ($7 \times 25 \times 170$ mm^3) required to cover the muon stop volume.

All parts of the apparatus were taken into operation during a long beam period ("run") in 2003. In November 2003 the $2S - 2P$ resonance frequency was searched in a range from 49.7409 THz to 49.8757 THz, corresponding to $r_{\rm p}$ values between 0.844 and 0.905 fm. The laser was shot at fixed frequency values spaced by about 10 GHz, in accordance with the natural linewidth of the $2S - 2P$ transition of 18.6 GHz at FWHM. A new sophisticated method to analyze the data, in particular the LAAPD pulse shapes, was developed in 2004. No resonance line was observed, and this negative results has to be attributed to the lack of statistics. Although only about 0.5 background events per hour have been measured, the event rate was not sufficient due to the limited measuring time ranging from 5 to 10 hours per measured frequency point. The statistics were too low to exclude the existence of the resonance line in the above–mentioned scanned region. A signal rate of only 0.5 events per hour (on resonance) was achieved. However, for the future, several improvements of the apparatus are planned and partially already realized. The future event rate is expected to be 24 times larger than the present one, and this should lead to a successful search of the resonance. Additionally the laser uptime should increase by a factor of 2.

More than 10^6 x rays from μp K_α, K_β, and $K_{\rm rest}$ transitions at 1.898, 2.249, and 2.46 keV, respectively, have been detected in the 2003–run. This is much more than in any muonic hydrogen experiment performed at low gas density. Despite the failure in the search of the resonance line, new physical results about the μp cascade and the $2S$ quenching have been obtained from a detailed analysis of the large number of data. For the first time the "short–lived" component of the $2S$ state was directly observed. It corresponds to $\mu{\rm p}_{2S}$ atoms with a kinetic energy of a few eV which undergo collision–induced $2S - 2P$ transitions with subsequent deexcitation to the ground state. The other $\mu{\rm p}_{2S}$ atoms are decelerated by elastic collision below 0.31 eV which corresponds to the

$2S-2P$ energy threshold in the laboratory system. Collisional excitation to the $2P$ state is forbidden for these atoms. These "long–lived" atoms were found in previous experiments to deexcite at a slower rate (relative to the "short–lived" component) via a resonant formation of excited muonic molecules and a subsequent nonradiative dissociation to the ground state [10,11]. Combined with the total population of the $2S$ state, $(2.49 \pm 0.17\%)$ [14], the new measurement of the short–lived component is an indirect determination of the long–lived component which represents the relevant population for the laser experiment. Both the indirect and the direct determination (independent measurements) of the long–lived μp_{2S} population are in agreement, *i.e.,* they predict a long–lived population of $\sim 1\%$ at 0.6 hPa (cf. §G.4).

Three theses have been written on the subject of the muonic hydrogen Lamb shift experiment. The thesis of L. Fernandes [15] of Coimbra University describes the development of LAAPDs as 2 keV x ray detectors. The thesis of L. Ludhova [16] is devoted to the analysis of the data and reports on the first observation of μp cascade time, together with the population and the lifetime of the $2S$ short–lived component. This thesis describes the present status of the μp Lamb shift experiment with emphasis on the spectroscopic part.

Chapter 2

Present status of the $2S - 2P$ Lamb shift in muonic hydrogen

Since the muon mass is about 200 times larger than the electron mass, the muon wave–function overlaps with the proton $(m_\mu/m_e)^3 \sim 10^7$ stronger than that of the electron (in hydrogen), leading to an increased sensitivity to the hadronic structure of the nucleus (charge and magnetic moments, nuclear polarizability). The leading finite size effect in muonic hydrogen contributes to about 2% to the $2S - 2P$ Lamb shift, *i.e.,* to $-3.979(62)$ meV for $r_{\rm p}$ =0.8750(68) fm [1] and to $-4.16(17)$ meV for $r_{\rm p}$ =0.895(18) fm [6], whereas it contributes only to 1.4×10^{-4} in the $1S$ Lamb shift in hydrogen. The Lamb shift measurement in muonic hydrogen aims to improve the precision of the proton radius by a factor of 20 compared to the value extrapolated from electron–proton scattering data. Therefore a calculation of all other contributions to a precision considerably better than 0.17/20 meV is required, *i.e.,* ∼0.001 meV.

S states of μp differ from those of ordinary hydrogen atom mainly in two respects: the vacuum polarization effect is the most important QED contribution, and there is a higher sensitivity to the nuclear structure. The role of the vacuum polarization contribution in the energy spectrum of μp atoms is increased by the decrease of the atomic radius. The electron Compton wavelength (λ_e) which approximately describes the size of charge distribution of the e^+e^- pairs produced by the vacuum polarization, is of the same order as the muonic Bohr radius ($a_0^{\mu\rm p}$):

$$\frac{a_0^{\mu\rm p}}{\lambda_e/2\pi} = \frac{\hbar^2/m_r e^2}{\hbar/m_e c} \simeq \frac{285 \text{ fm}}{386 \text{ fm}} \simeq 0.74 \,, \tag{2.1}$$

and therefore the S-state muonic wave–functions overlap strongly with the charge distribution of the virtual e^+e^- pairs.

In the following the present status of the theoretical prediction of the muonic hydrogen Lamb shift is presented. Different methodologies and results of various authors are presented in order to better point out the uncertainties of the various contributions and the problems. The majority of the contributions are treated in the papers of K. Pachucki [17, 18] and M. I. Eides *et al.* [19]. A compilation of all terms known in 2002 are given by P. Indelicato and E. -O. Le Bigot [20]. Interesting new aspects are presented in a recent paper of E. Borie [21]. For a comprehensive but not updated review the reader is referred to the work of E. Borie and G. A. Rinker [22]. It is interesting to note that very recently some contributions to the Lamb shift have been computed by A. Pineda [23] starting from heavy–barion effective field theory, which gives a methodologically more independent cross check of the predictions. For an introduction about

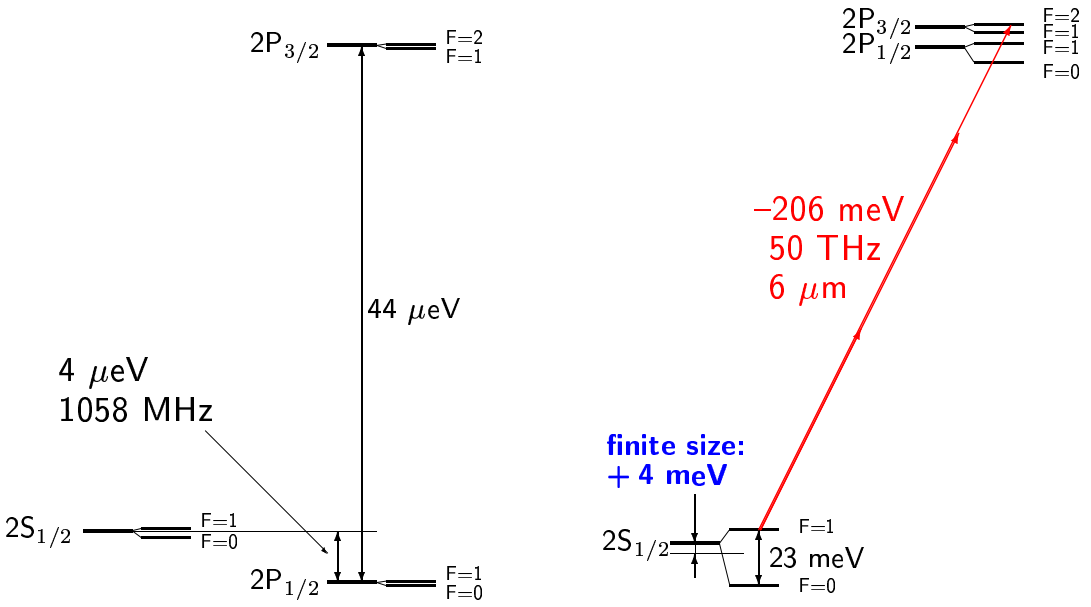

Figure 2.1: Schematic representation of the $n = 2$ energy levels in electronic hydrogen (left) and muonic hydrogen (right). Note the different energy scales for the two atoms. The indicated 4 μeV energy difference corresponds to the "classical" Lamb shift, dominated by the self–energy terms. The vacuum polarization in muonic hydrogen attracts the $2S$ state below the $2P$ state. The laser transition is indicated in red.

bound–state energy levels the reader is referred to Appendix A. This Appendix gives a definition of Lamb shift, and presents the various contributions to the $1S$ Lamb shift in hydrogen with emphasis on the self–energy and nuclear finite–size corrections.

2.1 Vacuum polarization

In the perturbative approach, QED corrections to the Dirac energy levels are derived from the scattering approximation using Feynman diagrams. The scattering amplitudes in momentum space are computed using Feynman rules. The Fourier transform of the scattering amplitude which corresponds in coordinate space to the potential $V(r)$ (in first Born approximation) is then used to compute the energy level shift given by $\Delta E = \langle\bar{\Psi}(r)|V(r)|\Psi(r)\rangle$ where Ψ describes the atomic wave–function.

This approach is used to compute the effect of the vacuum polarization (VP). The Feynman amplitude S corresponding to a one–photon Coulomb scattering of a lepton with initial four–momentum p and final four–momentum p' by an infinitely heavy nucleus with form factor $F(q^2)$ is [22]

$$S = -u^\dagger(p')u(p)V(q)(2\pi)^4\,\delta^4(p' - p - q) \tag{2.2}$$

where q is the four–momentum transfer and

$$V(q) = -4\pi Z\alpha\frac{F(q)}{\mathbf{q}^2} = \int d^3r\, V(r)e^{-i\mathbf{qr}} \tag{2.3}$$

The Fourier transform for a point–like nucleus ($F(q^2) = 1$) gives the Coulomb potential $V(r) = Z\alpha/r$. The effect of the vacuum polarization is best described by the modification

Figure 2.2: Vacuum polarization insertion in the photon propagator.

of the photon propagator as shown in Fig. 2.2, which can be expressed using the Feynman rules as

$$\frac{1}{\mathbf{q}^{\,2}} \longrightarrow \frac{1}{\mathbf{q}^{\,2}} + \frac{1}{\mathbf{q}^{\,2}}\Pi(q^2)\frac{1}{\mathbf{q}^{\,2}} + \cdots \ . \tag{2.4}$$

The vacuum polarization potential $V_{\rm VP}$ in first order (Uehling potential) can be then expressed in momentum space as

$$V_{\rm VP}(q) = -4\pi Z\alpha \frac{F(q^2)}{\mathbf{q}^{\,2}} \ \frac{\Pi(q^2)}{\mathbf{q}^2} \ . \tag{2.5}$$

In perturbation theory the energy shift due to the vacuum polarization potential is

$$E_{\rm VP} = \int \frac{d^3q}{(2\pi)^3} \frac{-4\pi Z\alpha F(q^2)}{\mathbf{q}^{\,2}} \frac{\Pi(q^2)}{\mathbf{q}^{\,2}} \int d^3r \ |\Psi(r)|^2 e^{-i\mathbf{qr}} \ . \tag{2.6}$$

The leading–order contribution to the $2S-2P$ energy–shift is then

$$E(2P-2S) = \int \frac{d^3q}{(2\pi)^3} \frac{-4\pi Z\alpha F(q^2)}{\mathbf{q}^{\,2}} \frac{\Pi(q^2)}{\mathbf{q}^{\,2}} \int d^3r \ (|\Psi_{2P}(r)|^2 - |\Psi_{2S}(r)|^2) e^{-i\mathbf{qr}} \ . \tag{2.7}$$

Two different approaches are followed by Borie [21] and Pachucki [17, 18]: the first works with relativistic and the second with nonrelativistic wave–functions. Borie has calculated the value of Eq. (2.7) for both the point–like nucleus ($F(q^2)=1$) with nonrelativistic and relativistic point–like wave–functions, and for an extended nucleus ($F(q^2)\neq 1$) for point–like relativistic wave–functions (cf. with results of Refs. [17, 18]). Results are given in Table 2.1. The effect of finite proton size on the VP contribution is the difference between the values of the Uehling contribution calculated with point–like and finite size nucleus. From Table 2.1 it is -0.0083 meV which may be parametrized as $-0.0109\, r_{\rm p}^2$. This finite size correction to the VP is diagrammatically represented by the first graph in Fig. 2.3. An additional finite–size with VP correction is given by the second diagram of Fig. 2.3 which contributes for about $-0.0164\, r_{\rm p}^2 \simeq -0.0128$ meV [17, 19].

Table 2.1: Uehling and Källen–Sabry contributions for different wave–functions: nonrelativistic/relativistic point–like/extended nucleus. The values for an extended nucleus were the same for the different structure functions, provided these functions have the same rms–radius. The values reported are calculated for the $2S_{1/2}-2P_{1/2}$ transition and are expressed in meV. The values are taken from Ref. [21].

Contribution	Uehling	Källen–Sabry
Point nucleus/nonrelativistic	205.0074	1.5080
Point nucleus/relativistic	205.0282	1.50814
$r_{\rm p}$ =0.875 fm/relativistic	205.0199	1.50807

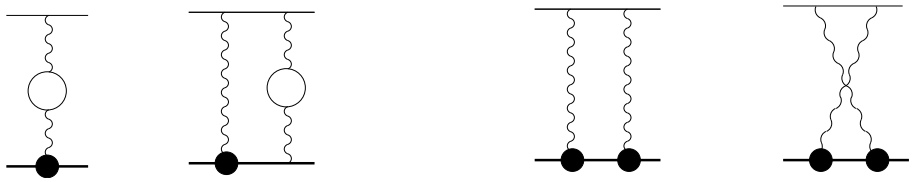

Figure 2.3: The first diagram is the correction of finite–size to VP. This is already accounted in the last row of the Uehling contribution with finite-size of Table 2.1. The second graph is a correction of combined VP and finite–size. The last two terms are finite size contributions to order $(Z\alpha)^5$ and have been computed in [17].

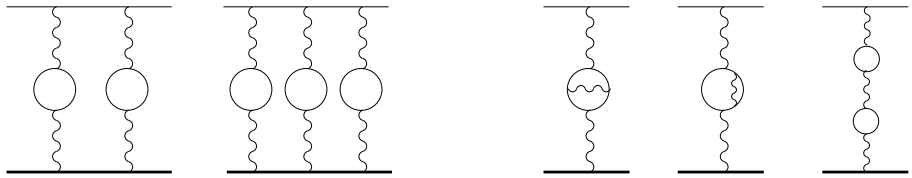

Figure 2.4: The first two graphs are the double and triple vacuum polarization (termed two and three iterations in [21]) corrections. The last three graphs on the right are the two–loop vacuum polarization insertion also named Källen–Sabry corrections.

Table 2.1 also shows results for the Källen–Sabry contributions which are diagrammatically represented by the last three graphs in Fig. 2.4. Since the VP is such a large effect in μp it is required to calculate effects represented by the double and triple VP shown in the first two graphs of Fig. 2.4. These contributions are termed by Borie " iteration VP". They have been calculated by Pachucki and Kinoshita to contribute to 0.151 meV [17,24]. An additional higher iteration including finite size and VP was already accounted for in the second graph of Fig. 2.3. To reach the required accuracy the following contributions have been evaluated [21]: Wichmann–Kroll (-0.00103 meV) and virtual–Delbrück ($+0.00135(15)$ meV) shown in Fig. 2.5. No calculation exists for the light–by–light contribution but it is expected to be of the same order, *i.e.,* $(\pm)0.001$ meV [25]. This represents one of the most significant unknown corrections to the μp Lamb shift.

A number of other radiative corrections corresponding to the graphs depicted in Fig. 2.6 have been computed. Contrarily to the hydrogen case, the one–loop self–energy contributes only to about 0.3% to the μp Lamb shift. The one–loop muon self–energy and muon vacuum polarization have been calculated using the corresponding formulas in normal hydrogen and their sum is $-0.667\,88$ meV [17, 21] (first two graphs in Fig. 2.6). The two–loop self–energy contributions which play an important role in hydrogen are here negligible, being estimated to be $-0.000\,06$ meV [17] (not shown in Fig. 2.6, but treated in detail in Appendix A for the hydrogen case).

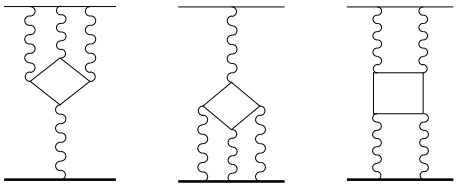

Figure 2.5: The first term is the light–by–light term $\alpha^3(Z\alpha)$, the second the Wichmann–Kroll $\alpha(Z\alpha)^3$ and the third the virtual Delbruck effect $\alpha(Z\alpha)^3$.

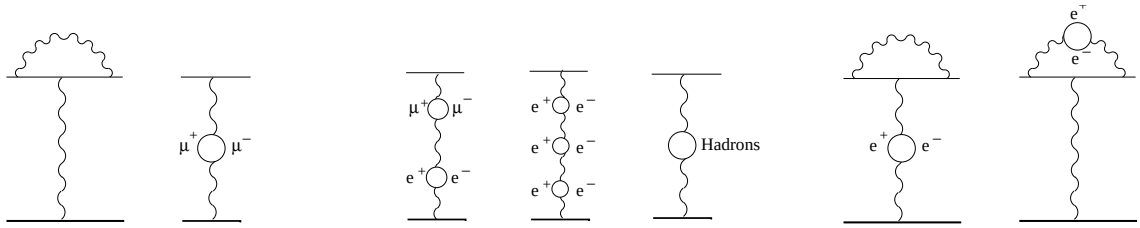

Figure 2.6: Other radiative corrections. Left to right: muon self–energy, muonic VP, mixed $e-\mu$ two–loop VP, three–loop VP which is one of the many sixth–order VP corrections [24], one–loop hadronic VP, and corrections to the muon self–energy due VP insert in external and radiative photon, respectively.

The mixed electron–muon two–loop VP is 0.00007 meV [21] and the rather difficult sixth–order VP contribution has been calculated by Kinoshita and Nio [24] with the result of 0.0076 meV. The hadronic VP amounts to about 0.011 meV [19, 26, 27]. Borie pointed out that these results have been calculated assuming the fact that the proton does not strongly interact with the hadrons in the virtual hadron loop. An estimation of this omission is difficult but she concluded that it could change the correction up to 50%. Additionally as previously mentioned Eides *et al.* [19] pointed out that the whole graph related to the hadronic VP could also contribute to the proton radius. It is not clear where this contribution should be assigned. Other authors [28–30] are of the opinion that corrections caused by the strong interaction between hadronic loop and proton are automatically considered in the definition of the proton radius and should not be treated separately. Note that very recently Pineda in the framework of heavy–barion effective theory has obtained a hadron polarization value for S states of $0.09039/n^3$ meV [23] which is in good agreement with the above given values.

The electron loop in the radiative photon (included in "fourth–order electron loops" by Borie) has been computed to be -0.00169 meV [21, 31] and is represented by the last but one graph of Fig. 2.6. Pachucki has estimated the contribution corresponding to a vacuum polarization insert in the external photon given by the last graph of Fig. 2.6 to be -0.005 meV [17].

2.2 Finite nuclear size

In muonic hydrogen the nuclear finite size effects give the second largest contribution to the energy levels. The main contributions related to the the proton finite size (cf. §A.8) are given by Ref. [32]

$$E_{\rm FS} = -\frac{2Z\alpha}{3}\left(\frac{Z\alpha m_r}{n}\right)^3\left[r_{\rm p}^2 - \frac{Z\alpha m_r}{2}\langle r_{\rm p}^3\rangle_{(2)} + (Z\alpha)^2\left(F_{\rm REL} + m_r^2 F_{\rm NR}\right)\right] . \tag{2.8}$$

The leading order finite size gives a correction of

$$-5.1975\, r_{\rm p}^2 = -3.979\ {\rm meV} \tag{2.9}$$

if $r_{\rm p}$=0.875 fm. The second term in Eq. (2.8) represented by the two last diagrams in Fig. 2.3 accounts for two–photon exchange, and contributes to [21]

$$\begin{aligned} -0.0347\, r_{\rm p}^3 &= -0.0232\ {\rm meV} \quad \text{(dipole form factor)} \\ -0.0317\, r_{\rm p}^3 &= -0.0212\ {\rm meV} \quad \text{(Gaussian form factor)} . \end{aligned} \tag{2.10}$$

This differs slightly from the value given by Pachucki. The dipole form factor which corresponds to an exponential charge distribution is more realistic since it is in fair agreement with the scattering data. However a comparison between the values obtained with the dipole form factor and the Gaussian form factor (which has not any physical meaning) shows the sensitivity of the energy levels on the charge distribution (proton shape). The uncertainty of the $2S - 2P$ transition energy related to the proton shape model is estimated to be of the order ± 0.002 meV, provided the different parameters describing the proton charge distribution are adjusted to reproduce the measured rms radius. Note that Sick and Friar are working to determine this third Zemach moment using only the world data on elastic electron proton scattering. Their results should be model independent.

The third term of Eq. (2.8) contributes to about 0.00046 meV [21]. For muonic hydrogen the relativistic corrections of order $(Z\alpha)^6$ are smaller than the two–photon exchange corrections of order $(Z\alpha)^5$, whereas the opposite is valid for hydrogen. As previously mentioned there are two finite size corrections to the VP represented by the two graphs of Fig. 2.3 which can be parametrized as $-0.0109\, r_{\rm p}^2 - 0.0164\, r_{\rm p}^2$. Additionally there is a recoil correction of 0.013 meV to the $2S - 2P$ energy difference [32].

The second largest Lamb shift uncertainty is given by the proton polarization. Rosenfelder [33] gives a value of 0.017(4) meV, Pachucki [18] 0.012(2) meV, and Faustov and Martynenko [34, 35] 0.016 meV. The $20 - 25\%$ uncertainties are dominated by the experimental errors of the ratio of the longitudinal to transverse polarized photon cross section, the parametrization of this ratio in function of Q^2, and the uncertainty in the measured inelastic structure function. We assumed an averaged value of 0.015(4) meV with the largest quoted uncertainty. New measurements of the $e^+e^- \rightarrow$ *hadrons* cross section in Frascati may lead to a better determination of the proton polarizability [36]. Presently this term is the limiting factor in the prediction of the Lamb shift (proton radius excluded). An effort is in progress [37] aiming to calculate the polarizability contribution in muonic hydrogen starting from heavy–barion effective theory. It may lead to a model–independent (not dependent on the phenomenological dipole parametrization) value of the polarizability contribution, leading to an even more model–independent value of the proton radius which can be extracted from our experiment.

For a point–like proton the contribution of the proton self–energy to the Lamb shift of S states is clear [38], but the problem is that the proton self–energy is modified by, and modifies as well, the finite size–effect. To avoid double counting of corrections (in the self–energy and in the finite–size) a preciser definition of the nuclear rms charge radius is necessary. Usually the rms charge radius is defined via the Sachs form factor (see Appendix D) which, according to Pachucki, is not correct at our level of precision, because the radiative corrections to G_E are infrared divergent and therefore they have to be regulated [18]. Pachucki has proposed a better definition of the proton charge radius via the low–energy behavior of two–photon scattering amplitude which lead to a clear separation of proton self–energy and finite–size contributions. The proton self–energy was computed to be -0.0099 meV [18].

2.3 Relativistic recoil corrections

As mentioned previously very different approaches have been developed by Borie and Pachucki to treat relativistic and recoil corrections. Borie computes the one–photon recoil corrections starting from the Dirac equation. An effective potential which replaces the external field Coulomb potential is constructed by writing the one–photon fermion–boson

scattering amplitude [22]

$$S = -Ze^2\bar{u}(p_3)\gamma^\mu u(p_1)\frac{F(q^2)}{q^2}\frac{(p_4+p_2)_\mu}{(4E_2E_4)^{1/2}}\,, \tag{2.11}$$

where p_1, p_3 are the initial and final four–momentum of the fermion, and p_2, p_4 the initial and final four–momentum of the "boson". By expanding the nucleus ("boson") energies E_2 and E_4 as $E_i \simeq M + p_i^2/2M$, an effective potential can be constructed which takes into account recoil corrections to leading order in $1/M$:

$$S \simeq u^+(p_3)\underbrace{\frac{Ze^2}{q^2}F(q^2)\left[1+\frac{\alpha\cdot(\mathbf{p}_3+\mathbf{p}_1)}{2M}\right]}_{V_{\rm eff}}u(p_1)\,. \tag{2.12}$$

The effective potential $V_{\rm eff}$ is then inserted into the two–body Hamiltonian

$$H = \alpha\cdot\mathbf{p} + \beta m + \frac{\mathbf{p}^2}{2M} + V_{\rm eff} \tag{2.13}$$

where $p = -p_3$ since we are in the center–of–mass system. This leads to a one–photon recoil correction for the $2S-2P$ state of -0.00419 meV.

On the contrary Pachucki includes relativistic and recoil correction via the Breit–Hamiltonian [39]

$$H_B = \frac{p^2}{2m} + \frac{p^2}{2M} + V + \delta H \tag{2.14}$$

where

$$\begin{aligned}\delta H =& -\frac{p^4}{8m^3} - \frac{p^4}{8M^3} + \frac{1}{8m^2}\nabla V + \left(\frac{1}{4m^2}+\frac{1}{2mM}\right)\frac{V'}{r}\mathbf{L}\cdot\sigma \\ &+ \frac{1}{2mM}\nabla^2\left[V - \frac{1}{4}(rV)'\right] + \frac{1}{2mM}\left[\frac{V'}{r}L^2 + \frac{p^2}{2}(V-rV') + (V-rV')\frac{p^2}{2}\right]\,.\end{aligned} \tag{2.15}$$

The prime represents the derivative with respect to r. If only the Coulomb interaction is included in V, the matrix element of the Breit Hamiltonian gives the correction to order $(Z\alpha)^4$ given by Eq. (A.12), which is 0.0575 meV [21,39]. If both Coulomb and VP potentials are accounted in V, an additional term of 0.00169 meV results [39]. Summing up the one–photon recoil calculated by Borie and the difference of the Uehling potentials calculated with relativistic and nonrelativistic wave–functions, gives a total recoil–relativistic correction of 0.00166 meV. Recoil and relativistic corrections for one–photon exchange computed by Borie and Pachucki agree therefore very well with each other. Evaluating the two–photon recoil for the $2S-2P$ transition gives a value of -0.04497 meV [17,19]. Higher–order radiative–recoil corrections give an additional contribution of -0.0096 meV [19].

Borie pointed out [25] that the two–photon recoil corrections need to be revised and that the next order recoil $(m/M)^2$ corrections have to be taken into account. A general algorithm has been developed by Czarnecki, Blokland, and Melnikov [40,41] which permits an expansion of the energy level of a bound–state with two constituents of masses m and M in powers of m/M and $(1-m/M)$. The developed method is applicable for pure recoil with several exchanged photons but also radiative–recoil corrections with several loops. It could be adapted to improve the recoil corrections in muonic hydrogen [28].

2.4 Fine and hyperfine structure

The determination of the "pure" Lamb shift from the $2S-2P$ transition frequency measurement requires the knowledge of fine and hyperfine structure contributions to the $n=2$ state. In hydrogen the measurement of the hyperfine splitting overcame the theoretical accuracy. Hence the $1S$ Lamb shift in hydrogen is extracted using the measured value. For the muonic case no measurement of the hyperfine and fine splitting is up to now available and therefore the subtraction of the hyperfine and fine splitting to get the "pure" Lamb shift has to rely on the theoretical predictions. It should be mentioned that in a second stage of this experiment a second transition between the $2S$ to the $2P$ states can be measured. The measured second transition will be then used to extract the "pure" Lamb shift instead of using the theoretical predictions of the fine and hyperfine contributions.

The hyperfine energy shifts for the $2S$ states ($F=0,1$) are given by the Fermi energy $E_{\rm Fermi}$ corrected for radiative, recoil, and finite–size contributions [42]

$$E_{\rm hfs}(2S) = E_{\rm Fermi}\left(1+\delta^{\rm QED}+\delta^{\rm FS}+\delta^{\rm pol}\right)\frac{[\delta_{F1}-3\delta_{F0}]}{4} \tag{2.16}$$

where

$$E_{\rm Fermi} = \frac{(Z\alpha)^4 m_r^3}{3mM}(1+\kappa_p)(1+a_\mu)\ . \tag{2.17}$$

with κ_p and a_μ the anomalous magnetic moment of the proton and the muon, respectively. $\delta^{\rm QED}\simeq 0.7\%$ represents the QED contributions dominated by the electronic VP contributions, $\delta^{\rm FS}\simeq -0.7\%$ is the correction related to the finite size of the nucleus which is dominated by the order $(Z\alpha)^5$ (two–photon exchange), that is by the Zemach radius, and $\delta^{\rm pol}\simeq 0.04\%$ is the proton polarizability correction. The result for the hyperfine splitting given by Borie is $E_{\rm hfs}(2S)=22.7806$ meV [21] whereas A. P. Martynenko gives $E_{\rm hfs}(2S)=22.8148(78)$ meV [42]. Borie neglects a recoil correction of 0.038 meV [17] and the proton polarizability of 0.011(2) meV [34, 42], but still both values are in slight disagreement.

For the fine and hyperfine contributions to the $2P$ state there is agreement between authors. They account for Uehling, Källen–Sabry, recoil and higher order anomalous magnetic moment corrections to the hyperfine splitting.

2.5 The $\Delta E(2P^{\rm F=2}_{3/2} - 2S^{\rm F=1}_{1/2})$ energy splitting

All the known contributions to the $2S^{\rm F=1}_{1/2}-2P^{\rm F=2}_{3/2}$ energy difference in muonic hydrogen are summarized in Table 2.2. They account for an energy splitting of

$$\begin{aligned}\Delta E(2P^{\rm F=2}_{3/2}-2S^{\rm F=1}_{1/2}) &= 209.968(5) - 5.2248\,r_{\rm p}^2 + 0.0347\,r_{\rm p}^3 \ \ [\text{meV}]\\ &= 50.7700(12) - 1.2634\,r_{\rm p}^2 + 0.00839\,r_{\rm p}^3 \ \ [\text{THz}]\\ &= 205.991(5)(62)\ \text{meV}\\ &= 49.8084(12)(150)\ \text{THz}\end{aligned} \tag{2.18}$$

with $r_{\rm p}=0.8750(68)$ fm. The first error refers to the uncertainty of the theory which is dominated by the proton polarizability and the second error refers to the uncertainty related to the proton radius. The above errors have to be compared with the aimed experimental precision of 6×10^{-3} meV corresponding to 1.5 GHz. A proton radius with about 10^{-3} relative precision can therefore be extracted if the $2S-2P$ transition frequency with a precision of ~ 1 GHz is measured.

Table 2.2: Summary of all contributions to the $\Delta E(2P^{F=2}_{3/2} - 2S^{F=1}_{1/2})$ energy difference in muonic hydrogen. The finite size corrections are given for r_p= 0.8750(68) fm [1]. The values for the estimated uncertainties are given only when they exceed 5×10^{-4} meV. The uncertainties in parentheses are dominated by the r_p uncertainty. When not stated the values are taken from Ref. [21]. The first uncertainty for the total Lamb shift refers to the theory, mainly given by proton polarizability, whereas the second uncertainty is related to the uncertainty of the r_p value. The light–by–light term is yet uncalculated.

Contribution		Value [meV]	Uncertainty [10^{-4} meV]
Uehling		205.0282	
Källen–Sabry		1.5081	
VP iteration		0.151	
Mixed $\mu - e$ VP		0.00007	
Hadronic VP [21, 23]		0.011	20
Sixth order VP [24]		0.00761	
Whichmann–Kroll		−0.00103	
Virtual Delbrück		0.00135	
Light–by–light		−	10
Muon self–energy and muonic VP (2^{nd} order)		−0.66788	
Fourth order electron loops		−0.00169	
VP insertion in self energy [17]		−0.0055	10
Proton self–energy [18]		−0.0099	
Recoil [17, 43]		0.0575	
Recoil correction to VP (one–photon)		−0.0041	
Recoil (two–photon) [19]		−0.04497	
Recoil higher order [19]		−0.0096	
Recoil finite size [32]		0.013	10
Finite size of order $(Z\alpha)^4$ [32]	$-5.1975(1)\, r_p^2$	−3.979	(620)
Finite size of order $(Z\alpha)^5$	$0.0347(30)\, r_p^3$	0.0232	(20)
Finite size of order $(Z\alpha)^6$		−0.0005	
Correction to VP	$-0.0109\, r_p^2$	−0.0083	
Additional size for VP [19]	$-0.0164\, r_p^2$	−0.0128	
Proton polarizability [18, 33]		0.015	40
Fine structure $\Delta E(2P_{3/2} - 2P_{1/2})$		8.352	10
$2P^{F=2}_{3/2}$ hyperfine splitting		1.2724	
$2S^{F=1}_{1/2}$ hyperfine splitting [42], $(-22.8148/4)$		−5.7037	20
Sum of corrections to Lamb shift		$209.968(5) - 5.2248\, r_p^2 + 0.0347\, r_p^3$ $= 205.991(5)(62)$ meV	

Chapter 3

Muon beam, target, and electronics

This Chapter deals with the muon beam line for the production of ultra–low energy negative muons, and the detector ensemble which records the physical signals, mainly low energy x rays and high energy electrons associated with the formed μp atoms.

The experiment is performed at the proton accelerator facility of the Paul Scherrer Institute (PSI). A high power 590 MeV proton beam with a beam current of about 2 mA ($\sim$ 1.2 MW) is transported to a meson production target, a rotating carbon wheel, and secondary beams of pions and muons are generated. Our experiment is installed at a low momentum ($10 - 120$ MeV/c) pion beam line (πE5) which is viewing the target with a rather large solid angle at 175° with respect to the primary proton beam. This beam line provides the worldwide highest intensity of low energy pions and muons.

The μp Lamb shift experiment requires to stop negative muons in a low pressure hydrogen target (0.6 hPa) to have long–lived μp_{2S} atoms. Only muons with kinetic energies below ~ 5 keV are stopped in a reasonably sized target vessel (*e.g.,* 20 cm length in beam direction), but the lowest beam momentum ever achieved at this channel was 10 MeV/c, corresponding to 500 keV energy. Reducing this beam energy by simple moderators is very inefficient. It was therefore necessary to develop an ultra–low energy muon beam. Section 3.1 describes this dedicated beam. In §3.2 the hydrogen target with its various components is described with focus on the detectors. The electronics system used for the data acquisition and its triggering system is briefly presented in §3.3.

3.1 Low–energy muon beam

To obtain a sufficiently high rate of laser–induced $2S-2P$ transitions, the $2S$ state lifetime has to be at least of the order of the laser delay time. To reduce collisional quenching of the $2S$ state (cf. §G.4), the negative muons are stopped in hydrogen gas at pressures below 1 hPa (0.6 hPa in the 2003–run). In order to efficiently stop muons at this ultra–low gas pressure and within the small target volume required for efficient laser–excitation, their initial kinetic energy has to be below 5 keV. The essential problem to design a low energy muon beam comes from the fact that muons are produced at MeV energies and that the deceleration process down to keV energies has to occur within the muon lifetime (2.2 μs). The simplest way to achieve this, is decelerating muons by energy loss in matter, but the efficiency of moderating a conventional muon beam to keV energies is rather poor due to energy straggling and angular scattering. A particular method adapted to positive

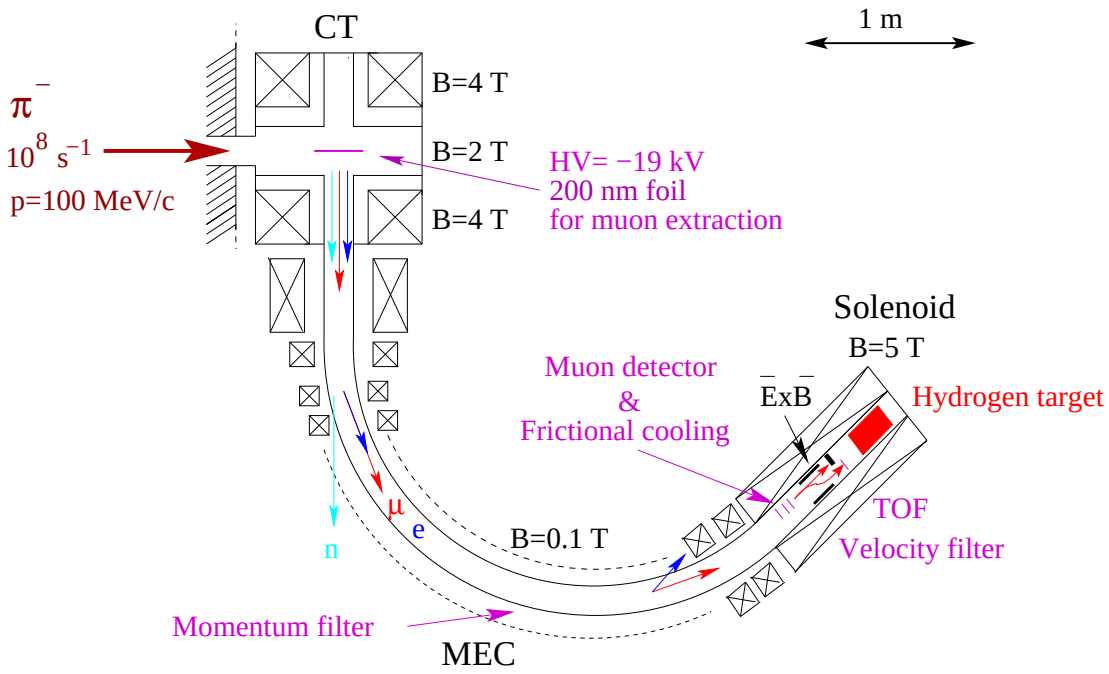

Figure 3.1: Lay–out of the muon beam, with cyclotron trap CT, muon extraction channel MEC and 5 Tesla solenoid.

muons [44] cannot be used for negative muons since they are forming exotic atoms.

The beam line producing the ultra–low energy negative muons consists of the cyclotron trap (CT) [45–47] for the production of low energy muons, the muon extraction channel (MEC) for their transport and selection, and a 1 m long 5 T solenoid with two transmission detectors for the muon trigger (see Fig. 3.1). The solenoid also encloses the hydrogen gas target with its detectors. The features of these three components of the beam line, which provide a ultra–low energy muon beam with small transverse size and low background are explained in the following sections. A photo of the PSI πE5 area with the muon beam line is shown in Fig. 3.2.

3.1.1 Cyclotron trap

The cyclotron trap developed by L. Simons is a magnetic trap produced by two superconducting ring coils at a distance of about 40 cm giving a magnetic field of 2 T in the median plane and 4 T at the coil centers (see Fig. 3.3). Negative pions (10^8 s^{-1}) with a momentum of 102 MeV/c with a momentum spread of $\Delta p/p = \pm 6\%$ (FWHM) from the πE5 channel are tangentially injected in the median plane of the trap where they hit a moderator. The position (radial: $r \sim 10$ cm) and thickness (5.4 g/cm^2) of the moderator are chosen such that the pions have a precession trajectory when they exit the moderator which minimizes the chance of a second hit on the moderator. After moderation the pions have a momentum of $40-60$ MeV/c, *i.e.*, near the "magic momentum" of 40 MeV/c which is optimal for the generation of muons at low energy. This feature maximizes the number of axially extracted muons.

About 30% of the moderated pions decay in flight into muons before returning back to the moderator or hitting the wall of the target vessel. Only a few percent of these muons have suitable momenta and angles accepted by the magnetic quasi–potential–well (radial

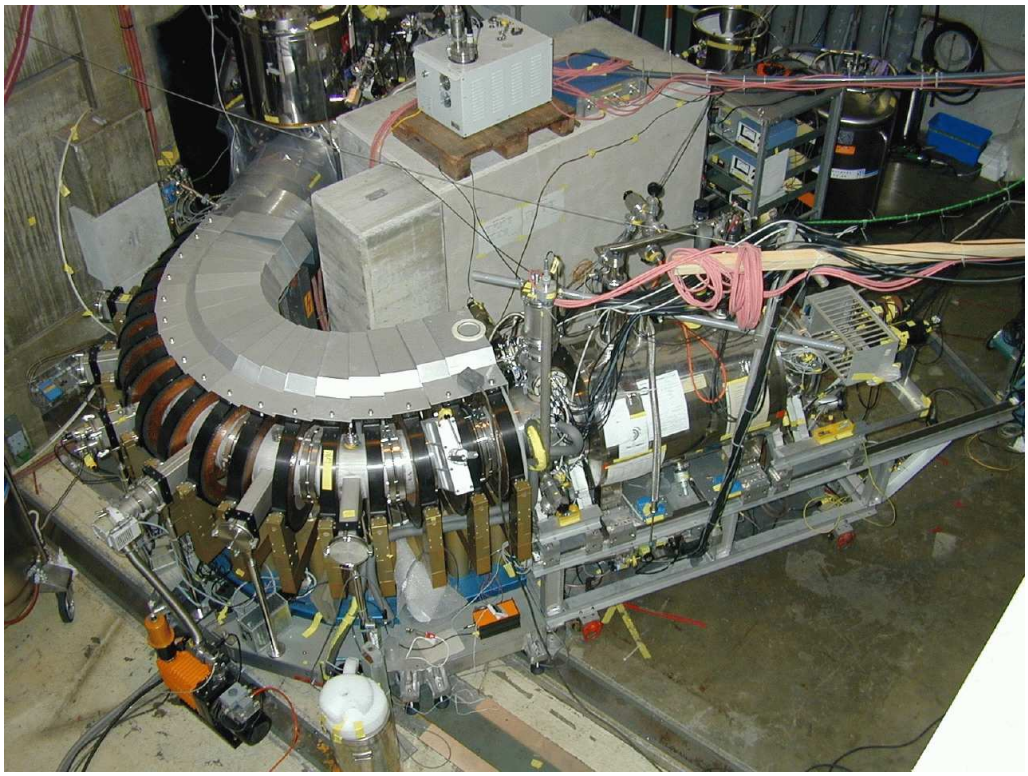

Figure 3.2: Photo of the PSI πE5 area. Hidden behind the concrete block in the upper part of the picture there is the CT. Partially visible is only the liquid helium vessel (metallic cylinder) for the superconducting coils. The curved structure composed by 17 ring coils is the MEC, which connects the CT with the 5 T solenoid (metal cylinder in right front). The dimensions of the apparatus may be compared with the size of the large concrete block which is $2 \times 2 \times 1$ m^3. The function of this concrete block is to shield the detectors mounted inside the bore-hole of the solenoid from neutrons originating mainly from the region around the CT.

and axial) formed by the CT field. Muons confined radially and axially are moderated when crossing a thin Formvar foil (cf. §3.2.4) of 20 μg/cm^2 (160 nm) thickness and 17 cm diameter placed in the median plane of the CT (see Fig. 3.3). On average the foil is crossed several hundred times. Muons produced at kinetic energies of a few MeV are thus decelerated within their lifetime to $10 - 50$ keV where axial extraction occurs. The axial magnetic confinement can be described by a quasi–potential which decreases with decreasing particle momentum and has a minimum in the median plane of the CT, as shown in Fig. 3.3. The Formvar foil is kept at negative high voltage. At sufficiently low muon energies, the electric force dominate over the magnetic confinement, and the muons leave the CT axially. A more quantitative discussion of this process is given below.

Inside the CT there is a high flux of neutrons, gamma rays *etc.* produced by pions stopping in the walls. This is a motivation for a concept where the muons, after moderation to keV energy, are extracted from the CT and guided to a separate measuring region, before they form muonic atoms.

In a uniform magnetic field a muon spirals along the magnetic field lines with a radius a [48]

$$a = \frac{p_\perp}{eB} \tag{3.1}$$

where $p_\perp$ is the transverse momentum of the particle and B the magnetic field. It can be

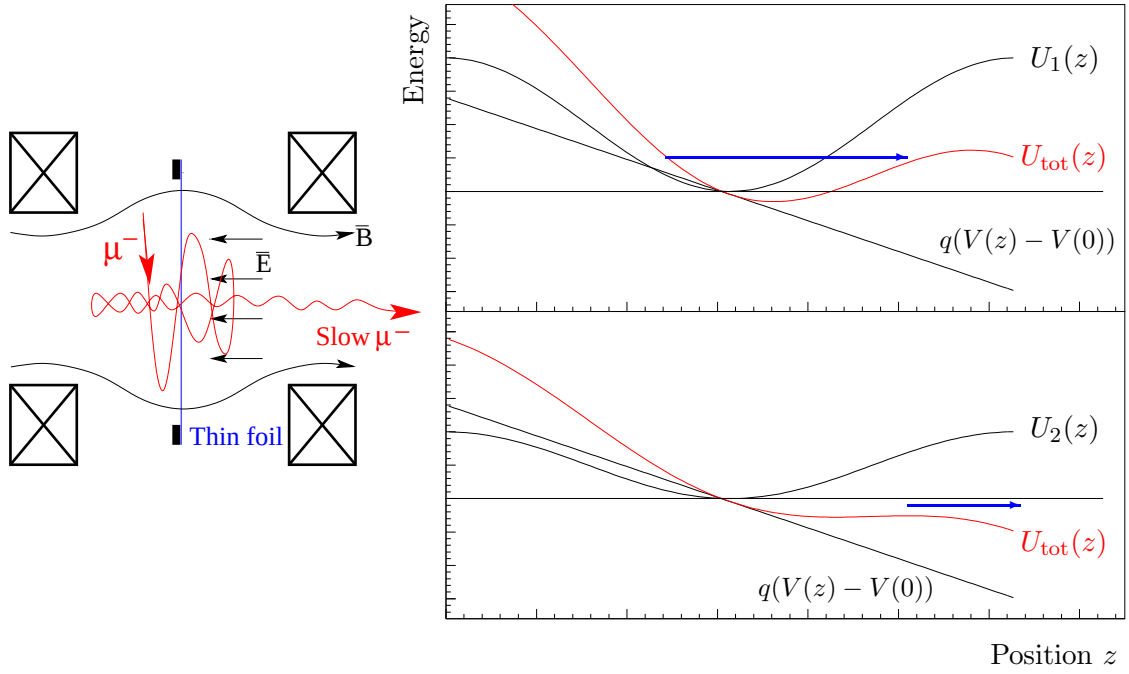

Figure 3.3: (Left): Schematic view of the CT for a plane containing the trap axis along which the muons are extracted. A thin foil (20 μg/cm^2) is used to slow down the muons during their lifetime and to produce an axial electric field for extraction. (Right): Principle of the axial extraction of the muons from the CT trap. The quasi–potential $U_i(z)$ depends on the transverse momentum. The potential related to the electric field caused by the foil in the center of the CT is $q(V(z)-V(0))$. The sum of the quasi–potential and the electrostatic potential is $U_{\rm tot}(z) = U(z) + q(V(z)-V(0))$. On the top figure the extraction does not occur due to magnetic reflection, whereas it occurs in the bottom figure ($U_2 < U_1$). Note that the plotted $q(V(z)-V(0))$ potential do not represent the real situation but MC simulations show that the resulting number of extracted muons is not affected by this simplification.

shown (see for example Ref. [48]) that for slowly varying fields the magnetic flux through the orbit of a particle is an adiabatic invariant. This constancy of flux can be expressed in several ways, *e.g.*,

$$\left.\begin{array}{l} Ba^2 \\ p_\perp^2/B \end{array}\right\} = \text{constant} \; . \tag{3.2}$$

The axial (parallel) momentum at any position along the z-axis can be determined by combining the second equation and the fact that the momentum of a particle in a magnetic field is constant,

$$p_\parallel^2(z) = p^2(0) - p_\perp^2(0)\frac{B(z)}{B_0} \tag{3.3}$$

which leads to the axial quasi–potential

$$U(z) = \frac{1}{2}\frac{p_\perp^2(0)}{mB(0)}B(z) \; . \tag{3.4}$$

This means that with increasing magnetic field the axial kinetic energy $T_\parallel = p_\parallel^2/2m$ is converted into transverse energy $T_\perp = p_\perp^2/2m$, until $T_\parallel$ vanishes, and the particle turns then back in the opposite direction (reflection). The CT is therefore a trap for particles

which satisfy the condition

$$\left|\frac{p_{\parallel}(0)}{p_{\perp}(0)}\right| < \left(\frac{B_{\max}}{B(0)} - 1\right)^{1/2} . \tag{3.5}$$

The basic idea of the extraction developed by L. Simons, F. Kottmann, and D. Taqqu, is to add an axial electric field E, parallel to the magnetic field in the central region of the CT. To produce the required DC electric field the Formvar foil is made conductive by sputtering on its surface a 3 nm thick layer of nickel, and is kept at a high voltage of $V = -19$ kV (the CT walls are at ground potential).

When crossing this foil the muons lose momentum without changing their direction, *i.e.,* after each foil pass the ratio of $p_{\parallel}(0)/p_{\perp}(0)$ remains constant (neglecting angular scattering). In the axial direction the field acts as a magnetic bottle, where the relevant criterion is the angle of the momentum vector relative to the magnetic field lines, and not its absolute value. However the presence of the electric field leads to a dependency on the absolute momentum. Particles are extracted from the magnetic trap when [47]

$$T_{\parallel}(0) > T_{\perp}(0)\left(\frac{B_{\max}}{B_0} - 1\right) - qV . \tag{3.6}$$

where $T_{\parallel}(0)$, $T_{\perp}(0)$ and $B_0 \simeq 2$ T are respectively the axial kinetic energy, the transverse kinetic energy and the magnetic field in the trap center, $B_{\max} \simeq 4$ T the maximal magnetic field which is reached at the coil centers, $V \simeq -19$ kV the high voltage on the foil and $q = -e$ the muon charge ($qV > 0$). With decreasing energy the probability to turn the momentum vector out of the confinement regime into the loss (extraction) cone will increase. Muons having left the foil with low total kinetic energy will gain enough momentum in axial direction to leave through the loss cone. The muons exit the collimator in the axial bore hole (20×18 mm^2) of the trap at low energy because the electric force wins over the confining force of the magnetic mirror, when the (transverse) kinetic energy is low. The majority of the muons are extracted with $20 - 50$ keV energy. The minimal kinetic energy is given by the high voltage applied to the thin foil, *i.e.,* $T_{\min} \simeq 20$ keV.

However, a fraction of the muons is extracted also when no electric field is applied, because the momentum vector is turned by angular scattering (within the foil) into the magnetic loss cone which in our case has an opening angle of $\sim 45°$. Most of these muons are ejected at energies of a few keV since angular scattering increases with decreasing kinetic energy, but a few muons leave the trap at much higher energies of a few hundreds keV. The choice of the metalized Formvar foil was motivated not only by mechanical properties but also by its low–Z material composition (C, H, O and Ni) which leads to a small probability for large angle scattering, and therefore to a relatively low number of muons extracted at high energies.

A foil thickness of 20 μg/cm^2 is expected to be the optimum. A thinner foil does not sufficiently decelerate the muons during their lifetime, whereas thicker foils absorb too many low–energy muons before they may be extracted. Simulations predict that a stack of thinner foils kept at different potentials may lead to a better deceleration and less absorption of the muons. Such a configuration was tested in 2002 but its operation was unsuccessful due to plasma formation and hence discharge between the foils. Plasma formation is caused by traps formed by the combined effect of electric and magnetic fields.

The number of muons extracted (and detected) as function of the foil HV is given in Fig. 3.4. In the measuring period in 2003 only one foil was used in order to avoid plasma formation. Special care was taken in the design of the mechanical assembly of electrodes,

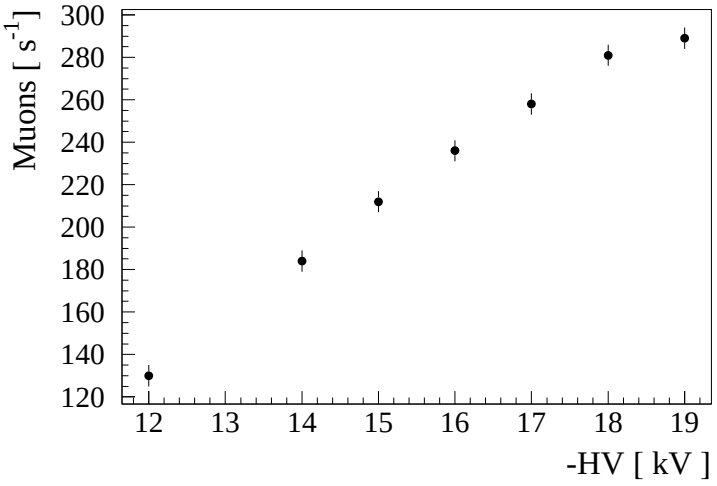

Figure 3.4: Number of "useful" extracted muons detected with the stack detectors (cf. §3.2) as function of the HV (negative value) on the foil placed in the center of the CT trap. Each signal in S_1 in coincidence with a signal in S_2 (with the correct time–of–flight delay corresponding to muon which stop in the hydrogen gas target) is considered a muon. The efficiency of this muon detection is approximately 35%. The measurements have been performed for a single foil of 20 μg/cm^2 thickness.

insulators, and HV cables, to avoid plasma discharges in the CT. For a single foil of 20 μg/cm^2 thickness, more than 800 s^{-1} muons have been measured to enter the target with energy between $2 - 6$ keV through a 16×6 mm^2 collimator.

3.1.2 Muon extraction channel

The extracted low–energy muon beam is highly contaminated with keV energy electrons (produced when charged particles spiraling in the CT cross the extraction foil), neutrons (produced by pions hitting the CT walls), high energy electrons from muons decay and muons with energies above 50 keV. Therefore a toroidal assembly of coils was constructed (see Figs. 3.1 and 3.2) in order to transport the "good" muons with $20 - 40$ keV energy from a region of high radiation to the 5 T solenoid where the laser experiment is performed. The toroidal MEC acts as momentum filter which has a high transmission for particles with momenta around 2 MeV/c corresponding to muons with 20 keV energy. It is made from 17 identical coils forming a toroidal magnetic field with 130° curvature and 1 m curvature radius with an average magnetic induction of 0.15 T.

If the magnetic field is radially symmetric it can be shown that the spiral center of a charged particle follows the magnetic field lines. Since the MEC magnetic field has a "small" horizontal gradient (toroidal shape), charged particles follow only approximately the magnetic lines. In our geometry the charged particles undergo a small vertical drift (out of the plane in Fig. 3.1) relative to the magnetic field lines. Particles with different momenta undergo different vertical drifts and thus momentum selection can be achieved by placing collimators at the correct vertical positions. This vertical drift caused by the gradient of the magnetic field in horizontal direction can be understood qualitatively as being the consequence of different gyration radii a as the particle moves in and out of regions of larger than average and smaller than average field strengths. Since $a \sim p_\perp$, higher momentum particles having larger gyration radii probe regions which have a larger

magnetic field differences relative to lower energy particles, and therefore undergo a more pronounced vertical drift. Similarly since $a \sim 1/B$ a smaller magnetic field induces larger vertical drifts. Monte Carlo simulations showed that 2 MeV/c particles undergo a maximal vertical drift relative to the magnetic field lines of about ~ 4.5 cm, whereas the high flux of keV energy electrons (low momentum $p_e \sim 0.14$ MeV/c for 20 keV energy) have an almost negligible vertical drift.

To keep the trajectory of the 2 MeV/c muons in a horizontal plane the 17 solenoids producing the toroidal field are tilted by $\sim 4°$ from the vertical axis. The magnetic field is kept at a relatively low level (0.15 T) for optimum filtering, *i.e.,* to enhance the drift of the particle. Consequently special care was taken to obtain adiabatic field gradients in the transition zones between CT and MEC, and between MEC and 5 Tesla solenoid. To guarantee adiabatic transport of the muons from the CT to the MEC two additional solenoids of 0.45 T and 0.25 T respectively have been inserted as shown in Fig. 3.1. No additional coils are required between the MEC and the 5 T solenoid which has no iron return yoke, contrary to the CT.

In summary the MEC acts as a cleaning filter separating muons with the desired momentum from the high flux of gamma rays, neutrons, electrons and too energetic muons which are present at the CT exit. Charged particles with momenta above 5 MeV/c (and neutral particles) are not transported through the curvature, and electrons of few keV energies are separated vertically from the muons by several cm in the toroidal field. Particles with about 2 MeV/c momentum are transported to the solenoid with 90% probability, regardeless of their masses. The majority of the electrons exiting the CT have momenta much higher than 2 MeV/c, *e.g.,* the fraction of muon decay electrons with energies below 5 MeV is only 2×10^{-3}. The 90% transport probability from CT to 5 T solenoid does not take into account muon decay. The corresponding muon time of flight is typically 1 μs.

A 1 m thick concrete block is inserted between the CT and the solenoid to absorb neutrons originating in the CT which do not stop in the CT walls and could reach the various detectors in the solenoid producing background (see Fig. 3.2).

3.1.3 The 5 T solenoid with the muon detector

The muon stop volume has to be kept as small as possible in order to match the requirements of high laser–induced transition probability and large solid angle for the x-ray detection. At a given gas density, the axial dimension of the stopping volume is determined by the muon energy distribution. In practice, the required muon energies have to be a few keV. To have a small transverse dimension of the stopping volume the gas target with x-ray detectors and cavity mirrors is mounted inside a superconducting solenoid (1 m long, 20 cm bore hole, 5 T magnetic field). The 5 T magnetic field ensures a small beam size since the particles follow the magnetic field lines and since their gyration radii are reduced accordingly to Eq. (3.1). Additionally the high magnetic field guarantees that the beam size defined by collimators (16×6 mm^2) is kept constant along the following beam path, in particular in the gas target where large angle scattering occurs. Before entering the hydrogen target, muons are slightly compressed in phase space, decelerated to $3 - 6$ keV, and detected to trigger the laser and the data acquisition system.

The apparatus mounted inside the solenoid is shown in Fig. 3.5. The muons first cross a transmission detector (S_1). It is a nontrivial task to detect keV energy muons (which have a range of only ~ 20 μg/cm^2) without stopping them. The detector consists of several rings defining a potential with an "uphill" and a "downhill" region for the

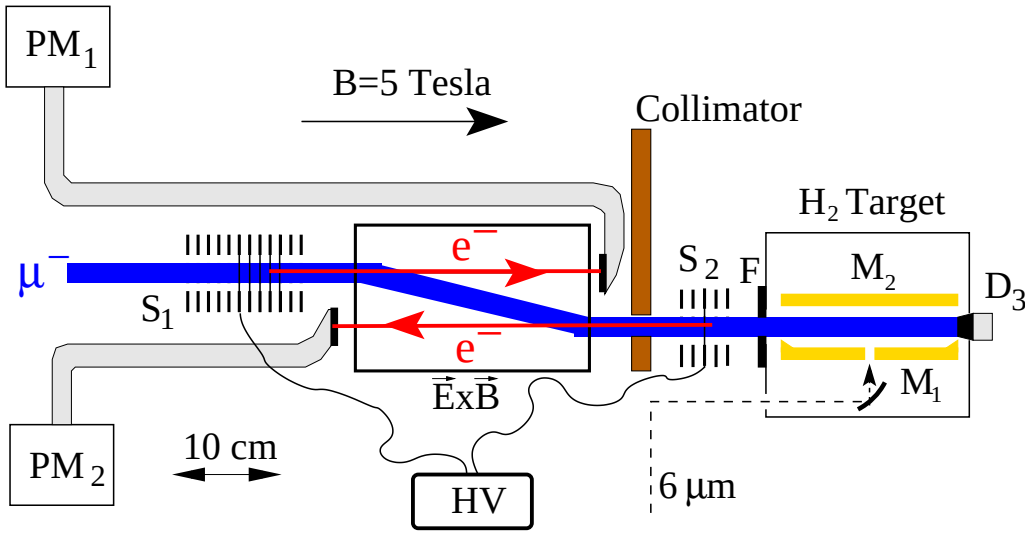

Figure 3.5: Schematic view of the apparatus mounted inside the 5 T axial solenoid. The picture is not to scale. The muons enter from the left and cross two stacks of ultra–thin carbon foils, S_1 and S_2, which act together with PM_1 and PM_2 as two muon detectors. The $\vec{E} \times \vec{B}$ filter (shown in side view) separates μ^- from e^-. The gas target is filled with 0.6 hPa hydrogen gas and it is separated by the vacuum of the muon beam line by a 30 nm thick Formvar foil (F). The laser cavity mirrors (shown in top view) are placed sideways of the muon stop volume. The 6 μm laser light enters the vacuum vessel and the gas target and reaches the multipass mirror cavity (M_1, M_2) through a hole in M_1. The detector D_3 detects muons which did not stop in the hydrogen gas. Two LAAPD arrays are mounted above and below the muon stop volume (not shown in the picture).

negatively charged muons (see Fig. 3.6). Five of these rings are used as a support for ultra–thin conducting carbon foils with 4 μg/cm^2 thickness, the so called "stack of C-foils". These five rings are kept at typical high voltage of -12.5, -10.7, -8.9, -7.1 and -5.3 kV, respectively. The resulting axial electric field between foils accelerates the charged particles. This acceleration partially compensates for the muon energy loss in the foils, decreasing therefore the probability that a muon is absorbed in the (following) foils.

Moreover when muons cross the C-foils, secondary electrons are emitted and are accelerated by the stack electric field towards a downstream plastic scintillator connected with an external photo multiplier tube (PM_1) via a long Lucite light–guide (Fig. 3.5). Between stack and scintillator an $\mathbf{E} \times \mathbf{B}$ filter induces a velocity dependent transverse drift. The drift velocity

$$v_D = \frac{E}{B} \tag{3.7}$$

leads to a drift of

$$x_D = \frac{E}{B}\frac{l}{v_{\|}} \tag{3.8}$$

where $l = 29$ cm is the axial length of the electric field, and $v_{\|}$ the axial speed of the charged particle. The electric field is produced by a 29 cm long plate capacitor held at -3 and $+6$ kV at a distance of 2 cm. Muons of about 8 keV energy exiting S_1 are shifted vertically by $x_D \simeq 8$ mm, and therefore pass the scintillator. On the contrary the much faster electrons released in the stack foils are not noticeably shifted by the electric field ($x_D \simeq 0.6$ mm) and therefore hit the scintillator producing a S_1 signal. Note that the $\mathbf{E}\times\mathbf{B}$ filter is acting as a mass filter for particles with the same momentum. The S_1 foil stack

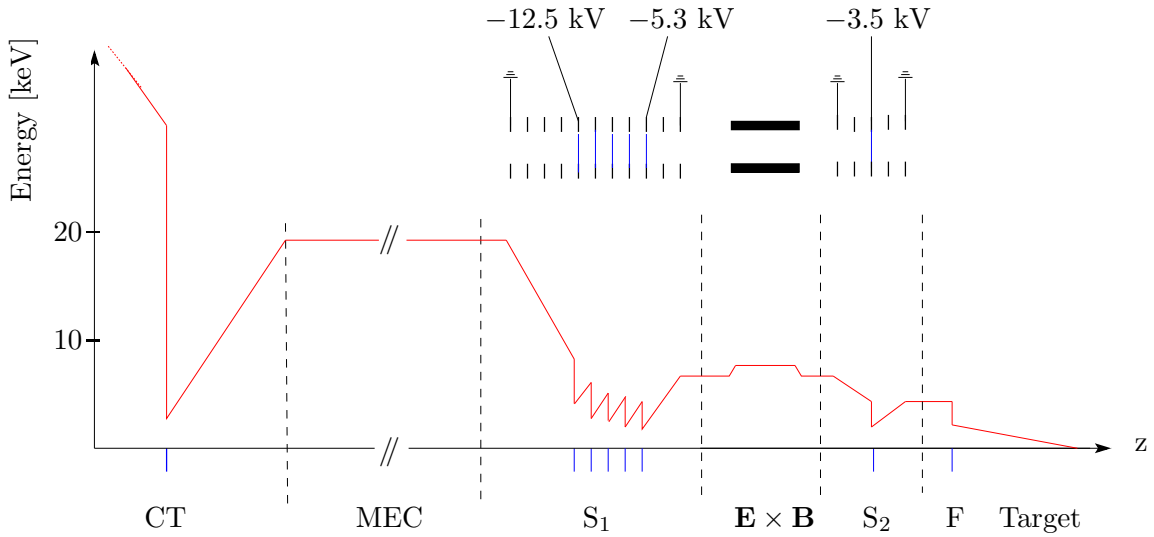

Figure 3.6: Muon kinetic energy between the CT trap and the hydrogen gas target. The position of the several foils is marked (blue lines) on the z-axis. On top are shown S_1, $\mathbf{E}\times\mathbf{B}$ and S_2. When muons cross the 30 $\mu g/cm^2$ foil in the center of the CT, they lose $20-50$ keV energy, depending on energy and angle. From the CT center they undergo an axial acceleration which is sufficient for extraction. In the magnetic field of the MEC the muon kinetic energy does not change. Similar as in the CT, the increase of magnetic field experienced by the particles leaving the MEC and entering in the 5 T solenoid does not change the total particles energies. However a conversion of translational (axial) kinetic energy into energy of rotation (transverse) occurs. Since the first foil of S_1 is at a voltage of -12.5 kV, the muons loose 12.5 keV kinetic energy before reaching the first carbon foil. The 4 $\mu g/cm^2$ thickness ($\sim$ 20 nm) of these foils causes an energy loss of about 2.5 keV. The muons are then accelerated towards the remaining foils which are held at progressively lower potentials (-10.7, -8.9, -7.1, -5.3 kV respectively). Further downstream the muons enter into a region of transverse electric field produced by two parallel plates held at $+6$ and -3 kV, respectively. Muons traveling in the central plane between the two plates experience an increase of potential of $+1.5$ kV. Before being stopped in the hydrogen gas target the muons cross the S_2–foil and the 4 $\mu g/cm^2$ target window (Formvar (F)). In the target they progressively loose energy with an average stopping power of 2×10^{-15} eV cm^2/atom. Some muons reach the gold surface at the target end which partially acts as a reflector.

acts simultaneously as a detector for keV–muons, reduces the muon energy (energy loss in foils) and reduces the phase space volume of the muon beam by frictional cooling [49].

Further downstream the muon crosses a second stack (S_2) with only one C-foil, placed in front of the target (see Figs. 3.5 and 3.8). The released secondary electrons are accelerated upstream (anti–parallel to the muon beam) and detected by another plastic–scintillator assembly, providing a second muon signal S_2.

Muon detection efficiencies of 88% and 42% are measured for the first and the second stack, respectively. This difference is given by the different number of carbon foils and the different muon kinetic energies. The stack detectors have time resolutions better than 10 ns.

Muons leaving the second stack cross the target window (F) which separates the vacuum from 0.6 hPa of hydrogen. At the end of the gas target a LYSO (Lutetium Yttrium Orthosilicate doped with Cerium) scintillator read out with a photomultiplier (D_3 in Fig. 3.5), is installed as anti–detector for muons which do not stop in the gas (cf. §3.2.3).

The evolution of the muon kinetic energy from the CT until it is stopped in the hydrogen gas target is plotted in Fig. 3.6.

If a muon induces a signal in both S_1 and S_2 detectors with the correct time delay (TOF corresponding to axial kinetic energies of muons which efficiently stop in our target), there is a "good" muon entering the target. If in addition, no signal is detected in D_3, the muon is accepted and a trigger for the pulsed laser and the data acquisition system is delivered. Hence these $S_1 \cdot S_2 \cdot \bar{D}_3$ signals, properly anti–gated by the laser dead time, provide an electronic trigger signal for the laser.

The rate of muons detected as $S_1 \cdot S_2$ coincidence within a TOF–interval corresponding to kinetic energies of 3−6 keV, is 320 s^{-1}. It drops to 240 s^{-1} when the D_3 anti–coincidence is active. In summary a muon stopping rate of 70 s^{-1} is achieved for a hydrogen gas pressure of 0.6 hPa, in a stop volume of $5 \times 15 \times 194$ mm^3, with a muon energy in front of the target window of $3 - 6$ keV. The difference between the $S_1 \cdot S_2 \cdot \bar{D}_3$ signal rate and the muon stopping rate has several reasons: muon stop in the S_2 foil or entrance window, muon decay before muon stop, and inefficiency of the D_3 detector.

3.2 Gas target

The hydrogen gas target with the 2 keV x-ray detectors and the multipass cavity for the laser light is located inside the PSC solenoid which is kept under vacuum. A schematic view of the target assembly is shown in Fig. 3.7. Muons with a few keV energy cross the entrance window (19×8 mm^2), a thin foil of 4 $\mu g/cm^2$ supported by gold–plated tungsten wires (15 μm diameter, 0.4 mm spacing), separating 0.6 hPa of hydrogen gas from the vacuum of the muon beam line. They stop in a volume of $5 \times 15 \times 194$ mm^3 which is elongated in direction of the muon beam because of the low hydrogen pressure. Two rows of 10 LAAPDs (13.5×13.5 mm^2 active area each) as detectors for 2 keV x rays are mounted at the top and bottom side of the muon stopping volume, and two mirrors at the left and right side to enhance the laser light intensity for the $2S - 2P$ transition. The laser light illuminates the stop volume transversely, because it is not possible to mount laser mirrors on the muon beam axis. The vertical dimension of the laser mirrors is made as small as possible since the x-ray detectors have to be positioned as close as possible to the muon beam to enhance solid angle. A mirror height of 12 mm turned out to be large enough to illuminate a 7 mm high volume, and the LAAPDs are at a distance of 8 mm from the muon beam axis. In front of the LAAPDs 2 μm thick polypropylene foils are

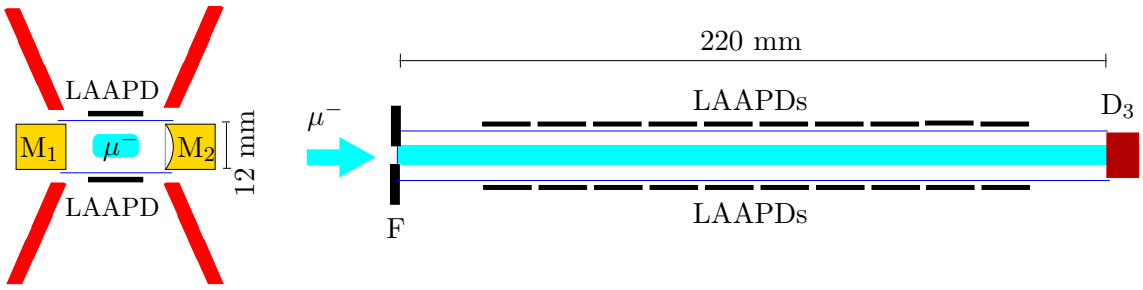

Figure 3.7: (Left): Schematic view of the target for a plane perpendicular to the muon beam axis. (Right): Schematic view of the target for a vertical plane containing the muon beam axis. Cyan: muon stopping volume, Red: electron paddles, Black: LAAPDs, Blue: entrance (Formvar, F) and LAAPDs (polypropylene) windows, Dark red: D_3 detector, Gold: M_1, M_2 laser cavity mirrors.

installed as vacuum windows with a good transparency ($\sim 94\%$) for 2 keV photons.

Laser light enters the target via a CaF_2 window. It is then focused by an off–axis parabolic mirror into a small hole of 0.6 mm diameter in one of the cavity mirrors. The light then spreads out between the two mirrors, illuminating the muon stop volume. Fig. 3.8 shows the target chamber (opened) used in the 2002 beam time (with only 6 LAAPDs per side).

3.2.1 Detectors for the 1.9 keV energy x rays: the LAAPDs

Our experiment requires the detection of laser–induced 1.9 keV x rays of the muonic hydrogen K_α transition. There are several critical constraints restricting the possible choice for the x-ray detector. The x-ray detector has to be compact (the whole target assembly with cavity mirror and detectors has to fit in the 20 cm diameter bore hole of the 5 T solenoid) and has to be insensitive to the strong magnetic field. It has to reach an energy resolution of 30% and a time resolution below 50 ns for 1.9 keV photon energy in order to keep the background at a low level. Due to the low signal rate, the solid angle for x rays has to be maximized, *i.e.,* the detector has to have a large area and has to be mounted as near as possible to the volume where the muonic hydrogen atoms are formed. Additionally the detector is mounted in vacuum and in an environment with a rather high

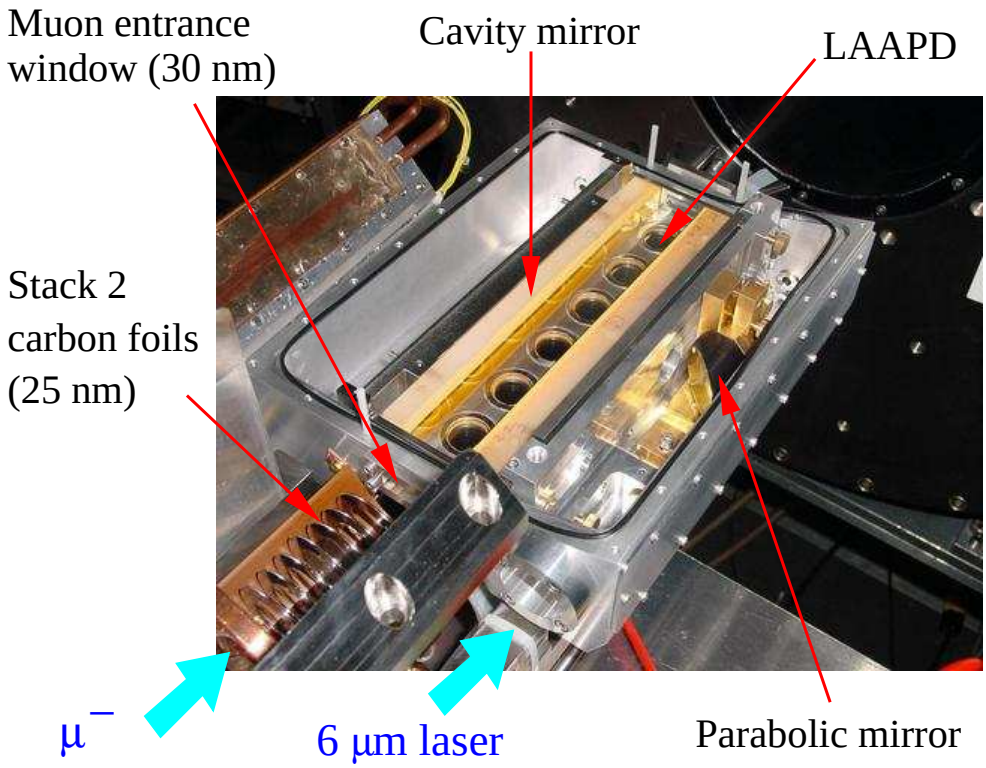

Figure 3.8: Picture of the open target for the beam time 2002. Muons stop between the mirrors of the laser cavity (golden surface) which are 190 mm long. A laser pulse is reflected and focused by the parabolic mirror, and is injected into the multipass cavity via a hole in one of the mirrors. The light homogeneously spreads out between the two mirrors. The laser–induced events are detected by the LAAPDs (black round spots). In the beam time 2003 we have replaced the 12 round shaped LAAPDs [50] with 20 square shaped LAAPDs [51] to enhance solid angle for x-ray detection.

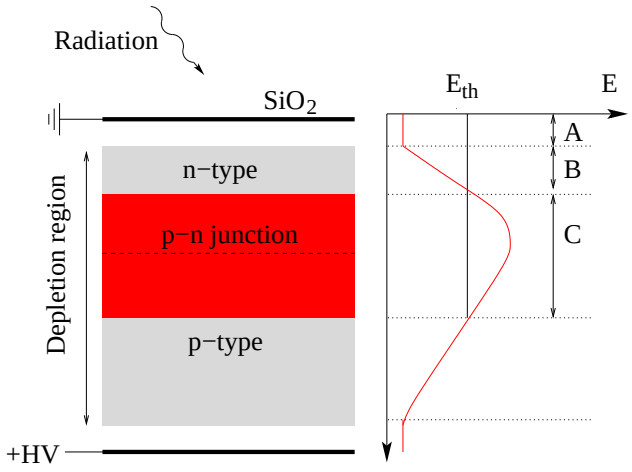

Figure 3.9: Schematic view of an LAAPD with its electric field distribution. X rays absorbed in the first protective layer of the LAAPD (SiO_2) do not give any signal. Only x rays absorbed in region (B) can undergo a full gain amplification. For x rays absorbed in region (A) a fraction of the generated primary charge is lost before the multiplication region is reached, whereas x rays absorbed within the amplification region (C) undergo only partially the multiplication process. E_{th} is the threshold electric field above which charge amplification occurs.

level of neutron–induced radiative processes as well es electromagnetic and acoustic noise. Large area avalanche photodiodes (LAAPDs) have been chosen as x-ray detectors [52–56].

LAAPDs are silicon photodiodes (p-n junctions) with internal gain. This gain ($< 10^3$) is obtained applying a high reverse bias voltage to the photodiode, which establishes an intense electric field inside the LAAPD. Figure 3.9 represents schematically a LAAPD section and the electric field inside the photodiode. Electron–hole pairs are produced by the impinging radiation (light, x rays, charged particles). The number of those pairs scales linearly with the energy of the absorbed particle. The primary electrons are accelerated by the electric field. The energy reached by the accelerated electrons in the p-n junction is sufficient to ionize silicon atoms, producing new electron–hole pairs. The produced secondary electrons are also accelerated by the field, producing an avalanche process which is then collected at the cathode.

The active zone can be divided into three different regions (see Fig. 3.9), with different time and amplitude responses to the absorbed x ray. X rays absorbed in the drift region (A) produce electrons that drift slowly towards the depletion region (B) due to the weak electric field. When those electrons reach the depletion region they are quickly conducted to the multiplication region (C) where the amplification occurs. Due to the slow drift in the drifting region electrons may be captured. The possible electron capture causes a decrease of the pulse amplitude. If the x rays are absorbed in the depletion region (B), the produced electrons rapidly move towards the multiplication region where they undergo an amplification equal to the photodiode gain. The amplitude of this pulses follow a Gaussian distribution. X rays absorbed in the multiplication region (C) produce electrons that will be only partially amplified. The amplitude of these pulses varies continuously down to zero. The signal arising for an x ray which is absorbed behind the multiplication region is given only by the primary generate charge. X rays of a few hundred keV energy absorbed in this region (with very low probability) may generate pulses similar to a 2 keV x ray undergoing an amplification process.

X rays may be absorbed in any of the three regions giving rise to an energy spectrum

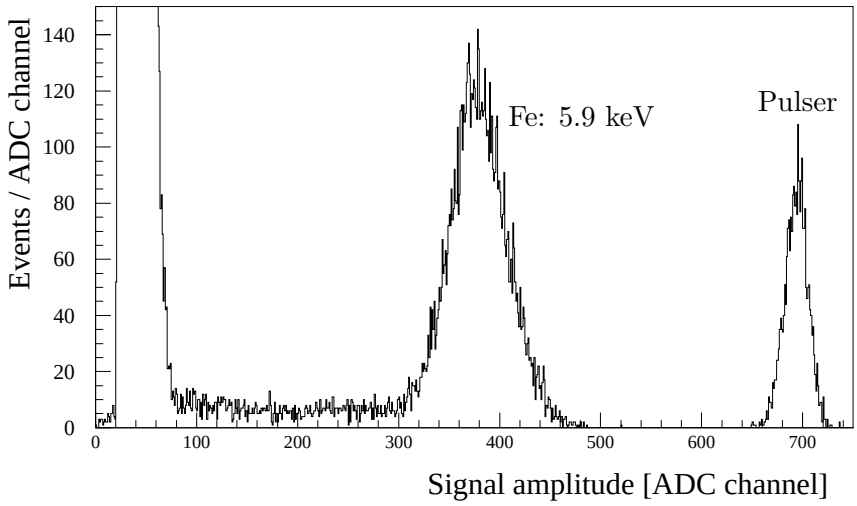

Figure 3.10: Measured energy spectrum when the LAAPD is irradiated by a ^{55}Fe source (5.9 keV). The peak arises from x rays absorbed in region (B) whereas the tail originates from zone (A) and mainly (C). On the right side there is a peak which arises from a pulse generator. To its width contributes only the electronic noise (mainly preamplifier) but not any physical processes in the LAAPD.

(amplitude distribution) as shown in Fig. 3.10 for a measurement of the 5.9 keV energy transition of an iron source. The tail in the lower energy side is associated with pulses originated in zone (A) and (C). This tail to lower energy represents a source of background for our experiment. In fact any particle with energy higher than 2 keV may induce a signal in the LAAPDs which fake a 2 keV particle. As will be seen later background processes are given by μC lines with energy between 5 to 90 keV (see Table H.1). Since the LAAPDs thickness that is useful for x-ray detection is only a few tens of micrometers, their detection efficiency decreases rapidly for x-ray energies above 5 keV (see Fig. 5.10). X rays with energies above 5 keV are predominately absorbed in region (C) since it is the thicker region and therefore they shows a large tail in the 2 keV region.

The dark current of the LAAPD–preamplifier system limits the achieved detector energy resolution and the "minimum detectable energy". Dark current results mainly from the thermal generation of electron–hole pairs in the LAAPD and in the FET (field effect transistor) at the preamplifier input, and therefore the dark current is strongly reduced with decreasing temperature of the detector and the preamplifier. Additionally the LAAPDs gain strongly increases with decreasing temperature since the resistivity of crystalline silicon decreases with decreasing temperature. We have therefore cooled and stabilized ($\pm$0.1 K) the whole LAAPD–preamplifier system to -30°C by circulating cold ethanol through a small heat exchanger which was in thermal contact with the LAAPD mount.

At low gain values the energy resolution improves with increasing gain, up to a gain around 200 where the optimum is obtained for the 5.9 keV x rays. Higher gain increases the effect of spatial non–uniformity of the LAAPD gain and also the dark current. However we have operated our LAAPDs at gains of $200 - 400$ to ensure that the amplitude of the 1.9 keV x ray signal is sufficiently above the noise level without worsening the resolution. The resolution (FWHM) obtained for 5.9 keV x rays was 11% for the best LAAPDs and 15% on average, whereas for the μp K_α x rays the measured average value was of 32% [52] (cf. §5.3). The above results are obtained with RMD LAAPDs [51]. At the preamplifier's

output, the height of a 1.9 keV x–ray signal is about 2 mV. The signal rise time was of the order of 100 ns. After further amplification the signals were sent from the beam line region to the counting room (40 m distance) and stored in an 8 bit wave–form digitizer ("Flash ADC", FADC), operated at 140 MHz.

3.2.2 Electron detectors

About 0.5 laser–induced events per hour are expected on resonance (cf. §6.5). As only a small fraction of the triggers can result in a $2S - 2P$ transition, the background has to be kept very low. This is achieved by requiring the detection of the muon decay electron ($\mu^- \to e^- \nu_\mu \bar{\nu}_e$) after the detection of the 1.9 keV K_α x ray. The signature of the laser–induced transition is given by the detection of a 2 keV x ray in the laser time window, *i.e.,* at times where the laser is illuminating the muonic atom. Requiring the detection of a delayed electron (with respect to the x ray) ensures that the measured x ray signal is correlated with a muonic atom deexcitation and reduces therefore the background in the laser time window.

Four plastic scintillator plates ("electron paddles", $250 \times 60 \times 5$ mm^3) mounted in an X-shape (see Fig. 3.7) are dedicated for this purpose. They are grouped in two pairs, each one connected with a PMT via a Lucite light–guide. Muon decay electrons spiraling in the magnetic field hit these scintillators and deposit up to MeV energy. Additionally also the LAAPDs and the D_3 detector contribute to the detection of the electrons giving a total electron detection efficiency of 65.4% in a time interval $0.1 - 7.1$ μs relative to the 2 keV x-ray time [16].

3.2.3 Anti–coincidence detector

An anti–coincidence detector (D_3) for muons entering the target but not stopping in the hydrogen gas was implemented. For the trigger of the laser and data acquisition system, additional to the $S_1 \cdot S_2$ coincidence, it is required that D_3 does not detect any signal. Thus the laser and the data acquisition system are triggered only for muons which have crossed S_1 and S_2 but did not reach D_3 (see Fig. 3.7). The implementation of D_3 in the 2003 run allowed us to lower the hydrogen gas pressure from 1.4 hPa (in 2002) to 0.6 hPa, at a comparable event rate, since this rate is mainly limited by the laser repetition rate and not by the muon stopping rate.

The B-field of the solenoid keeps the transverse muon beam size to the value given by the collimator, and therefore muons not stopping in the gas target hit a small area at the end of the target vessel. The D_3 detector is made by a ~ 0.12 μm thick layer of gold evaporated on one side of a LYSO scintillator crystal ($34 \times 24 \times 20$ mm^3). The opposite side is glued on a Lucite light–guide which transports the scintillation light to a PMT.

When a muon impinges on the gold surface of the D_3 detector, it is either captured by the high–Z gold atoms, or it is back–scattered into the gas. If the muon is absorbed in the gold, a muonic cascade immediately occurs which produces x rays from a few hundreds keV to several MeV energy, and Auger–electrons of keV energy. The x rays in the hundred keV region are optimally detected since they escape from the gold layer and are absorbed ($\sim 50\%$ solid angle) in the scintillator. Part of the MeV energy x ray escape the LYSO scintillator since the attenuation length of 1.15 cm at 511 keV is of the order of the crystal dimension. The probability that a muon transfered to gold is detected is expected to be close to unity.

If the muon is not absorbed in gold it is back–scattered into the hydrogen gas. At our conditions a reflection probability of about 60–80% was deduced from the data [16]. Therefore the anti–coincidence detector not only increases the trigger quality, *i.e.,* the fraction of muon stops per trigger, but due to its reflection property it increases also the absolute number of muon stops.

A disadvantage of the anti–coincidence detector is that it introduces an additional delay between μp formation and arrival time of the laser pulse. The trigger for the laser being $S_1 \cdot S_2 \cdot \bar{D}_3$, an additional delay of 200 ns relative to the $S_1 \cdot S_2$ coincidence has to be introduced, corresponding to the maximum time required for a muon to travel from S_2 to D_3.

3.2.4 Intermezzo about foils

Several types of foils have been used in our target and beam line; specifically the Formvar foil in the CT, the carbon foils in the stack detectors, the Formvar foil of the target muon entrance window, and the polypropylene and lithium foils in front of the LAAPDs.

– *Polypropylene foil in front of the LAAPDs:* These foils placed in front of the LAAPDs separate the hydrogen gas target from the vacuum system. Their thickness is about 2 μm (200 μg/cm^3). They also stop μp_{1S} atoms drifting towards the detectors which could produce a dangerous background.

  If μp atoms strike the LAAPD material (Si), muon transfer from the proton to the Si atoms occurs, and μSi is formed in a highly excited state. The following muonic cascade would represent a dangerous source of background at the time where the laser events are expected. Especially refilling of the possible K-electron vacancies produces x rays of 1.74 keV energy (with 75% yield) which would fake laser–induced K_α x rays.

  Fortunately no muon transfer to Si but to C occurs, because the μp_{1S} atoms hit the polypropylene ($\sim (CH_2)_n$) windows in front of the LAAPDs. The related μC^* deexcitation is also a source of background (cf. Chapter H). However it generates much less background for three reasons. First, the yields for x rays with energies in the 2 keV region are reduced due to Auger emission (see Table H.1). Second, the Auger electrons emitted with energies from few keV to few tens of keV do not reach the detector surface, since their gyration radius is < 0.1 mm, in the magnetic field, whereas the distance foil–detector is ~ 1 mm. Moreover, refilling of the K-vacancies originate x rays of 0.28 keV energy which are not seen in the LAAPD.

  The $\mu p \rightarrow \mu C$ transfer cross section is $\sigma^{\rm exp}_{\rm transfer} = 3 \times 10^{-19}$ cm^2 for μp atoms with 2 eV kinetic energy [57]. This energy represents approximately the maximal kinetic energy of the μp atoms hitting the foils at the time when the laser enters the mirror cavity. Taking into account the angle and kinetic energy distributions of the μp atoms imping on the foil surface and possible scattering processes, a foil of 3 μm thickness is expected to absorb the majority of the μp.

– *Li foils and radioactive coating of the enhancement cavity.* We anticipate at this point (cf. § 4.11) that the mirrors of the laser cavity (M_1 and M_2 in Fig. 3.7) have 26 layers of ZnSe and ThF_4 as dielectric coating. The LAAPDs are therefore exposed to α particles produced by Thorium decay if they were not protected by Li foils mounted in front of the polypropylene windows. Figure 3.11 shows the energy spectrum of the

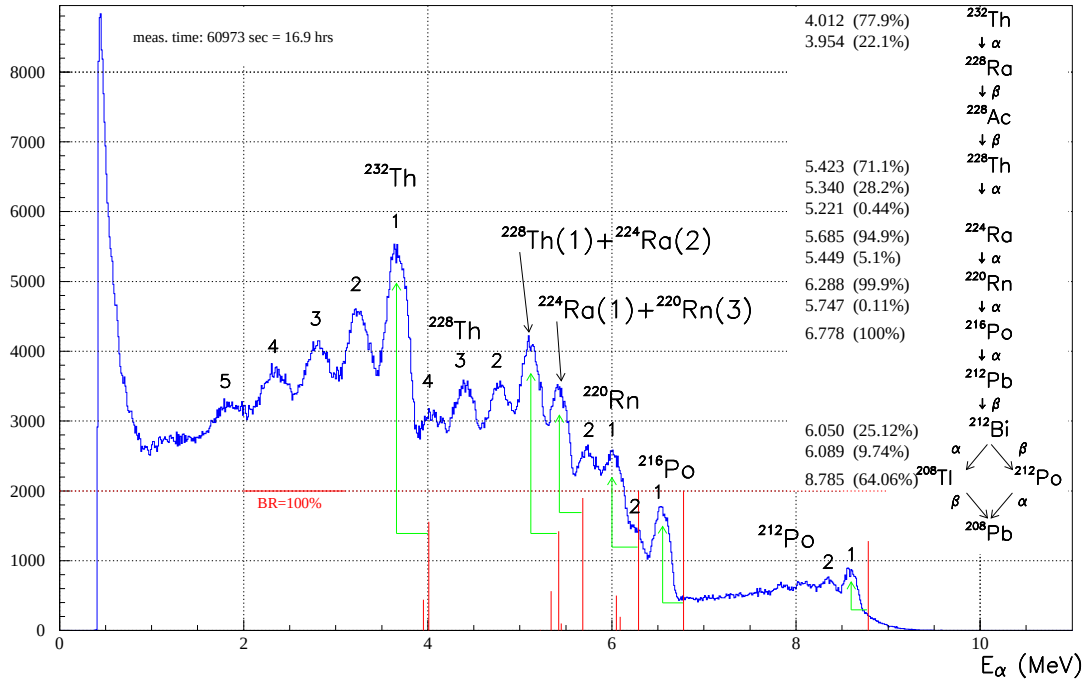

Figure 3.11: Energy spectrum of the α particles emitted by the Th present in the dielectric coating of the 6 μm cavity mirrors. The short vertical lines represent the expected energies of the α particles. The energy loss of the α particles when crossing material is leading to this structure. Those α particles which need to cross only one ZnSe layer cause the peaks numbered 1. ZnSe is the outermost layer of the coating. The peaks No. 2 are caused by α particles which have to cross two ZnSe and one ThF_2 layer, and so on.

emitted alpha particles measured by a Germanium detector. The problem is that α particles cause very large signals attributed to plasma discharge in the avalanche region which led to instabilities in the LAAPDs operation. Two out of 12 API LAAPDs [50] were even destroyed after a week of irradiation during the 2002–run.

To avoid the risk of LAAPD damage or slow deterioration, we shielded the LAAPDs during the data taking in 2003 with a 175 μm thick lithium sheet. The lithium was sandwiched between two 1 μm thick polypropylene foils in order to avoid oxidation (when exposed to air during installation) and placed at the inner side of the window foils. No chemical reaction of Li with (0.6 hPa) hydrogen gas was observed after several weeks of operation.

The Li sheet turned out to be sufficiently thick to absorb the α particles. Unfortunately Li also partially absorbs the K_α x rays. About 60% of the 1.9 keV x rays are absorbed by the various layers which are placed in front of the LAAPDs (see Fig. 5.10).

– *Formvar foil in the CT, and target entrance window:* The characteristic of these foils is that they are very thin. They have been produced in our group by dissolving Formvar (82% poly–vinyl–acetat, $\sim C_5O_2H_8$) in 1,2–Dichlorethan, and by homogeneously spreading this solution over a water surface [58]. The solvent immediately evaporates and a thin foil is left on the water surface which can be carefully fished out. For the CT, foils with 17 cm diameter and thicknesses down to about 10 $\mu g/cm^2$ ($\sim$ 80 nm)

have been produced which have been made conductive by successive sputtering of a 3 nm thick layer of nickel. The muon entrance window (19×8 mm^2 surface) is made by a Formvar foil (without any Ni layer) of 4 μg/cm^2 ($\sim$ 30 nm) thickness. Windows foils with thickness down to 2 μg/cm^2 have been produced.

3.3 Electronics of the data acquisition system

A brief overview of the ideas underlying the electronic system used for the data acquisition of the μp Lamb shift experiment is given here. For a detailed description of the whole system see Ref. [16].

- *Event gate:* If a muon crossing S_1 generates a signal with amplitude above threshold a S_1G gate of 80 ns width is opened. Similarly if the muon causes a signal above threshold in S_2 a short pulse S_2D (10 ns width) is generated. If S_2D overlaps in time with the S_1G gate a coincidence signal T_1 is generated. The width of the S_1G gate is given by the TOF interval for muons stopping with high probability in the hydrogen gas. If the muon reaches D_3 and generates a signal a 230 ns gate D_3G is opened. A coincidence between T_1 (delayed by 200 ns) and the anti–D_3G gate produces the MUON–STOP signal. The delay of 200 ns corresponds to the maximal time required for a muon leaving S_2 to reach D_3.

- *Laser trigger:* The MUON–STOP signal fires both excimer lasers under the condition that they are ready. This condition is achieved by requiring the laser to be triggered by the MUON–STOP signal in anti–coincidence with a 14 ms long gate generated when the laser is fired. If this gate is on, it means that the laser is recovering from the previous shot and is not yet ready to be triggered again. The excimer lasers have been electrically decoupled from the electronics using two fast (5 ns reaction time) opto–couplers to avoid large pick–up signals induced by the discharges of the excimer lasers, traveling back from the excimer laser to the data acquisition system.

- *Computer trigger:* The MUON–STOP signal generates a 12 μs long "event gate" (EVG). This gate defines the time window where signals from the various detectors are considered. Each LAAPD signal is split into two: one is fed to a waveform digitizer (WFD), and the other to a shaping amplifier (200 ns integration time) followed by a discriminator. If the signal from an LAAPD exceeds the discriminator threshold, corresponding to $\sim$ 1 keV x-ray energy pulses a gate is opened indicating that this LAAPD contains data worth to be read out.

- *Data reading and clearing:* Reading of the data, *i.e.,* transfer from the CAMAC units to the computer, starts at the end of the EVG under the condition that at least one LAAPD had a signal. MIDAS is used as data acquisition system [59]. Various ADCs, TDCs and WFDs record the signals from LAAPDs, electron and laser detectors. The total read out time is up to a few ms, depending on the number of WFDs which have shown a signal. At the end of the read–out process a clear signal is sent to reset the ADCs and TDCs in order to accept a new trigger signal. If no relevant signal is detected within the EVG a clear signal is immediately sent. Resetting is achieved within 10 μs, *i.e.,* it is much faster than data reading. In the time between the S_1 signal and the end of the reset process no other muon events are accepted by the trigger electronic.

Within the 14 ms laser dead time, on average three more muons are detected to enter the apparatus. No laser trigger is generated in such cases, but an EVG is opened in order to collect as many x-ray events as possible, including background, which can thus be studied with $3-4$ times more statistics than for laser events alone.

Timing and amplitude information are required for all detectors, *i.e.,* for the muon detectors (S_1, S_2 and D_3), the x ray detectors (LAAPDs), the electron detectors (electron paddles, LAAPDs, D_3), and various detectors monitoring the laser system. The LAAPDs and two laser photo–detectors signals are recorded with WFDs. The use of WFDs offers the possibility for an accurate and flexible offline analysis of the signals. The most relevant times are recorded by TDCs and PTDCs (Pipeline TDC). While TDCs can record only the first signal within an EVG, the PTDCs we used were able to record up to 16 signals within one EVG. The PTDCs are crucial for the detection of so called *second muons* which enter the apparatus within the EVG triggered by a so called *first muon* (cf. §5.4).

Chapter 4

The laser system

In this Chapter the laser system that fulfills the requirements of our experiment is described [60]. A multistage laser system has been developed which provides 0.2 mJ pulse energy tunable at 6 μm wavelength. The laser is triggered at a maximum 60 s^{-1} repetition rate by muons entering the apparatus at random times. A new type of multipass cavity has been developed to provide a homogeneously illuminated volume ($7 \times 25 \times 170$ mm^3).

The requirements on the laser system are summarized in Table 4.1. The most stringent requirement is a short delay between laser trigger and output 6 μm pulse. The laser has to be triggerable upon muon entry to the apparatus (rate of 240 s^{-1}) in a stochastic way, with a short delay $\lesssim 1.5\,\mu$s (due to the 1.3 μs lifetime of the $2S$ state at 0.6 hPa pressure), and has to have the shortest achievable dead time between two shots. A determination of the $2S-2P$ line position with 30 ppm uncertainty corresponds to an accuracy of 1.5 GHz for the laser frequency. The laser bandwidth has to be small compared to the natural linewidth of 18.6 GHz and the required tunability of $\sim$ 250 GHz is determined by the uncertainty of the rms proton charge radius.

Muonic hydrogen has a reduced mass 186 times that of normal hydrogen causing oscillator strengths $1/(186)^3$ times weaker than the corresponding ones in hydrogen. The energy density required to saturate the $2S-2P$ transition is 16.5 mJ/cm^2 (cf. Appendix E). This fluence has to be obtained in the atom–laser interaction volume of $17 \times 7 \times 170\,mm^3$. This is achieved if the 6 μm laser system provides pulses with $\sim$0.2 mJ energy. Reliability of the whole system during the measuring time of about 200 hours during the beam time period of few weeks is essential.

For reasons we will discuss below we developed a laser system whose main components

Table 4.1: Requirements on the laser system for the muonic hydrogen $2S-2P$ Lamb shift measurement.

Requirements		Comments
Frequency	50 THz	Corresponding to $\lambda = 6\,\mu$m
Bandwidth	< 2 GHz	$\Gamma_{2S-2P} = 18.6$ GHz (FWHM)
Tunability	250 GHz	Large r_p uncertainty
Energy/pulse	$\gtrsim 0.2$ mJ	Illuminated volume $25 \times 7 \times 170\,mm^3$
Triggerability	Stochastic	μ^-p formation time is random
Repetition rate	100 s^{-1}	100 s^{-1} results in 1 event/hour
Delay	$\lesssim 1.5\,\mu$s	1.3 μs lifetime of the $2S$ state
Reliability	10^8 shots	Many days with 100 s^{-1} shots

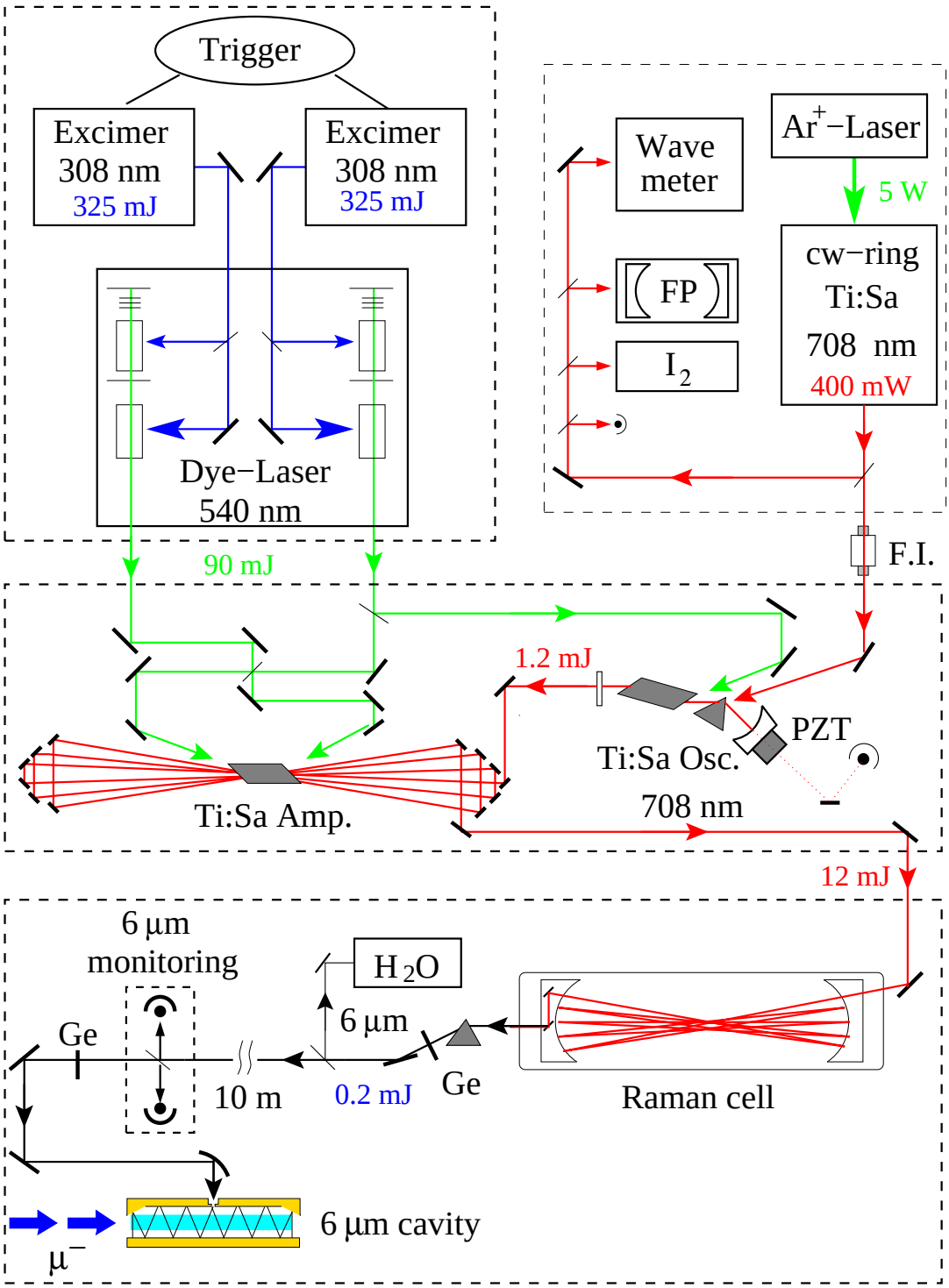

Figure 4.1: Schematic view of the laser system. The main components are a pulsed excimer–dye laser system, a tunable cw Ti:Sa laser, a pulsed oscillator–amplifier Ti:Sa laser, a Raman cell, and a 6 µm multipass mirror cavity with its diagnostic system. FP: Fabry–Perot, I_2: iodine absorption cell, H_2O: water absorption cell cell, PZT: piezo transducer, FI: Faraday isolator.

are shown in Fig. 4.1. Two high power XeCl excimer lasers provide the pumping energy (320 mJ each) for the whole system. Their pulses have a 1.2 μs delay relative to the trigger signal. No other laser with such a short delay and large pulse energy is commercially available. Each excimer pumps a two–stage multimode nontunable dye laser which converts the 308 nm excimer laser pulses to 47 mJ pulses at 540 nm. They in turn pump an injection–seeded oscillator–amplifier titanium sapphire (Ti:Sa) laser system which delivers 12 mJ at 708 nm. The wavelength tunability and bandwidth of the Ti:Sa oscillator, and therefore of the subsequent amplifier and 6 μm light, are controlled by a single–mode cw–Ti:Sa laser stabilized on a calibrated Fabry–Perot (FP) cavity.

Wavelength conversion from the visible to the infrared is made by a third–Stokes Raman shifter operated with 14 bar H_2 gas. For our conditions, efficient Raman conversion needs the TEM_{00} mode and pulse length less than 10 ns, which is obtainable with a short cavity length Ti:Sa oscillator. The third–Stokes Raman shifter converts the wavelength from 708 nm to the 6 μm region yielding a pulse energy of 0.2 mJ.

The infrared light is transported over a 12 m long path to the mirror cavity surrounding the muon stop volume. Two mirrors located on the left and right side of the muon stop volume form a nonresonant 6 μm multipass cavity. One of the mirrors has a hole of 0.6 mm diameter where the laser light is focused and enters the cavity. The light then is reflected back and forth between the two mirrors, and spreads out almost homogeneously illuminating the whole muon stop volume. The part of the confined light which is reflected back at the hole position escapes from the multipass cavity and is detected by a fast infrared photo–detector. This provides a diagnostics for the light circulation inside the multipass cavity.

This laser scheme was developed since in the 6 μm region, there exist no commercially available tunable and rapidly triggerable lasers which provide sufficient energy. However, a tunable 6 μm laser can be realized by using a tunable laser in the visible region (*e.g.,* Ti:Sa) pumped by a high–power laser. Its wavelength can then be converted (frequency mixing, OPO, Raman) to 6 μm. Stochastic triggering and short delay excludes the use of a standard high–power low–repetition–rate ($<$ 100 Hz) Nd:YAG laser as they require around 100 ms for inversion buildup. Continuously pumped Q–switched YAG lasers can possibly provide the necessary pulses but available commercial models have too low pulse energy and too long delay times (2 μs) due to the use of AOM switching and low gain per pass. Hence we decided to use excimer lasers which can be triggered within 1 μs and provide sufficient energy to fulfill our requirements. For efficient down–conversion to the 6 μm wavelength, we used a H_2 Raman cell with low threshold and high efficiency. Possible alternative schemes could be constructed using an OPO–based $HgGaS_2$ crystal [61] or by frequency mixing methods [62] but the reliability at relatively high repetition rates has not yet been demonstrated.

4.1 Excimer lasers

The most restrictive requirement on the laser system is the short delay between muon arrival and laser pulse. Two commercial Lambda Physik series LPX200 XeCl excimer lasers [63] are used.

The active medium of these lasers is a diatomic excited molecule termed excimer (in our case $XeCl^*$). Since excimer molecules have a lifetime as short as a few nanoseconds they require a fast excitation mechanism. The excitation process is provided by a fast electric discharge applied to a gas mixture that in our case is made of Xe (60 hPa), HCl (80 hPa)

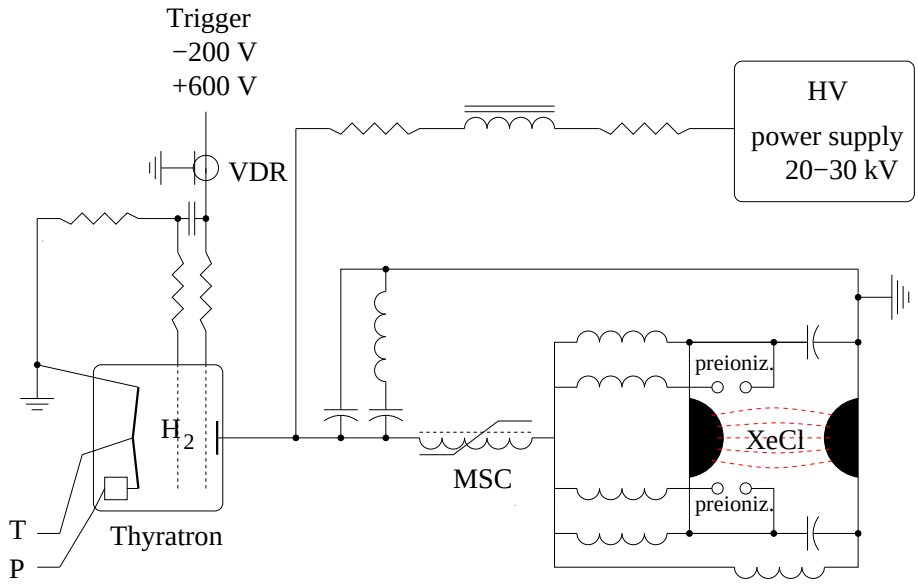

Figure 4.2: Principle arrangement of the main components of the LPX200 excimer laser. VDR: voltage dependent resistor, MSC: magnetic switch compressor.

and Ne (2900 hPa). These diatomic molecules are bound only in excited states, while their ground state is repulsive, implying high gain and high energy capability. Because of these characteristics, excimer–laser deliver high energy pulses with short delay relative to the electronic trigger.

A schematic of the electrical discharge circuit of the LPX lasers is shown in Fig. 4.2. To ensure adequate population of the excited state, about 10^{15} cm^{-3} electrons are required, which corresponds to a current density of about 10^3 A/cm^2. The discharge operates therefore at very high peak currents and very short rise times.

Thyratrons are used as high voltage switches. The thyratron is basically a capacitor filled with H_2 gas with a grid between the electrodes (see Fig. 4.2). Its cathode is a continuous electron emitter. The electron emission rate is given by the cathode temperature which is resistively warmed–up and controlled by an external voltage (T, in Fig. 4.2). A small negative voltage of −200 V on the grid is sufficient to prevent the emitted electrons to reach the anode. However a fast switch of this voltage to a positive value of the order of 600 V opens the way for the acceleration of the emitted electrons from the cathode to the anode with formation of an avalanche in the H_2 gas, and a discharge of the energy stored in the thyratron. The avalanche formation depends also on the H_2 gas pressure which is controlled by a second voltage (P) acting on a gas reservoir.

The released thyratron current pulse is compressed in the saturable magnetic switch inductance (MSC) and rapidly switched into the low impedance gas. Excimer discharges have very low impedance ($\sim 10^{-1}\Omega$). The energy stored in the capacitors finds then its way to ground via the gas discharge which terminates after approximately 30−50 ns. Large and homogeneous cross–section of high voltage discharges require a start–up electron density of 10^7 to 10^8 cm^{-3} which is provided by pre–ionization. For a LPX200 excimer laser the gas volume used for the discharge is $25\times10\times1500$ mm^3, *i.e.,* a pulse top–flat cross–section of 25×10 mm^2.

To shorten the delay of the commercial laser three changes have been studied. First the electronics providing the fast switch of the grid voltage from −200 to 600 V was modified.

Its delay time was shortened from 230 to 120 ns. Second, the number of varistors (Voltage Dependant Resistor VDR) between the thyratron grid and the ground have been reduced by a factor 2. The grid voltage can therefore reach a higher positive value which leads to an additional decrease of the thyratron switching time of about 200 ns (from 300 to 100 ns). Finally the MSC was removed and the resulting effects were studied on a LPX300 excimer laser during the beam time 2002. The MSC switch is unidirectional and blocks current reversal from the discharge which damages especially the thyratron. This removal therefore had to be accompanied by a reduction of the bulk capacitance in order to reduce the circuit mismatch, *i.e.,* the current reversal. A decrease of the total delay of about 600 ns with only a small ($< 10\%$) output pulse energy decrease was obtained. However some damages at the electrodes of the laser tube have been observed, which may be explained by an incomplete compensation of the circuit mismatch. Therefore for the beam time 2003 we have not undertaken any removal of the MSC inductance. In summary, only the trigger electronics of the LPX200 excimer lasers was modified for the beam time in 2003, and the resulting total internal delay was 1.2 μs.

Between consecutive pulses the active laser gas volume has to be exchanged totally to avoid discharge instabilities. This is achieved by a high–flow gas circulating system. No measurable energy variations were noticed between 10 and 100 Hz repetition rate. The time necessary to recharge the laser capacitors is the limiting factor in the laser firing rate; 10 ms are required and during this time, termed "dead time", the laser is inoperable.

The laser amplification in the discharging gas is very high ($\sim 10\%$ cm^{-1}), leading to saturation after only a few resonator round trips, which reduces the optical feedback requirement. Simple uncoated CaF_2 or MgF_2 windows have been used as outcoupler. Together with a high–reflector they formed a flat–flat 1.5 m long cavity. A laser pulse width of about 30 ns has been measured, which is essentially given by the time necessary to discharge the capacitors, due to the fast optical pulse buildup (high gain).

With each discharge a small amount of the halogen forms a stable metal–chloride molecule. This leads to a reduction of the output pulse energy, which may be attributed to a reduction of the number of lasing molecules, but also to the fact that these metallic molecules stick to the laser optics causing absorption of the circulating laser beam. Gas purifier and electrostatic filters are used to partially clean the gas mixture. During beam time the gas mixture and the optics of the excimer laser needed to be changed once a day. Special care was undertaken to prevent air to enter the laser head during window exchange (fast change with laser head continuously flushed) since any contaminant may be burnt on the laser electrodes causing its degradation. After every window exchange the laser head was cleaned by purging the laser head with several bar of high purity helium gas. Cleaning and passivation of the electrodes by firing the laser with 1 bar of He or a mixture of HF (100 hPa) and He (2.5 bar) was undertaken when for some reason there was a long beam break.

To avoid electrical pick–up caused by the fast electrical discharge, the excimer lasers are enclosed in a double Faraday cage. The electrical noise (transported mainly by the ground line) produces a pick–up signal in the LAAPDs exactly in the time interval where the laser induced events are expected. To minimize this noise the discharge formation was continuously kept at optimal conditions by replacing the excimer gas mixture and by optimizing the thyratron cathode and H_2 gas temperatures (P,T), or by replacing the whole thyratron. The LAAPDs pick–up signal (which is superimposed on the laser induced 2 keV signal) recorded in the FADCs was thus kept at a tolerable level, and could be eliminated by a suitable subtraction procedure in the offline analysis.

Summarizing two commercial Lambda Physik series LPX 200 XeCl excimer lasers are used, each of which delivers 320 mJ output energy at 308 nm with a maximal repetition rate of 100 Hz. The trigger electronics of the excimer lasers was modified to decrease the internal delay to 1.2 μs. The time necessary to recharge the laser capacitor bulk is 10 ms, and during this dead time the laser is inoperable. When the laser is stochastically triggered the dead time has to be enlarged to 14 ms to avoid intolerable energy and profile fluctuations of the dye laser output pulse. A muon trigger rate of 240 s^{-1} and a laser dead time of 14 ms results in an average laser repetition rate of 55 $s^{-1} \simeq (1/240 + 0.014)^{-1}$ s^{-1}. This means that the laser is fired on average for every fourth detected muon which enters the target.

4.2 Dye lasers

Each of the two excimer lasers pumps its own dye laser oscillator–amplifier system. The oscillator is a 10 cm long linear flat–flat resonator. Each resonator has a $T = 10\%$ output–coupler, an 8–element–Brewster–plate polarizer, and a Bethune dye cell. The Bethune (prism) cell depicted in Fig. 4.3 allows homogeneous transverse pumping, yielding a nearly Gaussian transverse profile [64]. The oscillator resonator length is made as short as possible to maximize the time overlap between the oscillator pulse and the excimer pulse within the dye amplifier cell. The dye laser oscillators are pumped with 12% of the available excimer laser light and deliver 20 ns long pulses (see Fig. 4.8) with 5 mJ at 540 nm. These pulses are then amplified to 45 mJ, leading to an optical–to–optical efficiency of 14%. Pulse to pulse energy fluctuations are about 10% and strongly depend on the time between successive pulses (these typical values are measured with new dye solutions and at a stochastic rate of 55 s^{-1}).

In contrast to the oscillator, the amplifier cells are not Bethune cells, but are transversely pumped from one side only, which results in a nonuniform illumination over the cross section of the excited volume. The highest gain occurs right on the inner face of the cuvette side, causing diffraction effects. A reduction of these effects and an enhancement of the dye lifetime are accomplished by reducing the solvent viscosity, increasing the dye solution flow, and decreasing the dye concentration. For the same reason, the output energy and profile quality progressively decreases with increasing repetition rate. Several dyes were tested which have an emission band that overlaps with the absorption band of

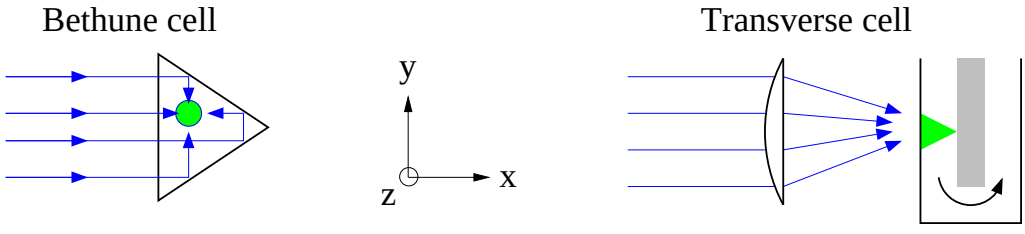

Figure 4.3: Schematic view of the Bethune and transversely pumped dye cell. The excimer laser pump pulse propagates along the x-axis. The Bethune cell is a prism with a hole (2.5 mm diameter, 4 cm long) in which the dye solution flows. Both dye laser light and dye flow propagate along the z-axis. The hole position is chosen such that the excimer light pumps the dye solution almost homogeneously. In the transverse cell used for the amplifiers the dye solution flows as indicated by the arrow, whereas the dye laser light is emitted in z-direction. The excimer light pumps the dye solution only from one side.

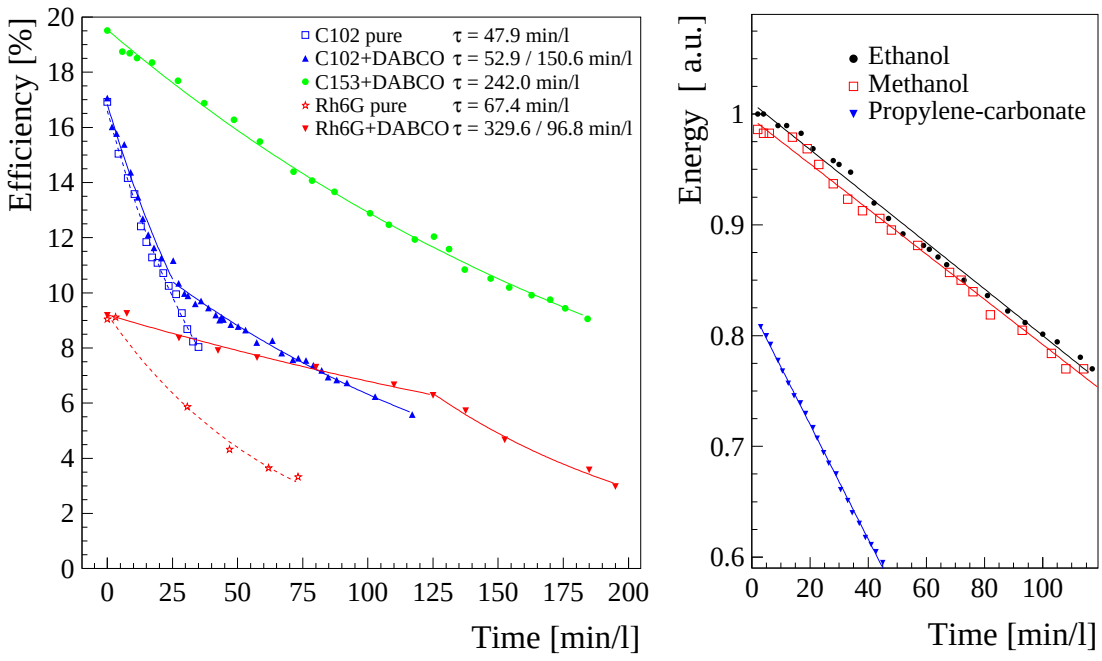

Figure 4.4: (Left): Efficiencies and lifetimes of several dye solutions. The dye–laser efficiency is plotted as function of the time when pumped by 308 nm light from an excimer. The dye–laser used for this measurement is different from the laser used in our experiment. (Right): Comparison of the Coumarin 153 lifetimes for different solvents: methanol, ethanol and propylene–carbonate, for the laser used in the search for the resonance. The dye–laser was operated at 50 Hz with 390 mJ pump energy (308 nm). When dissolved in propylene–carbonate the lifetime of Coumarin 153 is reduced by almost a factor of three when compared to methanol or ethanol. The measurements shown on the right can not be directly compared with those on the left since the setup is different.

Ti:Sa [65, 66]: Coumarin 102, pure and mixed with DABCO (a triplet quencher), pure Coumarin 307, Coumarin 153 mixed with DABCO, and Rhodamine 6G, pure and mixed with DABCO. We found that the combination of Coumarin 153 with DABCO has the longest lifetime under the intense UV irradiation of our XeCl excimer lasers, and it was therefore used. Some of the test results are shown in Fig. 4.4.

Propylene–carbonate, methanol, and ethanol were tested as dye solvents. Methanol and ethanol show similar behavior and, when compared with propylene–carbonate, give a factor of three longer dye lifetime and 20% more output energy at 50 Hz. Moreover, at 50 Hz repetition rate, relative to 1 Hz, the output energy is decreased by about 30% for propylene–carbonate and 15% for ethanol and methanol. A further factor of two enhancement of the dye lifetime is achieved by dissolving the triplet quencher DABCO in the dye solution. The dye–lasers used in the resonance experiment had 5.5 ℓ dye solution each (Coumarin 153+DABCO+methanol) and showed an energy output decrease of 13% in 4 hours when operated at 50 Hz (Fig. 4.4). Methanol is used in the amplifier cells, whereas the oscillators are operated with the more expensive ethanol solvent because methanol produces a white coating on the Bethune cell tube. This layer, which dramatically reduces the energy output, is strongly dependent on the surface quality of the tube walls, and does not occur with ethanol. Methanol is used in the amplifier cells which have better surface quality and do not exhibit this effect. The dye mixture of the oscillator consists of 0.8 g Coumarin 153 and 1.6 g DABCO per liter of ethanol, whereas the amplifier mixture

consists of 1.0 g dye with 2.0 g DABCO per liter of methanol.

During data taking the dye solutions were changed on average $2-3$ times a day, that is about 30 ℓ of dye solution are used per day (15 hours of operation). As said above the typical efficiency with new dye is about 14% whereas the dye was exchanged when its efficiency was around 12%. The gas mixtures of the excimer lasers are exchanged once per day, and the excimer laser optics are cleaned at the same time.

The output pulse energy was found to be independent on the polarization of the excimer laser light, which was achieved by using a polarization–dependent high–reflector in the excimer laser. Naively thinking a pump beam polarized along the y-axis would be preferable because the induced dipole moment radiates mainly in the z-direction. However the polarization independent results show that there are collisional depolarization effects in the dye solution on a sub–nanosecond time scale.

4.3 Continuous wave Ti:Sa laser

The wavelength of our 6 μm source is controlled by a continuous wave (cw) Ti:Sa laser at 708 nm [67, 68]. Its amplifying medium is a Brewster–cut Ti:Sa crystal (15 mm long, water cooled) which is pumped by 5 W of green light from a multi–lines Ar^+ laser. At 708 nm an output power of 400 mW was routinely achieved. The laser is tunable from 690 to 750 nm. The lower wavelength limit is given by the spectral gain profile of the Ti:Sa medium which peaks at 780 nm, whereas the maximal wavelength is presently given by the reflectivity of the mirrors $M_3 - M_5$ (see Fig. 4.5). The laser is operated single–mode using several wavelength selective elements. When the laser is locked and stabilized on an external stable Fabry–Perot cavity (FP) the laser bandwidth is about 1 MHz. The absolute frequency of the cw Ti:Sa laser has an uncertainty of 100 MHz which is given by the uncertainty related to the calibration of this FP (cf. §4.9). This uncertainty is smaller than needed for the $2S-2P$ experiment, and no attempt was made to improve the FP calibration.

The cavity is formed by 2 curved (M_1, M_2) and four flat mirrors ($M_3 - M_6$). The spherical mirrors of 15 cm curvature radius are placed near the Ti:Sa crystal. M_1 is dichroic (maximal reflectivity for $690-820$ nm and maximal transmission for the pump beam) allowing the pump beam to be precisely overlapped with the red beam inside the Ti:Sa crystal. The incidence angle on M_1 and M_2 is chosen in order to compensate the astigmatism originated by the Brewster–cut Ti:Sa crystal.

The principle of the selection of the direction of lasing inside the ring cavity is the following. A Faraday rotator (birefringent plate in magnetic field) is placed inside the cavity. It induces a rotation of the laser polarization by an angle Θ which depends only on the direction of the magnetic field. The polarization is therefore rotated independently of the direction of lasing of the beam in the laser cavity. Except between $M_4 - M_5 - M_6$, the beam path is in the horizontal plane. The mirror M_5 is placed above this plane. Hence the system of mirrors $M_4 - M_6$ induce a polarization rotation of $\pm\Theta$ depending on the way of rotation of the circulating light inside the laser cavity. For one way of rotation therefore the system of mirrors compensates the effect of the Faraday rotator, whereas for the other way the polarization is rotated by 2Θ per round trip. Since the laser is equipped with several Brewster–cut plates only one way of rotation is then selected.

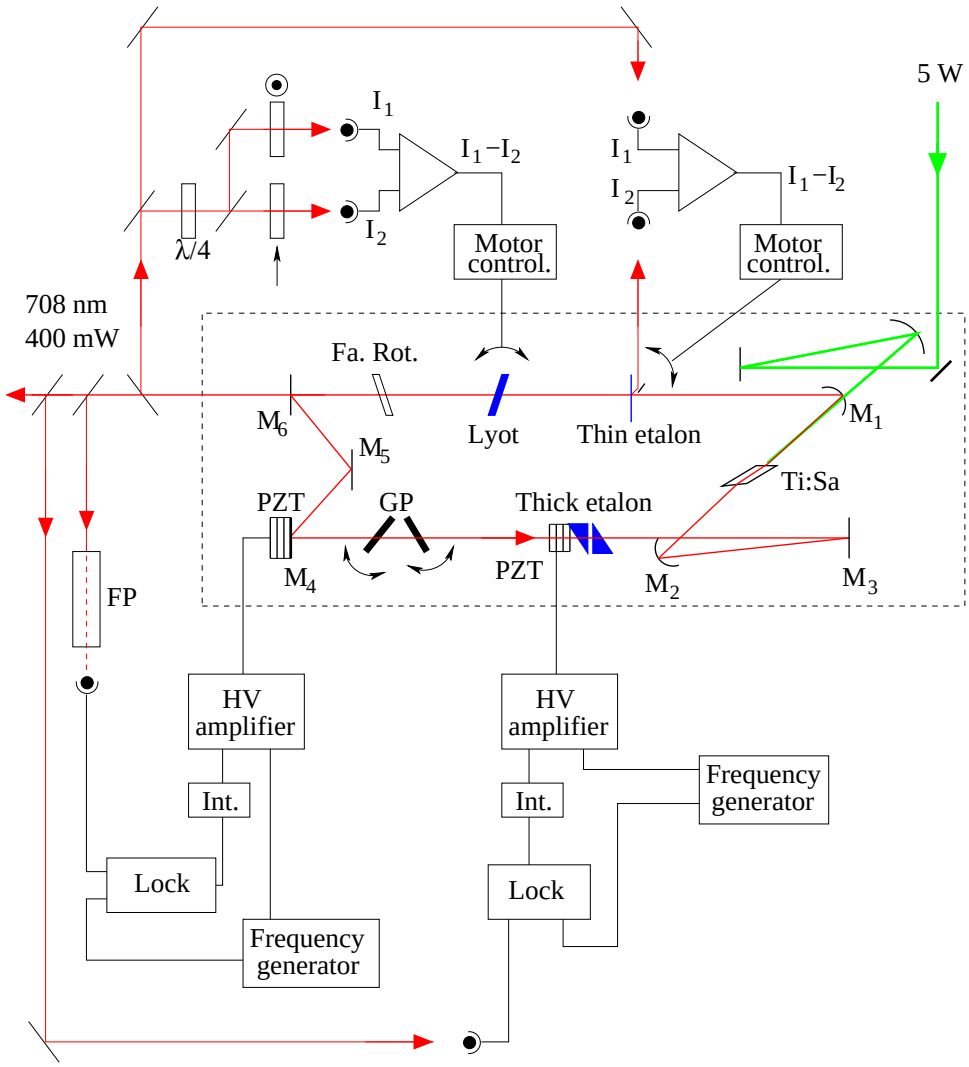

Figure 4.5: Schematic view of the Ti:Sa continuous wave laser with its frequency stabilizing electronics. M_i: mirrors, Fa. Rot.: Faraday rotator, FP: Fabry–Perot cavity, PZT: Piezoelectric element, GP: Galvo-plates.

4.3.1 Wavelength control

We will describe the wavelength selective elements in the order of increasing selectivity. The Lyot filter which is composed of three birefringent plates with different thicknesses, has a spectral selectivity of about 0.4 nm. It is placed close to Brewster–angle and can be rotated by a servo motor.

A thin silicon plate (thin etalon) of 0.7 mm thickness is acting as a two–wave interference filter with a free spectral range of about 150 GHz. The horizontal incidence angle between the laser beam and the plate is also controlled by a servo motor. A rotation of this plate relative to the direction of the laser beam causes a change of the apparent plate thickness, leading to a different wavelength selection.

The thick etalon is made of two prisms with an air gap of 8 mm, corresponding to a free spectral range of 19 GHz. The prism surfaces forming a Fabry–Perot cavity have been made reflective with a reflectivity of about 30% whereas the other planes are almost

at Brewster–angle. A piezo–electric transducer (PZT) connected to one of the prisms is used to change the prism spacing leading to a frequency sweep of about 400 GHz.

Finally the cavity length can be changed using two Galvo driven tilt plates of 10 mm thickness inserted close to the Brewster angle, and moved by a motor in a symmetrical way. The 1.6 m cavity length corresponds to cavity modes of about 200 MHz spacing. This length can be stabilized by a PZT element mounted on the cavity mirror M_4.

4.3.2 Frequency stabilization

The laser is made mono–mode with the thick etalon locked on the cavity mode which gives the maximal output power. The prism mounted spacing is modulated at a frequency of 2.2 kHz. This causes an intensity modulation of the laser output which is detected by a photodiode and used to lock the prisms spacing to maximum output power. The laser can then be tuned while remaining on the selected cavity mode. The frequency stability is achieved by locking the laser cavity length on a stable external FP cavity (cf. §4.9). This cavity has a free spectral range (FSR) of 1.56 GHz and the finesse of 310. Thus the corresponding FP fringe linewidth is about 5 MHz. The laser cavity length is modulated at 100 kHz by a cavity mirror (M_4) mounted on a PZT element. The laser light transmitted through the external FP cavity is detected. Again a lock–in system is used to produce the dispersion shape and to maintain the cw–Ti:Sa laser resonant with the FP interferometer. As previously anticipated the resulting laser bandwidth is estimated to be 1 MHz.

Both thin etalon and Lyot filter are equipped with motors. To continuously tune the laser on a large range without mode hopping it is necessary to lock also the Lyot filter and the thin etalon. The principle of this lock–in is to compare two intensities detected with photodiodes. For example the reflection of the laser beam circulating in the cavity from the slightly tilted thin etalon is used to lock the thin etalon. The reflected intensity is locked on a side of the cosine–shaped fringe (close to the minimum) by comparing it with a reference intensity. The difference between the two signals is kept to zero by adjusting the angle of the plate with the motor.

When the Lyot filter is tuned a small rotation of the output laser polarization is induced. Therefore the difference signal for the Lyot filter lock–in loop is obtained from a polarization analysis of the Ti:Sa laser output.

When the cavity length is changed with the motorized Galvo plates, with all other elements locked, a tuning range of more than 250 GHz without mode jumps was routinely reached also in the noisy environment of our laser hut. This feature is not mandatory for the search for the $2S - 2P$ resonance since it is searched by locking the cw–laser on the external FP transmission fringes. However it is used to calibrate the FP at 708 nm by recording simultaneously a large iodine absorption spectrum and a FP transmission spectrum.

4.4 Pulsed Ti:Sa oscillator and amplifier

4.4.1 Oscillator

The resonator arrangement of the pulsed Ti:Sa oscillator is presented in Fig. 4.6. The design maximizes the output pulse energy, minimizing the output pulse duration. The short optical resonator length of 7 cm results in a short output delay (56 ns) relative to the pump pulse, and creates a short pulse length (7 ns). The Brewster–cut Ti:Sa crystal (15 mm length, $\alpha = 1.8\,\mathrm{cm}^{-1}$, with a figure of merit > 300 [69]) is placed in a flat–concave

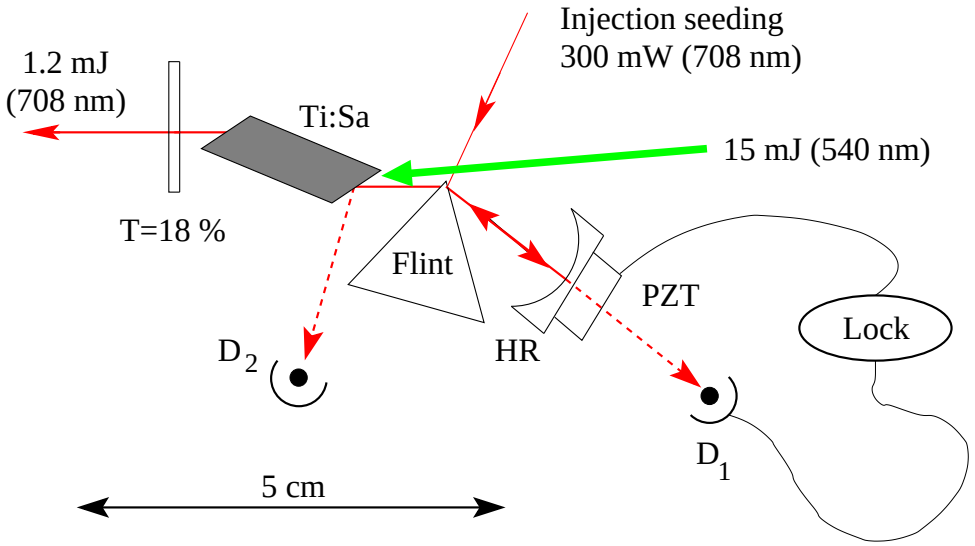

Figure 4.6: Pulsed Ti:Sa oscillator. HR: High reflector: PZT, Piezoelectric element, D_1 and D_2: photodiodes.

(4 m radius of curvature) stable resonator. At 708 nm, the gain in the Ti:Sa crystal is half that of the maximum [66], so that an equilateral flint prism, inserted at minimum deviation angle, is needed to force the oscillation at 708 nm. The oscillator frequency is precisely controlled by injection seeding from the above described cw Ti:Sa laser.

At a stochastic rate of 55 s^{-1}, the Ti:Sa oscillator delivers 1.2 mJ per pulse at 708 nm when pumped with 15 mJ from one dye laser (cf. §7.1 for a YAG laser as pump laser). Between 10 s^{-1} and 60 s^{-1} a 20% decrease in pulse energy at 708 nm is observed that can be attributed to a deterioration of the dye laser beam quality. The beam energy and profile of the 540 nm pump laser deteriorates as the delay time between pulses shortens.

4.4.2 Injection seeding

Injection–seeding is chosen for wavelength selection and tuning of the pulsed oscillator. The simplicity and precision of the cw–laser frequency control is directly transferred to the pulsed oscillator. Beside the prism no other wavelength selective elements are needed in the oscillator which minimizes optical losses within the resonator, maximizing the output energy.

The 708 nm cw–light is resonantly coupled into the oscillator cavity via reflection on the prism surface (see Fig. 4.6). Light incident on the prism at the minimum deviation angle $\alpha_{\min} = 53.72°$ ($\alpha_{\text{Brewster}} = 58.19°$) is partially reflected towards the high reflector (HR). The low coupling efficiency (0.23%) requires a large cw power of 300 mW, but has the advantage that there is only weak optical feedback (cw and pulsed) to the cw–cavity. Because of its unidirectional ring cavity geometry, the cw–Ti:Sa laser is highly insensitive to any feedback, but a Conoptic 713 Faraday isolator (see Fig. 4.1) is used to further reduce feedback, mainly because of the wavemeter.

The cavity length of the pulsed 708 nm oscillator is servo–locked to the cw–laser frequency. This is achieved by modulating the cavity length at 78 kHz and detecting the transmitted intensity with D_1. The lock–in system stabilizes the cavity length to have maximum transmission. Proper operation of the injection seeding is monitored by

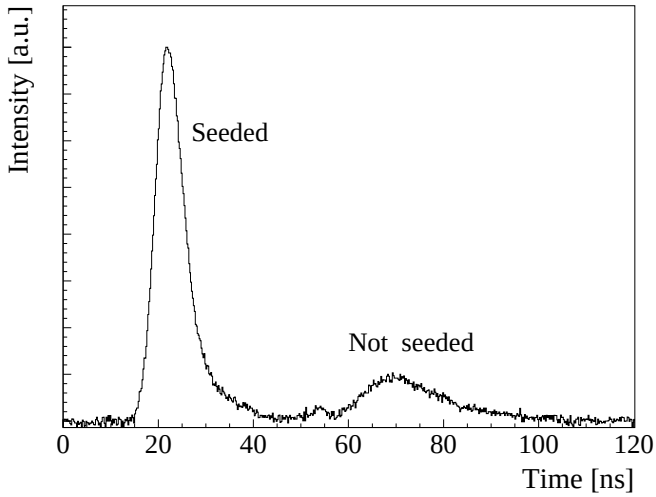

Figure 4.7: Oscillator output pulse when the oscillator is properly seeded. The signature of proper injection seeding is the appearance of a double peak structure. The relative amplitude of the two pulses depend on the alignment. The first pulse originates from injection–seeding photons, whereas the second pulse originates from noise photons in the oscillator crystal.

observing the temporal profile of the pulse on the fast photodiode D_2 as shown in Fig. 4.7 and monitoring the oscillator pulse wavelength with a spectrometer. A double pulse structure appears when the oscillator is properly injected. The first pulse originates from the photons which were circulating inside the oscillator cavity before the pump pulse produces population inversion in the gain medium. Thus the first pulse is present only when the oscillator is properly seeded. The second pulse has its origin from spatial hole burning and different transverse mode distributions between pumping and injection–seeded lasing. This second pulse is not affecting the amplification process of the first pulse (in the Ti:Sa amplifier) because it is entering the Ti:Sa amplifier only when the first pulse has already finished the last pass. The population inversion left by the first pulse when the second one enters the amplifier is not sufficient for amplification. Therefore this second pulse, which wavelength is not well defined, is not above the Raman threshold, and therefore does not reach the 6 μm cavity.

4.4.3 Chirp in the Ti:Sa oscillator

As will be further discussed in §4.8 the calibration of the whole laser system is performed directly at 6 μm. However this occurs only a few times during data taking. In between, the frequency of our laser source is controlled by the cw Ti:Sa laser at 708 nm with the help of a calibrated FP. The frequency of the cw Ti:Sa laser and the frequency of the 6 μm pulse are related by

$$\nu_{\mathrm{cw}} - K = \nu_{6\ \mu\mathrm{m}} \tag{4.1}$$

The constant K is mainly given by three times the Stokes shift. A small contribution to this constant is also given by chirping effects in the Ti:Sa oscillator and amplifier during the pulse formation. For our experiment it is essential that K does not vary in time and does not depend on frequency since we can determine K only during some special calibration runs. A variation of K caused by a variation of the chirping effect will thus lead to a small error in the determination of the output frequency at 6 μm. The chirp

occurring in the Ti:Sa oscillator is studied in order to determine the size of this frequency shift variation.

Ideally, the oscillator frequency should be equal to that of the seed cw laser and its bandwidth given by the Fourier transform of its pulse length. However, some frequency shift and additional broadening occur due to time dependent changes in the Ti:Sa crystal refractive index caused by optical and thermal effects during the pulsed pumping and the lasing process [70]. We developed a simple model to describe the frequency changes during the pulse formation.

The frequency is defined as the time derivative of the phase Φ of the electromagnetic field

$$\nu(z,t) = -\frac{1}{2\pi}\frac{d\Phi}{dt} = -\frac{1}{2\pi}\frac{d}{dt}(kz - \omega t) \tag{4.2}$$

where k is the wave vector and ω the angular frequency. When a laser beam traveling in z-direction in a medium extending from z_0 to z_1 experiences a time-dependent refractive index n, its instantaneous frequency ν at z ($z_0 < z < z_1$) is [71]

$$\nu(z,t) = \nu(z_0,t_0) - \frac{1}{\lambda}(z - z_0)\frac{dn}{dt}\,, \tag{4.3}$$

where λ is the wavelength inside the medium. The frequency shift $\Delta\nu$ per round trip experienced by a wave traveling inside the oscillator cavity is given by Eq. (4.3) [71]:

$$\Delta\nu = -\frac{2L_c}{\lambda}\,\frac{\Delta n}{\Delta t} \tag{4.4}$$

where Δn is the refractive index change in Δt and L_c the crystal length. Note that the variation of the refractive index in time occurs only in the Ti:Sa crystal, and that the variation of the crystal length due to thermal expansion can be neglected in the ns time scale of the pulse formation.

There are two sources causing a change of refractive index during the pulse buildup: one related to the excited population density N^{exc} and the other one related to the crystal temperature T, both of which vary during the pulse formation. The pumping and lasing processes dynamically affect the population inversion, inducing a change of the refractive index which is [72][1]

$$\Delta n^{\mathrm{opt}} = C^{\mathrm{opt}}\,N^{\mathrm{exc}} \qquad \text{with} \qquad C^{\mathrm{opt}} = (1.4 \pm 0.6) \times 10^{-24}\,\mathrm{cm}^3\,. \tag{4.5}$$

This has to be attributed to the susceptibility difference between the excited and ground state of the Ti^{3+} ions. In addition, there is an increase of the crystal temperature ΔT during pumping (phonon relaxation between excited states) and lasing (phonon relaxation to the ground state). The resulting T-induced change in refractive index can be calculated using $\Delta n^{\mathrm{therm}} = (dn/dT)\Delta T$ with $dn/dT = 12.6 \times 10^{-6}\,\mathrm{K}^{-1}$ [69].

Knowing the rates of absorbed and emitted photons during the pulse formation is possible to calculate the change of population inversion and the heat deposited in the crystal. Therefore the pulse formation inside the cavity was simulated and compared with measurements in order to trace the rate of absorbed (pump) and emitted (oscillator output pulse) photons.

[1] The C value given in Ref. [72] takes into account not only the purely optical change of refraction index, but also the thermal contribution by lasing. Associated with each *photon* emitted from the excited state there is a relaxation *phonon* in the ground state. From Fig. 2 of the cited article, the thermal component can be extracted and subtracted from the value $C = (1.1 \pm 0.5) \times 10^{-24}$ cm^3 to give the purely optical component $C^{\mathrm{opt}} = (1.4 \pm 0.6) \times 10^{-24}$ cm^3.

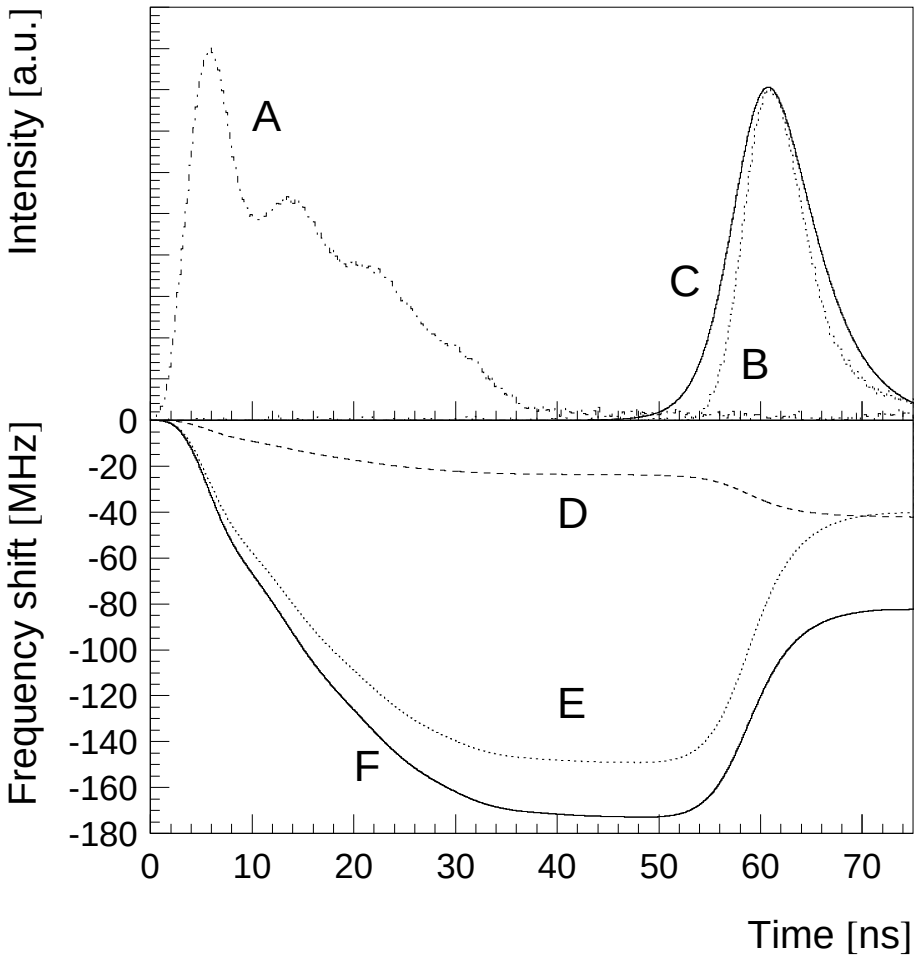

Figure 4.8: Time distributions of measured and simulated pulse intensities and frequency shift for the Ti:Sa oscillator. (Top): Measured pump pulse intensity (A), measured output pulse intensity (B), and simulated output pulse intensity (C). (Bottom): Simulated oscillator frequency shift versus time caused by the thermal effect (D), optical effect (E), and the sum (F).

The elementary rate equations for the number of photons $m(t)$ inside the cavity and the inverted population $N^{\mathrm{exc}}(t)$ are used to model the pulse formation in the oscillator cavity [73]:

$$\frac{dm(t)}{dt} + \gamma_c m(t) = +KN^{\mathrm{exc}}(t)m(t) \tag{4.6}$$

$$\frac{dN^{\mathrm{exc}}(t)}{dt} + \gamma_2 N^{\mathrm{exc}}(t) = -KN^{\mathrm{exc}}(t)m(t) + P(t) \tag{4.7}$$

where γ_c is the total cavity decay rate, γ_2 and P the decay and pumping rate of the inverted population and K is the coupling coefficient between photons and atoms describing the stimulated emission.

Numerical integration of Eq. (4.6) and Eq. (4.7) permits tracing the pulse formation $m(t)$ and the evolution of the population inversion $N^{\mathrm{exc}}(t)$ during the pulse buildup. The pump intensity time profile and the pump–to–output pulse delay are taken from measurements. Only the absolute value of the pump energy density is assumed to be a free parameter since the pump beam size at the crystal surface is poorly known. It is

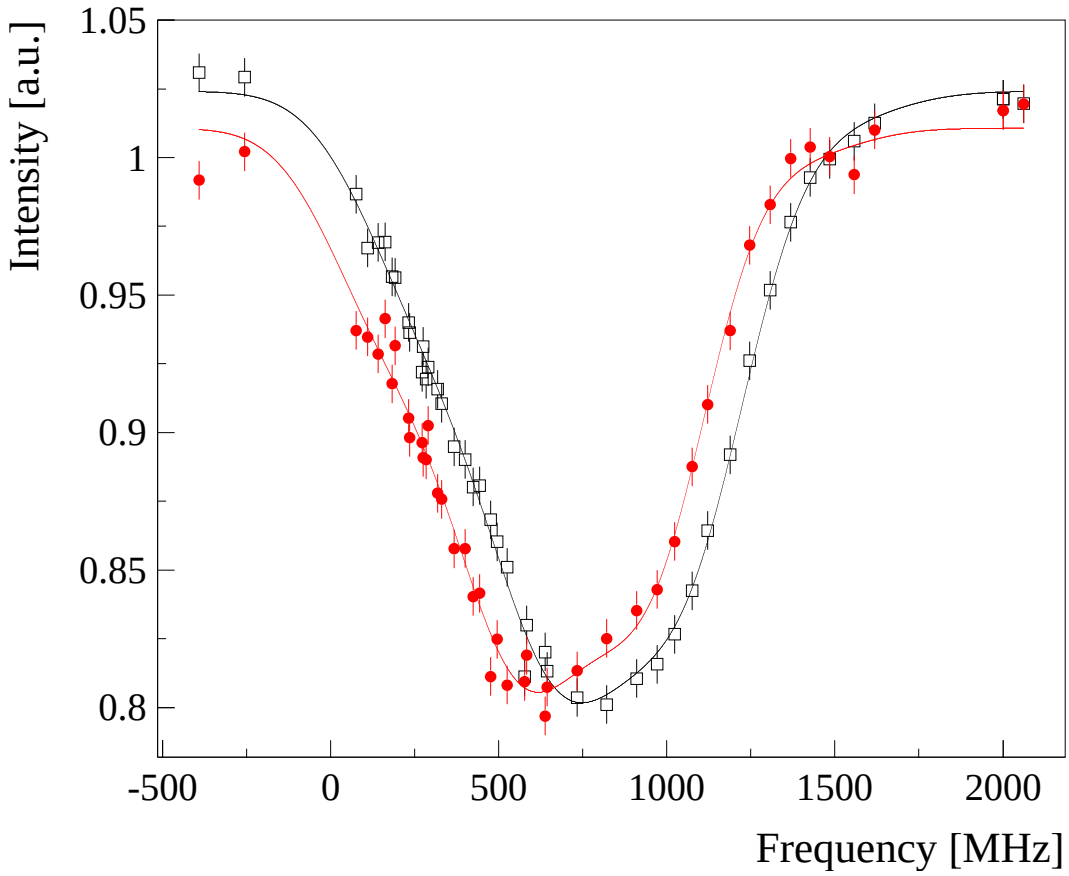

Figure 4.9: Frequency scan of the cw Ti:Sa master laser (full red circles) and pulsed oscillator slave laser (empty black squares) over an iodine absorption line. In both cases the detuning of the master laser relative to a FP fringe defines the frequency axis.

tuned to have a pump–to–output pulse delay equal to the experimentally determined one (see Fig. 4.8).

Pulse length and energy of the oscillator pulse $m(t)$ resulting from the model reasonably reproduce the measured values. Moreover $N^{\mathrm{exc}}(t)$ and $dN^{\mathrm{exc}}(t)/dt$ combined with Eq. (4.5) and the dn/dT value, predict the time evolution of the refractive index. The frequency shift is then determined using Eq. (4.4) and is plotted in Fig. (4.8). The frequency changes from a value of about -170 MHz (relative to the cw) at the pulse's leading edge to -85 MHz at the pulse tail. A mean chirp shift with respect to the cw–seeder of $\Delta\nu = -(110 \pm 30)$ MHz and a broadening of $\delta\nu_{\mathrm{chirp}} = (65 \pm 30)$ MHz (FWHM) are therefore expected. The uncertainty is dominated by the error in C^{opt}.

The frequency shift between the cw–injected light and the pulsed output light is measured by scanning the I_2 absorption line labeled "430" in Ref. [74]. Both pulsed and cw–laser light are injected into a 50 cm long cell operated at an I_2 gas pressure of 2 hPa, and a temperature of 365°C. Their transmission curves are shown in Fig. 4.9. The asymmetric line shape is caused by the underlying unresolved components of the transition. The transmitted cw light is fit using a phenomenological model with seven Gaussian functions, which defines the reference absorption line shape. The absorption measurement of the pulsed light is fit with the reference line shape convoluted with an additional Gaussian which describes the pulsed laser spectral distribution. The position of the additional

Gaussian gives the mean frequency shift whereas its width gives the laser bandwidth. A simultaneous fit of both absorption measurements is performed ($\chi^2 = 83$ for 80 degrees of freedom). The laser shift and width uncertainty extracted from the fit procedure are conservatively enlarged by a factor of 2 to take into account possible inaccuracies of the line–shape model. A (-110 ± 10) MHz red shift of the pulsed light relative to the seed laser frequency is measured, in good agreement with the above chirp model. A laser width of (130 ± 120) MHz (FWHM) is measured which is in agreement with the theoretically estimated width (Fourier–limit $\sim$ 125 MHz (FWHM), frequency chirp $\sim$ 65 MHz). The chirping might cause lasing at a second longitudinal mode. A scan over a frequency range of ± 3 GHz has hence been performed but no evidence for a second longitudinal mode was seen.

The simple model developed above to estimate the frequency shift predicts a dependence of the frequency shift on the pump pulse energy (see also Fig. (6) in Ref. [70]). The pulse–to–pulse dye energy fluctuations and slow variations (due to dye and excimer gas degradation) cause frequency shift variations of about 20 MHz. The dependence of the frequency shift on the laser frequency due to a different heat deposition is negligible at our level of precision. Concluding the oscillator output pulse frequency is shifted on average by (110 ± 10) MHz from the frequency of the cw laser. This shift takes into account pulse–to–pulse energy fluctuation when the measurement was performed, but does not account for slow dye degradation and renewal. However the simulations predict that the deviation of the dye pulse energy from the value when the chirping measurements was performed, causes chirping shifts which differs less than 20 MHz from the measured value.

4.4.4 Ti:Sa amplifier

The oscillator output pulse (1.2 mJ at 708 nm) is amplified roughly by a factor of ten in an eight–pass amplifier (see Fig. 4.1). The beam is refocused on each pass. The amplifier crystal is pumped longitudinally from both sides, and water cooled to 10°C. In 2003–run the maximum optical–to–optical energy conversion efficiency was 18%, but the routine operating conditions are normally 14% (cf. §7.1 for updated values).

The amplification process is more efficient for the leading edge of the pulse and thus a pulse shortening is expected. A reduction of pulse width from 7 ns to 6 ns (FWHM) between input and output pulse is measured. Similar to the oscillator, the amplifier introduces some frequency chirp. The resulting frequency shift per pass $\Delta\nu^{\text{pass}}$ is

$$\Delta\nu^{\text{pass}} = -\frac{L_c C}{\lambda} \frac{\Delta N^{\text{exc}}}{\Delta t'} \tag{4.8}$$

where ΔN^{exc} is the change of inversion population in the time $\Delta t'$ necessary to cross the crystal. The experimental relation $\Delta n = C N^{\text{exc}}$ with $C = (1.1 \pm 0.5) \times 10^{-24}$ cm^3 is used [72] [2]. The pumping process does not induce any frequency shift because the crystal is pumped before the red pulse from the oscillator reaches it. Only the change of population inversion caused by the red pulse amplification leads to a frequency shift. The chirp resulting from the eight–pass amplifier is estimated to be (20 ± 15) MHz, which is negligible in the context of our experiment.

[2] In contrast to the oscillator case, the constant C of Ref. [72] can be inserted directly here.

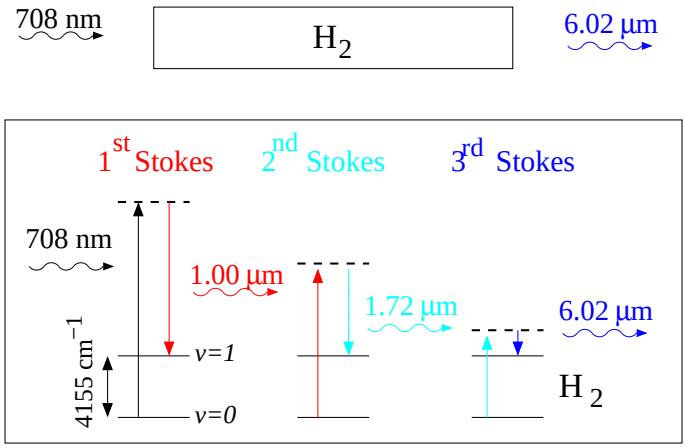

Figure 4.10: Simplified representation of the sequential Raman scattering for the production of the third Stokes radiation at 6 µm when a pump pulse of 708 nm is injected into a cell filled with H_2. At each Stokes conversion a hydrogen molecule is excited from the ground to the first vibrational level. The virtual level (dashed line) is associated with the much higher lying electronic excited state not shown in the picture. Therefore this nonresonant Raman laser will be broadly tunable without large changes in gain.

4.5 Raman cell

Sequential vibrational Raman scattering in H_2 in a multiple–pass–cell (MPC) [75] is used to convert the 708 nm pulse to the 6 μm region as depicted in Fig. 4.10. Hydrogen is ideally suited for this purpose since it not only provides reasonable gain at modest pump intensities, but also has the largest Stokes shift ($Q_{01}(1) = 4155.2\ \mathrm{cm}^{-1}$)[3]. The n$^{\mathrm{th}}$ Stokes wavenumber $\bar{\nu}_n$ is related to the pump wavenumber $\bar{\nu}_\mathrm{p}$ ($= \bar{\nu}_{\mathrm{Ti:Sa}}$) by

$$\bar{\nu}_n = \bar{\nu}_\mathrm{p} - n\, Q_{01}(1) \tag{4.9}$$

with $\bar{\nu} = 1/\lambda = \nu/c$, where $\bar{\nu}$ is the wavenumber, λ the wavelength and ν the frequency.

Three sequential Raman shifts convert an input wavenumber of 14128 cm^{-1} (corresponding to 708 nm) by $3 \times 4155.2\,\mathrm{cm}^{-1}$, to 1662 cm^{-1} (which is 6.02 μm) passing through 1.00 μm (first Stokes) and 1.72 μm (second Stokes). Any tuning of the input frequency tunes the output frequency by the same amount, since

$$\delta\nu_n = \delta\nu_\mathrm{p}\ . \tag{4.10}$$

The plane–wave Raman gain coefficient for a Stokes field E_s is computed by inserting in the wave equation describing the propagation of the Stokes field a driving polarization at the Stokes frequency given by $P_\mathrm{pol} = i\epsilon_0\chi_r''|E_p|^2E_s$ where χ_r'' is the Raman susceptibility and E_p the electric field of the pump beam. The plane–wave Raman gain g_plane is found to be [76]

$$g_\mathrm{plane} = \frac{4\pi P\chi_r''}{\lambda_s n_s n_p \epsilon_0 c} = GP\,, \tag{4.11}$$

where λ_p and λ_s are the pump and Stokes wavelengths, P the pump power, χ_r'' the Raman susceptibility, n_p and n_s the indices of refraction at pump and Stokes frequencies, c the

[3]Notation relative to $Q_{\nu\nu'}(l)$: this vibrational Stokes shift (Q) occurs between rotational–vibrational levels from a state with initial vibrational quantum number ν to a state with final vibrational quantum number ν'. l is the rotational quantum number.

speed of light, and ϵ_0 the free space permittivity. In the absence of pump depletion the power P_s of the Stokes waves along the propagation axis is then

$$P_s(z) = P_s(0)e^{GPz} \tag{4.12}$$

The input power of the Raman cell $P_s(0)$ is usually provided by the spontaneous Raman noise.

The optical function of the multipass cell is to provide an extended interaction volume ($\Rightarrow$ large z) for the stimulated Raman scattering by periodically refocusing the pump ($\Rightarrow$ large P) and Raman radiation in such a manner that the confocal parameter of both waves remain unchanged. This is accomplished by mode matching and injecting the pump radiation along a specific off–axis path of the MPC [77].

The Stokes gain (exponent) per transit g, for a Gaussian intensity pump profile of confocal parameter b_p and Stokes intensity profile of confocal parameter b_s is found to be [78]

$$g = \frac{8PG}{(\lambda_p + \lambda_s)} \frac{\sqrt{b_p b_s}}{(b_p + b_s)} \tan^{-1}\left(\frac{L}{\sqrt{b_p b_s}}\right), \tag{4.13}$$

where L is the length of the gain medium (mirror spacing of the Raman cavity). The maximum power gain per transit occurs when both pump and Stokes beams have equal confocal parameter $b_s = b_p = b = 2\pi\omega_{p0}/\lambda_p$ where ω_{p0} is the minimum pump spot size at the focus. For sufficiently tight focusing the factor $\tan^{-1}(L/b)$ asymptotically approaches $\pi/2$, and the Raman gain becomes pump power dependent instead of intensity dependent. Combining Eq. (4.11) with Eq. (4.13) results in a Stokes gain coefficient per pass for pump and Stokes beam with the same confocal parameter b of [75]

$$g = \frac{16\pi P\chi_r''}{(1 + \lambda_p/\lambda_s)\lambda_s^2 n_s n_p \epsilon_0 c} \tan^{-1}\left(\frac{L}{b}\right). \tag{4.14}$$

Several conclusion can be drawn. First the Raman gain is maximized by tight focusing. Beyond this, the only way to increase the gain further is to increase the pump power or by repeated focusing in the active medium. The overall–gain per transit (between the Raman cell mirrors) is proportional to $[(1 + \lambda_p/\lambda_s)\lambda_s^2]^{-1}$. The rapid decrease in Raman gain with increasing pump and Stokes wavelength makes stimulated Raman scattering more difficult in the infrared region.

Relaxation of the requirement for high pump power is achieved by repeated focusing in the active medium. The Raman gain enhancement is accomplished through the use of a multiple–pass cell using curved mirrors. The net gain exponent g_n after n transits through the cell is given by [76]

$$g_n = g\,\frac{1 - R_p^n}{1 - R_p} + n\ln(R_s) \tag{4.15}$$

where R_p and R_s are the mirror's reflectivity for pump and Stokes beam, respectively. The first term accounts for reflection losses of the pump beam, and the second for reflection losses of the generated Stokes pulse.

The multipass geometry is achieved using a Herriott–type [79] spherical interferometer at other than confocal spacing. The off–axis injected radiation (through an off–axis hole in one mirror) can be made to execute a path producing a circular pattern of equally spaced spots on each of the reflectors. By also requiring that the beam pattern closes itself after

m passes, one is assured of maximum utilization of the MPC volume. The angular rotation of the spot pattern at each pass is given by [77]

$$\Theta = \cos^{-1}(1 - L/\rho) \tag{4.16}$$

where ρ is the mirror curvature radius, and L the mirror spacing. The confocal parameter b of the structure can be expressed as [77]

$$b = \rho \sin\Theta\,. \tag{4.17}$$

The closure condition requires that

$$m\Theta = 2\nu\Theta = 2\pi\mu \tag{4.18}$$

where 2ν is the number of passes to closure, and μ is an integer equal to the number of azimuthal revolutions that the propagating beam makes around the MPC optical axis.

The Raman cell, a $\sim$ 2.5 m long steel tube, is filled with 14 bar of H_2 ($<$ 0.1 ppm impurities). It encloses two spherical silver–coated copper mirrors (1 m radius of curvature, 12.7 cm diameter, with dielectric protection layers [80]) and a measured reflectivity of R = 97.7% at 708 nm. The mirror spacing is 1.9325 m giving a confocal parameter b = 36.1 cm and a 33 passes configuration with Herriott's parameters μ = 14, ν = 17. Both mirrors have a 12.7 mm diameter off–axis hole for injection and extraction of the light beam 50.5 mm from the axis. The mirror with the hole for the extraction of the light can be rotated, enabling adjustment of the number of passes, providing the means to optimize the number of passes to a given Stokes order. Pulse extraction has to occur before ray path closure. Light at 708 nm is mode matched to the confocal parameter with a telescope. This also guarantees that the beam has the same diameter after each round trip. Perfect mode matching is not necessary, since small fluctuations in spot size can usually be tolerated.

For a pulse at 708 nm with 12 mJ energy and 6 ns length, Eq. (4.14) indicates that the gain from noise will produce the first Stokes in the first half pass, and the second Stokes within the second pass. For the third Stokes production with g = 0.4, the remaining 31 passes are essential. Even if the reflectivity at 1.7 μm is larger than at 708 nm as one would expect for Ag, the resulting gain is not sufficient to explain the obtained output energy at 6 μm ($g_{31} \to 12$ for $R_p \to 1$). This can therefore be explained only if four–wave mixing which initializes the third Stokes radiation is taken into consideration [76], [81]. The equation governing both four–wave mixing and stimulated Raman scattering is given for the third Stokes field by [82]

$$\frac{\partial E_{S3}}{\partial z} = -\frac{\omega_{S3}}{2cn_{S3}}\chi_R''(|E_{S2}|^2 E_{S3} + E_p E_{S1} E_{S2} e^{i\Delta kz}) \tag{4.19}$$

where E_{Sn} in the n$^{\text{th}}$ Stokes electric field and $\Delta k = -(k_p - k_{S1}) + (k_{S3} - k_{S2})$ is a measure of the linear dispersion of the medium (H_2 gas has a small dispersion). Similar equations may be written for all four fields. The first term leads to the stimulated Raman scattering and the power gain described in Eq. (4.11), whereas the second term describes the four–wave mixing. The stimulated Raman scattering requires initial photons which can be provided by the noise (as in the production of the first and second Stokes) or by four–wave mixing which depends on the other three beams. Initially the third Stokes production is dominated by four–wave mixing since all pump, first and second Stokes beams are present.

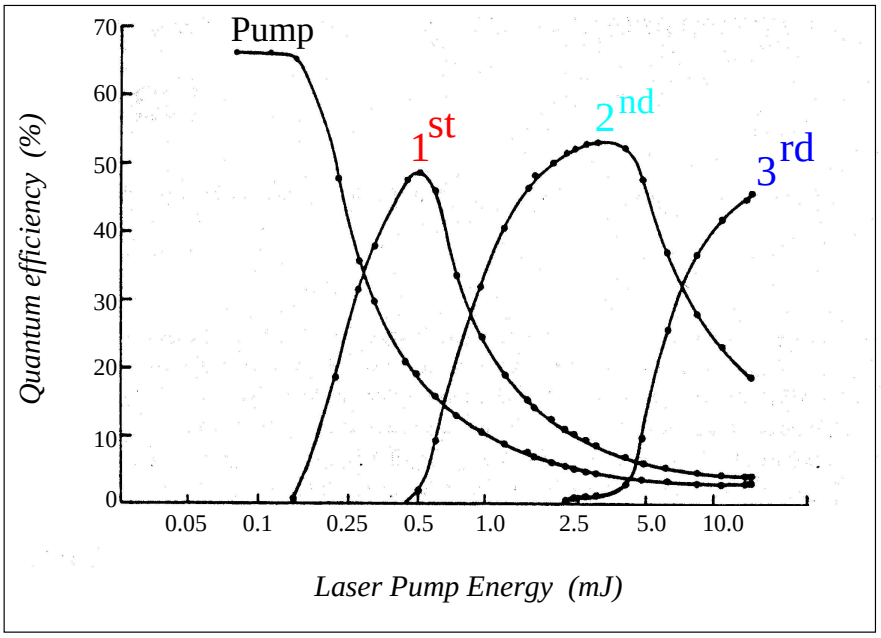

Figure 4.11: Measured quantum efficiency (photons out/photons in) for production of first Stokes (0.97 μm) second Stokes (1.62 μm), and third Stokes (5 μm) radiation as a function of the injected pump energy (690 nm) for a pulse length of 7 ns (Courtesy P. Rabinowitz [75]).

When sufficient 3$^{\text{rd}}$ Stokes power is available then the stimulated Raman gain overtakes the four–wave mixing.

A measurement of the conversion of the pump radiation into first, second and third Stokes as a function of the input energy has been measured by Rabinowitz *et al.* for the same Raman cell as used in our experiment and is shown in Fig. 4.11. Note however that this was performed at a pump wavelength of 690 nm, corresponding to a third Stokes shift to 5 μm. A model incorporating four–wave mixing and including anti–Stokes production reproduces the measured efficiencies [75]. Since the gain scales linearly like $[(1+\lambda_p/\lambda_s)\lambda_s^2]^{-1}$ the threshold for the production of the third Stokes at our wavelengths is the threshold inferred from Fig. 4.11 properly scaled for the wavelengths dependency: $E_{\text{th}}^{6\,\mu\text{m}} = E_{\text{th}}^{5\,\mu\text{m}} \times 1.45 = 6.5$ mJ.

Figure 4.12 shows the 6 μm output of the Raman cell plotted as a function of the 708 nm input pulse energy. A threshold pump energy of 6.5 mJ is visible which corresponds to the expected value. With an average input energy of 12 mJ, a mean output energy of 0.2 mJ at 6 μm is measured which corresponds to a quantum efficiency of 14%. An input pulse length of 6–7 ns, the shortest pulse length delivered by the Ti:Sa laser, is chosen to maximize the Raman efficiency. In the steady state regime the Raman gain scales with the pump power (see Eq. (4.14)), favoring short pulses, whereas the gain decreases for very short pulses when the transient regime becomes dominant [83]. Measurements in Ref. [84] show that the transient regime for $Q_{01}(1)$ Stokes production at 14 bar of H_2 is approached for pulses below 5 ns.

Measurements of the transverse distribution of the Stokes beam showed that more than 98% of its energy is in the lowest order Gaussian mode [75]. Consequently an efficient Raman process requires pump light in the TEM_{00} mode in order to maximize the overlap between pump and Stokes beams. The TEM_{00} mode of each Stokes order ensures matched

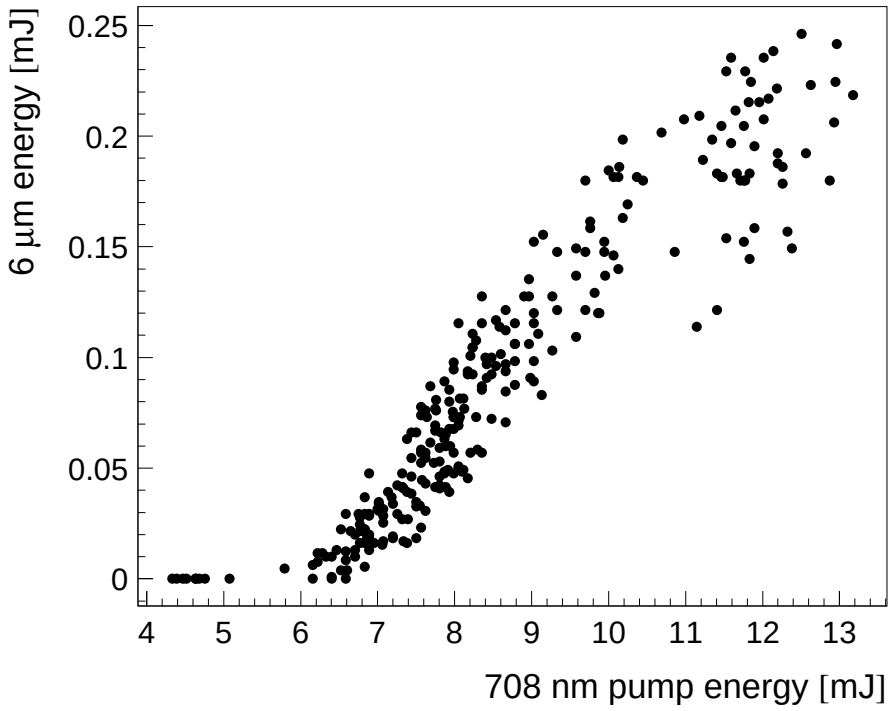

Figure 4.12: Measurements of the Raman conversion efficiency. Plotted is the third Stokes (6 μm) output energy versus the 708 nm pump pulse energy.

reflection at the mirrors, reducing resonator losses [85].

Because of water absorption in the second and third Stokes region, the cell is equipped with a gas circulating system connected to a LN_2 cold trap which removes water from the amplifying medium. Pump photons (708 nm), first Stokes (1.00 μm), second Stokes (1.72 μm), first rovibrational Stokes (1.07 μm), second rovibrational Stokes (1.91 μm) and weaker first (547 nm) and second (446 nm) anti–Stokes together with the 6.02 μm third Stokes photons exit the Raman cell. A CaF_2 prism is used to separate the 6 μm light, and two AR–coated ($5 - 8$ μm) Ge–plates remove all parasitic light remaining on the 6 μm beam axis.

4.6 $Q_{01}(1)$ Stokes–shift in H_2

Equation (4.9) leads to a determination of the $Q_{01}(1)$ Stokes–shift in H_2 when the pump frequency ν_p and the 3^d Stokes ν_3 frequency are measured (cf. §§4.8 and 4.9). A comparison between ν_3 measured using a water line absorption and the related cw–laser frequency measured with the FP at 708 nm gives a value of $Q_{01}(1) = 4155.219(1)$ cm^{-1} for the Stokes–shift in H_2 at 295 K and 14.0(1) bar. Corrections for the chirps of (-110 ± 10) MHz measured in the Ti:Sa oscillator, and of (20 ± 15) MHz calculated for the amplifier are taken into account.

The Stokes shift depends on the H_2 pressure and temperature. It may be expressed as [86]:

$$\nu_R = \nu_R(0) + \alpha\rho + \beta\rho^2 \,, \tag{4.20}$$

where $\nu_R(0) = 4155.2547(1)$ cm^{-1} [87] is the zero pressure Raman shift transition fre-

quency, ρ the density expressed in amagat[4] and α, β are coefficients which depend only on the temperature. Using an averaged β value of 0.14(1) MHz/amagat^2 [88, 89] a value $\alpha = -85(3)$ MHz/amagat can be extracted from our measured Stokes–shift value. Other measured values are $-90(3)$ MHz/amagat [90] and $-98(1)$ MHz/amagat [86].

However this discrepancy between the values for the Stokes shift is not affecting the accuracy of our experiment since our frequency measurement relies only on 6 μm water lines and the FP fringes spacing, as discussed in the next section. Nevertheless it is important to notice that a change of the Raman cell pressure or temperature has the effect to change the Stokes shift. A possible pressure or temperature–induced Stokes shift variation may be corrected using Eq. (4.20). A change of 1 bar of the Raman cell pressure, for example, will induce a Stokes shift variation smaller than 100 MHz which means a change of the 6 μm frequency smaller than 300 MHz. The above cited values of α can be used to correct for this pressure variation. The difference between the various values of α leads to a difference of about 40 MHz in the frequency determination of 6 μm pulses if the Raman cell is operating at a pressure which differs by 1 bar from the pressure when the laser source was calibrated (cf. §4.8). But we kept the pressure stable to < 0.1 bar

We anticipate at this point that the bandwidth of the 6 μm light measured at the Raman cell exit is (680 ± 140) MHz (cf. §4.8). Hence it is much broader than the 708 nm Ti:Sa pulse which is measured to be (130 ± 120) MHz (cf. §4.4.3). It can be concluded that the Raman gain process contributes a broadening of about 650 MHz. This number can be compared to the upper limit of the broadening given by the spectral width of the Raman gain, which at our conditions is 690 MHz (see Eq. (1) in Ref. [86]). The maximum expected broadening for the three sequential Stokes shifts is therefore about 2 GHz. This value is reduced to the measured 650 MHz by gain narrowing processes occurring during the Stokes pulse buildup.

4.7 Water absorption

In the 6 μm region of our interest the water molecule exhibits several rovibrational lines as shown in Fig. 4.13. The absorption of 6 μm light in air is given by

$$I(z) = I(0)\, e^{-az} \tag{4.21}$$

where a is the absorption coefficient shown in Fig. 4.13 which was calculated for 50% relative humidity. For example consider the water line shown in Fig. 4.13 (middle) which is in the frequency region where the $2S-2P$ transition is expected. If the laser is on resonance with this line only $e^{-az} = e^{-72} \simeq 5 \times 10^{-32}$ of the 6 μm light reach the target (12 m beam path from Raman cell to muon beam line, 50% humidity). To reduce absorption of the 6 μm light is therefore necessary to reduce the water vapor content on the 6 μm path. This was achieved by surrounding the beam path with boxes and pipes and flushing them with dry nitrogen (boil–off from LN_2 vessel). An intensity reduction by less than 10% was measured at the entrance of the target when the laser light was on resonance or not with the water line, which mean that the water vapor was diluted by about 1000 times.

A systematic shift may be caused if the water absorption line is within the $2S - 2P$ resonance, since the laser intensity seen at different frequencies will be different. However the possible systematic shift is minimized by placing the 6 μm photo–detector which

[4] 1 amagat is the density of a gas at 273 K and 1 atm. 14.0 bar at 295 K corresponds to 12.8 amagats.

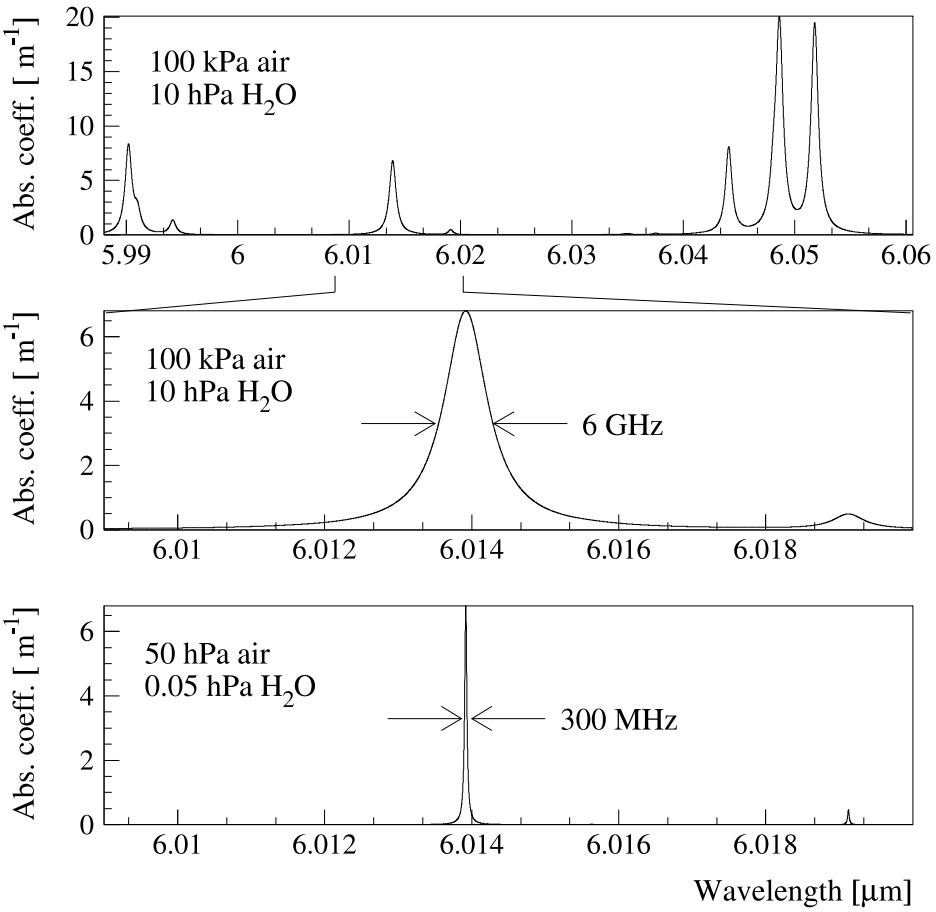

Figure 4.13: Water absorption coefficient as a function of the frequency for a relative humidity of 50% (which corresponds to 10 hPa of H_2O in 10^5 Pa of air at room temperature). These data have been extracted from the HITRAN database [91].

measures the 6 μm pulse energy close to the muon beam line where the laser beam enters the vacuum system enabling the possibility for correcting this shift when data are analyzed.

Nevertheless the presence of water lines in the region of the $2S-2P$ muonic resonance line, whose absolute positions are known with 2 MHz accuracy, is very advantageous for wavelength calibration of our laser system. This will be the topic of the next section.

4.8 Frequency calibration of the 6 μm light

Calibration of the 6 μm wavelength is performed by measuring a water absorption line. The line at 6.014 μm (1662.80968(7) cm^{-1}) labeled "37" in Ref. [92] is scanned by tuning the cw–laser at 708 nm. The cw–laser is referenced to a calibrated FP cavity with a free spectral range of 1.5 GHz [93] (cf. §4.9). A wavemeter is used to unambiguously determine the FP fringe number.

The absorption measurements were made by having the 6 μm light traverse a 37 cm long cell filled with 55 hPa of air at 35% humidity ($T = 23$ °C). Additional desorption from the walls results in a H_2O partial pressure of 1.0(5) hPa. Similar measurements are performed at 20 and 3 hPa total pressure. The 6 μm beam line is flushed with dry N_2

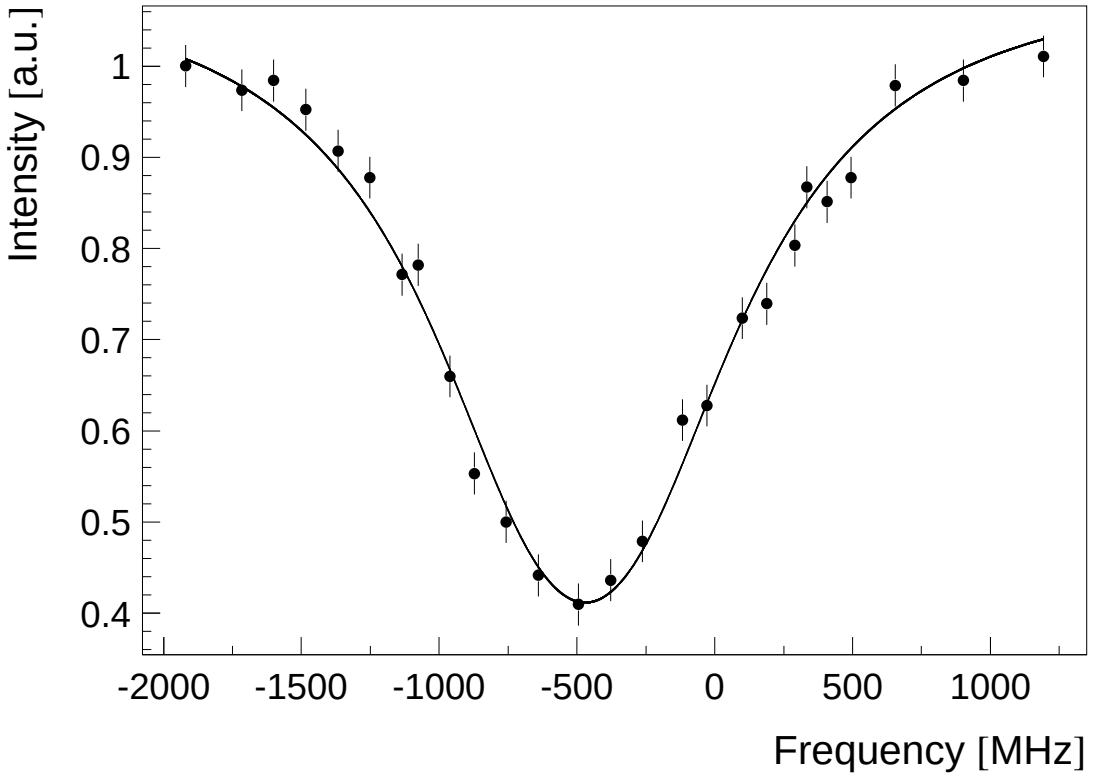

Figure 4.14: Wavelength calibration of the 6 μm light by scanning a water line. The intensity transmitted through a 37 cm long cell filled with 55 hPa air is plotted versus frequency relative to a Fabry–Perot fringe at 708 nm. The centroid position is −470 MHz from the FP fringe with fringe number N_{H_2O} ($\Delta\nu_{\rm cal} = -470$ MHz).

gas to avoid absorption by water vapor in the ambient air. Averaging over 128 pulses per point is necessary because of the intensity fluctuations of the 6 μm laser. Figure 4.14 shows the transmitted 6 μm laser beam intensity versus the cw–Ti:Sa laser frequency referenced relative to one FP fringe with fringe number $N_{\rm H_2O}$. The errors are estimated based on the scatter of multiple measurements at a subset of frequency points.

The absorption curve is fit with the function

$$F^{\rm laser}(\nu) \otimes (1 - e^{-\,L^{\rm pressure}(\nu)\,\otimes\,G^{\rm Doppler}(\nu)}) \tag{4.22}$$

where $\otimes$ represent the convolution operator, and $F^{\rm laser}$ is the laser spectral distribution with amplitude, position and width as free parameters. $L^{\rm pressure}$ describes the pressure broadening (Lorentzian with $\Gamma = 325$ MHz [91]), and $G^{\rm Doppler}$ the Doppler broadening (Gaussian with 150 MHz at FWHM) of the water line. The statistical error in the determination of the line–center position is 10 MHz. This error was enlarged to 50 MHz to accommodate for systematics caused by a possible laser frequency drift since the laser is not locked to the FP during the scan. The gain narrowing process in the Raman cell may cause $F^{\rm laser}$ to be different from a Lorentzian corresponding to a pressure broadened Raman transition. The absorption measurement is fit for the two extreme cases of a purely Lorentzian and a purely Gaussian laser spectral distribution. The resulting laser bandwidths are (540 ± 30) MHz and (820 ± 40) MHz (FWHM), respectively. We assumed an average value of (680 ± 140) MHz at FWHM.

4.9 FP calibration and stability

The frequency of our laser source is controlled by the cw Ti:Sa laser at 708 nm. When searching the $2S-2P$ resonance the cw–Ti:Sa laser is locked on a transmission fringe of the FP. It is therefore necessary to calibrate our FP as well as to check its long term stability.

The flat–concave (60 cm radius of curvature) FP cavity is made of mirrors optically contacted on a Zerodur spacer of about 10 cm and maintained under vacuum (7×10^{-6} hPa) by an ion getter pump. The vacuum cell is inserted in a heavy brass box to attenuate mechanical vibrations and fast thermal fluctuations. The reflectivity of each dielectric mirror is 99.5% in the $700-800$ nm range corresponding to a finesse of ~ 310.

The FP free spectral range, defined as the frequency difference between two successive transmission peaks, is

$$I^{\mathrm{FP}} = \frac{c}{2L} \tag{4.23}$$

where c is the speed of light and L the mirror spacing. The FP transmission peaks frequency is then given by

$$\nu_{\mathrm{FP}} = N \cdot \frac{c}{2L} \tag{4.24}$$

where N is an integer (fringe number).

In a first stage I^{FP} was roughly measured with the help of a wavemeter. This was achieved by locking the cw–laser on FP transmission peaks distributed approximately according to a geometrical progression (N, $N+1$, $N+2$, $N+4$, $N+8$, $N+16$ $\cdots$) in the 708 nm region and by measuring its frequency with a wavemeter. At each step the I^{FP} is determined with such an accuracy which enables to determine unambiguously the FP fringe of the successive step relative to the initial arbitrary fringe number N. A relative accuracy of 10^{-5} was reached with this method. This precision is insufficient to determine unambiguously the absolute fringe number N with the wavemeter.

This FP was also used for another experiment in Paris [94]. The calibration was there made with three Rb lines around 780 nm known with an accuracy better than 1 MHz. Two Ti:Sa and one diode laser were operated at 780 nm. One laser was locked on the FP while other one was locked on a Rb line. The frequency difference between the two lasers was measured with beat frequency techniques (see Fig. 4.15). The frequency ν_L of the laser locked on a FP fringe with frequency ν_{FP} is related to the beat frequencies ν_{beat} and the frequency of the atomic transitions ν_{Ref} via

$$\nu_L = \nu_{\mathrm{FP}} = \nu_{\mathrm{Ref}} \pm \nu_{\mathrm{beat}} \ . \tag{4.25}$$

The absolute frequencies of the Rb lines are thus related the laser locked on the FP, and consequently to the FP itself. Hence the frequencies of three FP fringes close to the three Rb lines were determined in this way.

For the 708 nm region only one laser was available and therefore the beat technique was not applicable. As the iodine lines are wide and known with an accuracy of only 220 MHz [74] the absolute calibration is done simply by recording simultaneously the transmission through the FP and an iodine absorption cell when the laser is scanned. The calibration performed in the 780 nm region is sufficiently precise to determine any iodine line in the 708 nm region without any ambiguity. Six FP fringes' frequencies close to six iodine lines were determined with this method. Moreover to make sure of the iodine line identification several long frequency scans of about 250 GHz range (without mode

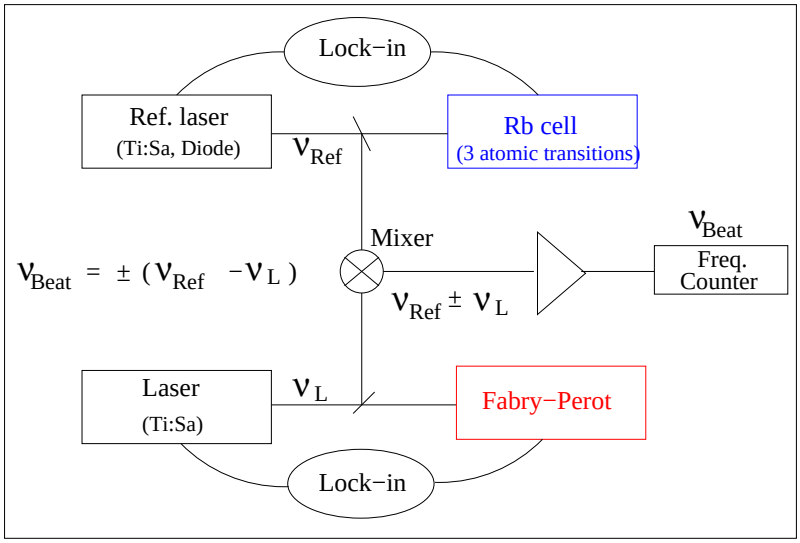

Figure 4.15: Schematic view of the apparatus used to calibrate the FP with Rb lines. Beat frequency technique is used to determine the frequency of the FP transmission peak whose position lies closely to a Rb line.

hopping) have been performed in the $700-708$ nm region (the 700 nm region is important for the second transition frequency in muonic hydrogen and for muonic deuterium).

In the following we will consider two corrections to the simple expression of Eq. (4.24): the Fresnel dephasing and a frequency dependent change of the cavity length due to the use of a dielectric mirror coating. The Fresnel dephasing Φ_{Fresnel} is related to the curvature of the mirror, and is expressed by

$$\Phi_{\text{Fresnel}} = \frac{1}{\pi} \arccos\left[(1 - L/R_1)(1 - L/R_2)\right]^{1/2} \tag{4.26}$$

where R_1, R_2 are the curvature radius of the FP mirrors. This dephasing depends only on the cavity geometry and not on the laser frequency.

A frequency dependent dephasing is caused by the dielectric coating of the mirror. With increasing frequency the average reflection position is shifted deeper into the dielectric structure of the coating. Therefore the effective cavity length L experienced by the laser light is slightly frequency dependent and may be described by [94]

$$L = L_0(1 + \epsilon N) \tag{4.27}$$

where L_0 is the average "zero–order" FP length, N (which is linearly proportional to the frequency) is the fringe number on which the laser is locked and ϵ is a dimensionless parameter which takes into account the small change of cavity length. Inserting Eq. (4.27) in Eq. (4.23) gives

$$I^{\text{FP}} \simeq I_0^{\text{FP}}(1 - \epsilon N) \tag{4.28}$$

where $I_0^{\text{FP}} = c/2L_0$. The resonance condition is then

$$\nu_L \simeq N I_0^{\text{FP}}(1 - \epsilon N) + I_0^{\text{FP}} \Phi_{\text{Fresnel}} \, . \tag{4.29}$$

The Fresnel dephasing can be eliminated by making the difference of two measured frequencies

$$\nu_{L_1} - \nu_{L_2} \simeq I_0^{\text{FP}}(N_1 - N_2)(1 - \epsilon(N_1 + N_2)) \, . \tag{4.30}$$

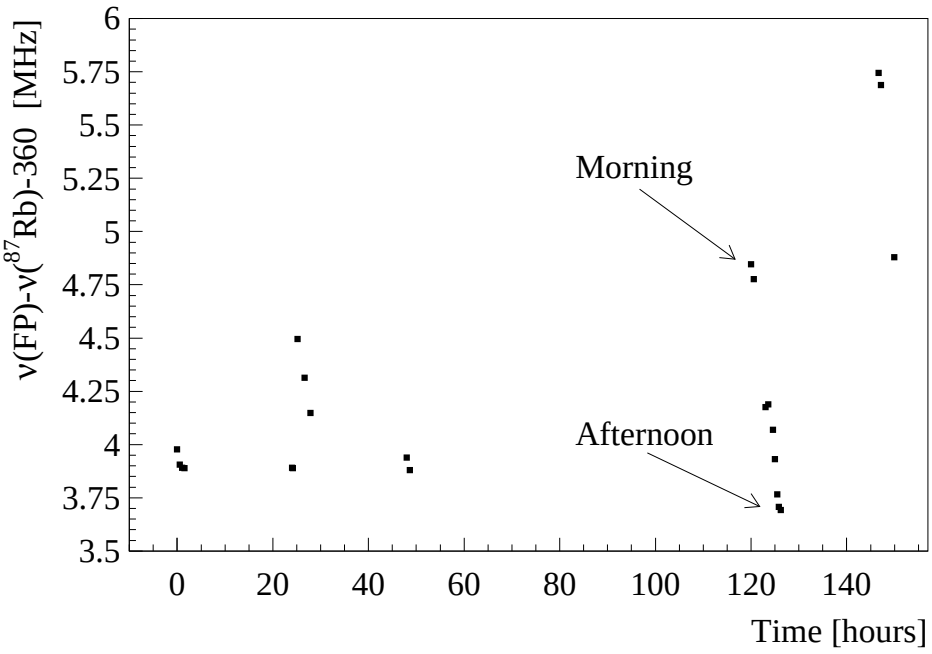

Figure 4.16: Measurement of the drift of a FP transmission peak's frequency at 780 nm. The beat frequency between a laser locked on a ^{87}Rb line at 385 THz and a second laser locked to a FP transmission peak close to this line is measured for one week. The rapid variations have to be attributed to temperature variations (day–night oscillations) which cause a change of the FP length.

Fitting the nine measured FP transmission frequencies (three close to Rb and six close to I_2 lines), with Eq. (4.30), both the zero order free spectral range $I_0^{\rm FP}$ and the phenomenological parameter ϵ can be extracted. It was found that $I_0^{\rm FP} = 1497.46(6)$ MHz and $\epsilon = 1.5(8) \times 10^{-10}$. [5] Note that $N \sim 3 \times 10^5$. The relatively large errors associated with $I_0^{\rm FP}$ and ϵ are due to their strong correlation, but this does not affect the precision of the absolute positions of the FP transmission peaks. The absolute frequency of the laser stabilized on a FP fringe is calculated using

$$\nu_L = \nu_{\rm Rb} - I_0^{\rm FP}(N_{\rm Rb} - N)(1 - \epsilon(N_{\rm Rb} + N)) \tag{4.31}$$

where $\nu_{\rm Rb}$ is the frequency of a FP peak close to a precisely known Rb atomic line. The frequency gap between the Rb reference line and $\nu_{\rm Rb}$ was determined with beat frequencies techniques as described above.

We conclude that any FP transmission peak around 708 nm is known with an absolute precision better than 100 MHz. The distance between two transmission peaks at 708 nm is known with a precision better than 1 kHz.

To measure the long–term stability of our FP we used the same apparatus as depicted in Fig. 4.15 and determined the beat frequency between one laser stabilized on a FP fringe and another stabilized on an atomic line. Any FP cavity drift would cause a change of the beat frequency. In Fig. 4.16 the beat frequency is plotted as function of time. The fast changes of the beat frequency which are visible in the figure are attributed to

[5] For the FP with metallic mirrors used in the $1S - 3S$ hydrogen experiment $\alpha = 1.4 \times 10^{-14}$ [95] was found. This is much smaller than our value for dielectric mirrors since the reflection on a metallic mirror occurs at the surface.

periodic temperature variations in the laboratory in the night–day succession (~ 0.5 K). The stability of the laser locked on a FP fringe was found to be better than 10 MHz over several weeks. Its stability and bandwidth is therefore sufficient for our purpose.

4.10 Summary of the frequency control of our laser system

In Fig. 4.17 all the properties of our laser system with regards to the wavelength control are summarized. The cw Ti:Sa laser, when locked on a FP fringe, has a bandwidth of 1 MHz. Since the frequency of the FP transmission fringes are known with an accuracy of 100 MHz in the 708 nm region, the cw laser frequency is also known with this accuracy. A wave–meter which has an accuracy of about ± 400 MHz is sufficiently accurate to enable an unambiguous determination of the FP fringe number on which the laser is stabilized. The wave–meter is a moving Michelson interferometer which is referenced to a temperature stabilized He:Ne laser. The refractive index of the air is corrected for humidity, temperature and pressure in order to reach the 400 MHz accuracy.

Apart from a small frequency chirp of about $-90(20)$ MHz the frequency of the pulsed Ti:Sa laser (oscillator+amplifier) corresponds to the frequency of the cw–Ti:Sa laser due to injection seeding. The control of the proper injection seeding is achieved by monitoring the delay of the oscillator output pulse relative to the pumping pulse (dye pulse), by the double peak structure of the output pulse and by a spectrometer. The excimer–dye laser system has no influence on the wavelength of the 6 μm source since it just provide the pump energy. The Raman process shifts the frequency by a constant amount given by three times the Stokes frequency. Since the absolute frequency at 708 nm and the Stokes shift (including pressure and temperature corrections given in Eq. (4.20)) are known, the frequency of the 6 μm pulse may be deduced. However a preciser calibration of the 6 μm pulse is achieved using water absorption lines available in the 6 μm region which are known with a precision better than 2 MHz. The frequency of the cw Ti:Sa laser relative to a FP fringe is measured when the 6 μm pulse is resonant with a water line (cf. §4.8).

To search for the $2S-2P$ line the laser needs to be detuned from the water line. Since a water line is present right in the middle of the search range which is ~ 250 GHz wide, the cw Ti:Sa laser has to be detuned by up to hundred FP fringes from the one related to the water line ($N_{\mathrm{H_2O}}$). When we search and scan for the muonic resonance we lock the cw Ti:Sa laser on FP fringes. The frequency of the 6 μm pulse is then

$$\nu_L = \nu_{\mathrm{H_2O}} - I_0^{\mathrm{FP}}(N_{\mathrm{H_2O}} - N)(1 - \epsilon(N_{\mathrm{H_2O}} + N)) + \Delta\nu_{\mathrm{cal}} \tag{4.32}$$

where $N_{\mathrm{H_2O}}$ is the FP fringe number used for the water line calibration measurement, $\nu_{\mathrm{H_2O}}$ the water line frequency and $\Delta\nu_{\mathrm{cal}} = (470 \pm 50)$ MHz the frequency difference between this reference FP peak and the corresponding position of the water line in the 708 nm region (see Fig. 4.14).

Since the FP fringe spacing is known with an accuracy of better than 1 kHz it follows that the 6 μm light is known with an accuracy which is resulting from the quadratic sum of 50 MHz ($\delta\Delta\nu_{\mathrm{cal}}$), $(N_{\mathrm{H_2O}} - N) \times 1$ kHz $\simeq 0.1$ MHz (FP peak spacing accuracy) and 2 MHz (water line position) which is 50 MHz. Note that for the precise determination of the frequency of the 6 μm pulse we don't need to make use of the absolute frequency of the FP transmission peaks and of the Stokes shift value.

Small systematic shifts may occur which worsen the accuracy of the frequency of our laser between the time of the frequency calibration and the measuring time. Chirp

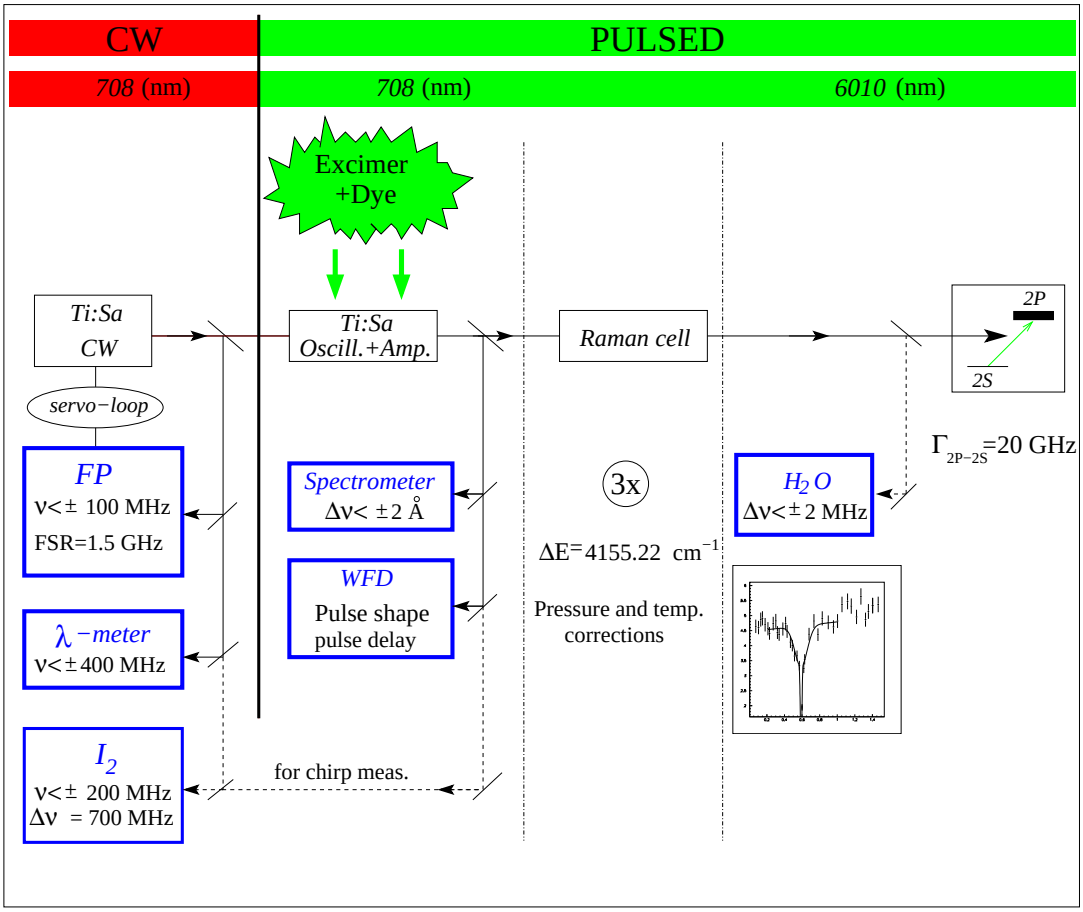

Figure 4.17: Frequency control of our 6 μm laser source. The cw–Ti:Sa laser is locked on the external FP. Apart from a chirp effect which is measured via I_2 absorption, the pulsed Ti:Sa laser has the same frequency as the cw one. The 6 μm source is precisely calibrated using a H_2O line. The I_2 line is also used to calibrate the FP whereas the Lambda-meter is used to determine the FP fringe number. The beams shown with dashed lines are used only during frequency calibration measurements.

variations in the Ti:Sa laser, pressure and temperature variations in the Raman cell and FP length variation contribute to this uncertainty. The variation of the chirp effect due to energy variations of the dye laser pulses is about ±20 MHz (cf. §4.4.3). A variation of the pressure and temperature of the Raman cell leads to a variation of the Stokes shift which may be corrected with a precision better than 10 MHz if the pressure in the Raman cell changes by 0.25 bar (cf. §4.6). The frequency of a FP peak in the 780 nm region was measured to drift less than 10 MHz in several weeks (see Fig. 4.16). Since for the precise determination of the 6 μm frequency we make use only of the FP spacing, the drift caused by systematic variations of the FP are $100/(3 \times 10^5) \cdot 10$ MHz, *i.e.,* totally negligible.

In conclusion the frequency of our 6 μm source is known over the whole required searching range and for all the time necessary to search the resonance line with an accuracy of 55 MHz. This value accounts for all possible systematic drifts of our apparatus.

4.11 The 6 μm multipass cavity

The 6 μm light is coupled into an intensity enhancement cavity placed inside the hydrogen target for the excitation of the $2S - 2P$ transition. Figure 4.18 shows the geometry of the multipass mirror cavity. The muon stop volume ($5 \times 15 \times 194$ mm^3) is elongated in direction of the muon beam (z-axis) because of the low hydrogen pressure. The laser light illuminates the stop volume transversely, because it is not possible to mount laser mirrors on the muon beam axis. Therefore rather long laser mirrors left and right of the muon beam are used. Above and below the muon beam, the x-ray detectors have to be positioned as close as possible to the muon beam for solid angle efficiency (see Fig. 3.7. Hence the vertical dimension of the laser mirrors is made as small as possible. 12 mm high mirrors turned out to be large enough to illuminate a 7 mm high volume.

Laser light enters the cavity through a 0.63 mm diameter hole in mirror M_1 and is reflected between the two mirrors on the order of a thousand times. The cylindrical mirror M_2 confines the light in the vertical direction, whereas the two cylindrical pieces glued to the main flat piece of mirror M_1 guarantee the confinement in the horizontal $\hat{z}$ direction. The radius of curvature R_1 of the additional cylindrical pieces is made four times the mirror spacing d ($R_1 = 4d = 100$ mm), as for this value the reflection conserves the incoming horizontal angles, in order to avoid an increase of the mean horizontal reflection angle. Simultaneously, the radius of curvature R_2 of the cylindrical mirror M_2 has to be different from R_1, to avoid undesired resonant effects: R_2 is chosen to be 110 mm. Because of its unusual shape, the mirror M_1 is manufactured in three separate substrate pieces (the flat part and two cylindrical end parts) and then glued together [96]. Fused silica is chosen as substrate material, and a broadband reflectivity of 99.97% at 6 μm is achieved using a 26 layer dielectric coating of ZnSe and ThF_4 [97]. The 6 μm light is transported to the multipass cavity by Cu mirrors and CaF_2 lenses and windows (see Fig. 4.20). The 12 m long optical beam line is surrounded by boxes and tubes flushed with dry N_2 gas in order to avoid laser light absorption in water. The light is bent by 90° and focused in the mirror hole center. The beam has a minimum waist of 0.1 mm in the hole and

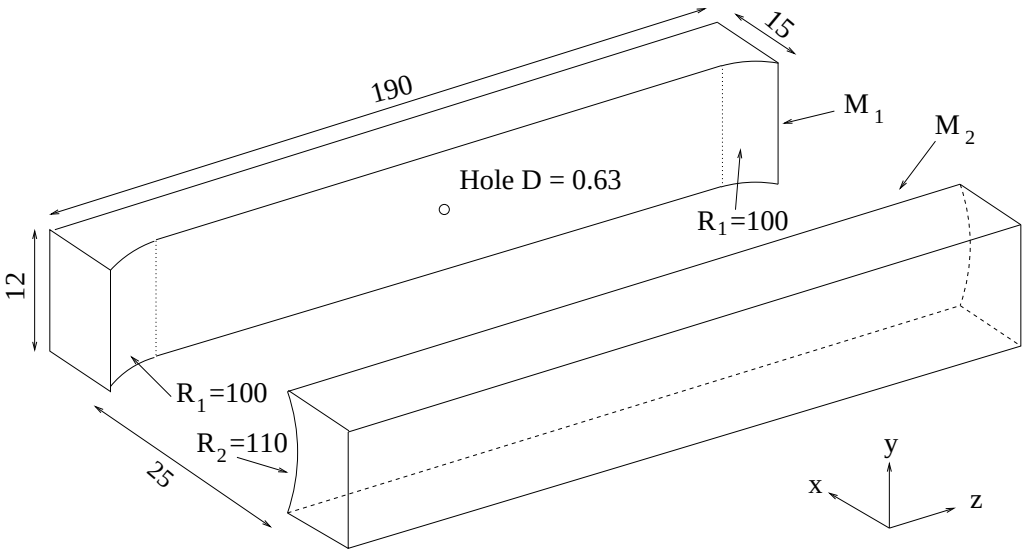

Figure 4.18: Sketch of the 6 μm multipass cavity. The figure is distorted to visualize details. All dimensions are given in mm.

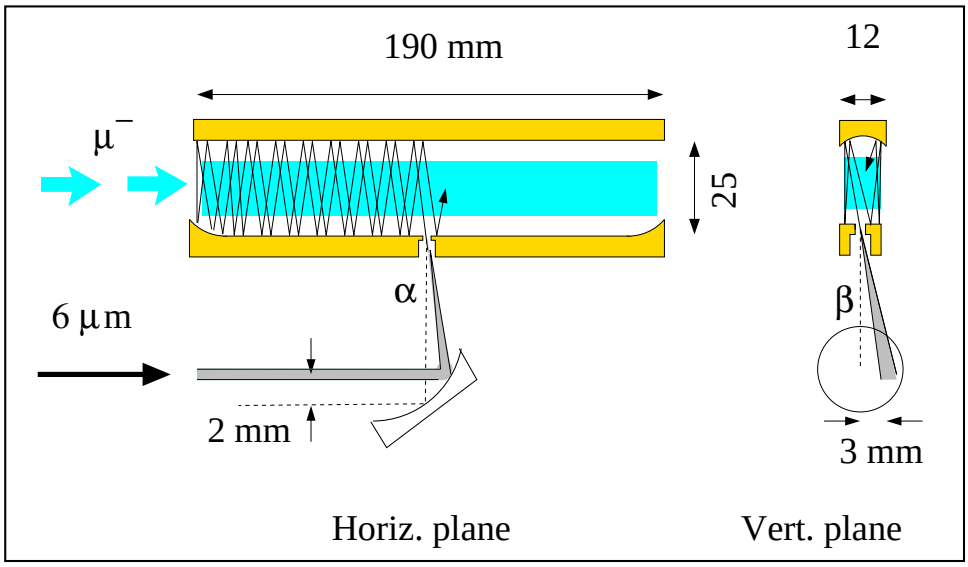

Figure 4.19: Off–axis coupling into the 6 μm cavity. The 2 inch focal length of the parabolic gold–coated mirror focused the 6 μm beam to the center of the 0.63 mm diameter hole.

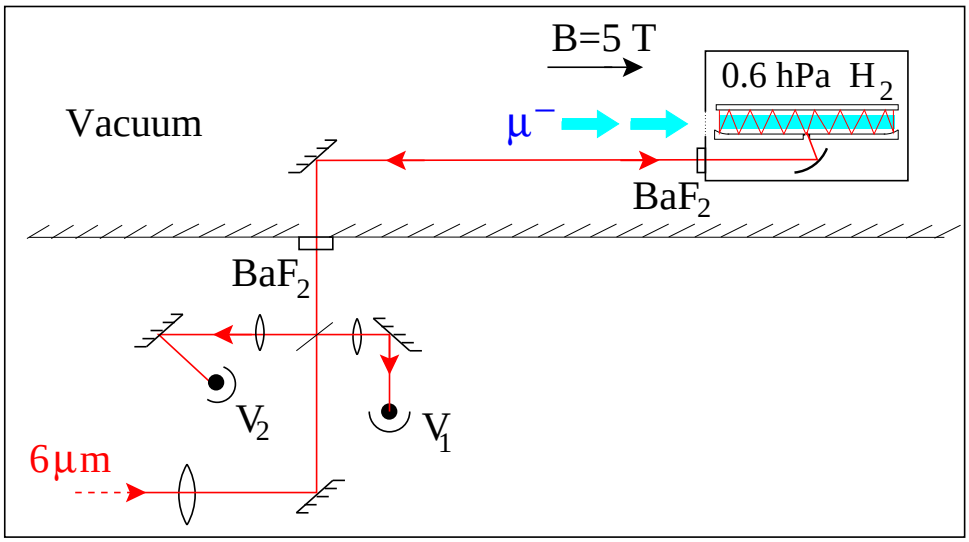

Figure 4.20: Monitoring system for the 6 μm cavity. Before entering the vacuum system, part of the 6 μm light is reflected by a 45° CaF_2 plate and focused on a fast infrared detector V_1. The transmitted pulse crosses the vacuum and target windows and enters the cavity. Part of the light escaping from the entrance hole travels back on the same axis as the incoming light and is detected with a second infrared detector V_2.

a confocal parameter of 10 mm. To optimize the illuminated volume and minimize the losses through reflection from mirror M_2 back out the injection hole, the light is introduced at horizontal and vertical angles relative to the injection hole axis of $\alpha = 40$ mrad and $\beta = 65$ mrad, respectively. In practice, the beam is first aligned on axis, *i.e.*,, the light entering the cavity is directly reflected back out through the hole. The beam impinging on the paraboloid is then parallel shifted by 2 mm horizontally and 3 mm vertically, which results in a change of the cavity beam entrance angles of the values noted above. The coupling scheme guarantees low losses, uniform filling of a large and elongated volume,

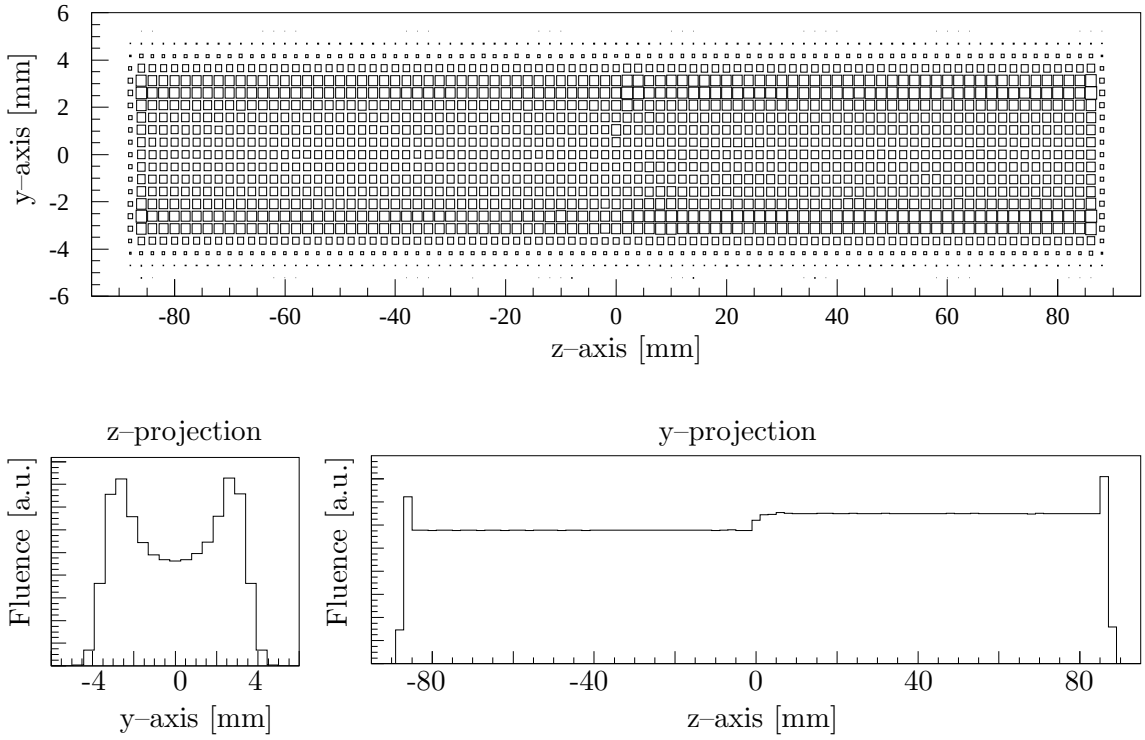

Figure 4.21: Simulated light intensity distribution inside the 6 μm multipass cavity, with projections. The intensity step visible in the y–projection is a consequence of the injection scheme. This asymmetry is washed out in the z-projection due to a larger number of round trips oscillating in y–direction between the two mirrors (Courtesy R. Pohl).

and robustness against cavity and injection misalignment. Mirror tilts as large as 7 mrad (vertically) and 0.5 mrad (horizontally) are tolerable.

One of the major characteristic of this cavity and its injection is its stability. The cavity is first aligned when the target is open and at air pressure as in Fig. 3.8. Then the target is closed, the 5 T solenoid moved and connected to the muon beam line, and then the whole beam line and target are pumped to vacuum. The magnetic field and the LAAPDs cooling is switched on and the hydrogen gas is flushed through the target. After four weeks of measuring time the cavity resulted to be still aligned. No PZT or other remote control of the cavity was necessary.

Figure 4.21 shows the simulated intensity distribution inside the cavity using ray tracing. The resulting spatial intensity distribution shows a 30% non–uniformity in the transverse direction whereas it is quite uniform longitudinally. Using Gaussian optics for the y–direction gives very similar results. Losses due to the (measured) mirror reflectivity of 99.97% and back reflection via the 0.63 mm diameter hole are taken into account, as well as losses due to light "spillover" in y or z-direction caused by cavity and/or injection misalignments.

The main cavity losses are given by the non–ideal reflectivity of the mirrors and by the light escaping from the coupling hole. The escaping light is used to monitor the time distribution of the intensity inside the cavity which depends on the overall cavity and injection alignment. It is separated from the entering light with a tilted CaF_2 plate and is focused on a fast infrared detector (Hg–Cd–Zn–Te semiconductor [98]) as shown in Fig. 4.20.

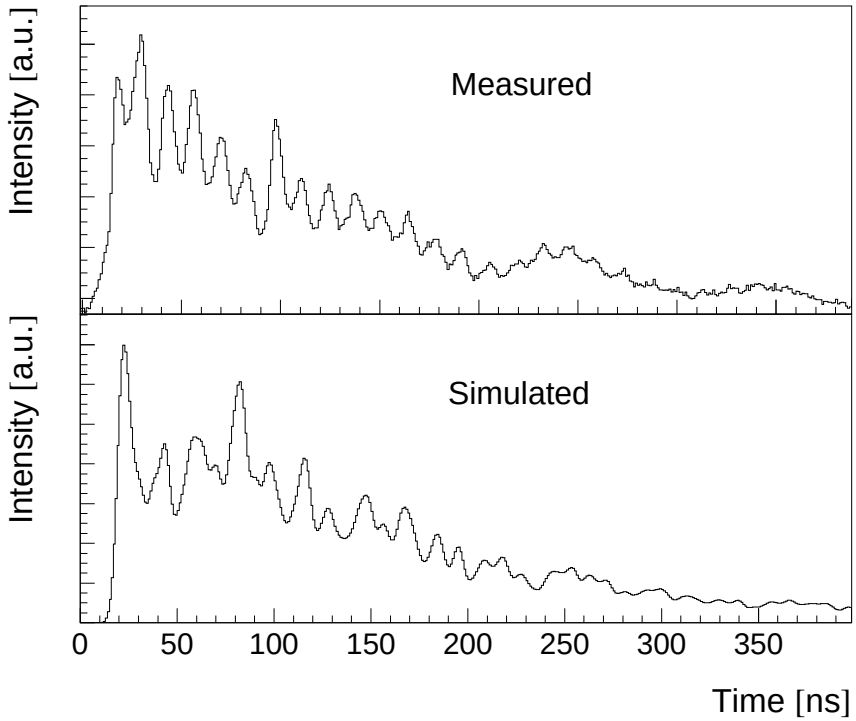

Figure 4.22: Time distributions of the light escaping the cavity. The mean lifetime of 140 ns corresponds to 1700 reflections between the two mirrors.

Typical measured and simulated intensity time distributions of the escaping light are shown in Fig. 4.22. From these time distributions an average lifetime of about 140 ns for the light in the cavity is deduced. Taking into account the distance between the cavity mirrors (25 mm), that corresponds to 1700 reflections between the two mirrors. The number of reflections N between the two cavity mirrors can be expressed as

$$N = \frac{1}{(1-R)+L} \tag{4.33}$$

where $R = 99.97\%$ is the measured reflectivity and L represents other losses. Losses of laser light through the coupling hole can be estimated by assuming a homogeneous 6 μm intensity distribution in the illuminated volume. The average relative loss (through the hole) per reflection is given by the ratio of hole surface $A_{\rm hole} = 0.63^2 \cdot \pi/4$ mm^2 to illuminated transverse area $A_{\rm light} = 170 \times 7$ mm^2

$$L_{\rm hole} = \frac{1}{2}\frac{A_{\rm hole}}{A_{\rm light}} \simeq 1.3 \times 10^{-4} \, . \tag{4.34}$$

The factor 1/2 takes into account the fact that the light impinges on the mirror with the hole only every second reflection. Additional losses $L_{\rm add} \simeq 0.02\%$ are required in order to explain the measured mean average number of reflections via Eq. (4.33), $L = L_{\rm hole} + L_{\rm add}$. This additional loss may be attributed to an increased scattering from the 10 μm thick regions where the two cylindrical end–parts of M_1 are glued to the flat part. The elaborate cavity simulation with input reflectivity $R = 99.95\%$ predicts a lifetime of 140 ns and losses through the coupling hole of about 16–19%. Our simple model predicts escape losses $L_{\rm hole}/((1-R)+L_{\rm hole}+L_{\rm add}) \simeq 20\%$, which is in good agreement with the detailed

calculation. The slightly lower losses found by the simulation may be attributed to the lower light intensity at the hole position (see z-projection of the light distribution in Fig. 4.21) compared to the simple model based on a homogeneous distribution.

Since the time–integrated spatial intensity distribution of the light inside the cavity is relatively homogeneous, the fluence F is given approximately by

$$F \simeq \frac{E_{\rm in}^{\rm laser} n_{\rm refl}}{A_{\rm cav}} \,, \tag{4.35}$$

where $E_{\rm in}^{\rm laser}$ is the pulse energy entering the cavity, $n_{\rm refl} = 1700$ the measured average number of reflections, and $A_{\rm cav} = 17 \times 0.7\,{\rm cm}^2$ the illuminated transverse cavity area. A 6 μm laser pulse energy of 0.12 mJ is therefore sufficient to saturate the $2S-2P$ transition (corresponding to a fluence of $F \simeq 16.5\,{\rm mJ/cm}^2$). A $\mu{\rm p}_{2S}$ atom which has survived to the time the laser enters the cavity has thus a probability of $(1-e^{-1})$ to be excited to the $2P$ state if the laser is resonant with the transition and is providing a pulse with 0.12 mJ energy (cf. Appendix E). The detailed simulations confirmed this, leading to a value of 0.1 mJ. Taking into account various losses on the beam path from the Raman cell to the cavity, about 0.2 mJ are required at the Raman cell exit to saturate the transition.

The ripple structure — visible in Fig. 4.22 — of the back–reflected light corresponds to a space–time correlation of the light intensity distribution in the cavity directly following the injection. Its period is approximately given by the average time needed for the light to reach the cylindrical end part of the cavity and return to the entrance hole, which is $\sim$16 ns for a mean horizontal injection angle of 40 mrad. At later times, the ripple structure is washed out due to the angular divergence of the injected beam and the imperfect conservation of the horizontal angle at each end–part reflection. The simulation reproduces the main characteristics of the light leaving the cavity. The precise position and intensity of the individual peaks of the ripple structure depends on the injection angle and cavity misalignment. No attempt was made to try to precisely reproduce the measured time spectrum since each Monte Carlo simulation.

4.12 Summary

We have developed a powerful, fast triggerable, 6 μm laser beam with 55 ${\rm s}^{-1}$ (stochastic) repetition rate. Two excimer pumped dye lasers operating at 540 nm are used to pump an oscillator–amplifier Ti:Sa laser. A reliable and simple injection seeded Ti:Sa oscillator has been developed. An output pulse of 1.2 mJ energy, 7 ns width at 708 nm is achieved (without the use of Q-switching methods), with a pump energy of 15 mJ. The simulated oscillator characteristics (pulse length, energy output and frequency chirp) are in good agreement with the measured values. The 8–pass Ti:Sa amplifier delivers a pulse energy of 12 mJ at 708 nm which is converted to 6 μm via a Raman shifter. The Raman cell produces 0.2 mJ of 6 μm light corresponding to a quantum efficiency of 14%.

The total delay of the 6 μm pulse from trigger to multipass cavity entry is 1.6 μs, corresponding to the sum of the following delays: excimer–dye laser (1220 ns), Ti:Sa oscillator (55 ns), Ti:Sa amplifier (45 ns), Raman cell (200 ns) and various beam paths (80 ns). The laser tunability is between 5.5 and 7 μm. The maximal wavelength is limited by the Raman gain which decreases at longer wavelengths (see Eq. (4.14)) whereas the minimal wavelength is limited by the spectral profile of the Ti:Sa gain. The absolute frequency of the tunable 6 μm source stabilized on an external FP is deduced from a water line absorption measurement with an accuracy of 55 MHz; the bandwidth is 680 MHz.

To enhance the intensity of the 6 μm light, a multipass cavity providing a large illuminated volume ($7 \times 25 \times 170$ mm^3) has been developed. The multipass cavity confines the 6 μm light with a lifetime of 140 ns which corresponds to about 1700 reflections between the cavity mirrors. An output pulse energy of 0.2 mJ from the Raman cell is found to be sufficient to saturate the $2S - 2P$ transition. The 6 μm source, the multipass cavity and associated diagnostics meet the requirements for the muonic hydrogen $2S$ Lamb shift experiment and have been operated continuously for 4 weeks during the search for the $2S - 2P$ resonance in 2003–run.

Chapter 5

Measurements

This Chapter describes how the data recorded by the various detectors are identified, merged in distributions and analyzed. Section 5.1 describes the technique with which the LAAPD signals recorded in the WFD (wave form digitizer) are processed. How various signals are identified and the events classified is described in §5.2. The most important spectra are presented in §5.3, §5.4 and §5.5 together with the relevant cuts which are used all through the analysis of the data. Timing calibration of the whole apparatus and detection efficiency for the x rays are given in §5.6 and §5.7, respectively. This overview is rather detailed because this knowledge is important not only for the analysis of the resonance data described in Chapter 6, but also for the background study presented in Appendix H.

5.1 Analysis of the waveform digitizer signals

The 8-bit WFD records the whole time evolution of a LAAPD signal ($0 - 255$ dynamic range) during ~ 14.3 μs (2048 channels of 7 ns) like an oscilloscope. The diversity of the WFD signals which have been recorded is demonstrated in Fig. 5.1. A standard WFD spectrum has a flat baseline with superimposed negative–going, single (a–d) or multiple (e–g) pulses. Each individual pulse represents the LAAPD response to an x ray or an electron. The LAAPD detection efficiency for high energy x rays is small and therefore there is a trend that small amplitude pulses are induced by x rays and large amplitude pulses by electrons. The maximal full dynamic range available for the pulse corresponds to an incident x-ray energy of $8 - 13$ keV, depending on the LAAPD. Higher amplitude pulses are out of the WFD dynamic range as shown in (d–g). Such signals will be referred to as "saturated signals".

The analysis of the WFD spectra first eliminates non–physical signals and then identifies the time and the energy of the pulse(s) inside a single WFD record. A negative–going edge corresponds to a normal pulse due to an x ray or an electron (i, j). A periodically oscillating pulse structure ("ringing") is attributed to plasma discharges in the LAAPDs mainly caused by alpha particles or large–amplitude signal caused by electrons. A positive pulse (overshoot) is attributed to crosstalk between LAAPDs in time coincidence with a large signal in one LAAPD (h). The maximum possible number of pulses of our interest is three and corresponds to the physical case, that a 2 keV μp x ray, delayed 4.9 keV μC x ray and a muon decay electron are detected in the same LAAPD (g). This corresponds to the signature of a known background event (cf. Appendix H). The maximum allowed number of positive–going edges is one, corresponding to a possible crosstalk (h). There-

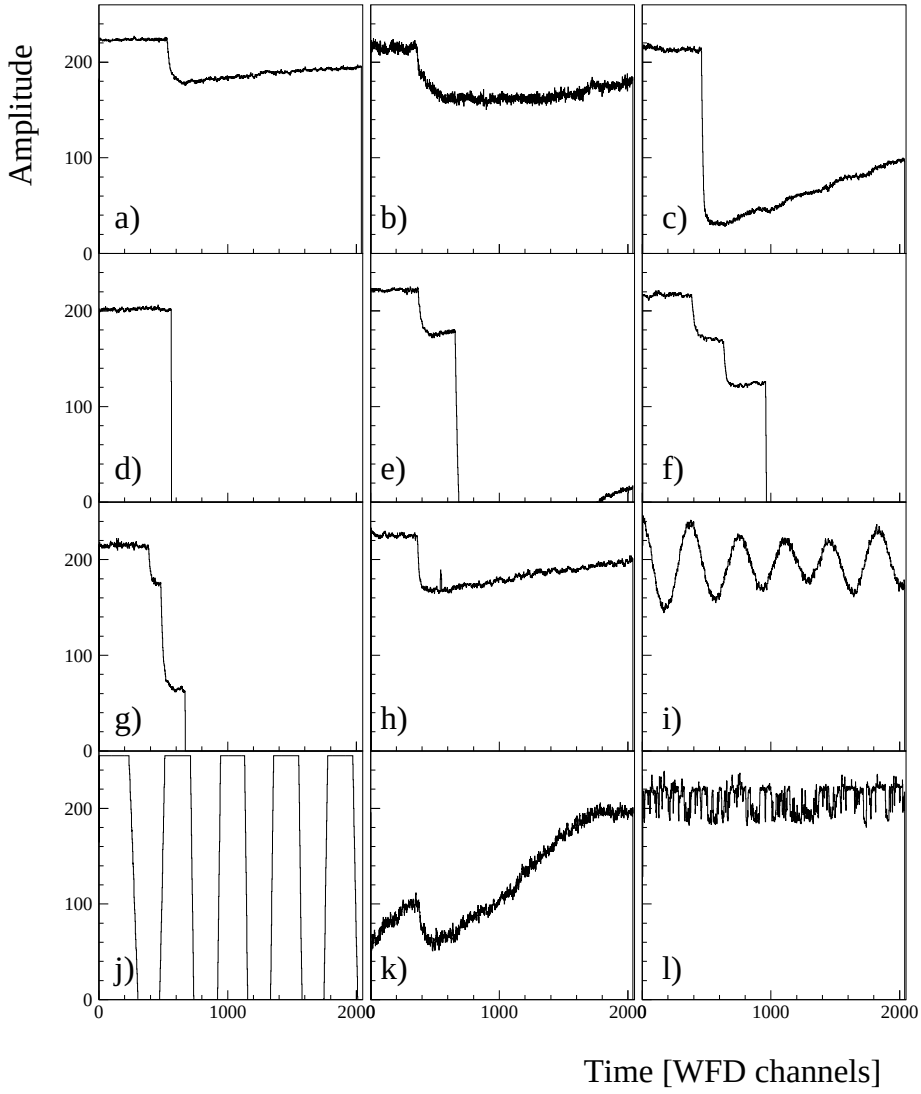

Figure 5.1: Examples of typical WFD spectra (7 ns/channel, total time range 14.3 μs). (a, b, c, d) Single pulse spectra: signals due to x rays with energy of ∼ 2 keV from (a) a high quality LAAPD and (b) from a noisy LAAPD; (c) higher amplitude signal within the WFD dynamic range, (d) saturated high–amplitude signal out of this dynamic range, most probably from an electron. (e) Double pulse spectrum: first pulse from a 2 keV μp x ray, second pulse due to a muon–decay electron. (f, g) Triple pulse spectra: (f) two 2 keV μp x rays and an electron signal, (g) 2 keV μp x ray signal, followed by a delayed second pulse due to a 4.9 keV μC x ray and third pulse from a muon decay electron. (h, i, j, k, l) Other types of WFD spectra: (h) an overshoot due to crosstalk, (i, j) ringing, (k) pulse superimposed over a steep baseline, (l) an example of an irregular structure (Courtesy L. Ludhova).

fore, if the number of identified negative–going edges is larger than three or the number of positive–going edges is larger than one, the spectrum is identified as ringing and the whole event is discarded.

Otherwise, when an edge is found, the corresponding pulse is fit using a standard pulse leaving as free parameters the amplitude and the time when the pulse starts. The standard pulse is obtained for each one–hour run and each LAAPD by averaging a set of measured 2 keV pulses. The fitted amplitude and beginning of the pulse lead respectively

to the energy and the time of the detected radiation. When the first pulse is identified it is subtracted from the measured WFD spectrum, and the procedure is iterated in order to identify successive pulses.

5.2 Event classification

As previously explained the signals measured by the various detectors (LAAPDs, electron paddles, S_1, S_2, D_3 and laser diodes) during an EVG are recorded. Energy and time information of all detectors are required. For the LAAPDs this information is extracted from the fitting procedure of the pulses in the waveform digitizer, whereas the other detector signals have been recorded with TDCs and ADCs.

5.2.1 Signal versus particle identification

Photons of less than 10 keV energy interact with matter by the point–like photo–effect where only one detector is affected, whereas electrons deposit energy along their path. In the 5 T magnetic field the muon decay electrons have a maximal gyration radius of 3.5 cm and may therefore hit several detectors. If a pulse in a LAAPD is detected in time–coincidence with any pulse in another LAAPD or electron detector, this signal is classified as an *electron*. If several LAAPDs show a signal in time coincidence and the sum of their energies is above a certain threshold value, the ensemble of these signals is identified as an *electron*. However it is possible than an electron induces a signal only in one LAAPD and is not detected by any other detector.

The identification of single pulses in one LAAPD relies on the amplitude of the signal. For energies above $E_x^{\mathrm{hi}} \simeq 8$ keV the single signal is classified as *electron*, for intermediate energies between $E_x^{\mathrm{low}} \simeq 1$ keV and E_x^{hi} the signal is classified as *x ray*, whereas below E_x^{low} it is classified as *neutron* (E_x^{low} and E_x^{hi} is chosen individually for each LAAPD). Pulses with an amplitude below E_x^{low} can not arise from x rays of that energy since the absorption layer in front of the LAAPDs excludes the possibility to detect such low–energy x rays. Some of this pulses may be correlated with neutrons.

It should be emphasized that this signal classification relies on an average behavior of the particles interacting with the detectors. It may occur that an electron deposits such a low energy in the LAAPD that it is identified as an *x ray*, or that a high energy x ray, *e.g.,* from a μC transition, is classified as an *electron*. Signals detected by the electron paddles are classified as *electron* because x rays and neutrons have a small reaction probability in the plastic scintillator material. In addition, D_3 signals with large amplitudes ($D_3{}^{\mathrm{hi}}$) are also classified as *electron* because x rays have either smaller energies or are not absorbed in the LYSO crystal.

5.2.2 Event construction

All signals detected within one EVG are classified as described above and ordered in time. Different event classes have been constructed, describing the time sequence of *x rays* (x) and *electrons* (e) within the EVG. The largest fraction (70%) of the measured events contains only one electron, *i.e.,* corresponds to the e event class which is not further considered in the analysis. The second largest contribution is the xe event class, that is, an x ray followed by an electron signal. This category accounts for 12% of the total number of events and is the class which is used for the search of the laser resonance. This choice was

motivated by the fact that the requirement of a delayed electron considerably reduces the background (see next section). The *x* event class accounts for 8% of the total number of events. A comparison between the number of events in the *x* and *xe* event classes leads immediately to a rough estimate of the electron detection efficiency of about 60%. All other event classes like *xx, xxx, xxe, xee, ee, eee, ex, exe* ... are helpful for background studies. The *xx* and *xee* classes (0.1% and 0.9%, respectively) are also considered for the resonance search.

5.3 X-ray and electron energy spectra: K_α energy cut and delayed electron cut

In order to study the LAAPD response to electrons, energy spectra of LAAPD signals in time coincidence with electron detectors (paddle+D_3^{hi}) are constructed. As is clearly visible in Fig. 5.2 the electron energy distribution is mainly concentrated in two regions which may be explained as follows. If the electron is striking an LAAPD at the margin of its active region, where only a part of the created charge is collected or the gain is small, it will give rise to the low energy component of the spectrum. The majority of the electrons on the contrary cross the active area of the LAAPD and give rise to the high energy component of the spectrum. There is a non–Gaussian tail towards higher energies. More energy is deposited at increasing electron incidence angles (relative to the normal of the detector). The angle distribution of the electron impinging on the LAAPDs leads to the tail at higher energy.

As previously mentioned, signals in the LAAPDs with an energy below $E_x^{hi} \simeq 8$ keV are considered as *x ray*, under the condition that they are not in time coincidence with another signal in any other detector. In contrast, for the construction of the spectrum in Fig. 5.2 a signal in the LAAPDs was required in time coincidence with another signal in the electron detectors. However it may occur that an electron crosses one LAAPD producing a low–energy signal but does not hit any other detector. This signal would be classified

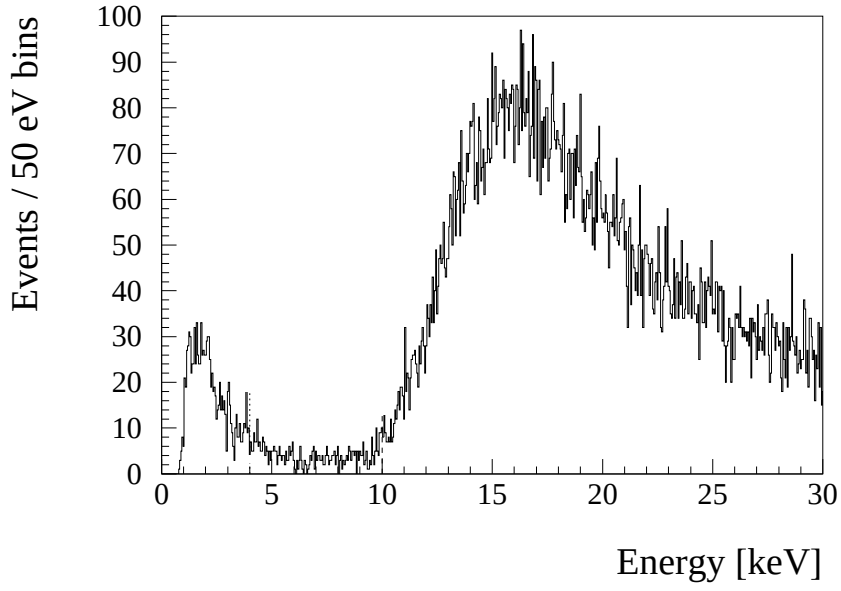

Figure 5.2: An example of an LAAPD electron energy spectrum.

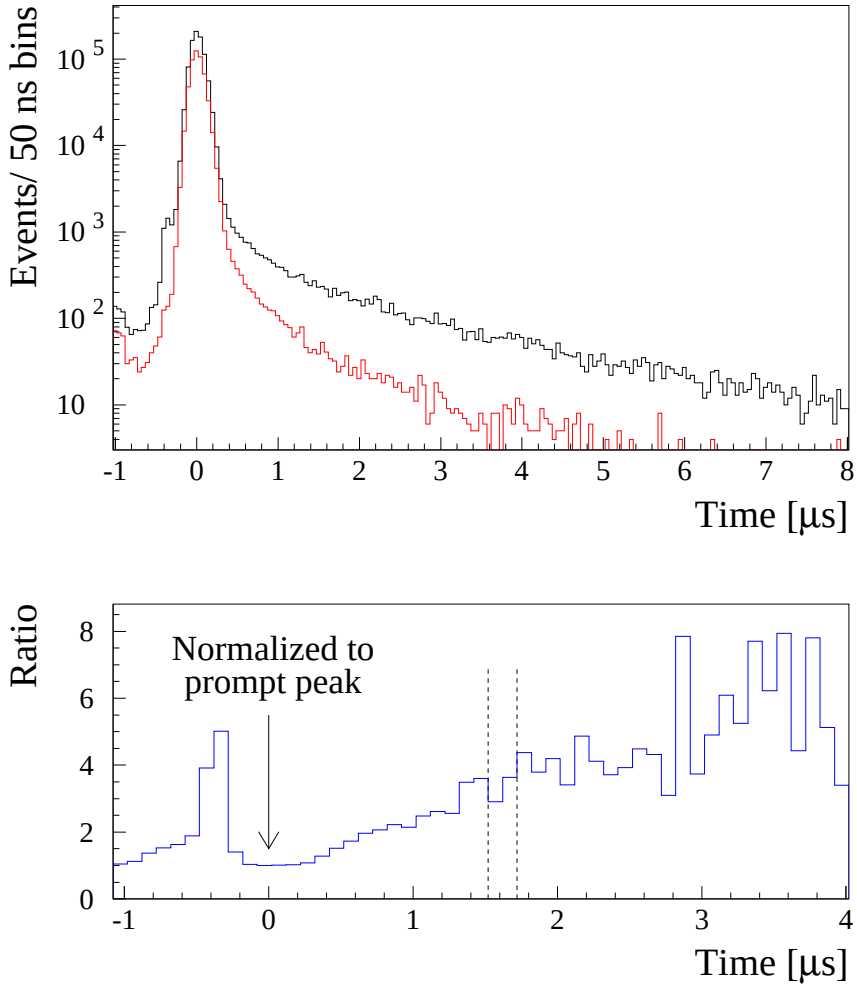

Figure 5.3: Demonstration of the DELE cut effectiveness. (Top): 2 keV x-ray time spectrum for the xe event class (red) compared to the x-ray time spectrum where no delayed electron is required, given by the sum of the x, xe, xee, xx and xxe event classes (black). (Bottom): Normalized ratio of the above plotted histograms. At time zero corresponding to the "prompt" peak the ratio is one (due to normalization). At delayed times it increases showing that the DELE cut strongly reduces the number of delayed 2 keV x rays. In the laser time window ($t \in [1.5, 1.7\ \mu s]$), represented by the two dashed vertical lines, the xe event class shows a factor of four less background. The peak at negative times has to be attributed to electrons from muon decay in flight before muon capture occurs. The large fluctuations for times larger than 3 μs are caused by statistics.

as an *x ray* although it originates from an electron. This represents a dangerous source of background events if the so called "delayed electron" cut (DELE) was not introduced. The requirement of the delayed electron which satisfies $t_e - t_x \in [0.1, 7.1\ \mu s]$ corresponds to the DELE cut.

In order to ensure that the detected *x ray* is not faked by an electron (which represents the largest event class), a detection of a delayed (with respect to the *x ray*) *electron* is required. Moreover the requirement of a delayed electron further increases the probability that the detected x ray is correlated with the muon, reducing the misidentification of possible uncorrelated background. Therefore for the laser experiment only the *xe* class of events was taken into account.

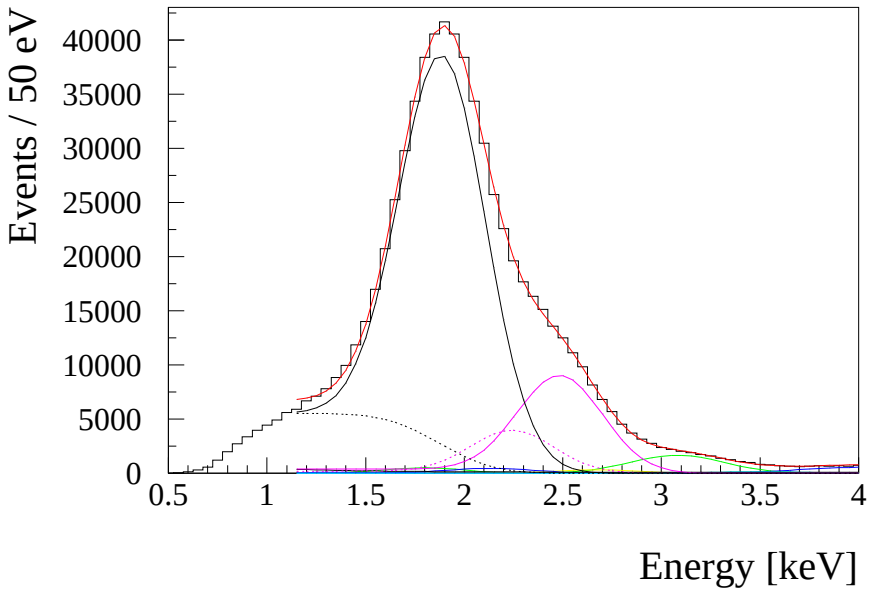

Figure 5.4: Example of an x-ray energy spectrum with DELE cut. Only the 10 LAAPDs with the best energy resolution are considered. The total fit function (red solid line) is the sum of: μp K_α peak (black solid line) and its tail (black dotted), μp K_β (magenta dotted) and μp $K_{\rm rest}$ (magenta solid), μN transitions (green and yellow solid) and in blue μO transitions (Courtesy L. Ludhova).

A demonstration of how DELE cut reduces the relevant background is given in Fig. 5.3 where the *x-ray* time spectrum for *xe* events is compared with the time spectrum of all 2 keV events (given by the sum of all accepted event classes having as a first signal an *x ray*). The peak at time zero originates from the deexcitation process following the μp formation, *i.e.,* it correspond to the Lyman–series deexcitation occurring in the "prompt" cascade. Its width is mainly given by the distribution of muon stopping times. The laser induced events are expected to appear in the laser time window between 1.5 to 1.7 μs. However no such events can occur in these graphs since only no–laser events were considered here. Therefore the tail at delayed times corresponds to the background for the laser experiment, and it is essential for the laser experiment to reduce this tail. As can be extracted from the bottom graph, the detection of a delayed electron improves the signal/background ratio in the laser time window by almost a factor of four.

The *x-ray* energy spectrum has a peak at 2 keV which originates from the deexcitation process following the μp formation (see Fig. 5.4). As previously explained 99% of the formed μp atoms emit a Lyman–series x ray within 100 ns after muon capture ("prompt" deexcitation). The energies and yields of the K_α, K_β, and $K_{\rm rest}$ x rays are given in Table 5.1. The resolution of the detector is not sufficient to clearly separate the various Lyman–transitions. The x ray spectrum is fit with three lines. Each line is described by a Gaussian and a tail toward low energy. Mathematically this tail is described by a "Gaussian complementary error function", *i.e.,* the integral from the right to the left of a Gaussian. Physically this tail arises from x rays absorbed in region (A) where the produced charge may be partially captured before it reaches the amplification region and in region (C)(see Fig. 3.9). The resulting energy resolution is $\sim$ 27% (FWHM) for the K_α peak [16].

Since the signature for a laser–induced transition is the emission of a K_α x ray, only *x rays* with an energy from approximately 1.5 to 2.5 keV are considered during the search

Table 5.1: Energies and measured relative yields (interpolated for 0.6 hPa) of the μp K-series [14,99,100]. K_α and K_β are the $2P \rightarrow 1S$ and $3P \rightarrow 1S$ transitions, respectively. $K_{\rm rest}$ represents the sum of all transitions from nP states with $n > 3$ down to the $1S$ state. $Y_{\rm tot}$ is the total K–yield, $Y_{\rm tot} = Y_{K\beta} + Y_{K\alpha} + Y_{K{\rm rest}} \leq 1$.

Transition		Energy [keV]	Relative yield $Y_{\rm K}/Y_{\rm tot}$
$2 \rightarrow 1$	K_α	1.898	0.821(12)
$3 \rightarrow 1$	K_β	2.249	0.061(9)
$(> 3) \rightarrow 1$	$K_{\rm rest}$	2.45(2)	0.118(11)

of the resonance. The values for this K_α energy cut are adjusted for each LAAPD individually, depending on its energy resolution in order to optimize the K_α peak detection while discarding x rays having other energies (background reduction).

5.4 Second–muon cut

There is a small but not negligible probability that during an EVG a second muon enters the target at random times, slows down and forms a μp atom. Such a muon is termed *second muon* whereas the muon opening the EVG is termed *first muon*. A 2 keV μp x ray related to a *second muon* may occur at laser time and thus fake a laser induced event.

The time difference between a muon crossing S_1 and the detection of the "prompt" deexcitation after the μp formation is measured to be in the interval $350 - 850$ ns. This time window is given by the time required by the muon to reach the target, to slow down, to be captured and deexcite to the ground state. If there is a *second muon* detected in S_1 $350 - 850$ ns before a measured x ray, the event is rejected. Since the S_1 signal is fed also to a PTDC which can register multiple hits, several muons can be recorded within the same EVG. In a similar way, the S_2 detector can be used to detect a *second muon* entering the target, but this possibility was precluded due to a large pickup noise of the excimer lasers in the S_2 detector.

The effectiveness of the *second muon* cut is demonstrated in Fig. 5.5. The red line represents the background at delayed times which can not be eliminated by applying both the DELE and *second muon* cut. X rays correlated to *second muons* can be eliminated with an efficiency corresponding to the efficiency of the S_1 detector, *i.e.,* 85%. The delayed background which can not be eliminated by the *second muon* cut has its origin mainly from muon transfer to carbon (cf. Appendix H). When the μp_{1S} atoms drift and reach the polypropylene foils in front of the LAAPDs muon transfer occurs ($\mu p + C \rightarrow (\mu C)^* + p$). The peak visible in the spectrum at 4.9 keV arises from the $\mu C_{4\rightarrow 3}$ radiative transitions. The continuous background is always flat at energies above 6 keV and raises toward lower energies. The flat part corresponds to the tails (represented in §5.3 by complementary error functions) from $\mu C_{3\rightarrow 2}$ (14 keV), $\mu C_{2\rightarrow 1}$ (75 keV), and other Balmer and Lyman μC transitions. The origin of the low energy part is not fully understood. It may be caused by x rays absorbed in the LAAPDs drift region and/or behind the multiplication region with gain$\sim$ 1 (cf. §3.2.1). This transfer–induced background can not be eliminated by the *second muon* cut since it is caused by the *first muons* which drift to the target walls. The DELE cut can also not eliminate these background events since the muon lifetime in μC is very similar as in μp.

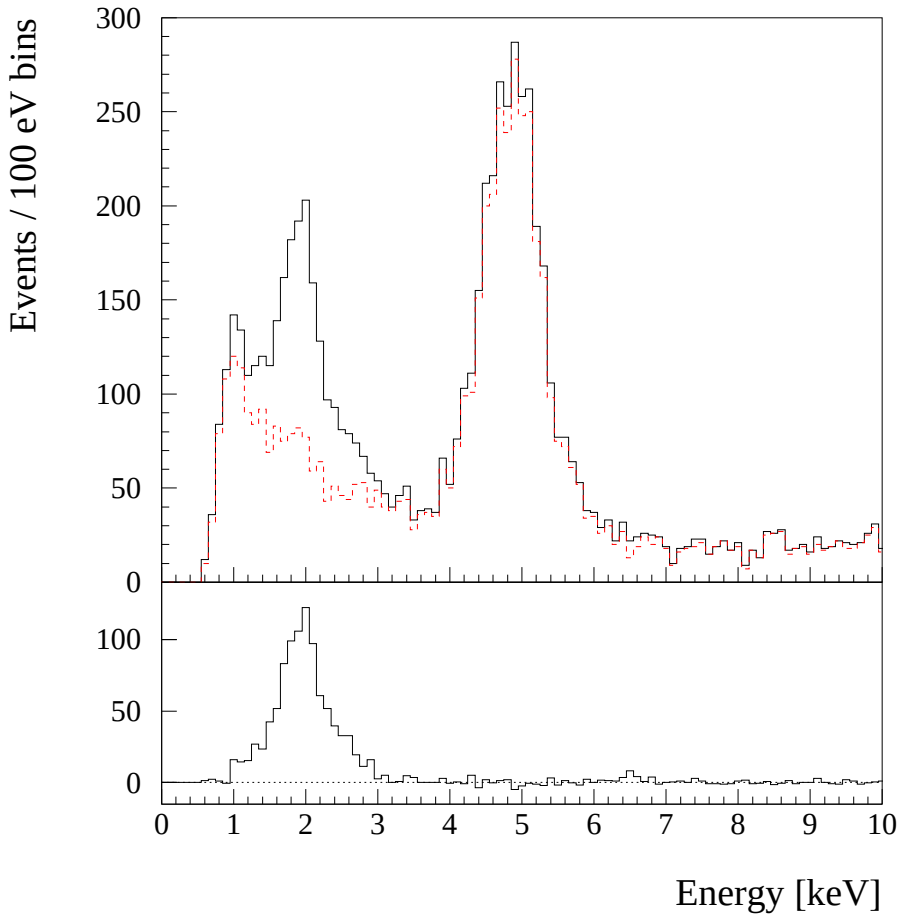

Figure 5.5: Demonstration of the "second muon" cut effectiveness for delayed x rays. (Top): energy spectra of x rays with t_x later than the "first muons" μp "prompt" peak. The solid–black and dashed–red spectra are without and with the "second muon" cut, respectively. The 2 keV peak is due to the "second muon" μp x ray. (Bottom): The difference of the black and the red spectra shown in the top part normalized in a way that 4.9 keV μC peak disappears.

5.5 Electron time spectrum

Energy and time spectra of the signals from the electron paddles are considered here. The 2D-histogram in Fig. 5.6 shows the energy E_e versus the time t_e of *electron* signals detected in the electron paddles. The time distribution of the events with energies above the plotted line have an exponential decaying time distribution with a decay constant corresponding approximately to the muon lifetime. Events with energies below that line have a higher level of time–independent background with respect to those above this line. This flat time distribution below the line corresponds to single photo–electron noise generated at the PMT cathode and neutron induced signals in the paddles scintillators and light–guides. In the search of the laser resonance it is important to accumulate all possible statistics. Therefore also signals below the single photo–electron line have been accepted. The acceptance of this low energy signals is motivated by the fact that also a large amount of muon–correlated signals have been detected below this line. Probably this single–photon signals arise from Čerenkov light produced by electrons striking the large Lucite light–guides but not the scintillators. These light–guides mounted down–stream are

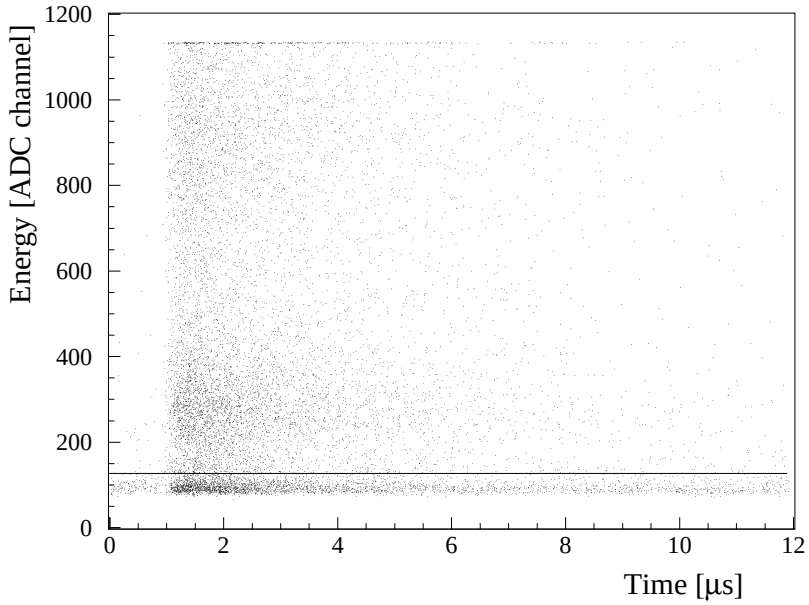

Figure 5.6: 2D spectrum of time t_e and energy E_e of the signals detected in the electron paddles. Similar result for the other paddle. Single photo–electron signals are expected to be below the solid horizontal line.

transporting the light produced in the paddle scintillators to the PMTs which are placed in a region of low magnetic field. The one–dimensional projection of the above 2D-histogram for energies below the solid line is shown in the top part of Fig. 5.7. As can be inferred from the histograms the number of detected "good" electrons is increased by 35% when the Čerenkov are included. As will be explained later in Appendix H, the inclusion of the noise in the paddle PMTs causes an increase of about 60% of the background events in the laser time window. At our low event rates due to Poisson statistic it is advantageous to increase the rates at a slightly worse signal–to–background ratio.

The time distribution shown in the bottom part of Fig. 5.7 for signals above the solid line — originated by muon decay electrons — should have an exponential time distribution with a lifetime of 2.197 μs (muon lifetime). A deviation from this behavior is observed which has to be attributed to the time–dependent drift of the μp atoms in the hydrogen gas. Two effects lead to the deviation from the expected behavior. First, while the μp atoms move toward the walls of the gas target, the electron efficiency increases due to an increase of solid angle because the μp atom is approaching the detectors. Second, when the μp atoms impinge on the target walls muon transfer to an atom of the walls occurs. The muon lifetime in such atoms changes because of nuclear capture process ($\mu^- + p \rightarrow n + \nu_\mu$) which increases approximately as Z^4 for light elements. If the muon is transfered to the C atoms of the polypropylene foils this effect is small, the muon lifetime is $\sim$2.0 μs instead of $\sim$ 2.2 μs [101]. However if transfer occurs to Zn or Se atoms which are the coating material of the cavity mirrors the muon lifetime is reduced to 160 ns. This will cause a time–dependent reduction of the number of measured electrons. At late times when all muons have transferred to the walls, the lifetime should be the μC lifetime since the muons captured in higher Z materials have already disappeared.

This time behavior of the electron detection is shown in Fig. 5.8 using the event class *xe*. The distribution of the time difference $t_e - t_x$ is plotted. This distribution is similar to the time distribution of the electrons in the electron paddles. This time spectrum is

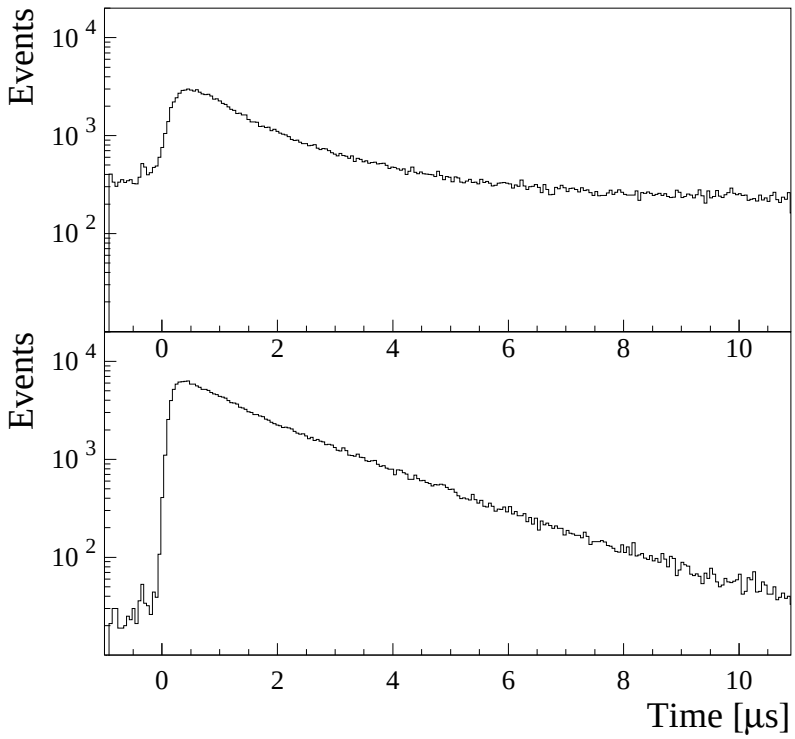

Figure 5.7: (Top): Time spectrum of electron paddle signals below the line plotted in Fig. 5.6 corresponding to single photo–electrons. The exponential part has to be attributed to Čerenkov light produced in the light–guides whereas the flat component arises from the single photo–electron noise. (Bottom): Time spectrum of the corresponding signals above the line. The different shape of the two peaks has to be attributed to variations of the detection efficiencies as a function of time, caused by the drift of the μp atoms in the gas target. Only the xe event class is considered in these spectra.

shown since, as will be later described, it can be used also for a timing calibration of our detectors. Moreover it includes contributions of the electron detection in all the electron detectors, LAAPDs and D_3 included. As will be explained later various background effects have a similar time distribution (cf. Chapter H).

It has to be noticed that this spectrum is constructed releasing the definition that a coincidence signal has to be attributed to an *electron*. Any LAAPD signal with energy below $E_x^{\rm hi}$ classified here as *x ray*, while the *electron* signal from any other detector may occur simultaneously. The sharp peak at time $t_e - t_x = 0$ is due to (physical) electrons detected at least in two detectors, one in an LAAPD where it deposits a low energy signal which is considered as an *x ray*.

As can be seen from Fig. 5.8, the electron detection probability increases at early times $(100 - 400$ ns) which has to be attributed to the drift of μp atoms to the target walls. At medium times $(0.8 - 2\ \mu$s) the decay time is considerably faster than the muon lifetime. This is caused by the fact that about 30% of the μp atoms drift to the ZnSe surface of the cavity mirrors, where most of the muons undergo nuclear capture without emitting a high–energy electron. The number of electrons from muon decay is correspondingly decreased in this time interval. Only at later times, the measured slope corresponds to the μC lifetime if a flat background is taken into account. This flat background is caused by the paddles noise.

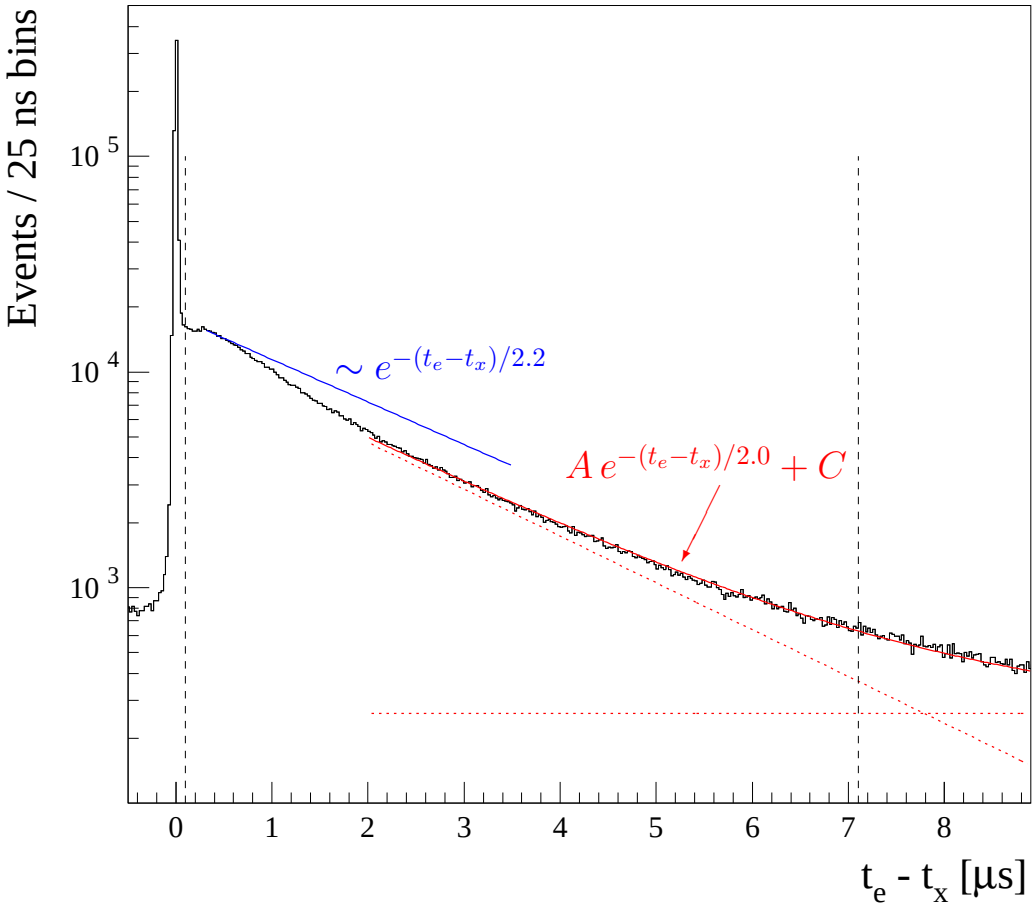

Figure 5.8: Time spectrum of the time differences $t_e - t_x$ for the xe event class. The time 0 represent the time of x–ray detection. No DELE cut is applied. The sharp peak at time 0 is due to the electrons detected at least in two detectors; once also in an LAAPD, where the electron deposited an energy below the $E_x^{\rm hi}$ threshold, and therefore is considered as an x ray. The two dashed vertical lines represent the DELE cut time window usually applied (not for this histogram) for the analysis of the data. The data are fitted for times larger than 2 μs with an exponential function with 2.0 μs lifetime (corresponding to the μC lifetime) and a flat background from paddles noise (red functions). The blue curve represents the time spectrum if transfer to the wall would not occur.

A detailed analysis of the time integrated electron detection efficiency for the various detectors has been reported in Ref. [16]. The total probability to detect a muon–decay electron is ∼66% for $t_e - t_x \in [0.1, 7.1\ \mu\text{s}]$. An exclusive contribution of the electron detectors (paddles+D_3) is ∼35%, and for the LAAPDs ∼13%. The remaining ∼18% are detected in both detector types.

5.6 Time calibration and resolution

The time difference between events measured by the same detector is directly measurable. However to compare the time difference between signals from different detectors the relation between the two detector time scales has to be known and constant. Beam particles or suitable radioactive sources may produce time–coincident signals in two or more detectors and are therefore usually used to perform time calibration and time resolution measure-

ments. In our case, the time calibration of the LAAPDs is based on muon decay electrons crossing at least one LAAPD and one electron detector. It is the 5 Tesla magnetic field forcing the muon to spiral around a magnetic field line which enhances the probability that a single electron hits several detectors. The electron time–of–flight between different detectors is negligibly short on our time scale.

The relative time between LAAPDs and electron detectors is defined with respect to one paddle detector. Histograms of the time differences between signals in one LAAPD and in the reference paddle are constructed for each LAAPD individually. These spectra show a peak which is caused by the physical coincidences (see Fig. 5.8). The delay offsets of each LAAPD are adjusted such that all resulting time difference spectra show the peak at the same position. The width of these peaks is related to the time resolution of the two detectors, LAAPD and electron paddle. An average time resolution of ∼20 ns between LAAPDs and reference electron paddle is measured. The same procedure can be applied to align the other electron detectors relative to the reference paddle.

In this way the relative time calibration of LAAPDs and electron detectors is achieved. However for the laser experiment it is crucial to know also the relative timing between the LAAPDs signals and the laser pulse entering the multipass mirror cavity. Special runs have been dedicated to the calibration of this relative timing where visible light (in time coincidence with the 6 μm pulse) was sent into the laser cavity. The visible light is detectable by the LAAPDs but not the 6 μm light. When searching for the resonance no visible light must enter the target, but for the calibration runs a visible light pulse from the Ti:Sa laser was transmitted through the Raman cell and sent to the target bypassing the Ge plates. The visible light from the Ti:Sa laser and the infrared light from the Raman cell are in physical coincidence and are detected by the LAAPDs and by the infrared detectors (V_1, V_2) respectively. The light intensity was chosen such that the amplitudes of the LAAPDs signals correspond to 2 keV x rays.

The time differences $\Delta t_i^{\mathrm{cal}}$ between the signals recorded in the WFD and TDC fed from the LAAPDs and laser–light detectors ($i = V_1,\ V_2,\ D_2 \dots$) are recorded during these time calibration runs:

$$\Delta t_i^{\mathrm{cal}} = t_{\mathrm{LAAPD}}^{\mathrm{light}} - t_i^{\mathrm{light}} \ . \tag{5.1}$$

Since the excimer laser delay varies in function of time, the arrival time of the laser pulse in the cavity is shifted accordingly. However the difference $\Delta t_i^{\mathrm{cal}}$ does not depend on the excimer delay. Therefore during the search for the resonance the laser pulse enters the cavity at the LAAPD time given by

$$t_{(\mathrm{LAAPD})}^{\mathrm{laser}} = t_i^{\mathrm{light}} + \Delta t_i^{\mathrm{cal}} \tag{5.2}$$

where t_i^{light} is the time measured by the laser detectors on a pulse–to–pulse basis, whereas $\Delta t_i^{\mathrm{cal}}$ is fixed and was measured only during the time calibration runs. $\Delta t_i^{\mathrm{cal}}$ is known with an accuracy of about ∼15 ns.

As shown in Fig. 5.9 the total laser delay fluctuates up to 200 ns for different runs. This variation is caused by fluctuations of the internal delay of the excimer laser which pump the Ti:Sa oscillator. The large decrease of delay time visible in the central part of the figure is caused by a change of the thyratron.

In the time calibration runs, the resulting time difference between a muon stop (or, more precisely, the emission of a 2 keV x ray) and the arrival of the laser pulse in the cavity is typically 1.5 μs. This number agrees with the sum of the total laser delay of ∼1.6 μs and the time needed to generate the $S_1 \cdot S_2 \cdot \bar{D}_3$ laser trigger signal of ∼0.32 μs reduced by the average muon slowing–down and cascade time of ∼0.44 μs.

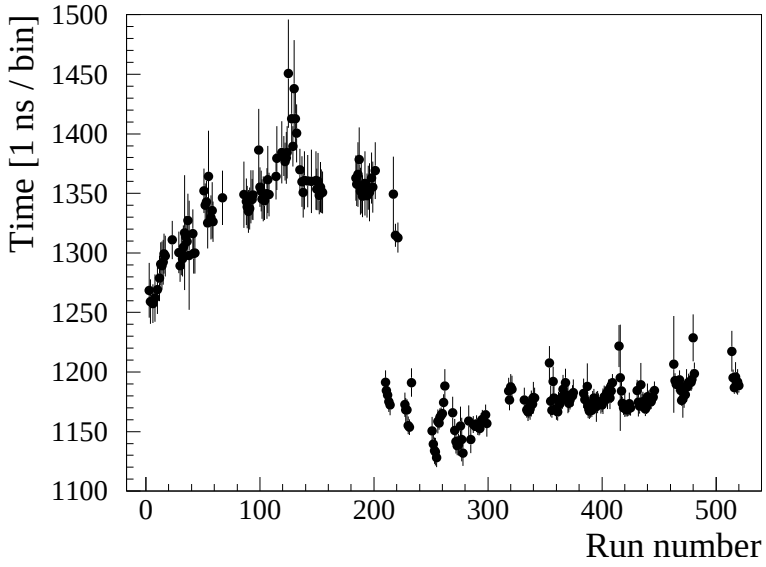

Figure 5.9: Timing of the V_2 signal as a function of run number. Each point represents a mean value for one run. In the middle of the data taking period the internal delay of the excimer laser was reduced by $\sim$ 200 ns. The error bars corresponds to the standard deviations measured on a pulse–to–pulse basis.

5.7 LAAPDs x-ray efficiency

The total detection efficiency of LAAPDs for x rays may be expressed as

$$\eta_x = \Omega\, \varepsilon_x \tag{5.3}$$

where Ω is the solid angle and ε_x the detector efficiency which is energy dependent. In the following it is described how to infer Ω, ε_x and η_x from measurements and Monte Carlo simulations.

5.7.1 Detector efficiency ε_x

The detector efficiency (including windows *etc.*) in function of the x-ray energy can be inferred by considering energy spectra of μp, μO and μN atoms [16]. Oxygen and nitrogen are contaminants of the hydrogen gas target on the few per mil level. The absolute x-ray light yields of the corresponding muonic cascades are known from measurements at low densities where no collisional interactions take place during the muonic cascade [57, 102].

We consider first the measured energy spectrum in the 2 keV region as shown in Fig. 5.4, composed mainly of μp(K_α), μp(K_β) and μp($K_{\rm rest}$) transitions. This spectrum is fit with three Gaussians and related tails as discussed in §5.3. The relevant free parameters are the three amplitudes A_i and the position of the K_α and $K_{\rm rest}$–lines, whereas the K_β–position was related to K_α according to the known energies (cf. Table 5.1). The fitted amplitudes A_i have to be proportional to the yields Y_i multiplied by the detector efficiency at the corresponding transition energy ε_i ($i = K_\alpha$, K_β and $K_{\rm rest}$):

$$A_i \sim Y_i\, \varepsilon_i\ . \tag{5.4}$$

The ratio of the amplitudes are

$$\frac{A_{K\alpha}}{A_{K\beta}} = \frac{Y_{K\alpha}}{Y_{K\beta}}\,\frac{\varepsilon_{K\alpha}}{\varepsilon_{K\beta}} \qquad \frac{A_{K\alpha}}{A_{K\rm rest}} = \frac{Y_{K\alpha}}{Y_{K\rm rest}}\,\frac{\varepsilon_{K\alpha}}{\varepsilon_{K\rm rest}} \qquad \frac{A_{K\beta}}{A_{K\rm rest}} = \frac{Y_{K\beta}}{Y_{K\rm rest}}\,\frac{\varepsilon_{K\beta}}{\varepsilon_{K\rm rest}}\ . \tag{5.5}$$

Therefore three detector efficiency ratios $\varepsilon_{K\alpha}/\varepsilon_{K\beta}$, $\varepsilon_{K\alpha}/\varepsilon_{K\mathrm{rest}}$ and $\varepsilon_{K\beta}/\varepsilon_{K\mathrm{rest}}$ are obtained.

To have additional efficiency values at different energies the circular transitions of μN and μO have been examined. The subsequent circular deexcitations $\mu\mathrm{N}_{6\to5}$, $\mu\mathrm{N}_{5\to4}$ and $\mu\mathrm{N}_{4\to3}$ at energies of 1.67, 3.08 and 6.65 keV, respectively, are emitted simultaneously, and pairs of two coincident transitions could be measured with sufficiently high statistics. This time coincidence is crucial in order to distinguish the low–intensity μN transitions from other processes of comparable intensity. For example consider the events with two x rays in time coincidence, where one energy is between 2.7 to 3.5 keV (corresponding to $\mu\mathrm{N}_{5\to4}$). The energy spectrum of the second x ray contains the peaks corresponding to the $\mu\mathrm{N}_{6\to5}$ and $\mu\mathrm{N}_{4\to3}$ transitions. The ratio of the $\mu\mathrm{N}_{6\to5}/\mu\mathrm{N}_{4\to3}$ amplitudes leads to the efficiency ratio $\varepsilon_{6.7\ \mathrm{keV}}/\varepsilon_{1.7\ \mathrm{keV}}$ in a much similar way as Eq. (5.5) for the μp atoms. Further pairs lead to additional efficiency ratios.

Only ratios of efficiencies are extracted from these measurements. To infer absolute values of the detector efficiency as function of energy three scaling factors have been introduced which define an absolute normalization for each of the three groups of measurements, μp, μN and μO. These factors have been adapted to a theoretical function describing the absorption probability of an x ray in the active zone of the LAAPDs and considering absorption losses in the various foils placed in front of the LAAPDs: polypropylene and Li foils as well as a Si layer (dead zone) of the LAAPD itself which is preceding the active zone of the LAAPD:

$$\varepsilon_x = \exp\left(-\frac{\bar{d}_{\mathrm{Li}}}{\lambda_{\mathrm{Li}}}\right)\ \exp\left(-\frac{\bar{d}_{\mathrm{CH_2}}}{\lambda_{\mathrm{CH_2}}}\right)\ \exp\left(-\frac{\bar{d}_{\mathrm{dead}}}{\lambda_{\mathrm{Si}}}\right)\ \left[1-\exp\left(-\frac{\bar{d}_{\mathrm{active}}}{\lambda_{\mathrm{Si}}}\right)\right] \tag{5.6}$$

where λ_{Li}, $\lambda_{\mathrm{CH_2}}$ λ_{Si} are the energy dependent attenuation length respectively in Li, polypropylene, Si [103], and the $\bar{d}$'s represent the average length of the x rays paths in the corresponding foils and detector layers. The last term accounts for the probability that the photon is absorbed in the active layer whereas the first three terms describe absorption losses. The average length $\bar{d}$ is related to the thickness of the corresponding layers as $\bar{d} = d/\cos\bar{\alpha}$, where $\bar{\alpha}$ is the average incident angle of x rays and d the layer thickness.

The average incident angle is computed with a Monte Carlo simulation for two physically possible angular distributions of the emitted x rays. The angular distribution for x ray which are not correlated with the laser light is isotropic, whereas laser induced x rays show a correlation with the direction of the laser polarization. For laser light polarized along the z-axis the angular distribution is [104]

$$D(\theta) = 1.175 - 0.525\ \cos^2\theta \tag{5.7}$$

where θ is the azimuthal angle relative to the laser polarization. The radiation is rotational symmetric around the z-axis. This angular distribution has a minimum in the direction of the laser polarization and a maximum at 90° relative to the polarization axis. Therefore we have chosen to enter the target with laser light polarized in the direction of the beam axis, to slightly enhance the probability to detected the laser–induced x ray. The effect of this angular correlation affects negligibly the number of x rays pointing on the LAAPDs and slightly the mean angle with which the x ray strikes the LAAPDs. It is found that the solid angle to detect an x ray in the LAAPDs originated in the μp formation volume is 31% for both isotropic and polarization–correlated distributions. However the mean incident angle on the detectors shows a small difference for the two distributions which corresponds to an

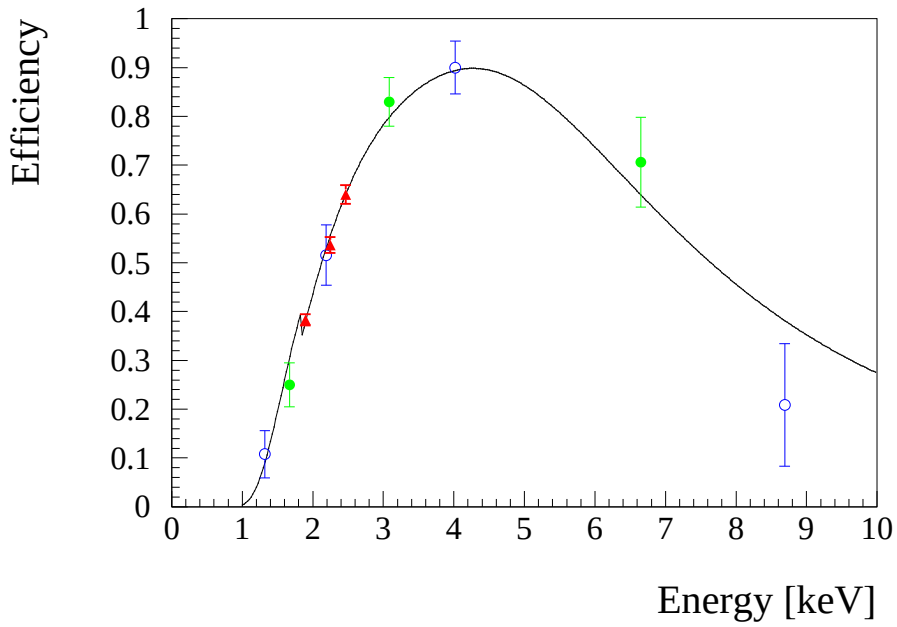

Figure 5.10: LAAPDs x-rays detection efficiency as a function of the x-ray energy. This efficiency accounts also for absorption losses in the foil preceding the LAAPDs. The measurements have been extracted from μp Lyman–series deexcitations (red bars), circular transitions in μN (green full circles), and circular transitions in μO (blue empty circles). The solid curve representing the "theoretical" expectation and the data points have been optimized to each other to have the best agreement.

average path length in the foils of $\bar{d} = 1.57\,d$ for the polarization–correlated distribution, and $\bar{d} = 1.68\,d$ for the isotropic distribution. Laser–induced x rays experience on average about $\sim 7\%$ less absorbing material than x rays from the "prompt" cascade.

An optimization procedure is performed in which the three scaling factors and the thickness of the various layers are optimized to have the best agreement between scaled measurements and the theoretical function of Eq. (5.6). The values of the various foil thicknesses have been allowed to slightly vary since they are not precisely known. The best agreement between data and scaled measurements is given in Fig. 5.10 which shows the LAAPD detection efficiency as a function of the x ray energy. The resulting thickness values are in agreement with the expectations [16].

The probability to detect a K_α x ray is $(38 \pm 4)\%$ whereas the probability to detect the 4.9 keV transition of carbon is $(88 \pm 5)\%$. The average detection efficiency for K_α, K_β and $K_{\rm rest}$ is $(42 \pm 4)\%$. Since high energy x rays mainly cross the active region without being absorbed, the efficiency at high energy decreases. The decrease at low energy, on the contrary, has to be attributed to absorption losses in the foils. The validity of these values for the detector efficiency is confirmed by the measurement of the total detection efficiency η_x which is presented in the next section.

5.7.2 Total efficiency η_x

The measurement of the total detector efficiency is inferred by the study of the following process. A μp atom is created and deexcites to the ground state emitting a 2 keV photon which may be detected. The μp_{1S} drift to the detector window foils, muon transfer to

carbon occurs which leads to the formation of μC atoms in excited state. $\mu C_{4\to 3}$ x rays of $\sim$ 5 keV energy may be emitted at delayed times corresponding to the time–of–flight needed for the μp atoms to drift to the target walls. Finally the muon decay electron may be detected.

We consider the following two event classes:

- delayed 5 keV followed by a muon decay electron (class: $5-e$) (no x ray preceding the 5 keV photon is detected)
- prompt 2 keV, followed by a delayed 5 keV and a muon decay electron (class: $2-5-e$)

Both event classes originate from the physical process described above, but for the first class the 2 keV photon is not detected. A comparison between the number of events in the 5 keV peak of these two event classes leads to a measurements of the total detection efficiency for 2 keV x rays. In order to reduce correlations between the detection of 2 keV and 5 keV photons which will distort the extraction of the 2 keV detection efficiency from these measurements, the time between 2 keV and 5 keV x ray was required to be larger than 800 ns. The total number of events in the 5 keV peak of the class $5-e$ (N_{5-e}) is proportional to $(1-\eta_x)$ whereas for the $2-5-e$ (N_{2-5-e}) event class is proportional to η_x (where $x = 2$ keV) and thus

$$\frac{N_{2-5-e}}{N_{5-e}} = \frac{\eta_x}{1-\eta_x} \,. \tag{5.8}$$

For this measurement the energy acceptance includes all μp(K_α), μp(K_β) and μp($K_{\rm rest}$) x rays, leading to an averaged efficiency at 2 keV. For 2 keV energy x rays the resulting measured efficiency is therefore

$$\eta_x^{\rm exp} = (11.0 \pm 1.0)\% \,. \tag{5.9}$$

For comparison, the solid angle $\Omega = (30.9 \pm 1.0)\%$ has been computed with a Monte Carlo simulation which accounts for the stop volume of the muons. Combined with the previously extracted "pure" detection efficiency $\varepsilon_{2-\rm keV} = (42 \pm 4)\%$ which is an average value for the K_α K_β and $K_{\rm rest}$ x rays it gives the total detector efficiency of

$$\eta_x^{\rm MC} = \Omega\, \varepsilon_{2-\rm keV} = (13.0 \pm 1.3)\% \tag{5.10}$$

which is in reasonable agreement with measurements.

Chapter 6

Search for the $2S - 2P$ resonance

This Chapter is devoted to the analysis of the data recorded during four weeks of beam time at PSI in November 2003 to search for the $2S - 2P$ resonance. Particular details of the analysis not presented in the previous Chapter are given here. No resonance line was found, and this is attributed to the lack of statistics, *i.e.,* to a too small laser–induced event rate, rather than a wrong frequency searching range. Some problems causing a lower signal rate than planned are presented in §6.4. An estimate of the laser–induced event rate and a measurement of the background rate are presented in §6.5.

6.1 "Laser ON" and "Laser OFF" data

A low–energy muon which fulfills the correct S_1–S_2–TOF condition and which stops in the hydrogen gas induces a trigger signal $S_1 \cdot S_2 \cdot \bar{D}_3$ under the condition that the data acquisition system is ready to accept such a muon event (MUON–STOP). This trigger signal opens a 12 μs long event gate (EVG) and triggers the laser system under the condition that the laser is ready. If within the EVG any signal above a set threshold is detected in the LAAPDs, the event is recorded, otherwise it is discarded. The trigger electronics is conceived in such a way that priority is given to events where the laser is fired, *i.e.,* the data acquisition system is always ready when the laser is ready to fire. The events are classified according to whether the laser system is fired ("Laser ON") or not ("Laser OFF"). Only "Laser ON" events were analyzed in the search of the resonance whereas "Laser OFF" events are used to study the background and to calibrate the detectors.

In order to consider an event to be a "Laser ON" event, it is important to ensure that the laser system not only fired but also that the 6 μm pulse had an acceptable energy. Therefore, for each "Laser ON" event it is checked that V_2 detects a reasonable signal. Since the laser system is triggered with the average rate of only 55 s^{-1} whereas the EVG could be opened with the average rate of 200 s^{-1}, additional "Laser OFF" events are recorded between two laser shots, *i.e.,* during the laser "dead time", in order to accumulate more statistics for the determination of the background. Additional "Laser OFF" data were taken during laser maintenance. The "Laser ON" events are further subdivided according to the laser frequency.

6.2 2 keV x-ray energy and time spectra

For the search of the resonance the event class xe composed of a μp K_α x ray (x) followed by an electron (e) is studied since the signature of a laser–induced event is the following:

– a muon (MUON–STOP) triggers the laser and data acquisition system.
– no signals are detected in any LAAPD or electron detector in the time interval preceding the arrival of the laser light in the cavity.
– in the laser time window (when the laser light is illuminating the μp atom) a x ray in the K_α energy cut is detected.
– a muon decay electron is detected in a delayed (relative to the x ray detection) time window.

The appropriate energy cuts for the K_α x rays were studied, and the values applied are shown in Fig. 6.1. The low–energy cut is in the interval from 1.3 to 1.6 keV, chosen for each LAAPD individually in order to accept as few low–energy background signals as possible, the level for which varied for each detector. The upper–energy cut is set for all LAAPDs to 2.6 keV which includes most of the 1.9 keV x-ray signals even for LAAPDs with poor energy resolution. The energy cut interval include more than 80% of the K_α transitions. The energy cuts are set asymmetric with respect to the 1.9 keV K_α line because the relevant background at delayed time increases toward lower energies (see Fig. 5.5). The x-ray energy spectrum of Fig. 6.1, which is summed up for all LAAPDs, can not be fit with a simple sum of three Gaussian distributions representing the K_α, K_β, and $K_{\rm rest}$ transitions since the various LAAPDs have different energy resolutions.

The background at delayed times is substantially reduced by requiring an electron from muon decay in the time interval between 0.1 to 7.1 μs relative to the x-ray time (see Fig. 5.8). The lower limit of this time window is given by the time resolutions of x-ray and electron detectors whereas its width is set rather large to maximize the electron

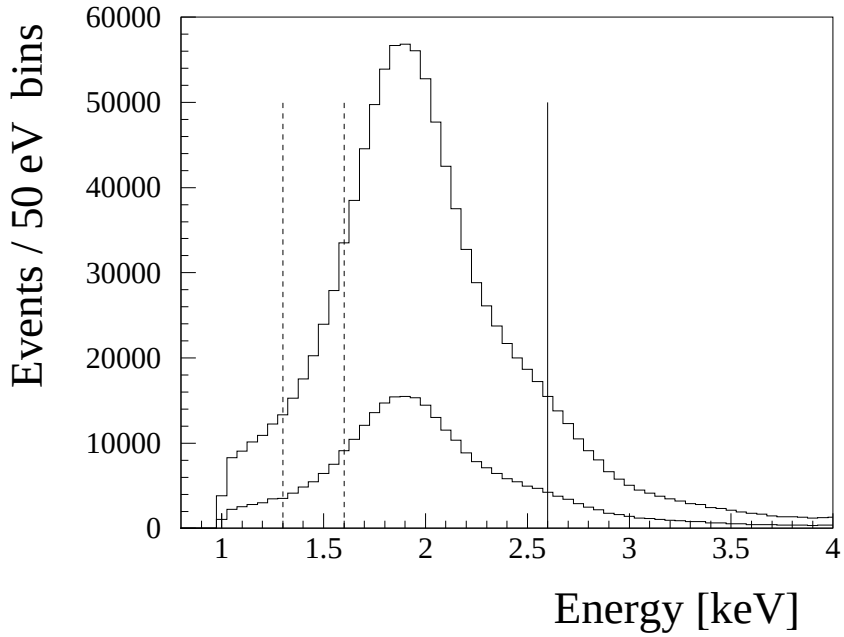

Figure 6.1: X-ray energy spectrum at 0.6 hPa hydrogen gas pressure from the xe event class. The higher statistics histogram (1.07×10^6 events) is the sum of "Laser OFF" and "Laser ON" events, whereas the lower statistics histogram shows only "Laser ON" data. The vertical lines indicate the energy cuts used in the search of the laser–induced μp K_α x rays. The two dashed lines represent the spread of the low–energy cut for different LAAPDs summed up for all 20 LAAPDs, while the solid line marks the high–energy cut common for all diodes.

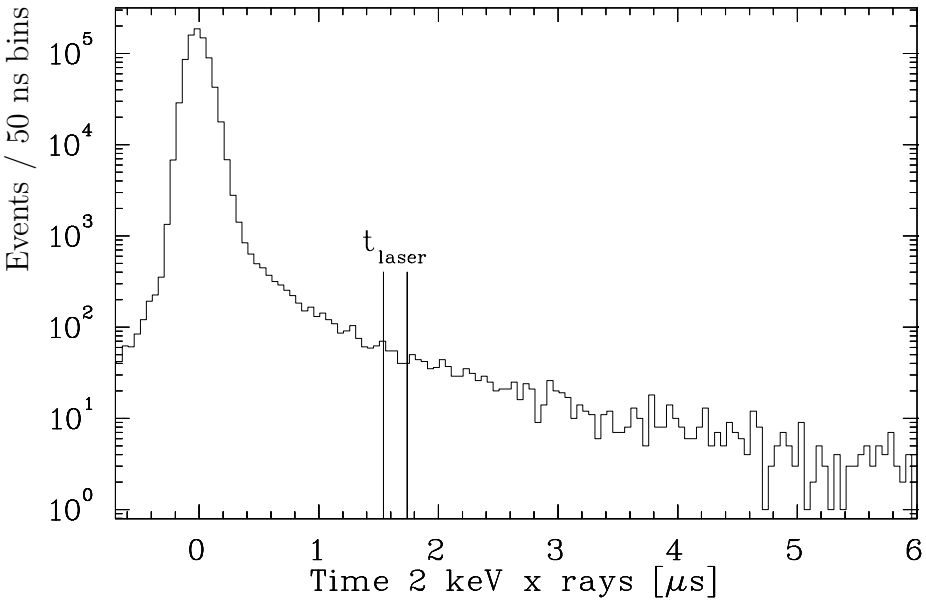

Figure 6.2: Time spectrum of 2 keV x rays (50 ns/bin). The "prompt" x rays appear around $t = 0$. The laser–induced events are expected in the time interval $1.52 - 1.72$ μs, indicated by vertical lines. No visible laser effect is expected for this spectrum where data taken at all laser wavelengths and without laser are summed up. The total number of "prompt" events is 7.8×10^5. The laser was fired for $\sim$30% of the events. The number of delayed events at laser time is 215, corresponding to a background ratio "delayed/prompt" of 2.8×10^{-4}. The gas pressure was 0.6 hPa.

detection probability. In order to accept as many LAAPD signals arising from muon–decay electrons as possible, the parameter $E_x^{\rm hi}$ defining the energy above which a certain LAAPD signal is identified as *electron*, is set as low as possible. The lower limit is given by the $\mu C_{4\to3}$ transition centered at 4.9 keV which represents the major background at delayed times. Signals up to 6.0 keV are therefore considered as *x rays*, and above this threshold as *electrons*. Further background suppression is realized by the *second muon* cut, *i.e.,* by suppressing events where a *second muon* is recorded in S_1 $350 - 850$ ns before a delayed x ray in the LAAPDs (cf. §5.4).

For the search of the $2S - 2P$ resonance, in addition to the *xe* event class which represents 92% of the total events used in the analysis, two other classes are considered: *xee* and *xx* which contribute respectively to 7% and 1%. The *xee* class is caused by a good events, *i.e.,* an event of the class *xe* followed by a second *electron* signal. The additional *electron* is not correlated with the *first muon* and is mainly due to electrons originating from a *second muon*. This *second muon* may form a μp atom where the K x ray is in most cases not detected (11% detection efficiency), but its decay–electron is detected (66% probability). If this happens after the detection of the μp x ray associated with the *first muon*, there is no reason to refuse such an event. The other relevant class *xx* corresponds to a K_α *x ray* followed by an electron which deposits less than 6 keV in the LAAPDs, and is therefore identified as a second *x ray* rather than an electron. The detailed analysis performed by L. Ludhova showed that these three event classes have a sufficiently low background level at delayed times to accept all of them for the search of our resonance.

Figure. 6.2 shows the K_α x-ray time distribution summed up for all LAAPDs and "Laser OFF" and "Laser ON" events, regardless of the laser frequency. The K_α *energy*, *second muon* and *delayed electron* cuts are applied. The peak is caused by the "prompt"

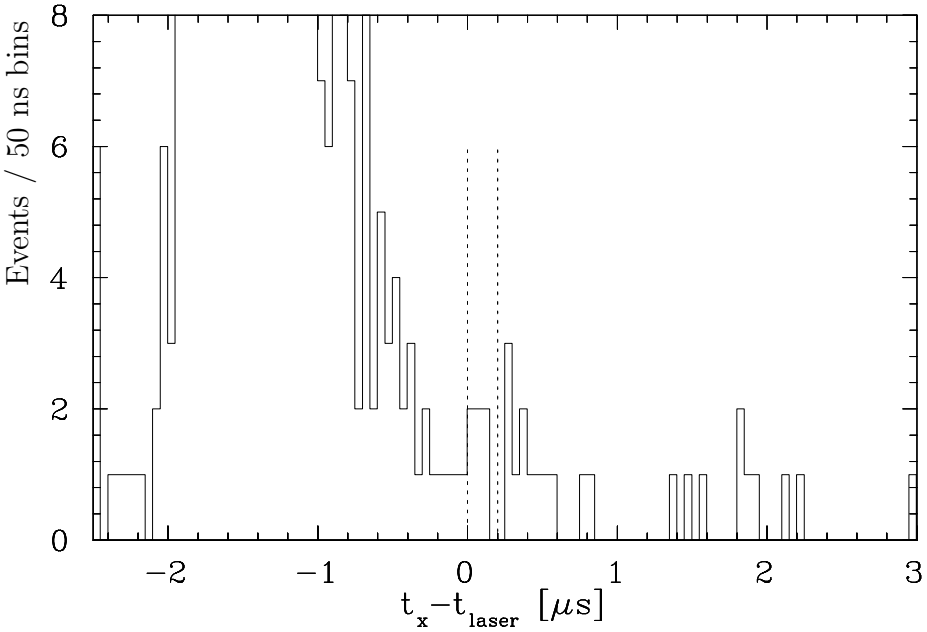

Figure 6.3: An example of a "shifted" time spectrum (50 ns/bin) of a the x rays with the μp K_α energy cut for all LAAPDs, measured for a particular laser frequency corresponding to the Fabry–Perot fringe number "282 843". Laser–induced events are expected in the time interval $[0-200$ ns$]$, indicated by the two dotted lines. The number of "prompt" events is 2.1×10^4.

μp K–transitions. A fraction $1 - \varepsilon_{2S} = 97.5\%$ of all formed μp atoms directly reach the ground state and about 1.5% of the atoms belong to the radiatively quenched $2S$ short–lived component with $\sim$ 150 ns decay time (see §G.3). The width of the peak of about 180 ns (FWHM) and its asymmetric shape are mainly given by the muon stop time distribution. The 2 keV events detected at times above 1 μs can not be explained by μp_{2S} radiative deexcitation (see Appendix H for its explanation). The slow μp_{2S} component ($\sim$ 1% population) decays radiationless to the ground–state — via formation of excited molecules with subsequent auto–dissociation — and does not contributes to the measured 2 keV time spectrum.

According to the time calibration between laser pulse and LAAPDs, the laser induced events are expected to be approximately in the time window between 1.5 to 1.7 μs shown in Fig. 6.2. It is approximate because the laser time varied up to 200 ns for different runs and has to be considered for each event individually. A width of 200 ns was chosen for this time window in accordance with the confinement time of the light inside the cavity ($\sim$ 140 ns) and the time resolutions ($\sim$ 35 ns FWHM for the LAAPDs) and small systematic uncertainties in the timing of the various detectors. One cannot expect to see an increase of the 2 keV x-ray signal in this spectrum since it contains "Laser OFF" and "Laser ON" events at all laser frequencies. However this figure is interesting because it shows the low background level: 215 background events in the laser time window between 1.52 to 1.72 μs for 7.8×10^5 prompt events corresponding to a "delayed/prompt" ratio of 2.8×10^{-4}. With currently $\sim$ 2000 "prompt" 2 keV events per hour with "Laser ON" condition, this corresponds to a rate of 0.5 background events per hour.

To search for the resonance, a set of 2 keV time spectra has to be generated at different laser frequencies, in order to observe the number of laser–induced 2 keV x rays in function of the laser frequency. For each of the 15 measured laser frequencies a spectrum of time

differences $t_x - t_{\text{laser}}$ between the 2 keV x-ray and the laser time was generated. Each event in these time spectra was corrected for the true arrival time of the laser pulse in the target cavity so that laser–induced events are expected in the laser time window between 0 and 200 ns. The start of the laser time window t_{laser} (in the LAAPD time reference system) corresponds to the time when the 6 μm pulse enters the mirror cavity (Eq. (5.2)).

An example of a $t_x - t_{\text{laser}}$ spectrum is shown in Fig. 6.3 for a laser frequency corresponding to the 282 843 transmission peak number of the FP cavity used for laser–stabilization. For this spectrum the *delayed electron*, the *second muon* and the μp K_α energy cuts are applied. The laser–induced K_α x rays are searched for in the laser time window between 0 and 200 ns. The "prompt" peak is positioned at around -1.5 μs. For a measuring time of 10.5 h, 2.1×10^4 events in the prompt peak and only 6 events in the laser time window have been measured. The "delayed/prompt" ratio is 2.9×10^{-4} which is compatible with the corresponding value extracted from the spectrum of Fig. 6.2, that is, this measurement is compatible with background.

6.3 Resonance line

Since the search for the resonance was performed for different laser frequencies at different conditions (measuring time, laser performance, muon beam rate) an appropriate normalization is required in order to compare the number of events measured in the laser time window for different frequencies. For each frequency the number of events measured in the laser time interval is divided by the number of "prompt" events, thereby normalizing to the true number of useful laser shoots at this frequency. Only events where the 6 μm pulse energy was above a threshold value are accepted in these spectra. Fig. 6.4 shows the normalized number of K_α x rays in the laser time window in function of the laser frequency which is expressed in terms of FP fringe numbers. The measured points cover a frequency interval of about 135 GHz around the frequency predicted using the rms proton radius value of the CODATA group [1]. The frequency of the most left point in Fig. 6.4 is 49.7409 THz, corresponding to a proton radius of 0.905 fm (cf. Eq. (2.18)), whereas the outermost point at the right side is at a frequency of 49.8754 THz, corresponding to 0.844 fm. Steps of 10.5 GHz (7 FP–numbers separated by 1.5 GHz each) were typically used for the frequency scan, to be compared with a linewidth of ~ 20 GHz (power broadening included). The expected number of the background level is given by the "Laser OFF" measurements and is shown as the "Avg. laser OFF" line. The lines "90% CL" and "99% CL" indicate the 90 and 99% confidence level for the hypothesis that the data contain only background. These CL are calculated using the measured averaged background level and the measurement time at each point to obtain the mean value of the corresponding Poisson distribution.

All data points are compatible with the average background level. No resonance line is seen in Fig. 6.4. Such a line is expected to have an amplitude of 2.5×10^{-4} (see §6.5) and a full–width at half–maximum of 14 in units of FP fringe numbers, *i.e.,* at least two data points should be higher than the average.

On the other hand, the statistics is too low to exclude the existence of a resonance effect in the frequency range of our measurements. This is illustrated in Fig. 6.5 which shows a Monte Carlo simulation of the search of the resonance line at our experimental conditions in 2003, *i.e.,* at a background rate of 0.5 events per hour (measured), at an estimated signal rate of 0.5 events/hour (cf. §6.5) for an average measuring time of 7 hours at each FP fringe (see Fig. 6.4 (Top)). The most favorable case is assumed where the centroid of

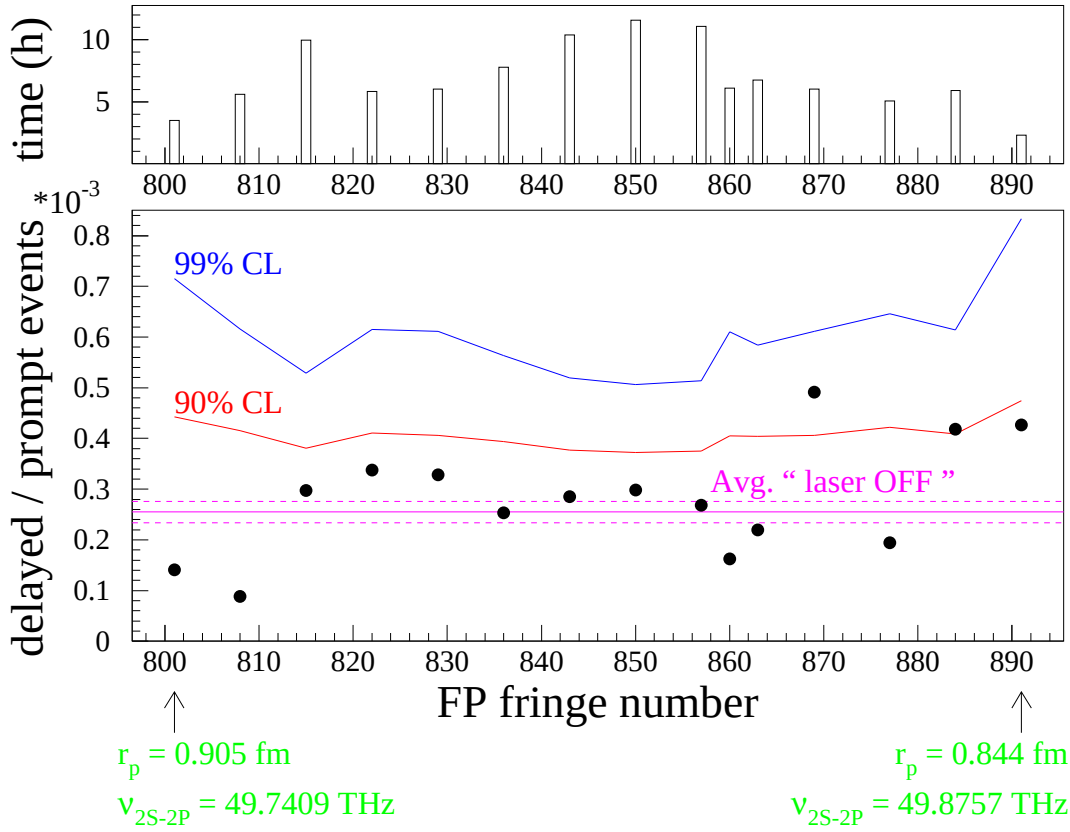

Figure 6.4: Result of the search for the $2S - 2P$ resonance line. Black dots are the number of measured events in the 200 ns wide laser time window normalized to the number of "prompt" events. The FP fringe number (with an offset of 282 000) is a measure of the laser frequency. The scanned region (49.7409 − 49.8757 THz) corresponds to rms proton charge radii in the interval from 0.844 to 0.905 fm. The confidence levels (CL) are calculated for the hypothesis that only background is present, with the Poisson distribution. The upper plot shows the approximate measuring time at each frequency.

the resonance line is on a measured FP peak. Only a quarter of the spectra shows a clear unique peak, whereas half of them have two or more candidates, and one quarter shows even no resonance, comparable to our data. We conclude that the statistics (number of events) collected in the measuring time 2003 was too low to make any positive or negative statement.

6.4 Problems during 2003–run

When the experiment was planned (1998) an event rate of about 5 events per hour was expected. As will be discussed in detail in the next section this rate dropped to 0.5 per hour at the condition of the 2003–run. This difference is attributed mainly to a too long laser delay (expected 700 ns, reached 1600 ns) and to the radioactive coating of the cavity mirrors.

Some of the LAAPDs were unexpectedly destroyed when irradiated by the few alpha particles per second emitted by the ThF_4 dielectric coating of the 6 μm cavity mirrors. Therefore we had to install a 175 μm thick lithium foil in front of the LAAPDs which

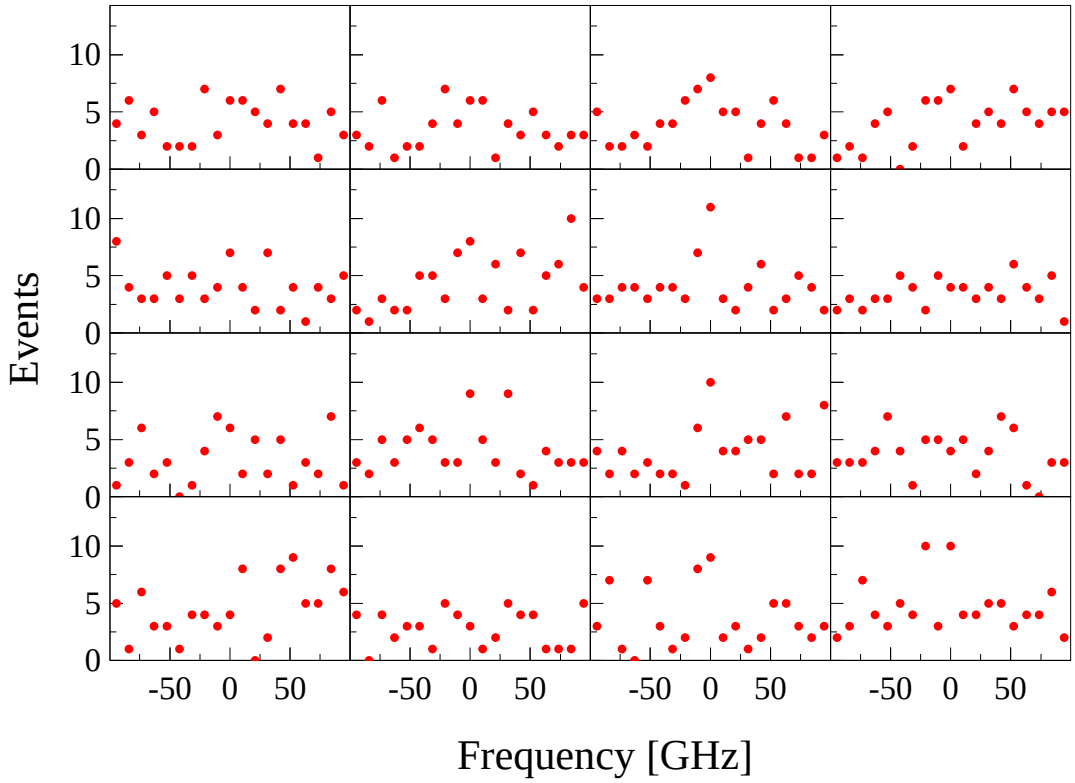

Figure 6.5: Sixteen simulated examples of the resonance search for a signal rate of 0.5 events per hour, a signal to background ratio of 1, and a measuring time of 7 hours at each point corresponding to the average value of the 2003 beam time. The resonance is assumed to be centered on the central FP. More than half of the spectra show no clear resonance effect.

absorbed the alpha particles, but also about 50% of the 1.9 keV x rays. This has lead to a reduction of the expected event rate by approximately a factor of 2.

To partially compensate for the long laser delay the target pressure was reduced in the 2003–run from the planned 1 hPa to 0.6 hPa. No problem with respect to the trigger quality and the number of stopped muons has been encountered because this pressure decrease was accompanied by the introduction of the anti–coincidence detector D_3 which enhances the trigger quality and the absolute number of muon stops (it reflects $\sim 70\%$ of the muons). However the fact that the μp atom may drift out of the laser–illuminated volume was underestimated.

Muonic hydrogen is formed in a volume of $5 \times 15 \times 194$ mm^3 corresponding to the muon stop volume. In the time between μp formation and the arrival of the laser pulse (which is of about 1.5 μs) the μp atom may leave the volume of $7 \times 25 \times 170$ mm^3 illuminated by the laser light. In addition both solid angle and transmission probability through the various foils in front of the LAAPDs for K_α x ray emitted by the μp_{2S} atom depend on the distance of the μp_{2S} atom from the target axis, which increases with time.

The total detection efficiency for K_α x rays in function of time is therefore computed with a Monte Carlo simulation which traces the diffusion of the μp_{2S} atoms in the hydrogen gas and the probability that laser–induced x rays reach the LAAPDs active region. Only μp_{2S} atoms which do not leave the laser illuminated volume contribute to this efficiency. The initial kinetic energy of the μp_{2S} atom is taken from measurements [10]. Both elastic and inelastic collision [13] with hydrogen molecule are taken into account to compute the

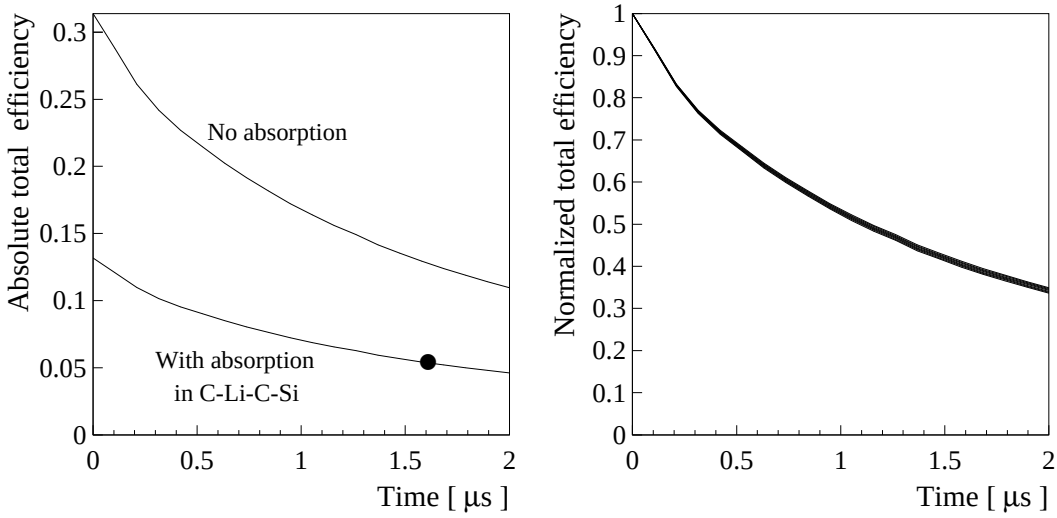

Figure 6.6: (Left): Simulated total detection efficiency as a function of time for laser–induced 2 keV x rays emitted isotropically by μp_{2S} atoms diffusing in hydrogen gas of 0.6 hPa pressure. The higher lying curve is computed assuming no absorption losses in the layers in front of the active region of the LAAPDs, whereas the lower lying curve accounts for absorption losses. The latter is normalized at time zero ("prompt" times) using the measured detection efficiency of 42% for 2 keV x rays (weighted average extracted from Fig. 5.10). The black circle represents the total efficiency at our conditions (laser delay and pressure) which is 5.2%. (Right): Total detection efficiencies for laser induced 2 keV x rays for various absorption losses normalized at time zero, i.e., when μp_{2S} atoms are formed. The relative decrease of detection efficiency caused by the drift is approximately independent on the absorption losses. At a delay of 1.6 μs corresponding to the mean time of the laser time window the drift process has reduced the detection efficiency of the laser–induced 2 keV x rays to 40% of the initial value.

drift of the μp_{2S} in hydrogen gas. The position where the x ray is emitted is given by the μp_{2S} atom position and the angle distribution is assumed to be isotropic (the small correction related to the polarization–dependent angular distribution is accounted by a separate factor).

The probability to detect K_α x rays emitted by μp_{2S} atoms which are in the laser illuminated volume ($7 \times 25 \times 170$ mm^3) as a function of time is shown in Fig. 6.6. The simulation predicts that for 0.6 hPa hydrogen pressure the total detection efficiency drops from 13.0% at the μp formation time to 5.2% at the mean average time the laser is confined in the cavity. The μp_{2S} lifetime and the laser–induced transition probability are not included in these values. A small enhancement of the detection probability from 5.2% to 5.6% is expected for laser–induced x rays due to laser polarization–dependent angle distribution. On the right graph of Fig. 6.6 the total detection efficiency is shown as a function of time normalized to the detection efficiency when μp atoms are formed. In the laser time window the detection efficiency has drop to about 40% of its initial value. This time behavior is found to be almost independent of the absorption losses.

6.5 Event and background rate in 2003 beam time

In the analysis of the data, the delayed laser–induced events are treated essentially as the "prompt" μp K-lines, *i.e.,* the same event classes with the same cuts are considered. Beam rate, detectors and cut–efficiencies are about the same. It is therefore possible to calculate the number of expected laser–induced events (on resonance) relative to the number of measured prompt K-lines transitions. The prompt 2 keV x ray are emitted at time $t_x \sim 0$ with a total yield $Y_{2\,\mathrm{keV}} \simeq 0.99$ that we approximate to 1. The expected rate for laser–induced events (on resonance), relative to the "prompt" ones, can be calculated as the product of the following numbers:

- *relative* $2S$ *state population* (0.011 ± 0.002):
  Only 1% of the total formed μp atoms reach the $2S$ long–lived state, whereas all the other contributes to the "prompt" deexcitation (cf. §G.4).

- *population of* $F = 1$ *hyperfine level* (0.65 ± 0.05):
  Assuming a statistical distribution of the initial $2S$ population, 3/4 of it is useful for the laser experiment since we excite only transition starting from the triplet state. However at thermal equilibrium the Boltzmann distribution predicts a triplet population ($P_{F=1}$) relative to the total population ($P_{\mathrm{tot}} = P_{F=1} + P_{F=0}$) in the $2S$ state of
  $$\frac{P_{F=1}}{P_{\mathrm{tot}}} = \frac{3e^{-\Delta E_{\mathrm{hfs}}/kT}}{1 + 3e^{-\Delta E_{\mathrm{hfs}}/kT}} \simeq 0.55 \tag{6.1}$$
  where $\Delta E_{\mathrm{hfs}} = 0.023$ eV is the $2S$ hyperfine splitting, and $kT = 0.026$ eV. When formed the $\mu\mathrm{p}_{2S}$ sublevels are statistically populated. No cascade process is known which may favor the population of the triplet or singlet state. Since no cross sections for the spin flip processes ($\mu\mathrm{p}_{2S}^{\mathrm{F=1}} + \mathrm{H}_2 \longleftrightarrow \mu\mathrm{p}_{2S}^{\mathrm{F=0}} + \mathrm{H}_2$) are available for the $2S$ state, is not possible to trace the time evolution of the population in the triplet–singlet system. We assume a triplet state population of 0.65 — between the statistical and thermal value — in the laser time. This is a conservative assumption because spin–flip processes requires "hard" collisions which have relatively small cross sections, resulting in small spin–flip rates at 0.6 hPa gas pressure.

- $2S$ *survival probability when laser pulse enters the cavity* (0.32 ± 0.06)*:*
  Using the measured collisional quenching rate of $\lambda^{2S}_{\mathrm{quench}} = 5.1^{+2.4}_{-2.1} \cdot 10^5\ \mathrm{s}^{-1} \times p\ [\mathrm{hPa}]$ [11] a $2S$ lifetime of $\tau^{\mathrm{long}}_{2S} = (1.32 \pm 0.24)\ \mu$s is expected at 0.6 hPa (cf. §G.4). It follows that the survival probability when the laser pulse enters the cavity ($t_{\mathrm{laser}} = 1.52\ \mu$s) is
  $$e^{-t_{\mathrm{laser}}/\tau^{\mathrm{long}}_{2S}} = e^{-1.52\,\mu\mathrm{s}/1.32\,\mu\mathrm{s}} = 0.32 \tag{6.2}$$

- $2S - 2P$ *transition probability in the mirror cavity* (0.30 ± 0.10)*:*
  The transition probability was numerically computed (see Fig. E.2) assuming a 0.2 mJ pulse at the exit of the Raman cell, a light intensity in the cavity with exponential decay constant of 140 ns, and for an observation time (laser the window) of 180 ns. Instead of the 200 ns laser time window used in the analysis a shorter time window is used which take into account the fact that the coupled light needs about 20 ns to fill homogeneously the volume. A transition probability of 0.5 results when the laser frequency is on resonance.

Additional losses due to lower pulse energies (energy fluctuations) and not optimally filling of the cavity volume (cavity injection misalignment) have been estimated to be of the order of 40%. The resulting transition probability is $0.5 \times (1 - 0.4) = 0.3$

– *Decrease of detected laser–induced x rays caused by the μp_{2S} drift* (0.40 ± 0.10)*:* This factor was computed using the cross sections of T. Jensen and the measured μp kinetic energy distribution shown in Fig. G.3. The initial stopping volume and the laser illuminated volume were assumed to be $5 \times 15 \times 194$ mm^3 and $7 \times 25 \times 170$ mm^3 respectively.

– *Decrease of laser–induced event rate (relative to "prompt" x rays) caused by the muons stop distribution* (0.9 ± 0.05)*:* It was measured that the muon stop distribution has its maximum close to the gold surface of the D_3 detector [16], *i.e.,* in a region which can not be illuminated by the laser light.

The resulting ratio for the number of expected laser–induced events (on resonance), relative to the number of prompt events, is therefore $0.011 \times 0.65 \times 0.32 \times 0.30 \times 0.4 \times 0.9 = (2.5 \pm 1.2) \times 10^{-4}$. As seen in Fig. 6.2, the measured number of background events in a 200 ns wide laser time interval, relative to the number of prompt events, is $215/(7.8 \times 10^5) = 2.8 \times 10^{-4}$. This ratio is 2.6×10^{-4} when the timing of each individual event is corrected.

Based on the estimated signal and the measured background rates a "signal/background" ratio of approximately one is expected in the laser time window. About 2000/h prompt 2 keV events (with the cut–conditions mentioned above) were measured. The rate expected for laser events "on resonance" is therefore $\sim 2000 \times (2.5 \times 10^{-4}) = (0.5 \pm 0.2)$/h which was not sufficient for the search of the resonance line (see Fig. 6.5).

Chapter 7

Future improvements of the apparatus

The experience from the 2003 measuring time is that the basic concepts of muon beam, detectors and laser system are sound and that the apparatus worked reliably. However, the event rate was too low. Future improvements will therefore concentrate on a substantial enhancement of this rate which will be achieved mainly by replacing the excimer–dye laser complex with cw–diode pumped Yb:YAG "thin–disk" laser which has a much higher repetition rate and smaller delay, and by removing the Li sheets in front of the LAAPDs. Section 7.1 presents the new technology of the thin–disk laser together with the first results achieved with a prototype adapted for our experimental conditions. In §7.2 the estimated improvement of event rate due to the apparative improvement is presented. Although the background level is already quite low, *i.e.,* 0.5 background events per hour, small apparative changes, based on the understanding of the various background components described in Appendix H, have been planned to strongly reduce the background level. This will be discussed in §7.4 and finally possible future extension of the experiment will be presented.

7.1 Thin–disk laser

The main improvement of the apparatus foreseen for a future beam period is to replace the two excimer and dye lasers by a laser with a shorter internal delay time and higher repetition rate. The new laser is based on the technology of so called "thin–disk" solid state lasers [105–109]. Thin–disk lasers have recently been incorporated into industrial welding and cutting equipment, demonstrating the efficiency and robustness of this technology [110]. Besides the outstanding properties of the thin–disk laser for cw–operation it is also well suited for pulsed laser systems with acousto–optical switching.

The thin–disk laser is a special kind of diode–pumped high–power laser. The difference to conventional rod lasers is the geometry of the gain medium: it is a thin disk, where the thickness in beam direction is considerably smaller than the laser beam diameter, and the generated heat is carried off dominantly through one end face, rather than in the transverse direction. The cooled end–face has a dielectric coating reflecting both the laser and the pump radiation which leads to a cavity scheme as shown in Fig. 7.1. Due to the small thickness of the disk (*e.g.,* $100 - 200$ μm for Yb:YAG), the temperature rise during laser action is small. In addition, the temperature gradients are dominantly in the direction perpendicular to the disk surface, because the disk is cooled and also

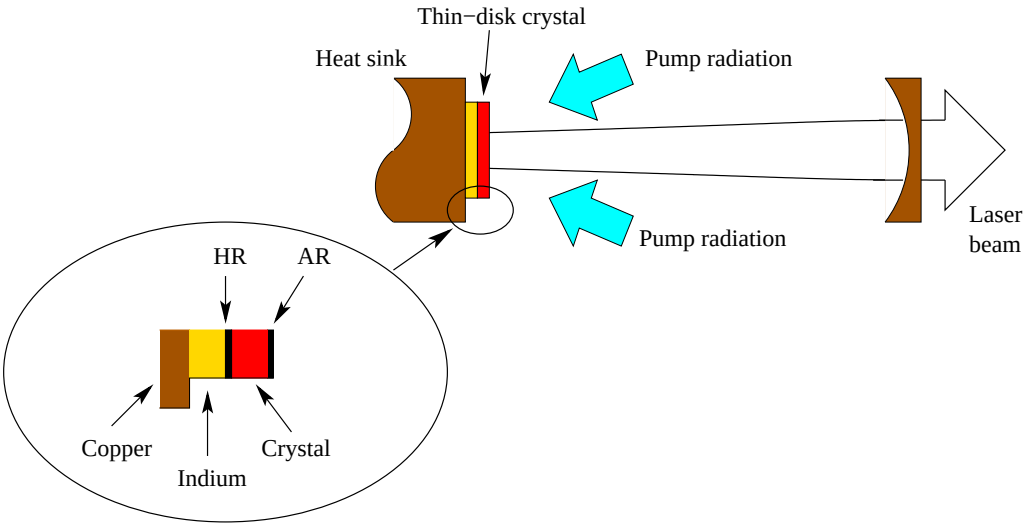

Figure 7.1: Principle of the thin–disk laser. The active laser medium (e.g.,Yb:YAG) is a disk with typically less than 200 μm thickness and a diameter of several mm (depending on the output power). The crystal is optically pumped from the front side of the disk by cw–laser diodes laser in a quasi–end–pumped design. An indium layer on the back plane of the crystal thermally connects the disk with a water–cooled heat sink.

optically pumped (quasi–end–pumped configuration) in axial direction. This results in a very good beam quality due to the weak thermal beam distortions (thermal lensing effect) and high efficiency since the temperature rise remains small (Yb:YAG has a quasi–three–level–scheme; pump absorption decreases with increasing temperature).

The small thickness of the disk leads to inefficient pump absorption in a single or double pass even for highly doped (typically 8% for Yb:YAG) crystals. Depending on the thickness and the doping level of the crystal, only a small fraction of the pump radiation is absorbed in the laser disk. Most of the incident pump power leaves the crystal after being reflected at the back side. The absorption is increased by successive redirecting and imaging of the pump beam on the crystal by a multipass arrangement composed of a parabolic mirror and a retro–reflector as shown in Fig. 7.2.

The good cooling capability of the thin–disk laser makes it possible to have a quasi–three–level–system as active material. Three–level–systems are highly efficient but require high pump power densities to reach the threshold. Yb:YAG is particularly suited for high power lasers since it is a quasi–three–level–system, which can be pumped with commercially available InGaAs–diode lasers at 940 or 970 nm and is lasing at 1030 nm. Its Stokes efficiency — defined as $\epsilon = \lambda_{\text{pump}}/\lambda_{\text{emitted}}$ — is therefore very high which implies a small heat deposition in the crystal. Moreover the long lifetime of its upper state ($\sim$ 1 ms) and the small emission cross–section (2×10^{-20} cm^2) offers the possibility to store a large amount of energy.

Pulsed Q-switched thin–disk lasers are developed since few years. Presently there are tests with a prototype version of a pulse laser which is adapted to our experimental requirements: a delay time from trigger to output pulse shorter than 1 μs, and an energy per pulse of about 50 mJ at 515 nm (after frequency doubling) for a repetition rate larger than 200 Hz. Figure 7.3 illustrates the schematic arrangement of the prototype Q-switched thin–disk laser. Besides the thin disk the cavity contains a thin–film polarizer (TFP) used as a polarization dependent outcoupler and a Pockels cell (PC) for Q-switch operation

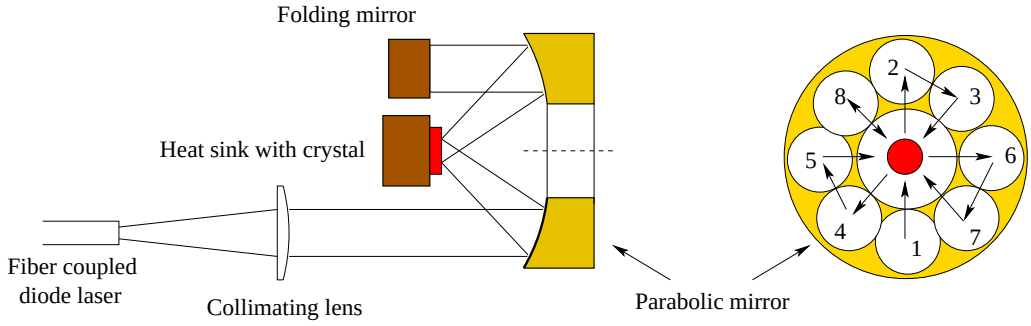

Figure 7.2: Optical pump design for the thin–disk laser with 16 pump beam passes. The radiation of the laser diodes is first homogenized and then focused by the parabolic mirror onto the disk. The power that is not absorbed is re–imaged several times on the crystal to optimize the pump efficiency. The light exiting the diode stack impinges on the parabolic mirror at position (1). After reflection on the disk (red circle) it reaches position (2). The folding mirror's system causes a rotation of the light on the parabolic mirror. When back reflected on the parabolic mirror (3) the pump light is again focused on the disk and reflected at position (4). When position (8) is reached a simple mirror reflects the light which then follows the same path backwards.

which induces polarization changes of the light circulating in the cavity. The thin–disk concept leads to a quite compact cavity design which is necessary to have a short laser delay.

The fundamental dynamics of the pulse formation in this Q-switched laser cavity is the following. The thin–disk is continuously pumped by the laser diodes. At times preceding the trigger pulse the laser is operating on a pre–lasing mode, *i.e.,* the Pockels–cell and $\lambda/4$–plate are adjusted such that the laser operates (in cw mode) close to the threshold. This is a kind of self–injection–seeding process. The pre–lasing ensures that a large number of photons is always circulating in the cavity resulting in a shorter pulse buildup time. When triggered, the PC first induces a rotation of the polarization in such a way that no light is transmitted through the thin film polarizer. The cavity is closed and thus the photons confined inside the cavity undergo an amplification process at low losses. When the population inversion has been removed by the circulating photons, the voltage on the PC is changed in such a way that the cavity is opened and the circulating power is extracted.

In first tests, the prototype laser has demonstrated to deliver 20 mJ at 1030 nm up to

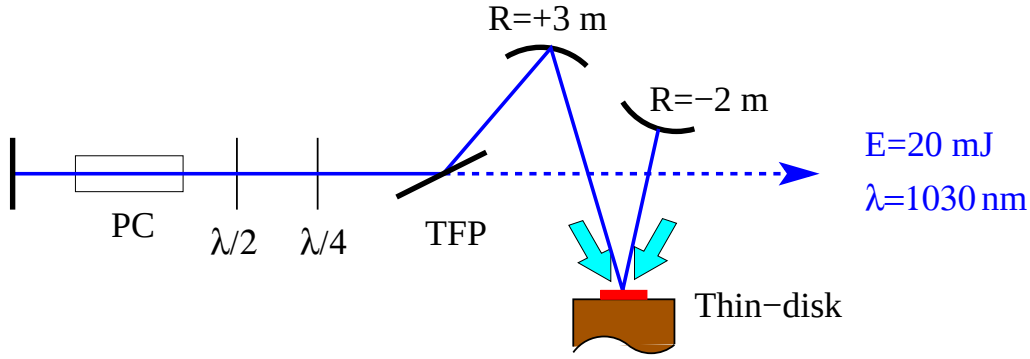

Figure 7.3: Schematic representation of the Q-switched laser resonator. TFP: thin–film–polarizer, PC: Pockels–cell. The beam size on the crystal is ∼4 mm in diameter and the cavity 68 cm long.

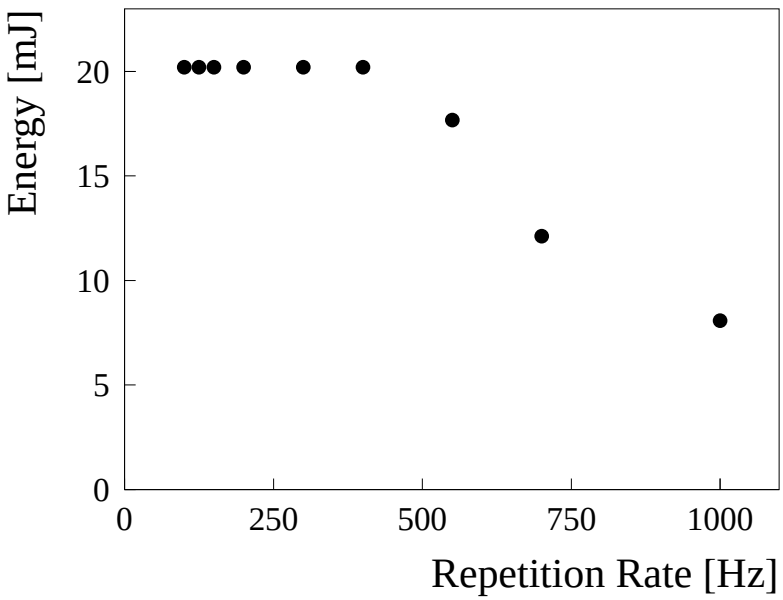

Figure 7.4: Measured output energy at 1030 nm of the thin–disk Q-switched Yb:YAG laser as a function of the laser repetition rate for 260 W of pump power.

400 Hz repetition rate with a pulse length of 25 ns (FWHM) and a total delay of 650 ns when pumped by 260 W. The measured output energy as function of the repetition rate is shown in Fig. 7.4. The decrease of the output energy starts at repetition rates above 400 Hz, *i.e.,* at a pulse–to–pulse time difference below 2.5 ms which is 2.5 times larger than the upper level lifetime.

The measured delay may be further reduced by optimizing the trigger electronics of the PC, and by shortening the optical pulse build–up reducing the cavity length. In addition the configuration of the cavity may be rearranged such that per round trip the crystal is crossed several times rather than once as in the present configuration. A crude estimate predicts that the pulse build–up time may be reduced to 550 ns.

In the first test mentioned above it was found that proper operation of the laser critically depends on the quality of the thin disk. A small impurity or crystal defect leads immediately to a damage of the crystal when operated in pulsed regime. For this reason the laser is assembled and operated in a clean room environment. For pulsed operation, a special effort has to be made to increase the optical damage threshold by increasing the quality of the beam circulating in the cavity (no hot spots) and by carefully studying the Q-switching dynamics to optimally extract the energy without damaging the crystal.

High laser output power can be achieved from one single disk by increasing the pump spot diameter while keeping the pump power density constant [107]. In the cw–regime the slope efficiency and the optical efficiency have been shown to be nearly independent of the pump spot diameter. The thin–disk laser presently in construction will be pumped with diodes delivering 800 W at 970 nm. With such a pump power and some improvements of the laser efficiency the aimed 90 mJ energy per pulse at 1030 nm should be reached. After external frequency doubling in a LBO crystal, 50 mJ at 515 nm can be expected (the measured spectral width of the pulse is 0.8 nm at FWHM).

The 50 mJ pulse energy at 515 nm are sufficient to pump the Ti:Sa laser. This pump energy has not to be as high as for the excimer–dye laser (90 mJ) due to the stability of

the disk–laser. A higher Ti:Sa pump efficiency can thus be realized. Very recently the Ti:Sa laser shown in Fig. 4.1, but pumped with a frequency–doubled Nd:YAG laser, has demonstrated to deliver 13 mJ energy when pumped with 50 mJ of green light. This was converted in the Raman cell to about 0.25 mJ energy at 6 μm. The Ti:Sa oscillator was pumped with a stable pulse of 12 mJ and delivered 2 mJ at 708 nm (with a pulse length of 6 ns) corresponding to an efficiency of 15%. The Ti:Sa amplifier was pumped with 38 mJ and delivered 13 mJ at 708 nm which corresponds to an efficiency of 29%.

7.2 Future event rate

Replacing the excimer–dye laser stage with the proposed thin–disk laser will result in a much higher laser repetition rate (triggered by muons) and a shorter laser delay time. The shortening of the delay time makes it possible to raise the hydrogen gas pressure. An estimate of the future event rate is given in the following which takes into account the new laser features, the higher gas pressure, the removal of the Li protective sheets in front of the LAAPDs, and the increase of the LAAPDs active area. The expected future rate is calculated relative to the event rate in the 2003–run.

- *The $2S$–survival probability at laser times will increase by a factor of (1.2 ± 0.1):* Replacing the excimer laser (1200 ns internal delay) by the disk laser ((550 ± 100) ns delay) will shorten the total delay time from muon stop to laser light by 650 ns, *i.e.,* from the present value of $\sim$1.5 μs to (0.85 ± 0.10) μs. The shorter laser delay makes it possible to raise the hydrogen gas pressure from 0.6 to, *e.g.,* 1.4 hPa. The $2S$ lifetime is therefore shortened from $\tau_{2S}^{\rm long} = 1.32$ μs to 0.86 μs. Note that the muon slowing–down time will be also shortened from about 500 to 300 ns at the higher pressure, but this is compensated by a reduction of the time needed to produce the laser trigger from 400 to 200 ns. As a matter of fact, at pressure above 1 hPa there is no need to wait for a D_3 signal since only few muons are not stopped before reaching the end of the target. Therefore the D_3 detector will be excluded from the muon trigger. The factor $\exp(-t_{\rm laser}/\tau_{2S}^{\rm long})$, which is relevant for the event rate, improves by a factor 1.2.

- *The average laser repetition rate will increase by a factor (3.0 ± 0.4):* The average laser repetition rate when the laser is triggered by muons entering the apparatus at random times is given by

$$n_{\rm laser} = \left(t_{\rm dead} + \frac{1}{n_{\rm muon}} \right)^{-1} \tag{7.1}$$

  where $n_{\rm muon}$ is the rate of muons trigger ($S_1 \cdot S_2 \cdot \bar{D}_3$) and $t_{\rm dead}$ the laser dead time. This muon rate will increase from the measured value $n_{\rm muon} = 240$ s^{-1} ($S_1 \cdot S_2 \cdot \bar{D}_3$) at 0.6 hPa to the measured value $n_{\rm muon} = 320$ s^{-1} ($S_1 \cdot S_2$) at the higher pressure. The laser dead time for optimum operation of the excimer–dye laser in the 2003–run was $t_{\rm dead} = 14$ ms, whereas for the thin–disk laser, it will be 2.85 ms (corresponding to 350 Hz repetition rate). The average repetition rate will thus increases from 55 s^{-1} to 167 s^{-1}.

- *The excitation and detection of laser–induced x rays will increase by a factor (3.4 ± 0.5):* The calculated loss of event rate connected with the drift of the μp_{2S} atoms takes into account both the fact that the μp_{2S} atoms leave the laser–illuminated

volume and the loss of detection probability when the μp atoms move away from the target axis. The drift of the μp_{2S} atoms will be reduced by the higher pressure and shorter laser delay. The detection efficiency of laser–induced x rays is reduced to 67% of the value if μp atoms would not drift. In run 2003 this reduction of detection efficiency was 40% at 1.6 μs laser average delay time and 0.6 hPa gas pressure (cf. Fig. 6.6).

Additionally a removal of the Li protective layer is planned since the radioactive coating of the cavity mirrors is foreseen to be replaced. The detection efficiency will be enhanced by a factor 1.9.

– *Optimization of muon stop volume (*1.2 ± 0.1*):* At 0.6 hPa hydrogen pressure the maximum of the muon stop distribution was near the gold surface of the D_3 detector where no LAAPD detectors are placed. At 1.4 hPa this distribution will be centered near the middle of the target where the x ray detection efficiency is larger. An increase of the x ray detection efficiency of about 20% is expected.

– *Shortening of slowing down time (*1.1*):* The increase of pressure reduces the time required for the muons to slow down by about 200 ns. The possible muon decay before μp formation is reduced by about 10% at 1.4 hPa relative to 0.6 hPa pressure.

– *Optimization of the light distribution inside the 6 μm cavity (*1.2 ± 0.1*):* A proper on–line monitoring system of the cavity alignment will be developed in order to ensure that the laser illuminates optimally the muon stop volume.

– *Optimization of laser stability (*1.1 ± 0.1*):* Due to the absence of dye and excimer gas degradation and pulse–to–pulse fluctuations related with these lasers, the stability of the disk–laser guarantees a higher percentage of laser shots with a reasonable laser pulse energy. A 20% increase of "useful" laser shots is assumed.

– *Increase of LAAPD active surface (*1.35 ± 0.1*):* New LAAPDs with larger active surface will increase the 2 keV detection solid angle, and will slightly reduce the losses related to the μp_{2S} drift.

The average event rate expected in the measuring time planned in 2006 will therefore be improved by a factor (29 ± 7) compared with the event rate in 2003. The expected event rate is thus (15 ± 6) per hour. Additionally the excimer–dye system required many hours of maintenance per day during which laser operation was not possible. The up–time of the laser system will therefore increase from 40% to approx. 80%.

7.3 Background rate

Table 7.1 summarizes the estimated background which can be extrapolated from Fig. H.5 since the relevant background processes are essentially pressure independent. Only the background related to the radiative deexcitation of the short–lived $2S$ state has to be corrected to account for its pressure dependence. The number of background events (pro formed atom) at 1.4 hPa in a time window $t \in [0.85 - 1.05\ \mu s]$ is estimated to be 5.2×10^{-5} events per formed μp atoms. It is important to notice that the background does not depend on the Li sheets, since it is caused by high energy x rays and electrons. Therefore the removal of the Li sheets is essential in order to increase the signal rate without increasing simultaneously the background rate. Since the background rate scales linearly with the

Table 7.1: Summary of the various background contributions (cf. Appendix H) expected in the laser time window, i.e., at time $t \in [0.85 - 1.05\ \mu s]$, for a pressure of 1.4 hPa, extracted from the time dependence shown in Fig. H.5.

Contribution	$B(t \in \Delta t_{\rm laser})$ [events/μp atoms]	Solution to reduce the background
transfer to LAAPDs window	41×10^{-6}	gold layer on foils
electron correlated		
2 keV correlated to muon decay	10×10^{-6}	increase threshold in paddles,
electron from paddle noise		additional scintillator
2 keV from *second muon*	1×10^{-7}	use also S_2 as
electron from *second muon*		*second muon* detector
2 keV from *neutron*	3×10^{-7}	—
electron correlated		—
short–lived $2S$ tail	1×10^{-7}	decreases with increasing pressure
sum	5.2×10^{-5}	

number of "Laser ON" events, to deduce the background rate at the planned experimental conditions the increase in number of "Laser ON" events has to be considered. It follow that at the future conditions the background rate is given by the measured background rate in 2003 run (0.5 bg events/h) properly scaled:

$$\begin{aligned} B_{\rm tot}(t \in [0.85 - 1.05\mu s]) \simeq & \frac{(5.2 \times 10^{-5})}{(1.9 \times 10^{-5})} \times 3.0 \times 1.2 \times 1.1 \times 1.1 \times 1.35 \times 0.5 \text{ [bg events/h]} \\ \simeq & (8.0 \pm 2.0) \text{ [bg events/h]} . \end{aligned} \tag{7.2}$$

The first term is the ratio of the total background given in Table 7.1 and Table H.2, and the last term is the background rate measured in 2003. The other terms takes into account the increase of laser triggers ($\times$3.0), the optimization of stopping volume ($\times$1.2), the increase of "good" laser shots which increase the number of events classified as "Laser ON" events ($\times$1.1), the shortening of the muon slowing down ($\times$1.1), and the increase of LAAPDs active area ($\times$1.35).

7.4 Possible background reduction

The signal rate expected for the future experiment will increase by a factor of 29 and the ratio "signal/background" by a factor of 29/16=1.8. Nevertheless some relatively small apparative changes have been planned which should substantially reduce the background.

– The energy threshold for the the *electrons* detected in the paddles was set in the 2003–run to a very low value in order to be able to detect also the Čerenkov light originated in the Lucite light–guides. This led to an increase of *electron* detection

in the paddles of 35%. However the background was also increased by a factor of 1.6. It is planned to cover the light–guides by plastic scintillators to obtain a better detection of those electrons which in 2003–run were producing Čerenkov light. All *electron* signals are then expected to have amplitudes above the threshold line plotted in Fig. 5.6. The discriminator threshold can thus be set above the one photo–electron peak, and the background will be reduced without loosing signal rate.

– By evaporating a thin layer of gold on the polypropylene foils the transfer–induced background may be strongly reduced. $(\mu\mathrm{Au})^*$ will be formed instead of $(\mu\mathrm{C})^*$ atoms. Several x rays and Auger electrons may be emitted during the μAu cascade. Since the muon lifetime in gold is strongly reduced by nuclear capture ($\tau_\mu^{\mathrm{Au}} = 73$ ns [101]), the DELE time window can be chosen in such a way that the electrons from muon decay in gold are not detected while reducing the detection efficiency for delayed electrons from μp by only $5-10\%$. Therefore the background connected with the transfer to carbon can be eliminated. However it has to be noted that the deexcitation in gold will probably induce signals in the LAAPDs which sometimes may be identified as 2 keV *x rays*. It is therefore important that the accidental rate in the paddles is lowered (as discussed above) to avoid fake *electron* signals.

  The thickness of the gold layer required to absorb $\mu\mathrm{p}_{1S}$ atoms preventing them to reach the polypropylene foils depends on μp kinetic energy. Monte Carlo simulations show that in the laser time window from 850 to 1050 ns most of the $\mu\mathrm{p}_{1S}$ atoms reaching the wall have kinetic energies below 5 eV. The cross section for muon transfer to gold ($\mu\mathrm{p} + \mathrm{Au} \rightarrow \mathrm{p} + \mu\mathrm{Au}$) calculated by Bracci and Fiorentini is [111]

$$\sigma_{\mu\mathrm{p}\rightarrow\mu\mathrm{Au}} \simeq \frac{0.42 \times 10^{-16}}{\sqrt{E_{\mathrm{kin}}}}\ [\mathrm{cm}^2] \tag{7.3}$$

  where E_{kin} is the kinetic energy expressed in eV. The absorption length of $\mu\mathrm{p}_{1S}$ atoms is defined as $l = 1/n\sigma_{\mu\mathrm{p}\rightarrow\mu\mathrm{Au}}$ where $n = 6 \times 10^{22}$ cm^{-3} is the density of gold atoms. Its value is hence

$$l \simeq 4\sqrt{E_{\mathrm{kin}}(\mathrm{eV})}\ [\mathrm{nm}]\ . \tag{7.4}$$

  A layer of about 25 nm turns out to be sufficient to stop most of the impinging μp atoms (the effective average thickness seen by μp atoms is about $1.6\, d_{\mathrm{Au}}$ which is further increased by scattering in Au). Compare this value with the range of a 1.9 keV x ray in gold of about 400 nm. Only 10% of the 2 keV x ray are absorbed by the 25 nm gold layer.

With these small apparative changes we hope to reduce the background rate by an order of magnitude whereas the signal rate will be reduced by only 20%.

7.5 Measuring time and search of the resonance

As previously mentioned the signal rate (S_{tot}) is expected to increase by a factor of (29 ± 7) and the background rate (B_{tot}) by a factor of (16 ± 4):

$$\begin{aligned} S_{\mathrm{tot}}(t \in [0.85 - 1.05\ \mu\mathrm{s}]) &\simeq 0.5\ [\mathrm{events/h}] \times 29 \quad = (15 \pm 6) \quad [\mathrm{events/h}] \\ B_{\mathrm{tot}}(t \in [0.85 - 1.05\ \mu\mathrm{s}]) &\simeq 0.5\ [\mathrm{events/h}] \times 16 \quad = (8 \pm 2) \quad [\mathrm{events/h}] \end{aligned} \tag{7.5}$$

The background rate given here does not take into account the above described possible background reduction. Note also that the background and signal rates are very often

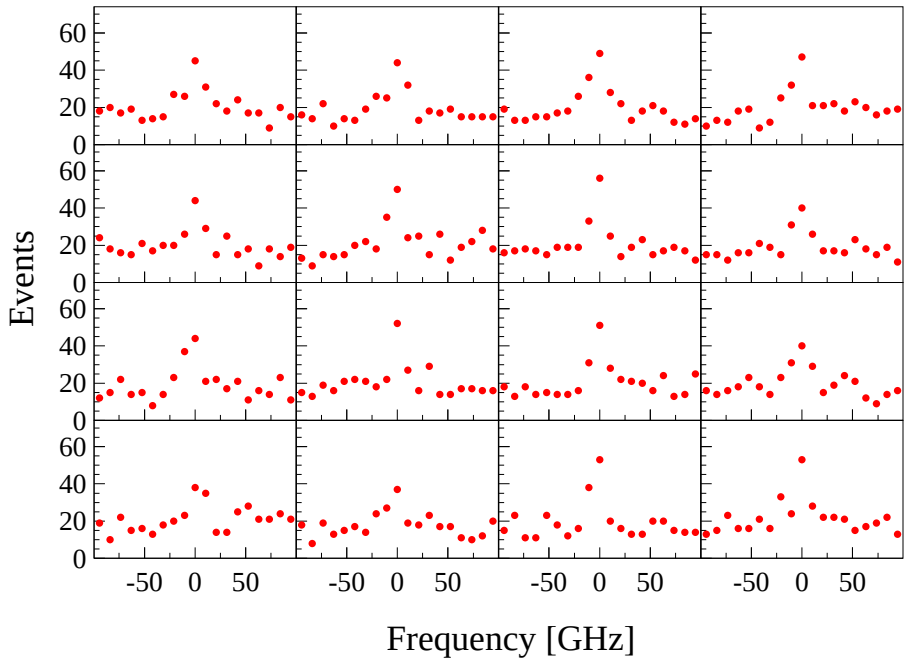

Figure 7.5: Simulated examples of the $2S - 2P$ resonance search for a signal rate of 15 events per hour, a background rate of 8 events per hour and for a measuring time per point of 2 hours corresponding to approximately 3 days of beam time. The number of events is plotted as a function of the detuning relative to the line centroid position. This simulation was performed assuming the resonance to be centered on the central Fabry–Perot fringe. Comparable statistical power results if the resonance if placed in between two measurement points.

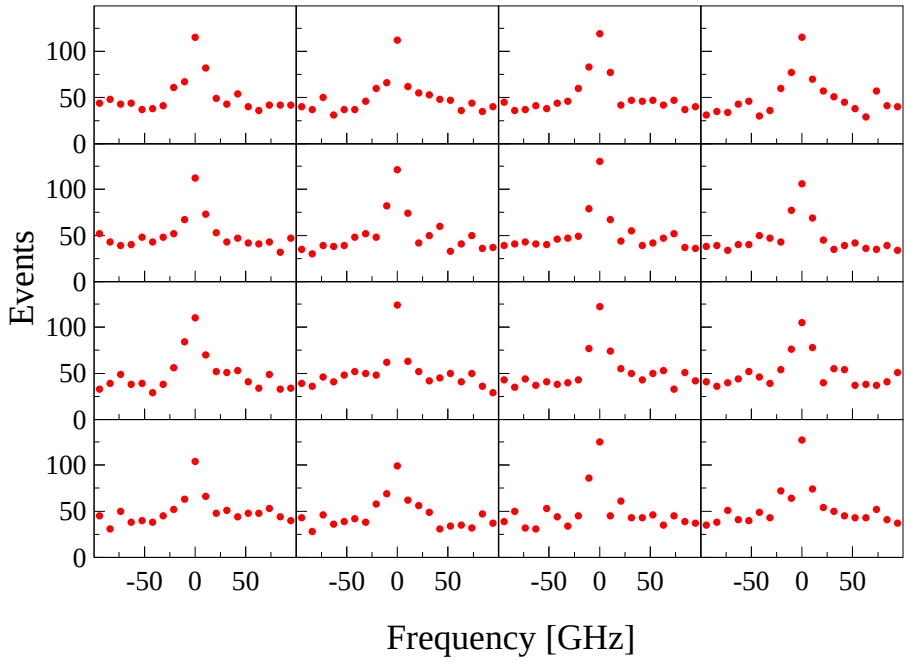

Figure 7.6: Simulated examples of the $2S - 2P$ resonance search. Same conditions as for Fig. 7.5, but for a measuring time at each point of 5 hours corresponding to one week of measuring time.

correlated, *i.e.,* an increase (decrease) of the signal rate often corresponds to an increase (decrease) by the same amount of the background rate.

With these expected signal and background rates the search for the resonance will take approximately 3 days since about 20 different wavelengths (corresponding to a scan range of 200 GHz) for about 2 hours each have to be measured. This results in 46 ± 7 events on resonance (signal+background) and of 16 ± 4 for each point outside the resonance line (background). The here given uncertainty is only the statistical uncertainty. The Monte Carlo simulations of Fig. 7.5 demonstrates the search of our resonance for 3 days of measuring time assuming the signal and background rates given in Eq. (7.5). It is found that one week of measuring time is then sufficient to find the resonance (see Fig. 7.6). The remaining beam time which will be of the order of 4 weeks will be used to measure the position of the resonance line to the proposed accuracy of 30 ppm.

7.6 Future extension of the experiment

The $2S_{1/2}^{F=0} - 2P_{3/2}^{F=1}$ transition in muonic hydrogen where the initial state corresponds to the lower $2S$ hyperfine level could be also measured. There is a considerable theoretical uncertainty related with the $2S$ hyperfine splitting (cf. Table 2.2), whereas the $2P$ fine and hyperfine splitting can be predicted exactly. A suitably weighted superposition of the $2S_{1/2}^{F=1} - 2P_{3/2}^{F=2}$ with the $2S_{1/2}^{F=0} - 2P_{3/2}^{F=1}$ Lamb shift measurements will give the "pure" $2S-2P$ Lamb shift in muonic hydrogen, removing the uncertainty related to the theoretical prediction of the hyperfine splitting (especially Zemach radius and proton polarizability contributions to the hyperfine splitting).

A measurement of the Lamb shift in muonic deuterium (μd) would lead to a test of the polarizability calculations to a precision near 1%. The laser wavelength for the $2S_{1/2}^{F=3/2} - 2P_{3/2}^{F=5/2}$ transition in μd is $\lambda = 5.90$ μm, corresponding to a Ti:Sa laser wavelength of 706 nm. From the theoretical side the μd polarization shift has been calculated with 2% precision [112]. To test the polarizability contribution in deuterium it is necessary to know the deuteron charge radius. This is achieved by deducing the proton radius from muonic hydrogen spectroscopy and combining it with the measured isotopic shift in ep–ed [113].

A very challenging experiment is in progress at MPQ Garching aiming to measure the $1S - 2S$ transition frequency of (trapped) He^+ ions with a frequency comb laser operated in the extreme ultraviolet (60 nm) [114]. Since the gross–structure of the energy levels scales as Z^2 (see Eq. (A.3)) and the Lamb shift as Z^4 (see Eq. (A.21)), the He^+ energy levels are much more sensitive to bound–state QED corrections than hydrogen. In particular the two–loop terms which presently have the largest uncertainty are of order Z^6. The high resolution spectroscopy of He^+ will therefore provide an enhanced test of bound–state QED. As for muonic hydrogen, the spectroscopy of muonic helium can be used to determine the nuclear size, *i.e.,* the ^{4}He– and ^{3}He–nucleus rms charge radii may be deduced if the Lamb shift in muonic helium is measured. This measurement may also be useful for the search of the resonance line in He^+. The spectroscopy of muonic helium can be performed with basically the same apparatus as described in this thesis. The lifetime of the μHe_{2S} atoms is longer at higher gas densities compared to μp_{2S} (*e.g.,* 1.6 μs at 10 hPa [115,116]) and its transition frequency corresponds, *e.g.,* to a wavelength of 812 nm ($2S_{1/2} - 2P_{3/2}$ in μ^4He), which is optimal for the Ti:Sa laser (no need of any Raman shift).

Appendix A

Theory of hydrogen energy levels

The determination of the rms proton charge radius from the μp Lamb shift experiment is essential for comparing the measured $1S$ Lamb shift in hydrogen with its theoretical prediction. A short overview of the basic ideas, challenge and problems related to the theory of hydrogen energy levels is given in this Appendix without the presumption to be complete. An accurate description of the energy levels over the range of 14 order of magnitude is necessary in order to reach the experimental accuracy of the $1S - 2S$ transition frequency. There are many corrections to the Dirac energies which contribute at this level of precision: radiative (QED), recoil (finite nuclear mass), recoil–radiative and nuclear structure corrections (finite nuclear size, nucleus polarizability).

In this Appendix focus is given to the problems related to the calculation of the one– and two–loop self–energy terms and to the effects related to the nonpoint–like nature of the nucleons. This may be justified since the one–loop self–energy represents the major contribution to the Lamb shift whereas the two–loop and finite size effects dominate the uncertainty in the prediction of the Lamb shift. The basic ideas and the theoretical status up to the year 2001 can be found in the overview article of Eides *et al.* [19].

A.1 Bohr energy levels

Since the electron to proton mass ratio is very small $m/M \simeq 1/2000$, it can be assumed as a first approximation that the mass of the nucleus is infinitely large. Hence the nucleus is considered as a static source of the Coulomb field. The Hamilton operator H for an electron of mass m and charge $-e$ in the field of a infinitely heavy Coulomb center with charge Ze is given by (SI units)

$$H = \frac{p^2}{2m} - \frac{Ze^2}{4\pi\varepsilon_0 r}\,, \tag{A.1}$$

where ε_0 is the free space permittivity and r the electron–proton distance. In first approximation the hydrogen energy levels are described by the stationary Schrödinger equation

$$H\,\Psi_{nlm}(r) = E_n\,\Psi_{nlm}(r)\,, \tag{A.2}$$

where Ψ_{nlm} is the electron wave function with n being the principal quantum number, l the orbital angular momentum and m the magnetic quantum number. The Bohr's energy levels corresponding to the energy eigenvalues E_n of this equation depend only on n and are

$$E_n = -R_\infty\, hc\,\frac{Z^2}{n^2} = -mc^2\frac{(Z\alpha)^2}{2n^2}\,, \tag{A.3}$$

where c is the speed of light in vacuum, h the Planck constant, $\alpha = e^2/(2\varepsilon_0 hc) \simeq 1/137$ the fine structure constant and

$$R_\infty = \frac{me^4}{8\varepsilon_0^2 h^3 c} = \alpha^2 \frac{mc}{2h} \tag{A.4}$$

the Rydberg constant. Finiteness of the nucleus mass can be included introducing the reduced mass m_r of the two–body system which is defined as

$$m_r = \frac{mM}{m+M} \,. \tag{A.5}$$

For hydrogen $m_r \simeq 0.9995\, m$. In the nonrelativistic case the introduction of m_r fully describes the two–body system. The hydrogen energy levels for a finite proton mass are described by Eq. (A.3) substituting m_r to m. The energy levels for an infinitely heavy proton and one with mass M differ about 0.05%.

The energy of an absorbed or emitted photon $h\nu$ is the energy difference between two levels $h\nu = E_n - E_{n'}$. Its spectrum is described by

$$\frac{1}{\lambda} = \frac{\nu}{c} = R_\infty \frac{m_r}{m} \left(\frac{1}{n^2} - \frac{1}{n'^2} \right) , \tag{A.6}$$

where n, n' are the principal quantum numbers of the two involved energy levels, λ and ν are the wavelength and the frequency of the photon, respectively. From now on through the text natural units $\hbar = c = \varepsilon = 1$ are used when not explicitly written.

A.2 Dirac energy levels

A better description of the hydrogen energy levels is given by the Dirac equation. It takes into account both the relativistic energy dependence of an electron on its momentum ($E = \sqrt{p^2c^2 + m^2c^4}$) and the 1/2 electron spin. Again in first approximation we consider the nucleus as an infinitely heavy static Coulomb source with charge Ze. In this a case an exact solution of the Dirac equation exists with energy eigenvalues (see, *e.g.,* Ref. [117])

$$E_{nj} = mc^2 \, f(n,j) \,, \tag{A.7}$$

where

$$f(n,j) = \left[1 + \frac{(Z\alpha)^2}{\left(n - j - \frac{1}{2} + \sqrt{\left(j+\frac{1}{2}\right)^2 - (Z\alpha)^2} \right)^2} \right]^{-\frac{1}{2}} \tag{A.8}$$

and j is the sum of orbital and spin angular momentum of the electron. States with the same principal quantum number n but different angular momentum j are split into n components of the fine structure. Expanding f in powers of $Z\alpha$ leads to [38]

$$\begin{aligned} E_{nj} \simeq\; & mc^2 - mc^2 \frac{(Z\alpha)^2}{2n^2} - mc^2 \frac{(Z\alpha)^4}{2n^3} \left(\frac{1}{j+\frac{1}{2}} - \frac{3}{4n} \right) \\ & - mc^2 \frac{(Z\alpha)^6}{8n^3} \left[\frac{1}{(j+\frac{1}{2})^3} + \frac{3}{n(j+\frac{1}{2})^2} + \frac{5}{2n^3} - \frac{6}{n^2(j+\frac{1}{2})} \right] + \dots \end{aligned} \tag{A.9}$$

The first term describes the relativistic mass energy and the second is the Bohr energy (cf. with Eq. (A.3)). The first, second, and the third term in the relativistic energy expansion

$$E = \sqrt{m^2c^4 + m^2p^2} \simeq mc^2 + \frac{p^2}{2m} - \frac{p^4}{8m^3} + \dots \,. \tag{A.10}$$

contributes respectively to the first, second, and third term in Eq. (A.9). The expansion in powers of $p^2/2m$ corresponds to an expansion in $(Z\alpha)^2$ and hence the relativistic corrections are given by an expansion over even powers of $Z\alpha$. Corrections of the Dirac eigenvalues that take into account the finiteness of the nucleus mass can not be fully accommodated as in the nonrelativistic case only by substituting m by the reduced mass m_r. The first term in Eq. (A.9) already has the correct mass dependence whereas the second term should be modified by a factor m_r/m to reproduce the Bohr's energy level. The electron motion in the Coulomb field is essentially nonrelativistic.

As starting point of a two–body relativistic theory one usually considers the Bethe–Salpeter equation [118]. Unfortunately it is very difficult to handle. This equation contains an infinite sum of all interaction kernels of the system. An approximation can be performed by truncating this infinite sum. The kernel which describes the dominant binding between the two particles is retained and is used to construct the effective Dirac equation whereas the remaining are evaluated in the framework of perturbation theory. The effective Dirac Hamiltonian $H^{\rm Dirac}$ obtained by retaining only the one–photon exchange kernel between electron and nucleus (no radiative corrections) is [119]

$$H^{\rm Dirac} = \alpha \cdot (\mathbf{p} - e\mathbf{A}) + \beta m + V + \frac{\mathbf{p^2}}{2M}\,, \tag{A.11}$$

where $\mathbf{p}^2/2M$ is the term describing the kinetic energy of the nucleus, $V = -Z\alpha/r$ is the Coulomb potential and $\mathbf{A}$ the Breit potential. $(V, \mathbf{A})$ is the four–potential caused by the proton at the electron position. The proton is considered to be spin–less. This equation is referred to as the external–field approximation since it is only a one–particle Hamiltonian. A general expression for the atomic energy levels resulting from Eq. (A.11) which takes into account the largest corrections caused by the finite mass M of the nucleus is [38]

$$\begin{aligned} E_{njl} = {} & mc^2 + Mc^2 + (f(n,j) - 1)\, m_r c^2 \\ & - (f(n,j) - 1)^2 \frac{m_r^2 c^2}{2(m+M)} + \frac{1 - \delta_{l0}}{(j+1/2)(2l+1)} \frac{(Z\alpha)^4 m_r^3 c^2}{2n^3 M^2}. \end{aligned} \tag{A.12}$$

The third term corresponds to the Dirac energy for a static Coulomb source corrected by the reduced mass to take into account the finite nucleus mass. The two last terms are recoil corrections. The last term is responsible for a small breaking of the l degeneracy of the Dirac eigenstates. The third and forth term are correct for all order in $Z\alpha$ for one photon exchange, whereas the last term is correct only to the first order in $Z\alpha$.

A.3 The Lamb shift

According to the Dirac equation with static Coulomb source the energy levels with same quantum numbers n and j are degenerate. Lamb and Retherford have measured in 1947 an energy splitting (called Lamb shift) of about 1 GHz between the $2S_{1/2}$ and the $2P_{1/2}$ energy levels. This energy difference is not the tiny l dependence in Eq. (A.12) which accounts for 2 kHz for the $2S_{1/2} - 2P_{1/2}$ energy splitting. This discovery together with the

discovery of the electron's anomalous magnetic moment has triggered the development of quantum electrodynamics (QED).

Generally speaking the "Lamb shift" is any deviation from the energy level predicted by the Dirac equation (partially corrected for the finite nucleus mass). In some application [19] the Lamb shift L_{njl} is defined as the sum of all contributions to the energy levels beyond the first four terms in Eq. (A.12) averaging over (or without considering) the hyperfine splitting [1] contributions $E^{\rm hfs}_{njlF}$

$$\begin{aligned} E^{\rm tot}_{njlF} &= mc^2 + Mc^2 + (f(n,j)-1)\, m_r c^2 \\ &\quad - (f(n,j)-1)^2 \frac{m_r^2 c^2}{2(m+M)} + L_{njl} + E^{\rm hfs}_{njlF} \end{aligned} \tag{A.13}$$

where $E^{\rm tot}_{njlF}$ is the total binding energy of the level characterized by the n, j, l, F quantum numbers, F being the total angular momentum. The first two terms always cancel out when energy differences between two levels are measured. The third term contributes about 2.5×10^3 THz to the $1S - 2S$ energy splitting in hydrogen, while the forth term (recoil) contributes about 22 MHz. The difference of $1S$ and $2S$ level Lamb shifts is about $L_{1S} - L_{2S} \simeq 8 - 1 = 7$ GHz. The hyperfine splitting of the $1S$ state is $E^{\rm tot}_{1S(F=1)} - E^{\rm tot}_{1S(F=0)} \simeq$ 1420 MHz. In muonic hydrogen the hyperfine structure is considered as a part of the Lamb shift.

This gives an overview of the size of the various contributions. Noticeable is the size of the main finite mass correction (m_r instead of m in the third term) of about 1 THz relative to the size of the Lamb shift of about 7 GHz. It is desirable that as much as possible of the correct mass dependence is included in the effective Dirac equation in order to avoid treating all effects of the motion perturbatively.

The Lamb shift does not arise in the framework of quantum mechanics with a potential but it requires field–theoretical methods which can be written in terms of Feynman graphs. This quantum electrodynamic (QED) corrections to the energy levels can be written in the form of a power series expansion in three small dimensionless parameters: α, $Z\alpha$, and m/M. These parameters, in particular α and $Z\alpha$, enter the wave function and the particle propagator (via the energy, see Eq. (A.18) in the next section) in a nonperturbative way. Although bound–state QED is nonperturbative, it is possible to make use of these small parameters to develop expressions in increasing order of smallness. However the nonperturbative nature of this expansion shows up in the coefficients of the power series. Some of these coefficients are not constants but slowly varying functions (*e.g.,* $\ln (Z\alpha)^{-2}$ in Eq. (A.22)) of the expansion parameters. Hence the energy shift caused by a given kernel can not be estimated by simply counting the powers in α and $Z\alpha$ it contains.

It is convenient to classify the various contributions to the Lamb shift in accordance with the small parameters they depend on. They may be classified in four groups which are listed in decreasing size: radiative, recoil, radiative–recoil, and finite nuclear size and structure corrections.

Radiative corrections : They take into account pure QED effects like self–energy and vacuum polarization for an electron in a Coulomb potential of an infinitely heavy and point–like nucleus. These contributions depend only on α and $Z\alpha$.

[1] The Dirac equation with a Coulomb source takes into account the electron spin but does not include the magnetic moment of the heavy nucleus, and hence the hyperfine contributions has to be taken into account separately.

Table A.1: Theoretical expectation (not updated) of the $1S$ and $2S$ Lamb shifts taken from M. Niering's thesis [120]. Note that uncertainty related to proton radius extracted from scattering experiment [121] has been underestimated. The first uncertainty of the summed contributions refers to the pure theoretical uncertainty and the second to the uncertainty caused by the uncertainty of the proton radius.

Contribution	$1S$ state [kHz]	Uncertainty [kHz]	$2S$ state [kHz]	Uncertainty [kHz]
radiative (one–loop)	8 181 285.5	0.2	1 046 061.43	4×10^{-2}
radiative (two–loop)	721	24	90.2	3×10^{-1}
recoil	2 402.118	0.002	340.3646	3×10^{-4}
radiative–recoil	−12 777.97	0.04	−1.635.437	5×10^{-3}
finite nuclear size	1167	32	145.8	4
sum	8172 798(32)(24)		1045 002.4(4.0)(0.3)	

Recoil corrections : They describe corrections due to the finite mass of the nucleus, apart for the two larger finite mass contributions which are already included in the third and forth term of Eq. (A.13), without considering any QED correction. These contributions arise from the fact that the introduction of the reduced mass can not account for all recoil corrections in a relativistic two–body system. They depend simultaneously only on $Z\alpha$ and m/M.

Radiative–recoil corrections : They take into account mixed radiative and recoil contributions, *e.g.,* recoil contributions with one or more photon loops on the fermion line. They depend simultaneously on α, $Z\alpha$, and m/M.

Finite nuclear size corrections : The assumption that the nucleus is point–like is released. The extension of the nuclear charge causes a deviation of the $(1/r)$ Coulomb potential. An additional contribution comes from the nucleus polarization which arises from the interaction of the electron with the nucleus excited in a virtual state.

It is fortunate that the different physics involved can be largely compartmentalized, *e.g.,* the recoil and nuclear structure corrections can be neglected when treating the main radiative corrections and vice versa. Nevertheless, the actual level of precision (experimental and theoretical) has reached a point where some corrections have to be treated together as the recoil–radiative corrections. Table A.1 summarizes the contributions to the hydrogen Lamb shift for the $1S$ and $2S$ state according to the groups defined above. Note that the reported values refer to the status in the year 1999. As will be explained later the theoretical uncertainty has been reduced in the past five years by an order of magnitude, whereas the uncertainty related to the proton radius from electron scattering experiments has been underestimated (cf. Eq. (A.38)). In the following, for brevity, it was chosen to report some details only for the radiative and the nuclear finite size corrections. This is justified since the radiative corrections are the largest ones and their uncertainty dominates the theoretical uncertainty of the Lamb shift besides the finite size effect. The finite size corrections contributes only 1.4×10^{-4} to the Lamb shift, but contain the largest uncertainty caused by the uncertainty of the rms proton radius extracted from electron scattering experiments.

Figure A.1: Self–energy graph for a free (left) and a bound (right) electron. Single and double straight lines represent the free electron propagator and the bound electron propagator respectively.

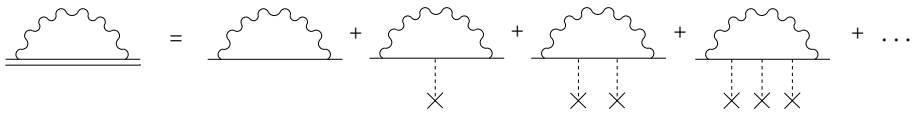

Figure A.2: Expansion of the bound self–energy in terms of Coulomb fields. The "X" represents the nucleus.

A.4 Radiative corrections

The main contribution to the radiative corrections and also to the Lamb shift is the electron self–energy. Its physical origin is the emission and re–absorption of a virtual photon by the electron, which is given schematically by the Feynman diagram in Fig. A.1. The modification of the Feynman propagator $\Sigma^{(1)}(p)$ caused by the one–loop self–energy can be calculated using the Feynman–law for vertexes $(-ie\gamma^\mu)$, photon $(iD_{\mu\nu}(k))$ and electron $(iS_F(q))$ propagator [122]

$$-i\Sigma^{(1)}(p) = \int \frac{d^4k}{(2\pi)^4} iD_{\mu\nu}(k)(-ie\gamma^\mu)iS_F(p-k)(-ie\gamma^\nu) \tag{A.14}$$

This integral is linearly divergent. Details of regularization and mass renormalization connected with this divergence are not reported here. The free–electron propagator S_F represented by a straight simple line in Fig. A.1 is

$$S_F(q) = \frac{1}{\not{q} - m}\,. \tag{A.15}$$

where $\not{q} = \gamma^\mu q_\mu$ with γ^μ being the four Dirac γ-matrices. Since the electron in hydrogen is bound to the nucleus a better starting point for the evaluation of the self–energy corrections is the Dirac equation which includes the external Coulomb potential V. Correspondingly the bound–electron propagator S_B (Dirac–Coulomb propagator) which is represented by a double straight line in Fig. A.1 (left), is

$$S_B(q) = \frac{1}{\not{q} - m - \gamma^0 V}\,. \tag{A.16}$$

Generally speaking the Dirac–Coulomb propagator contains corrections to the free propagator which can be developed in $Z\alpha$. In fact, it is possible to expand the Dirac–Coulomb propagator for large virtual photon energies in powers of the potential V [122]. This expansion makes use of the relation

$$\frac{1}{X-Y} = \frac{1}{X} + \frac{1}{X}Y\frac{1}{X} + \frac{1}{X}Y\frac{1}{X}Y\frac{1}{X} + \frac{1}{X}Y\frac{1}{X}Y\frac{1}{X}Y\frac{1}{X} + \cdots \tag{A.17}$$

With the abbreviation $D = \not{q} - m$ the electron propagator can be expanded as [122]

$$\frac{1}{\not{q} - m - \gamma^0 V} = \frac{1}{D - \gamma^0 V} = \frac{1}{D} + \frac{1}{D}\gamma^0 V \frac{1}{D} + \frac{1}{D}\gamma^0 V \frac{1}{D}\gamma^0 V \frac{1}{D} + \cdots \tag{A.18}$$

An expansion in V corresponds to an expansion in $(Z\alpha)^2$ since $V = Z\alpha/r$ and r scales like $Z\alpha$. The Feynman graphs corresponding to Eq. (A.18) are shown in Fig. A.2. Adding a photonic line to a graph increases its order by $Z\alpha$. Its contribution to the energy level is then about a factor $Z\alpha$ smaller.

The hydrogen energy level shift caused by the one–loop self–energy is given in first order by

$$\Delta E_{SE}^{(1)} = \langle \bar{\Psi} | \Sigma_{\text{bound}}^{(1)} | \Psi \rangle \,, \tag{A.19}$$

where $\Sigma_{\text{bound}}^{(1)}$ is the renormalized propagator modification caused by the one–loop self–energy for bound states. $\Sigma_{\text{bound}}^{(1)}$ is obtained by re–normalizing Eq. (A.14) evaluated for the Dirac–Coulomb propagator given by Eq. (A.16) instead of Eq. (A.15). Hence [122]

$$\Delta E_{SE}^{(1)} = ie^2 \int \frac{d^4k}{(2\pi)^4} D_{\mu\nu}(k) \langle \bar{\Psi} | \gamma^\mu S_B(p) \gamma^\nu | \Psi \rangle - \langle \bar{\Psi} | \delta m | \Psi \rangle \,, \tag{A.20}$$

where the term with δm represents the counter–term connected with the renormalization of the mass. The evaluation of Eq. (A.20) can be accomplished in two different ways: expanding S_B in powers of $Z\alpha$ as expressed in Eq. (A.18), that is in a perturbative way, or by treating S_B exactly.

A.5 Perturbative and all–order approaches to the self–energy

In the non–recoil limit two types of expansion (in α and $Z\alpha$) can be carried out in the evaluation of the radiative bound–state QED corrections. The first expansion in the number of loops present in the Feynman diagrams is governed by powers of α/π. In the bound–state QED problem every coefficient of the α/π expansion is developed in powers of $Z\alpha$ as shown for the one–loop self–energy in Eq. (A.18) and Fig. A.2. Every additional photonic line connecting the electron to the nucleus generates an additional power in $Z\alpha$.

The one–loop corrections (order of α/π) are by several orders of magnitude the largest contributions to the Lamb shift and are given by the electron self–energy and the vacuum polarization. In the following, focus is given on the evaluation of the self–energy term which is the most problematic and largest contribution to the Lamb shift. The vacuum polarization is discussed in the context of muonic hydrogen (cf. §2.1) where it plays the dominant role. Some of the two–loop corrections (order of $(\alpha/\pi)^2$) are diagrammatically shown in Fig. A.3. Following the same procedure that has lead to Eq. (A.20), similar expressions can be written for the two–loop self–energy diagrams (see *e.g.,* Refs. [123–125]). Because of the approximate $(Z\alpha)^4/n^3$ scaling law of the self–energy level shift,[2] it is

[2]The additional $(Z\alpha)^3/n^3$ term in Eq. (A.21) has it origin from the square of the electron wave–function at the origin $|\Psi_n(0)|^2$. The continuous emission and re–absorption of virtual photons by the electron results in a spread of its electric charge over a finite volume with radius $\langle r_{el}^2 \rangle$. This finite radius is generating a correction to the Coulomb potential which is $\delta V \sim \langle r_{el}^2 \rangle \delta(\vec{r})$. The energy shift ΔE calculated in first order perturbation theory for S state levels is then given by $\Delta E = \langle nS | \delta V | nS \rangle \sim |\Psi_n(0)|^2 \langle r_{el}^2 \rangle$. Similarly, the vacuum polarization and the nucleus finite size effect modify the Coulomb potential which can be described by a δ-function in the space representation, which leads to a dependence of the energy shift on $|\Psi_n(0)|^2$.

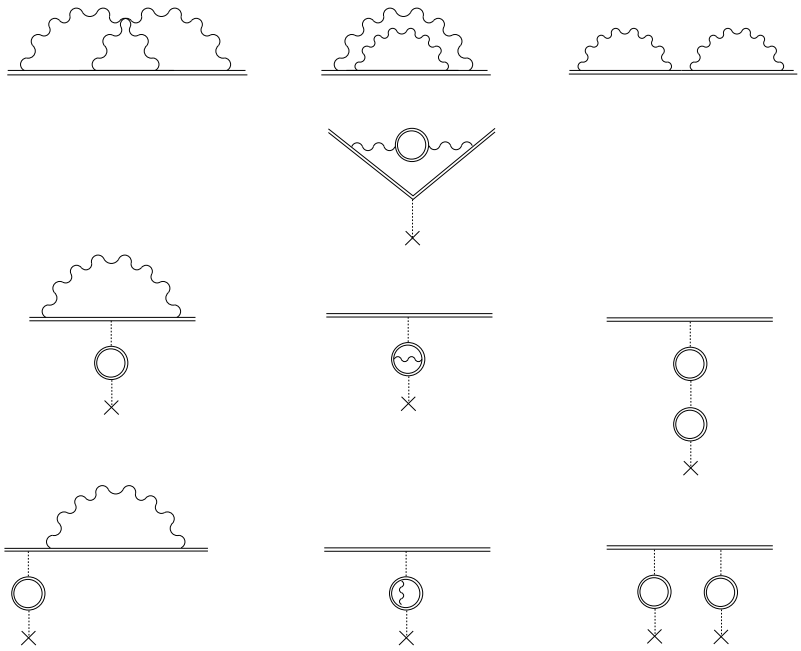

Figure A.3: The Feynman diagrams contributing to the two–loop QED energy. The first row represents the two–loop self–energy and are the most problematic terms. The double line denotes the bound–state electron propagator, i.e., it includes all Coulomb interactions.

convenient to express the shift of each state as

$$\Delta E_{SE}^{(1)+(2)} = m\frac{\alpha}{\pi}\frac{(Z\alpha)^4}{n^3}F_n(Z\alpha) + m\left(\frac{\alpha}{\pi}\right)^2\frac{(Z\alpha)^4}{n^3}G_n(Z\alpha) \tag{A.21}$$

where $F_n(Z\alpha)$ is a slowly varying function associated with the one–loop (α/π), and $G_n(Z\alpha)$ with the two–loop $(\alpha/\pi)^2$ corrections. As previously anticipated there exist two ways to calculate the integrals associated to $\Delta E_{SE}^{(1)+(2)}$. The first relies on a perturbative expansion of the Dirac–Coulomb propagator on $Z\alpha$, *i.e.,* the coupling constant to the external field [2, 3, 124, 126, 127], and the second one treats the Dirac–Coulomb propagator exactly [4, 123, 125, 128–130]. The coupling constant $Z\alpha$ for heavy elements (*e.g.,* for uranium $Z\alpha \simeq 0.67$) is not really small compared to 1. For high Z nuclei the semi–analytical expansion of $F_n(Z\alpha)$ and $G_n(Z\alpha)$ in terms of $Z\alpha$ and $\ln(Z\alpha)$ no longer converges, and in that case $F_n(Z\alpha)$ and $G_n(Z\alpha)$ must be evaluated with the numerical all–order exact method. Hence the perturbative method is valid only for low–Z ($Z \leq 5$ for the one–loop self–energy) systems. On the contrary the exact approach in the past has been predominantly used for the description of high–Z ($Z \geq 40$) hydrogen-like ions due to high numerical cancellations at low–Z.

However the numerical all–order (non perturbative) treatment of the one–loop self–energy for $Z = 1$ has nowadays overcome the limitations of the perturbative approach in $Z\alpha$ [129]. Recently the two–loop self–energy has been computed in the all–order approach for ions with $Z \geq 10$ [130]. An extrapolation to $Z = 1$ is possible [3, 130] as shown in Fig. A.7.

A.6 One–loop self–energy

In the perturbative approach the dimensionless quantity $F_n(Z\alpha)$ can be expressed as a semi–analytical expansion over $Z\alpha$ and $\ln(Z\alpha)$, [3]

$$\begin{aligned} F_n &= A_{40} + A_{41}\ln(Z\alpha)^{-2} + (Z\alpha)A_{50} \\ &\quad + (Z\alpha)^2\left[A_{62}\ln^2(Z\alpha)^{-2} + A_{61}\ln(Z\alpha)^{-2} + G_{SE}\right] \end{aligned} \tag{A.22}$$

The first index of the A coefficients gives the power of $Z\alpha$ (including the $(Z\alpha)^4$ pre–factor in Eq. (A.21)), whereas the second index corresponds to the power of the logarithm. $F_n = F_n(nlj, Z\alpha)$ and $A_{pq} = A_{pq}(nlj)$ depend on the atomic state with quantum numbers n, l, j. The work involved in calculating the A constants in Eq. (A.22) has involved many physicists and has extended over more than five decades. A complete list of the A coefficients is given in [1]. A_{40} contains the Bethe–logarithm $\ln(k_0(nl))$, and the self–energy remainder function $G_{SE}(Z\alpha)$ contains the higher order contribution in $Z\alpha$ to the one–loop self–energy and can be semi–analytically expanded as [131]

$$\begin{aligned} G_{SE}(Z\alpha) &= A_{60} + (Z\alpha)\left[A_{71}\ln(Z\alpha)^{-2} + A_{70}\right] \\ &\quad + (Z\alpha)^2\left[A_{83}\ln^3(Z\alpha)^{-2} + A_{82}\ln^2(Z\alpha)^{-2}A_{81}\ln(Z\alpha)^{-2} + A_{80}\right] . \end{aligned} \tag{A.23}$$

The higher–order terms in the potential expansion of the Dirac–Coulomb propagator and the relativistic corrections to the wave–function both generate higher order terms in $Z\alpha$ which are manifest in Eqs. (A.22) and (A.23).

Since the binding Coulomb field enters in a nonperturbative way and no closed–form expression for the Dirac–Coulomb propagator exists, already the calculation of corrections of $(Z\alpha)^2$ relative order is a highly non trivial task. The one–loop electron self–energy contributes to all orders in $Z\alpha$, and the separation in $(Z\alpha)^2$ relative contribution involves hundreds of terms. Additionally the series expansion in $Z\alpha$ is slowly convergent. The best evaluation of the G_{SE} term is hence based on a direct all–order numerical evaluation of the bound–electron propagator [132]. Calculating F_n in the all–order exact method and subtracting from it all the other contribution related to the A coefficients of Eq. (A.22) gives G_{SE}. The uncertainty of the one–loop self–energy to a given energy level arises entirely from the uncertainty of the G_{SE}.

The nonperturbative results are consistent with the results of the $Z\alpha$–expansion but are orders of magnitude more precise. The numerical uncertainty of the all–order calculation is $0.8 \times Z^4$ Hz [129], whereas the uncertainty related to the perturbative method is of 28 kHz, due to the truncation of the $Z\alpha$ expansion (unevaluated higher order terms).

A.7 Two–loop self–energy

Similar to the one–loop self–energy, the two–loop self–energy contributions to the Lamb shift, shown diagrammatically in the first row of Fig. A.3, can be expressed in the perturbative approach as

$$\begin{aligned} G_n &= B_{40} + (Z\alpha)B_{50} \\ &\quad + (Z\alpha)^2\left[B_{63}\ln^3(Z\alpha)^{-2} + B_{62}\ln^2(Z\alpha)^{-2} + B_{61}\ln(Z\alpha)^{-2} + G_{h.o}\right] , \end{aligned} \tag{A.24}$$

[3] The dominant effect of nucleus finite mass on the self–energy corrections can be incorporated by multiplying each term of $F_n(Z\alpha)$ by the reduced mass factor $(m_r/m)^3$, except for the magnetic moment term in A_{40} which is multiplied only by $(m_r/m)^2$ [38].

where $G_{h.o.} = B_{60} + (Z\alpha)(\dots)$. The calculation of the B coefficients [2,124,126,133–135] is at present one of the most challenging problems in bound–state QED, and it is the limiting factor of the theory. B_{40} which is the leading–order correction is quite small, $B_{40}(ns) = 1.409244$, whereas B_{50} was surprisingly found to be large, $B_{50}(ns) = -24.2668(31)$. This indicates a very slow convergences or even a nonperturbative behavior of the two–loop contributions. Insertion of the calculated B's values in Eq. (A.24) for the $1S$ state gives a more complete overview of this slow convergence:

$$\begin{aligned} G_n &= 1.409 - (Z\alpha)\,24.267 + (Z\alpha)^2[-0.296L^3 - 0.640L^2 + 49.838L - 61.6 + \cdots] + \cdots \\ &= 1.409 - 0.177 + [-0.015 - 0.003 + 0.026 - 0.003 + \cdots] + \cdots , \end{aligned} \tag{A.25}$$

where $L = \ln(Z\alpha)^{-2}$ and the B values are taken from Ref. [130]. The B coefficients are large and tend to grow with increasing order. Hence the estimation of uncertainty of higher order effects is rather problematic. Because of the large absolute magnitude of higher–order coefficients many terms have to be included for a reliable theoretical prediction. Higher order corrections in $Z\alpha$ are required, but the complexity of calculations of order $\alpha^2(Z\alpha)^7$ does not seem to make it feasible in the near future. A nonperturbative approach in the parameter $Z\alpha$ is therefore desirable even for hydrogen ($Z = 1$), but up to now this numerical approach is reliable only for ions with $Z \geq 10$.

The two–loop Bethe–logarithm, which forms the dominant part of the problematic coefficient B_{60}, has being evaluated for more than three decades. The most recent perturbative evaluation by K. Pachucki and U. Jentschura [2] gives $B_{60} = -61.6(3) \pm 15\%$ for the $1S$ and $B_{60} = -53.2(3) \pm 15\%$ for the $2S$ state. The 15% error is an estimate of the uncalculated terms (regions) and diagrams.

In the all–order calculation the reducible part of the loop after loop correction, the nested and overlapping diagrams of the two–loop self–energy are considered simultaneously. The first attempt to evaluate them to all orders was made by S. Mallapani and J. Sapirstein [123]. The contributions are rearranged in 3 groups referred as M, P, and

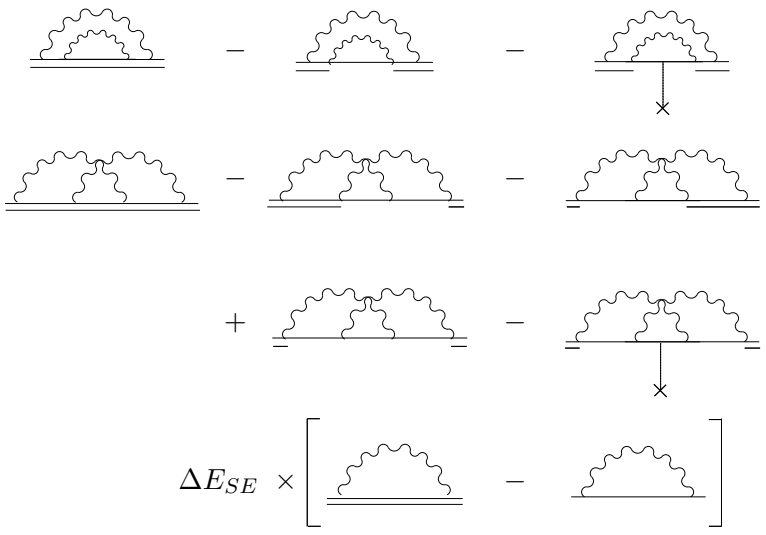

Figure A.4: Diagrammatic representation of the M *terms.* ΔE_{SE} *is the first–order self–energy correction [4].*

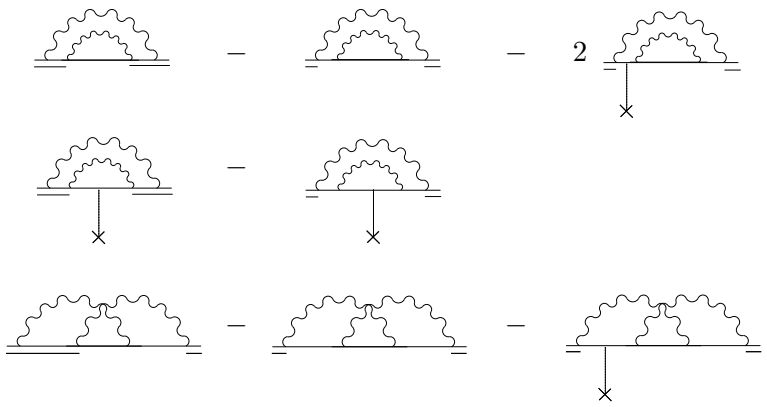

Figure A.5: Diagrammatic representation of the P *terms [4].*

F terms which are shown in Figs. A.4–A.6. This rearrangement is artificial since all 3 terms are divergent and a proper treatment has to consider them simultaneously. The M terms are made ultraviolet (UV)–finite by subtracting diagrams with some Dirac–Coulomb propagator replaced with the free propagator. The subtraction diagrams are chosen such that each of the 3 rows in Fig. A.4 is UV–finite. The diagrams are made UV–finite by subtracting diagrams with some Dirac–Coulomb propagators replaced by free propagators. Next the subtracted terms have to be accounted (in the P terms). Those who contain only free–electron propagators can be immediately evaluated with standard Feynman–parametrization techniques in momentum space, whereas the other ones are made UV–finite by subtracting another set of graphs where the Dirac–Coulomb propagators are again replaced by free propagators. This subtraction eliminates the overlapping UV–divergences which was caused from a UV–divergent subgraph and a bound–electron propagator in the same graph. Finally in the F term the last set of subtraction which contains only free electron propagators are collected. Different numerical methods are applied to the M, P, and F terms justifying this rearrangement [4].

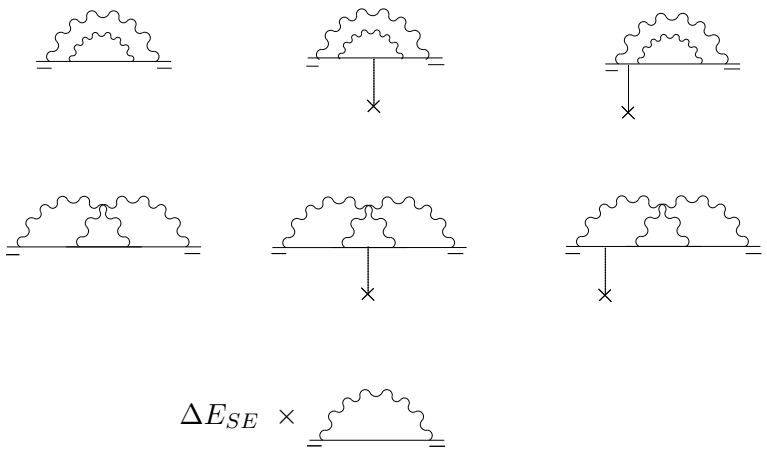

Figure A.6: Diagrammatic representation of the F *terms. The rightmost diagrams in the first two rows should be counted twice, accounting for two equivalent diagrams [4].*

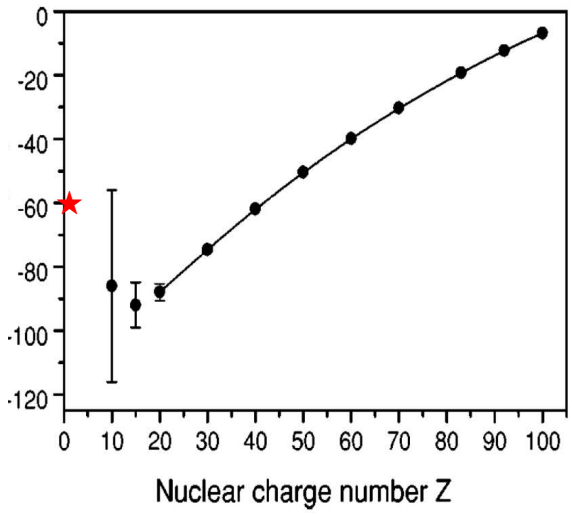

Figure A.7: B_{60} term for hydrogenic atoms with nuclear charge number Z calculated in the all–order approach (full circles). The extrapolation to $Z = 1$ gives a value of $B_{60} = -127 \pm 30\%$ [130]. The value computed with the perturbative approach shown with a star is $B_{60} = -61 \pm 15\%$ [2] (Courtesy E. Le Bigot).

The evaluation of G_n in all–order becomes problematic very fast as Z decreases, due to significant numerical cancellations. Up to now G_n is reliably calculated in the all–order approach only for ions with $Z \geq 15$ (see Fig.A.7). However an extrapolation to $Z = 1$ can be performed [3, 130]. Subtracting from the extrapolated $G_n(Z = 1)$ the values of all the calculated B coefficients in Eq. (A.24) results in $G_{h.o.}(1\alpha) = -127 \pm 30\%$ [130], which is significantly different from the value calculated from the perturbative approach. This difference leads to a difference in the $1S$ Lamb shift of 7 kHz. The error bar is dominated by the extrapolation procedure. Presumably the difference of the $G_{h.o}$ values calculated with perturbative and with the all–order approach has to be attributed to the incompleteness of the B_{61} and B_{60} coefficients. We assume therefore an averaged B_{60} for the $1S$ state of (-95 ± 35) which leads to a frequency shift of about (-10 ± 4) kHz. The two–loop self–energy contributions are quite significant when compared with the accuracy of 46 Hz for the measured $1S - 2S$ transition frequency.

A.8 Finite nuclear size and nuclear structure corrections

Although the characteristic atomic size of the order of the Bohr radius is orders of magnitude larger than the nucleus, the actual theoretical and experimental level of precision is sensitive to the nuclear structure. The nuclear contributions to the energy shifts are conventionally divided into two categories: those that directly involve only the properties of the nucleus in the ground state (*e.g.,* rms–radius), and those that involve virtual excited states (*e.g.,* polarizability). Presently both the finite size and the structure of the proton can not be calculated ab initio from QCD with sufficient precision necessary for a test between the theoretical prediction and measured Lamb shift. Fortunately to some degree of accuracy both the finite size and structure of the proton can be inferred from other measurements. The nuclear rms radius can be extracted from electron–proton scattering experiments and muonic hydrogen whereas the proton polarizability can be calculated using the photo–absorption cross section $\gamma + p \rightarrow X$ [33] measured in scattering experiments

$e + p \to e' + X$.

The typical wavelength for an atomic electron is so large compared to the nuclear size that only (the first) moments of the nucleus come into play. The nuclear charge form factor $F_1(\mathbf{q})$ is given by the Fourier transform of the nuclear ground state charge density ρ

$$F_1(\mathbf{q}) = \int d^3r\, \rho(\mathbf{r}) e^{i\mathbf{q}\cdot\mathbf{r}} \simeq Z\left(1 - \frac{\mathbf{q^2}}{6} r_{\rm p}^2 + \cdots\right) - \frac{1}{2} q^\alpha q^\beta Q^{\alpha\beta} + \cdots , \tag{A.26}$$

where $\mathbf{q}$ is the momentum transfer from the electron to the nucleus, and $Q^{\alpha\beta}$ the nuclear quadrupole–moment tensor. Due to the finite size effect the electric potential $V(r)$ of the nucleus differs from that of a point–like nucleus by

$$\delta V(r) = V(r) - \left(-\frac{Z\alpha}{r}\right) . \tag{A.27}$$

In momentum space this perturbation takes the form

$$\delta V(\mathbf{q}) = \frac{4\pi Z\alpha}{\mathbf{q}^2}\left(1 - F_1(\mathbf{q})\right) \simeq \frac{2\pi(Z\alpha)}{3} r_{\rm p}^2 - 2\pi Z\alpha \frac{q^\alpha q^\beta}{\mathbf{q}^2} Q^{\alpha\beta} . \tag{A.28}$$

These moments should dominate the nuclear corrections to atomic energy levels due to the low momentum of the photon exchanged in atomic systems. Transforming back in coordinate space gives [136]

$$\delta V(r) = \frac{2\pi(Z\alpha)}{3}\, r_{\rm p}^2\, \delta(r) - \frac{Q\alpha}{2r^3} \frac{3(\mathbf{S}\cdot\hat{\mathbf{r}})^2 - \mathbf{S}^2}{S(2S-1)} + \cdots , \tag{A.29}$$

where $\mathbf{S}$ is the nuclear spin operator and Q the nuclear quadrupole moment. For spin 0 and 1/2 nuclei $Q = 0$. The hydrogen level energy shift given by $\Delta E = \langle \bar{\Psi}(r) | \delta V | \Psi(r) \rangle$ is then

$$\Delta E = \frac{2\pi(Z\alpha)}{3}\, r_{\rm p}^2\, |\Psi_n(0)|^2 = \frac{2(Z\alpha)^4}{3n^3} m_r^3\, r_{\rm p}^2\, \delta_{l0} \simeq 1162(51)\, \frac{\delta_{l0}}{n^3}\ \text{kHz}. \tag{A.30}$$

where in the last equation it was made use of the nonrelativistic Schrödinger wave–function and of $r_{\rm p} = 0.895(18)$ fm. The largest corrections caused by the nonpoint–like nature of the nucleus is proportional to the second moment of the charge distribution, that is to the rms charge radius of the proton. The finite size contribution is non–vanishing only for S states. Since the proton charge is smeared out over a finite volume, the electron which is within this volume experiences a smaller attraction compared to the point–like case. This explains the up–wards energy shift caused by the proton finite size contribution. While in principle this shift should have some dependence on the detailed distributions $(\rho_i(r))$ of the charge inside the nucleus, that dependence is negligible as long as the rms radius of these distributions is the same $(r_p^2 = \int d\mathbf{r}\, r^2 \rho_i(\mathbf{r}))$. Equation (A.30) assumes a spherical charge distribution.

The Dirac wave–function $\Psi(r)$ which takes into account corrections to the Schrödinger–Coulomb wave–function $\Psi_{\rm Schr}(r)$ of relative order $(Z\alpha)^2$ is [32]

$$|\Psi(r)|^2 = |\Psi_{\rm Schr}(r)|^2 \left\{1 - (Z\alpha)^2 \left[\ln\frac{2mrZ\alpha}{n} + \Psi(n) + 2\gamma + \frac{9}{4n^2} - \frac{1}{n} - \frac{11}{4}\right]\right\} \tag{A.31}$$

where $\Psi(n)$ is the digamma function and γ the Euler's constant. The additional contribution to the energy shift is therefore

$$\Delta E = \frac{2(Z\alpha)^6}{3n^3} m_r^3\, r_{\rm p}^2 \left[\langle \ln\frac{2mrZ\alpha}{n}\rangle + \Psi(n) + 2\gamma + \frac{9}{4n^2} - \frac{1}{n} - \frac{11}{4}\right] \tag{A.32}$$

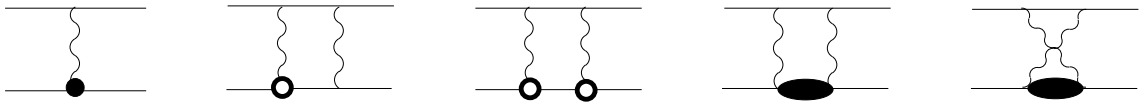

Figure A.8: Finite nuclear size contributions to the Lamb shift. The bold dot corresponds to the form factor slope $F_1(q^2)$ whereas the empty dots correspond to $(F_1(q^2)-1)$. The first term is the leading proton radius contribution in order $(Z\alpha)^4$, the second and third terms represent the nuclear size correction to order $(Z\alpha)^5 m$ with one and two form factors insertion. The last two diagrams are also of order $(Z\alpha)^5 m$ but they consider virtual excitation of the proton, i.e., its polarizability.

which is about 0.7 kHz [137] for the $1S$ state in hydrogen.

The leading finite size correction corresponding to Eq. (A.30) is graphically represented by the first diagram in Fig. A.8. The Feynman rule describing the interaction vertex between a low momentum photon and a nonpoint–like proton with finite mass is given by

$$\gamma_\mu \left(1 - \mathbf{q}^2 \left[\frac{1}{8M^2} + \frac{\langle r_{\rm p}^2 \rangle_E}{6} \right] \right) \tag{A.33}$$

where $\langle r_{\rm p}^2 \rangle_E$ is the charge radius defined via the Sachs form factor $G_E \simeq 1 - \frac{\langle r_{\rm p}^2 \rangle_E}{6} \mathbf{q}^2$ (see Appendix D for further details). The term proportional to $\langle r_{\rm p}^2 \rangle_E$ gives the energy shift of Eq. (A.30) whereas the other term proportional to $\frac{1}{8M^2}$ gives rise to the δ_{l0} term in Eq. (A.12) called the Darwin term (recoil correction).

Corrections of order $(Z\alpha)^5$ connected with the nonpoint–like nature of the proton are generated by the exchange of two photons diagrammatically represented by the second and third graph in Fig. A.8. The total contribution of order $(Z\alpha)^5$ with elastic intermediate states may be expressed as [32]

$$\Delta E = -\frac{m(Z\alpha)^5}{3n^3} m_r^3 \langle r_{\rm p}^3 \rangle_{(2)}, \tag{A.34}$$

where $\langle r_{\rm p}^3 \rangle_{(2)}$ is the third Zemach moment defined as

$$\langle r_{\rm p}^3 \rangle_{(2)} \equiv \int d^3 r_1 \, d^3 r_2 \, \rho(r_1) \rho(r_2) \, |\mathbf{r}_1 - \mathbf{r}_2|^3. \tag{A.35}$$

The third Zemach moment can not be directly measured like the proton radius which is directly connected with the low–momentum behavior of the form factor. Numerically this elastic contribution of the order $(Z\alpha)^5$ is -35.9 Hz for the $1S$ state [19, 32], *i.e.,* smaller than the contributions in $(Z\alpha)^6$ given by Eq. (A.32).

The intermediate state of the proton in the two–photon interaction may be excited in virtual states. The electron is polarizing the nucleus (similarly the moon is influencing the tides on the earth), and this induced dipole is causing an additional attractive potential between nucleus and electron which shifts the energy level down. For hydrogen the nuclear polarization shift obtained in [138] is

$$\Delta E = -0.070(13) \frac{\delta_{l0}}{n^3} \text{ kHz} \tag{A.36}$$

whereas a slightly different result was obtained in [33]

$$\Delta E = -0.095(7) \frac{\delta_{l0}}{n^3} \text{ kHz} \tag{A.37}$$

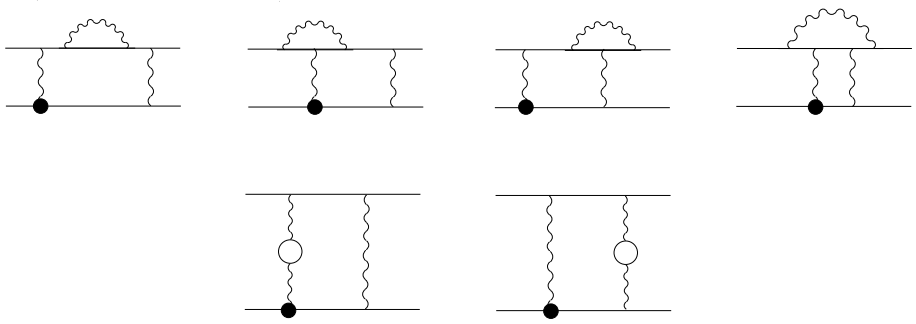

Figure A.9: Radiative corrections of order $\alpha(Z\alpha)^5 m\langle r_{\rm p}^2\rangle m_r^3$ to the finite size effect. The first row accounts for radiative corrections of the electron line whereas the second row accounts for polarization correction of the Coulomb line.

although they both make use of the same data for the proton polarizability. The polarizability contribution to the nS energy level represents the largest nuclear structure and size uncertainty, beyond the leading order.

Higher order radiative corrections of order $\alpha(Z\alpha)^5 r_{\rm p}^2\, m_r^3$ represented in Fig. A.9 contribute to the finite–size energy shift by -0.138 kHz for the $1S$ state in hydrogen [19].

A.9 Summary

The uncertainty related with the two–loop self–energy is the main source of uncertainty in the prediction of the Lamb shift, besides the uncertainty related to the finite size of the proton. The resulting theoretical value is

$$L_{1S}^{\rm the} = 8\,172\,901(51)(4)\ \text{kHz} \tag{A.38}$$

where the first error comes from the current uncertainty in the proton charge radius $r_{\rm p}$ =0.895(18) fm, and the second one from QED theory (mainly two–loop self–energy). This Lamb shift value was taken from [2] corrected for the averaged value of the B_{60} term as discussed in §A.7 and the new rms radius value from scattering experiment [6]. This can be compared with the experimental value deduced from frequency measurements of hydrogen transitions [5, 7]

$$L_{1S}^{\rm exp} = 8\,172\,840(22)\ \text{kHz}\ . \tag{A.39}$$

The uncertainty caused by the uncertainty of the proton rms radius prevents a precise comparison between the QED predicted and the experimentally determined Lamb shift. An improvement of the $1S$ Lamb shift knowledge by measuring the proton radius and by reducing the experimental error will serve as a consistency check between two different approaches to bound–state QED: perturbative and all–order numerical (in $Z\alpha$).

Appendix B

Bound–state QED test and extraction of Rydberg constant

This Appendix describes the achievable improvement of bound–state QED test and the improvement in the determination of R_∞ if the rms proton radius is extracted from the measurement of the $2S-2P$ Lamb shift in muonic hydrogen.

Quantum electrodynamics for free particles is one of the best tested theories in physics, *e.g.,* the calculation of the anomalous magnetic moment is advanced including hundreds of loops up to the 5–loop level. The theoretical value of the anomalous magnetic moment of the electron is tested to a level of 3.8×10^{-9} [1] and the comparison with experiment is limited by the experimental accuracy. Despite the enormous success of QED for free particles, the theory is less precise and less well tested for bound–states. Bound state QED deals mainly with one– and two–loop diagrams but for particles which are not free, *i.e.,* for particles bound by the Coulomb field. The limiting factor for comparison of bound–state QED predictions in hydrogen with measurements is the uncertainty related to the rms charge radius of the proton. New interest for bound–state QED which is essentially non–perturbative in the binding potential, comes from the development of quantum chromodynamics (QCD) where hadrons are bound–states of quarks. Bound–state QED can therefore serve as a platform to develop techniques for bound–states theories. In recent years, new techniques in non–perturbative studies have been very successful not only in the precision of calculations, but also in expanding the practical range of applicability, particularly to highly ionized atoms and inner shell levels of heavy atoms [139]. The non–perturbative calculation in hydrogen can be considered as a testing ground for bound–state QCD as well as for the QED of electrons in high electric and magnetic fields where deviations from the standard QED will be more pronounced.

The measurement of the rms proton radius with 10^{-3} relative precision via the $2S-2P$ μp Lamb shift opens the way to test bound–state QED to a relative accuracy of 3×10^{-7}. An exact calculation of the precision of the bound–state QED test and the determination of R_∞ requires a least square adjustment of all measured and calculated transition frequencies in hydrogen and deuterium which is beyond the scope of this work. However a simplified model to extract the experimental Lamb shift (L_{1S}^{exp}) is presented here. It accounts only for the measured $1S-2S$ and $2S-8S$ transition frequencies in hydrogen and uses a simplified model for the energy levels

$$E(nlj) \simeq \eta R_\infty \frac{1}{n^2} + L(nlj,\alpha)\,, \tag{B.1}$$

where $\eta = m_r/m$. For our purpose we can neglect small or precisely known contributions,

like the first recoil and relativistic corrections, because they are theoretically well known, or the hyperfine contributions since they are inferred from the very precise measurement of the hyperfine splitting [140].

B.1 Bound–state QED test

The standard way to extract the $1S$ Lamb shift $L_{1S}^{\rm exp}$ relies on combinations of measured transition frequencies in hydrogen and deuterium. For simplicity we consider here only the measured $1S-2S$ and $2S-8S$ transition frequencies in hydrogen (see Eq. (B.1)):

$$\begin{aligned} \nu_{1S-2S} &\simeq \eta R_\infty(1-1/4) \qquad +L_{1S}-L_{2S} \\ \nu_{2S-8S} &\simeq \eta R_\infty(1/4-1/64) \quad +L_{2S}-L_{8S} \\ L_{2S} &= 1/8 L_{1S} + \varepsilon \; . \end{aligned} \tag{B.2}$$

In our simplified approach we can neglect L_{8S} and $\varepsilon = L_{1S} - 8L_{2S} = -187\,231(5)$ kHz [141]. Solving for L_{1S}, eliminating R_∞ and L_{2S}, gives

$$L_{1S}^{\rm exp} \simeq 2.1\; \nu_{1S-2S} - 6.7\; \nu_{2S-8S} \; . \tag{B.3}$$

Since ν_{1S-2S} and ν_{2S-8S} are known with a precision of 46 Hz [7] and 8.6 kHz [5], respectively, the $L_{1S}^{\rm exp}$ uncertainty is given by

$$\Delta L_{1S}^{\rm exp} \simeq -6.7\, \Delta\nu_{2S-8S} \simeq 57 \text{ kHz} \; . \tag{B.4}$$

Including all other transition frequency measurements in hydrogen and deuterium ($2S-8D$, $2S-4S$, $1S-3S$, $2S-6S$, and $2S-12S/D$) this uncertainty is reduced to $\Delta L_{1S}^{\rm exp} = 22$ kHz [5]:

$$L_{1S}^{\rm exp} = 8\,172\,840(22) \text{ kHz} \tag{B.5}$$

whereas the theoretical value is (cf. §A.9)

$$L_{1S}^{\rm the} = 8\,172\,901(4)(51) \text{ kHz} \tag{B.6}$$

for $r_{\rm p}$ =0.895(18) fm. The uncertainty of $L_{1S}^{\rm exp}$ is caused by the uncertainty in the measurement of the transitions frequencies (the $1S-2S$ excluded). The first error in $L_{1S}^{\rm the}$ refers to the theoretical accuracy, whereas the second one comes from the current uncertainty of $r_{\rm p}$ determined via electron–proton scattering experiments.

The relative accuracy of the comparison between theory and experiment ($T^{\rm the-exp}$) depends on their uncertainties and may be expressed as

$$T^{\rm the-exp} = \frac{\sqrt{(\Delta L_{1S}^{\rm exp})^2 + (\Delta L_{1S}^{\rm the})^2}}{L_{1S}^{\rm exp}} \; . \tag{B.7}$$

We assume that the uncertainties can be quadratically added. Presently this comparison is limited by the poor knowledge of the proton radius,

$$T^{\rm the-exp} = \frac{\left(\sqrt{22^2+51^2+4^2}\right) \text{ kHz}}{8\,172\,840 \text{ kHz}} \simeq \frac{56 \text{ kHz}}{8\,172\,840 \text{ kHz}} \simeq 7\times 10^{-6} \; . \tag{B.8}$$

A measurement of $r_{\rm p}$ from the μp Lamb shift will reduce the uncertainty related to the proton radius by about a factor of 20. Bound–state QED calculations can then be tested to a relative precision of

$$T^{\rm the-exp} = \frac{\left(\sqrt{22^2 + (51/20)^2 + 4^2}\right)\ \text{kHz}}{8\,172\,840\ \text{kHz}} \simeq \frac{23\ \text{kHz}}{8\,172\,840\ \text{kHz}} \simeq 3 \times 10^{-6}. \tag{B.9}$$

The limiting factor is then the uncertainty related with the experimental determination of the Lamb shift.[1] However the groups of F. Biraben at LKB in Paris and T. W. Hänsch at MPQ in Garching are presently remeasuring the $1S - 3S$ transition which will lead to a decrease of $\Delta L_{1S}^{\rm exp}$. The measurement of the proton radius in μp with 10^{-3} relative accuracy will thus open the way for a comparison of bound–state QED calculations in hydrogen with experiments at a level of

$$T^{\rm the-exp} \simeq \frac{51/20\ \text{kHz}}{8\,172\,840\ \text{kHz}} \simeq 3 \times 10^{-7} \tag{B.10}$$

which is a factor of 20 more accurate than presently possible.

B.2 Rydberg constant

Similar to the Lamb shift, the Rydberg constant R_∞ can be extracted by combining differences of measured transition frequencies. For simplicity we consider again only the $1S - 2S$ and $2S - 8S$ transitions. Solving Eq. (B.2) as function of R_∞ gives

$$R_\infty = (7\nu_{2S-8S} - \nu_{1S-2S})\,\frac{64}{57\eta}\,. \tag{B.11}$$

Its uncertainty is then given by

$$\Delta R_\infty \simeq \frac{7 \cdot 64}{57\eta}\,\Delta\nu_{2S-8S} \simeq 46\ \text{kHz} \tag{B.12}$$

which leads to a relative uncertainty of

$$\frac{\Delta R_\infty}{R_\infty} \simeq 1.8 \cdot \frac{\Delta\nu_{2S-8S}}{\nu_{2S-8S}} \simeq 2 \times 10^{-11}\,, \tag{B.13}$$

where ν_{2S-8S}=770 649 350.0120(86) MHz [5]. When all transitions measured in hydrogen and deuterium are accounted for in a least square adjustment, R_∞ is extracted with a relative accuracy of 7.7×10^{-12} equivalent to an absolute uncertainty of 16 kHz [5]. Note that R_∞ extracted from deuterium and hydrogen are compatible.

R_∞ can be determined in an independent way if the proton radius is measured in muonic hydrogen,and by making use of the predicted $L_{1S}^{\rm the}$. It can be extracted by subtracting from the measured $1S-2S$ transition frequency the expected Lamb shift ($L_{1S}^{\rm the}$) for the rms radius measured in muonic hydrogen. Consider the $1S - 2S$ transition frequency:

$$\nu_{1S-2S} = \frac{3}{4}\eta R_\infty + \frac{7}{8}L_{1S}\,. \tag{B.14}$$

[1] The uncertainty of $L_{1S}^{\rm exp}$ implicit in the 2002–CODATA adjustment is 18.5 kHz, which leads to $T^{\rm the-exp} = 2 \times 10^{-6}$.

Solving this equation for R_∞ gives

$$R_\infty = \frac{4}{3\eta} \cdot \nu_{1S-2S} - \frac{7}{6\eta} \cdot L_{1S} \tag{B.15}$$

and hence

$$\Delta R_\infty \simeq \frac{7}{6\eta} \cdot \Delta L_{1S} \simeq \frac{7}{6\eta} \cdot \left(\sqrt{(51/20)^2 + 4^2} \right) \text{ kHz} \simeq 5 \text{ kHz} \tag{B.16}$$

The measurement of the proton radius will hence lead to an improvement of the R_∞ accuracy by a factor of 16 kHz/5 kHz $\simeq 3$ limited by the uncertainty of the QED theory. Presently the least square adjustment of the CODATA group predicts an improvement by a factor of 6 of the R_∞ determination if the radius is measured in μp [142] .

B.3 Lamb shift and R_∞ uncertainty related to α and m/M

Up to now we have assumed all constants describing the hydrogen energy level to be known infinitely precisely except for R_∞ and r_p. In the following we consider briefly what is the error in the prediction of the Lamb shift caused by the current uncertainty of $\alpha = 7.297\,352\,568(24) \times 10^{-3}$ [1] and the uncertainty of R_∞ caused by the current uncertainty of the electron to proton mass ratio $m/M = 5.446\,170\,2173(25) \times 10^{-4}$ [1].

B.3.1 Lamb shift uncertainty caused by α

The main contribution to the Lamb shift is given by the one–loop self–energy of Eq. (A.21):

$$E_{SE}^{(1)} = m \frac{\alpha}{\pi} \frac{(Z\alpha)^4}{n^3} F(Z\alpha) \; . \tag{B.17}$$

A variation of α by a standard deviation $\Delta\alpha$ will causes a variation of the self–energy of

$$\frac{\Delta E_{SE}^{(1)}}{E_{SE}^{(1)}} = 5\frac{\Delta\alpha}{\alpha} + \frac{F'\Delta\alpha}{F} < 2 \times 10^{-8} \tag{B.18}$$

where $F'\Delta\alpha = -9 \times 10^{-9}$ [129]. The prime represents the derivative with respect to α. This means that the bound–state QED test is limited by the uncertainty of the fine structure constant to a level of 2×10^{-8} which is beyond the target accuracy of 3×10^{-7} achieved when r_p is measured with a relative accuracy of 10^{-3}.

B.3.2 Uncertainty of R_∞ caused by the uncertainty of m/M

We can write η as

$$\eta = \frac{m_r}{m} = \frac{mM}{m(M+m)} \simeq 1 - m/M \; . \tag{B.19}$$

In Eq. (B.16) the R_∞ uncertainty was calculated assuming η to be exactly known. Releasing this assumption the uncertainty of R_∞ starting from Eq. (B.15) takes the form

$$\Delta R_\infty = -\frac{4}{3\eta^2} \nu_{1S-2S} \cdot \Delta\eta - \frac{7}{6\eta} \cdot \Delta L_{1S} + \frac{7}{6\eta^2} L_{1S} \cdot \Delta\eta + \frac{4}{3\eta} \cdot \Delta\nu_{1S-2S} \; . \tag{B.20}$$

The last two terms are negligible and the second term corresponds to Eq. (B.16). The first term takes into account the main uncertainty to R_∞ originated by the uncertainty of the electron to proton mass ratio which may be expressed has

$$\left(\frac{\Delta R_\infty}{R_\infty}\right)^{\left(\frac{m}{M}\right)} \simeq \frac{\Delta\eta}{\eta} \simeq \frac{\Delta(m/M)}{\eta} \simeq 2.5 \times 10^{-13} \; . \tag{B.21}$$

This mean that the uncertainty of the m/M ratio affects the uncertainty of the Rydberg constant at a level of $\Delta R_\infty^{(m/M)} \simeq 0.6$ kHz which has to be compared with Eq. (B.16). Thus the uncertainty related to m/M does not affect the determination of R_∞ when r_p is measured with 10^{-3} relative accuracy.

Appendix C

Electron–proton scattering experiments

Independent of hydrogen spectroscopic measurements, size and charge distribution of the proton have been determined in the past from electron–proton scattering experiments. This Appendix presents a short sketch how to extract the proton radius from scattering experiments. The formalism required to describe these experiments is used to define the proton form factors and charge radius. The usual approach to extract the proton rms radius can be divided in three steps:

- Calculate the most accurate electron–proton differential cross sections at low momentum transfer which includes recoil and radiative corrections.
- Nuclear structure contributions are extracted by comparing measured and calculated cross sections.
- The resulting nuclear structure data are then fit with an appropriate function to get the rms charge radius.

C.1 Elastic scattering cross sections

The covariant four–vector proton current is [117]

$$j^{\mu} = e\bar{u}(k')\left[\gamma^{\mu}F_1(q^2) + \frac{\kappa}{2M}F_2(q^2)i\sigma^{\mu\lambda}q_{\lambda}\right]u(k)e^{-i(k'-k)\cdot x}\,, \tag{C.1}$$

where γ^{μ} and $\sigma^{\mu\lambda}$ are Dirac matrices, κ the proton anomalous magnetic moment, M the proton mass, $F_{1,2}$ the proton form factors with $F_1(0) = F_2(0) = 1$, $q = k' - k$ is the four–momentum transferred to the proton, and u, $\bar{u}$ are Dirac spinors. This is the most general four–vector form that can be constructed from k, k' and q. There are only two independent terms γ^{μ} and $\sigma^{\mu\lambda}q_{\lambda}$, and their coefficients are functions of q^2 which is the only independent scalar variable at the proton vertex. Hence F_1 and F_2 are two independent form factors. They parametrize our ignorance of the detailed structure of the proton. If the proton would be a point–like particle, then $\kappa = 0$ and $F_1(q^2) = 1$ for all q^2. Because $q^2 < 0$ for scattering kinematics, it is convenient to use the variable $Q^2 \equiv -q^2$. The differential cross section which describes the electron–proton elastic scattering in the laboratory frame is then

$$\left(\frac{d\sigma}{d\Omega}\right)_{\text{Rosenbluth}} = \sigma_{\text{Mott}}\, f_{\text{recoil}}\left[\left(F_1^2 + \frac{\kappa^2 Q^2}{4M^2}F_2^2\right)\cos^2\frac{\theta}{2} + \frac{Q^2}{2M^2}\left(F_1 + \kappa F_2\right)^2\sin^2\frac{\theta}{2}\right] \tag{C.2}$$

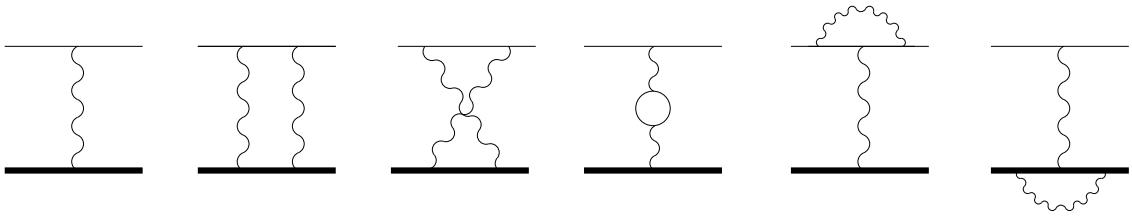

Figure C.1: Diagrams contributing to elastic $e-p$ scattering up to order α^3 in the cross section.

where θ is the scattering angle, σ_{Mott} the cross section for a spin–less point–like particle and $f_{\text{recoil}} = [1 + 2E_i \sin(\theta/2)/M]^{-1}$ the recoil factor. F_2, which primarily describes the magnetic properties of the nucleon, also contributes (in a minor way at small Q^2) to the charge distribution. In practice it is therefore better to use linear combinations of F_1 and F_2, and so the Sachs charge and magnetic form factors, G_E and G_M, are introduced [143]:

$$\begin{aligned} G_E &= F_1(Q^2) - \frac{\kappa Q^2}{4M^2} F_2(Q^2) \\ G_M &= F_1(Q^2) + \kappa F_2(Q^2)\,. \end{aligned} \tag{C.3}$$

No interference term $G_E G_M$ occurs in the cross section and Eq. (C.2) becomes

$$\left(\frac{d\sigma}{d\Omega}\right)_{\text{Rosenbluth}} = \sigma_{\text{Mott}}\, f_{\text{recoil}} \left\{ A_0(Q^2) + B_0(Q^2) \left[\frac{1}{2} + \left(1 + \frac{Q^2}{4M^2}\right) \tan^2 \frac{\theta}{2} \right] \right\}, \tag{C.4}$$

where

$$\begin{aligned} A_0(Q^2) &= \frac{G_E^2(Q^2)}{1 + \frac{Q^2}{4M^2}} && \equiv \widetilde{G}_E(Q^2) \\ B_0(Q^2) &= \frac{Q^2}{2M^2} \frac{G_M^2(Q^2)}{1 + \frac{Q^2}{4M^2}} && \equiv \frac{Q^2}{2M^2} \widetilde{G}_M(Q^2)\,. \end{aligned} \tag{C.5}$$

The form factors $\widetilde{G}_{E/M}$ have been proposed long ago but never popularly adopted. A_0 is associated only with the charge distribution whereas B_0 is associated only with the magnetic distribution.

The Feynman graphs contributing up to order α^3 to the elastic scattering cross sections are shown in Fig. C.1. In the leading order approximation (first diagram in Fig. C.1 which is proportional to α^2 in the cross section), the elastic electron–proton cross section in the laboratory frame, is given by Eq. (C.4). Calculations of the remaining diagrams of Fig. C.1 leads to corrections in order α. The total elastic cross section takes the form [144]

$$\left(\frac{d\sigma}{d\Omega}\right)_{\text{elastic}} = \left(\frac{d\sigma}{d\Omega}\right)_{\text{Rosenbluth}} (1 + \alpha R) \tag{C.6}$$

where R represents the radiative corrections which depends on the initial and final momenta of electron and proton.

Internal Bremsstrahlung processes which are diagrammatically shown in Fig. C.2 have to be taken into account. In electron–proton scattering soft photons may be emitted, with such a low energy (infrared divergence) that they are not detectable. The energy resolution ΔE^{res} of the detector used to measure the scattered electron energy decides if this emission of a soft photon has to be considered as an elastic or an inelastic process.

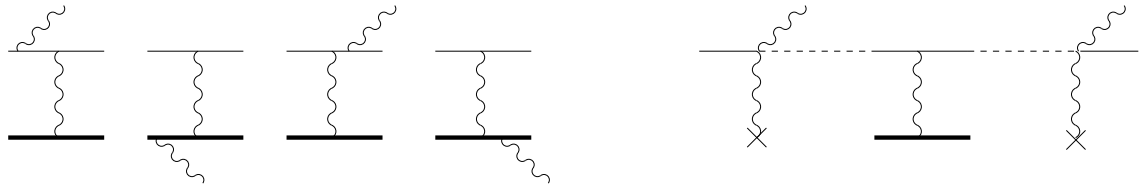

Figure C.2: The first four graphs represent internal Bremsstrahlung whereas the last describes the external Bremsstrahlung. Thin and thick straight line represent the electron and the proton, respectively.

The Bremsstrahlung cross section for the emission of a soft photon in the strong field of an external static field may be expressed as [144]

$$\left(\frac{d\sigma}{d\Omega}\right)_{\text{Bremsstrahlung}} = \alpha B_{\text{int}} \left(\frac{d\sigma}{d\Omega}\right)_{\text{Rosenbluth}} \tag{C.7}$$

where $B_{\text{int}} = B_{\text{int}}(\Delta E^{\text{res}})$ depends also on the detector resolution. The measured cross section is hence the incoherent (distinguishable process) sum of elastic and internal Bremsstrahlung processes for photons emitted with energy less than ΔE:

$$\begin{aligned}\left(\frac{d\sigma}{d\Omega}\right)_{\text{exp}} &= \left(\frac{d\sigma}{d\Omega}\right)_{\text{elastic}} + \left(\frac{d\sigma}{d\Omega}\right)_{\text{Bremsstrahlung}} \\ &= \left(\frac{d\sigma}{d\Omega}\right)_{\text{Rosenbluth}} [1 + \alpha(R + B_{\text{int}})] \ .\end{aligned} \tag{C.8}$$

Since the photon is massless both terms R and B_{int} are divergent. However these divergences cancel out in the sum $R + B_{\text{int}}$ which is always finite and defined. It was customary (see *e.g.,* Refs. [145, 146]) to generalize Eq. (C.8) to approximately account for all orders in α [147]

$$\left(\frac{d\sigma}{d\Omega}\right)_{\text{exp}} = \left(\frac{d\sigma}{d\Omega}\right)_{\text{Rosenbluth}} e^{\alpha(R+B_{\text{int}})} \ . \tag{C.9}$$

This generalization is not accepted by all authors. Only for the infrared part it is correct. For the vacuum polarization in order α^2 the uncertainty of this generalization may be of the order of 20% [29]. This is causing an increase of the uncertainty of the proton radius extracted from scattering experiments.

C.2 Measurements and extraction of the nuclear structure

Experimentally electrons are scattered by a target of liquid hydrogen. Initial momentum p and momentum of the scattered electron (p') are measured together with the deflection angle θ. Since the position of the elastic peak is well defined, $W^2 \equiv (k')^\mu (k')_\mu = M^2$, both the number of events $N(\Delta p', \Delta\theta)$ and the acceptance function $F(\Delta p', \Delta\theta)$ were converted to functions of the single variable $W^2 = M^2 + 2M\nu - Q^2$ where $\nu = p_0 - p'_0$. The differential cross section is then calculated in terms of measured quantities and correction factors as follows [145]:

$$\left(\frac{d\sigma}{d\Omega}\right)_{\text{meas}} = \frac{1}{Q_{\text{eff}}} \frac{1}{n} \frac{X_{\text{res}}}{R_{\text{corr}}} \int^{W^2_{\text{cutoff}}} \frac{N(W^2)}{F_{\text{acc}}(W^2)} \, dW^2 \tag{C.10}$$

where Q_{eff} gives the effective incident electron charge per kinematic point, and n the number of target nuclei per cm^2. The integral over W^2 gives the total number of detected

electrons, with the spectrometer acceptance up to an arbitrary cutoff value $W^2_{\rm cutoff}$. This cutoff is set large enough to include as much as possible of the elastic peak, yet small enough to avoid background from other processes. $F_{\rm acc}$ is the event acceptance function which account for various physical apertures, software cuts *etc.*. The factor $X_{\rm res} \simeq 1$ corrects for the number of events expected to be above $W^2_{\rm cutoff}$ due to finite energy resolution of the detectors. The factor $R_{\rm corr} = e^{\alpha(R+B_{\rm int}+B_{\rm ext})}$ represents the radiative corrections. It includes the QED and internal Bremsstrahlung corrections above discussed, but also corrections due to external Bremsstrahlung $B_{\rm ext}$ (not discussed above). This external Bremsstrahlung shown in Fig. C.2 can be understood as the straggling of the electron before and after the actual electron–proton scattering.

The size of the radiative corrections is $R_{\rm corr} \in [0.7 - 0.85]$ [145] depending on energy ($1.5 - 8$ GeV) and scattering angle. Additionally in the recent reevaluations of scattering experiments by Rosenfelder [148] and Sick [6], Coulomb corrections Δ_C calculated to the second order Born approximation are included. These Coulomb corrections take into account the distortion of the plane wave in the electrostatic field of the proton. The Coulomb corrections are small and positive, ranging from $(0.4 - 0.9)\%$ which is roughly the size of the experimental errors, and its inclusion increases the deduced proton radius by about 0.01 fm.

The interpretation of electron–nucleon scattering data in form of form factors is based on the one–photon exchange approximation. The measured cross sections are corrected for higher order contributions via $R_{\rm corr}$ leading to the measured one–photon exchange contribution, which can be compared with the Rosenbluth formula including Coulomb corrections [148]

$$\left(\frac{d\sigma}{d\Omega}\right)_{\rm meas} = \sigma_{\rm Mott}\, f_{\rm recoil} \left\{ A_0(Q^2) + B_0(Q^2) \left[\frac{1}{2} + \left(1 + \frac{Q^2}{4M^2}\right) \tan^2\frac{\theta}{2}\right]\right\} (1 + \Delta_C) \ . \tag{C.11}$$

C.3 Structure functions

Model–independent or model–dependent proton structure functions have been used to extract the rms–radius. The Standford rms radius of 0.805 fm [149] was extracted using an ("invalid") dipole form factor for low and high momentum data. Extraction of rms–radii which are model–independent is possible when expanding $G_E(Q^2)$ in terms of moments $\langle r^2\rangle$, $\langle r^4\rangle \ldots$,

$$G_E(Q^2) = 1 + \frac{Q^2\langle r^2\rangle}{6} - \frac{Q^4\langle r^4\rangle}{120} + \cdots \ . \tag{C.12}$$

At very small Q^2 in principle one could hope to neglect the Q^4 and higher terms, so that the $\langle r^2\rangle$–term can be determined without a specific form factor model. However small systematic errors in the normalization of the measured cross sections have a strong influence on the extraction of the rms–radius. The measured cross section leads to the unnormalized expansion

$$G_E(Q^2) = a_0 + a_1 Q^2 + a_2 Q^4 + \cdots \tag{C.13}$$

with $a_0 \simeq 1$, but not exactly equal to 1 (*e.g.*, a_0(Mainz) = 1.0014 [121], a_0(Orsay) = 1.020 [150], and a_0(Saskatoon) = 1.008 [151]). The true value of the proton radius has then to be defined as

$$r_{\rm p}^2 = \langle r^2\rangle = \frac{a_1}{6a_0} \ . \tag{C.14}$$

The normalization problems are experimentally connected with the uncertainty of the density of scattering centers n in Eq. (C.10), which varies also as a function of the incident electron beam current (target heating).

To reduce the influence of the normalization in the determination of the proton rms–radius it is necessary to include data at higher Q^2 which are sensitive to higher moments. For an exponential charge distribution of the proton the higher moments are increasing with order, $\langle r^4\rangle = 2.5\,\langle r^2\rangle^2$, $\langle r^6\rangle = 11.6\,\langle r^2\rangle^3$, giving large contributions to $G_E(Q^2)$.

There is no region in Q^2 space where the $\langle r^2\rangle$ term dominates the finite size to be able to extract the proton radius with, say, a 2% accuracy. Similarly there is no region in Q^2 space where the $\langle r^4\rangle$ moment can be determined without going into difficulty with the $\langle r^6\rangle$ term, and so on. The convergence radius of this polynomial expansion is limited by $Q < 1.4$ fm^{-1} [6].

To reduce these difficulties related to higher moments of the model–independent form factor, in the recent reanalysis of all scattering data Sick [6] made use of the continuous–fraction (CF) expansion

$$G_E(Q^2) = \frac{G_M(Q^2)}{\mu_p} = \cfrac{1}{1 + \cfrac{Q^2 b_1}{1 + \cfrac{Q^2 b_2}{1 + \cdots}}} \tag{C.15}$$

where $\mu_p = 2.793$ is the proton magnetic moment. The CF expansion was introduced to find a function in terms of its moments and to accelerate the problem of poorly converging series. The coefficient of the polynomial expansion a_i are related to the coefficients of the CF expansion b_i by $a_0 = b_1^2$, $a_1 = b_1^2 + b_1 b_2, \ldots$.

The determination of the rms radius by Sick used "all" the world electron–proton scattering data for $Q < 4$ fm^{-1}. Both charge and magnetic form factors $G_{E/M}$ have been parametrized with Eq. (C.15) with 5 parameters b_i, and the cross sections were corrected for Coulomb distortion. The final result of the rms charge radius of the proton is $r_{\rm p} = 0.895(18)$ fm. The uncertainty of ± 0.018 fm accounts for the systematic uncertainty (± 0.013 fm) dominated by the normalization, and for the fitting uncertainty (± 0.010 fm). The fitting uncertainty is related to statistics and to the error from the CF expansion which depends on the number of parameters and the size of the Q-region used.

Appendix D

Proton radius

In the first part of this Appendix we want to check if the definition of the proton radius used in scattering experiment is consistent with the definition in atomic physics. The reference source for these considerations is the article of Friar *et al.* [152]. The second part points out some problems related with the definition of the proton radius.

D.1 Proton radius in scattering experiments

We have seen in §C.1 that there are several options to describe the proton structure in terms of form factors: (F_1, F_2) in Eq. (C.1), (G_E, G_M) in Eq. (C.3) and ($\widetilde{G}_E$, $\widetilde{G}_M$) in Eq. (C.5). The rms charge proton radius is defined in the Breit frame by [153]

$$\langle r^2 \rangle_{\rm ch} = \int d\mathbf{r}\, r^2 \rho(\mathbf{r}) \tag{D.1}$$

where ρ is the $0^{\rm th}$ component of the four–vector j^μ defined in Eq. (C.1). The various charge mean square radii corresponding to the various form factors are given by

$$\begin{aligned} \langle r^2 \rangle_{\rm ch} &= -6\widetilde{G}'_E(0) \\ \langle r^2 \rangle_{\rm E} &= -6G'_E(0) \\ \langle r^2 \rangle_{\rm F} &= -6F'_1(0)\,, \end{aligned} \tag{D.2}$$

where the prime represents the derivative in d/dQ^2. The various mean square radii differ by amounts of the order $(1/M^2) \sim 0.044$ fm, and are formally identical in the nonrelativistic limit. Comparing the definition of the various form factors gives

$$\begin{aligned} \langle r^2 \rangle_{\rm ch} &= \langle r^2 \rangle_{\rm E} + \frac{3}{4M^2} \\ \langle r^2 \rangle_{\rm E} &= \langle r^2 \rangle_{\rm F} + \frac{3\kappa}{2M^2}\,. \end{aligned} \tag{D.3}$$

$\langle r^2 \rangle_{\rm E}$ is often called the proton radius. The difference between $\langle r^2 \rangle_{\rm ch}$ and $\langle r^2 \rangle_{\rm E}$ is given by the so called Darwin–Foldy term ($E_{DF} = 3/(4M^2)$). Although this term is part of the charge density it is by convention considered as a kinematic factor.

D.2 Proton radius in atomic hydrogen

The hydrogen energy level described by Eq. (A.12), contains a contribution which is proportional to δ_{l0}

$$\frac{(Z\alpha)^4 m_r^3}{2n^3 M^2}\delta_{l0}\,. \tag{D.4}$$

This expression has to be compared with the contribution which describes the leading–order nuclear–size correction:

$$\frac{2(Z\alpha)^4 m_r^3}{3n^3}\langle r^2\rangle\delta_{l0}\,. \tag{D.5}$$

Replacing $\langle r^2\rangle$ by $\frac{3}{4M^2}$ in Eq. (D.5) gives Eq. (D.4). This means that the Darwin–Foldy term in the hydrogen atom is by convention considered not as a part of the finite size but as a recoil correction.

Therefore both in the scattering experiment and in the atomic system the charge radius is defined in a consistent way with respect to each other: by convention, it neglects the Darwin–Foldy term. Hence $r_{\rm p}$ which is used all through this work is meant to be

$$r_{\rm p}^2 \equiv \langle r^2\rangle_{\rm E} = \langle r^2\rangle_{\rm ch} - \frac{3}{4M^2}\,. \tag{D.6}$$

D.3 Problems related to the definition of the proton radius

QED corrections make the definition of the proton radius questionable. The electron may be considered to have also a finite size due to QED corrections. It is customary to separate the various contributions which may be calculated in the framework of QED from the definition of the proton radius, *e.g.,* the proton self–energy may be considered to contribute to a part of the proton charge radius, or may be considered as a QED correction. Sometimes a clear separation and definition of corrections which have (or not) to be included in the form factors, *i.e.,* in the rms charge radius is a problem, in particular for the hadronic corrections.

A measurement of the proton radius with an accuracy better than 1% poses some theoretical questions about the definition of the proton radius. The problem of a proper definition of the proton radius was discussed by Pachucki in Ref. [18]. It resulted that a definition of $r_{\rm p}$ via the Sachs form factor is problematic since it define $r_{\rm p}$ only in leading order of the electromagnetic coupling α. Beyond this order, the form factor becomes infrared divergent. Very recently this problem was addressed by Pineda [23] within an effective field theory framework, connecting the physics at the hadronic scale (heavy–barion effective theory) with the physics at the atomic scale (potential non–relativistic QED). A natural definition of the proton radius can be given as a matching coefficient of the effective field theory, which does not depend on the scheme and scale on which the computation is performed. This results in a clear dependence of any observable on $r_{\rm p}$.

The general conclusion is: what is considered contributing to the form factors and what is considered a QED correction has to be consistently treated in hydrogen, muonic hydrogen and scattering experiments.

Appendix E

$2S - 2P$ transition probability

In this Appendix the probabilities for the various dipole transitions between the $2S$ and the $2P$ states of muonic hydrogen (see Fig. 2.1) are calculated, in order to chose the transition with the largest transition probability and to deduce the required laser intensity.

E.1 $2S - 2P$ transition probabilities and matrix elements

The transition between atomic states with absorption or emission of a photon is described by quantum mechanics. To calculate the rate of absorption of light with frequency ω from an initial state $|a\rangle$ with energy E_a to a final state $|b\rangle$ with energy E_b, we may use the "golden rule":

$$W_{ab} = \frac{2\pi}{\hbar} \left|\langle b|H_{\text{int}}|a\rangle\right|^2 \rho(\omega) \tag{E.1}$$

with

$$\rho(\omega) = \frac{1}{\hbar}\left(\frac{\Gamma}{2\pi}\right) \frac{1}{(\omega-\omega_0)^2 + (\Gamma/2)^2} \tag{E.2}$$

where $\Gamma = \Gamma_a + \Gamma_b$ is the total transition width and $\omega_0 = (E_b - E_a)/\hbar$ the resonance frequency. The Hamilton operator H_{int} which describes the muon–photon field interaction is

$$H_{\text{int}} = -\frac{e}{mc}\mathbf{p}\cdot\mathbf{A} + \frac{e^2}{2mc}\mathbf{A}^2 \tag{E.3}$$

Since the laser electric field is small compared to the atomic field the second term (order $\mathbf{A}^2$) can be neglected. In dipole approximation (wavelength of the transition much greater than the atomic size) the matrix element takes the form

$$\left|\langle b|H_{\text{int}}|a\rangle\right|^2 = 2\pi\hbar\alpha\, I \left|\langle b|\epsilon\cdot\mathbf{r}|a\rangle\right|^2 \tag{E.4}$$

where ϵ is the laser polarization, $\mathbf{r}$ is the coordinate operator of the muon, α the fine structure constant and I the laser intensity. Inserting Eqs. (E.4) and (E.2) in Eq. (E.1) gives a transition probability of

$$W_{ab} = \frac{2\pi}{\hbar}\alpha I_0 \frac{\Gamma}{(\omega-\omega_0)^2 + (\Gamma/2)^2} \left|\langle b|\epsilon\cdot\mathbf{r}|a\rangle\right|^2 . \tag{E.5}$$

The atomic states $|a\rangle$ and $|b\rangle$ are eigenstates of the total angular momentum $\mathbf{F} = \mathbf{L} + \mathbf{S} + \mathbf{I}$ where $\mathbf{L}$ is the orbital momentum, and $\mathbf{S}$, $\mathbf{I}$ are the muon and proton spin, respectively. These eigenstate may then be expressed as

$$|\beta, F, M\rangle = \sum_{M_S\, M_I\, M_L} CG \cdot |S, M_S\rangle\, |I, M_I\rangle\, |n, L, M_L\rangle \tag{E.6}$$

where $\beta=(n,L,S,I)$, $|n,L,M_L\rangle = R_{nL}(r)Y_{LM_L}(\theta,\phi)$ is the Schrödinger wave–function corresponding to the state described by the quantum numbers n,L,M_L which factorize in a radial $R_{nL}(r)$ and a spherical $Y_{LM_L}(\theta,\phi)$ component, and CG are Clebsch–Gordan coefficients. In the following we want to calculate the transition probability between eigenstates of the total angular momentum F' and F,

$$W(F',F)=\frac{2\pi}{\hbar}\alpha I_0\frac{\Gamma}{(\omega-\omega_0)^2+(\Gamma/2)^2}|\langle F|\epsilon\cdot\mathbf{r}|F'\rangle|^2\,. \tag{E.7}$$

Since the Zeeman component of the transition are not individually resolved the transition probability between the initial and final state has to take into account all possible transitions between Zeeman sublevels. Thus the probability of a transition $F'\to F$ can be obtained by summing Eq. (E.7) with respect to M and averaging over M'

$$W(F',F)=\frac{1}{N(F')}\sum_{M,M'}N(F'M')\,W(F'M',FM) \tag{E.8}$$

where $N(F')$ is the total population of the initial state and $N(F'M')$ the population of the initial state sublevels. For statistical population of the M'-sublevels it follows that

$$W(F',F)=\frac{1}{2F'+1}\sum_{M,M'}W(F'M',FM)\,. \tag{E.9}$$

Combining Eq. (E.9) with Eq. (E.5) it may be shown that

$$|\langle F|\epsilon\cdot\mathbf{r}|F'\rangle|^2=\frac{1}{2F'+1}\sum_{M,M'}|\epsilon\cdot\langle\beta FM|\mathbf{r}|\beta'F'M'\rangle|^2\,. \tag{E.10}$$

With the aid of the Wigner–Eckart theorem, we can factorize any matrix element for any tensor operator $Q_m^{(\lambda)}$ of order λ

$$\begin{aligned}\langle\beta FM|Q_m^{(\lambda)}|\beta'F'M'\rangle&=\frac{(F'M',\lambda m|FM)}{\sqrt{2F+1}}\langle\beta F||\mathbf{Q}^{(\lambda)}||\beta'F'\rangle\\&=(-1)^{J-M}\begin{pmatrix}F&\lambda&F'\\-M&m&M'\end{pmatrix}\langle\beta F||\mathbf{Q}^{(\lambda)}||\beta'F'\rangle\,,\end{aligned} \tag{E.11}$$

where $(F'M',\lambda m|FM)$ are Clebsch–Gordan coefficients which can be written as $3j$–symbols, and $\langle\beta F||\mathbf{Q}^{(\lambda)}||\beta'F'\rangle$ is the reduced matrix element. Using the orthogonality properties of the $3j$–symbols we obtain

$$\begin{aligned}\sum_{MM'}|\langle\beta FM|Q_m^{(\lambda)}|\beta'F'M'\rangle|^2&=|\langle\beta F||\mathbf{Q}^{(\lambda)}||\beta'F'\rangle|^2\sum_{MM'}\begin{pmatrix}F&\lambda&F'\\-M&m&M'\end{pmatrix}^2\\&=\frac{1}{2\lambda+1}\,|\langle\beta F||\mathbf{Q}^{(\lambda)}||\beta'F'\rangle|^2\,.\end{aligned} \tag{E.12}$$

Expression (E.12) does not depend on the choice of m, *i.e.,* it is valid for any component of the dipole vector $\mathbf{r}$ which means that this result is independent of laser polarization. Since $\mathbf{r}$ commutes with $\mathbf{I}$ and $\mathbf{S}$ it can be shown that

$$\begin{aligned}|\langle\beta F||\mathbf{Q}^{(\lambda)}||\beta'F'\rangle|^2&=(2F+1)(2F'+1)(2J+1)(2J'+1)\\&\begin{Bmatrix}J&F&I\\F'&J'&\lambda\end{Bmatrix}^2\begin{Bmatrix}L&J&S\\J'&L'&\lambda\end{Bmatrix}^2|\langle\beta L||\mathbf{Q}^{(\lambda)}||\beta'L'\rangle|^2\end{aligned} \tag{E.13}$$

where the brackets represent the $6j$–symbols. The reduced matrix element in L-basis can be expressed as (Wigner–Eckart theorem)

$$\langle \beta L||\mathbf{Q}^{(\lambda)}||\beta' L'\rangle = \frac{\sqrt{2L+1}}{(L'M'_L, \lambda m|LM_L)} \langle \beta L M_L|Q_m^{(\lambda)}|\beta L' M'_L\rangle \ . \tag{E.14}$$

The matrix element on the right side of Eq. (E.14) can be immediately calculated. The dipole operator $\mathbf{r}$ has rank 1 and for $m = 0$ is $Q_0^{(1)} = z$, and hence

$$\langle \beta L M_L|Q_0^{(1)}|\beta' L' M'_L\rangle = \langle nLM_L|z|n'L'M'_L\rangle = \int d^3r\ \Psi_{nLM_L}(\mathbf{r})\ z\ \Psi_{n'L'M'_L}(\mathbf{r}) \ . \tag{E.15}$$

Following the various steps from Eq. (E.10) to Eq. (E.15) the matrix element $|\langle F|\epsilon\cdot\mathbf{r}|F'\rangle|^2$ can be calculated for all $2S-2P$ transitions. The results are given in Table E.1.

However Eq. (E.13) is valid only if both F and J are good quantum numbers. This is the case for $F = 2$ and $F = 0$ states. For states with $F = 1$ the value of the matrix elements given in Table E.1 has to be multiplied by the factor Φ_0 [104] since J is not a good quantum number. Mixing occurs within states with $F = 1$.

For our experiment we have chosen the $2S^{\mathrm{F}=1}_{1/2} - 2P^{\mathrm{F}=2}_{3/2}$ transition since both the initial population $(2F'+1)$ and the matrix element are favorable relative to the other transitions. The initial state being a triplet state assures that 3/4 of the population of the $2S$ state are at disposition for the laser experiment. This assumes that the population is statistically distributed among the $2S$ substates (more details are given in §6.5).

E.2 $2S-2P$ linewidth

The transition linewidth $\Gamma = \Gamma_a + \Gamma_b$ is given by the sum of the individual states linewidth, given by the lifetimes of the corresponding states. The total probability for a spontaneous transition from $|a\rangle$ to $|b\rangle$ is in the dipole approximation [154]

$$A_{ab} = \frac{4}{3}\frac{e^2\omega_{ab}^3}{\hbar c^3}|\langle b|\mathbf{r}|a\rangle|^2 \ . \tag{E.16}$$

Summing Eq. (E.16) over all states $|b\rangle$ which have energy less than that of the initial state $|a\rangle$ one arrives at a total probability per unit time that the state is vacated through light

Table E.1: Matrix elements in dipole approximation for the various possible $2S-2P$ transitions in muonic hydrogen. The last column represents a multiplicative factor Φ_0 given in Ref. [104] which considers possible mixing between states with the same F but different J.

Initial state	Final state	$\lvert\langle F\lvert\epsilon\cdot\mathbf{r}\rvert F'\rangle\rvert^2$	Φ_0
$2S^{\mathrm{F}=0}_{1/2}$ $\rightarrow$	$2P^{\mathrm{F}=1}_{1/2}$	$3a_\mu^2$	0.47
	$2P^{\mathrm{F}=1}_{3/2}$	$6a_\mu^2$	1.27
$2S^{\mathrm{F}=1}_{1/2}$ $\rightarrow$	$2P^{\mathrm{F}=0}_{1/2}$	a_μ^2	—
	$2P^{\mathrm{F}=1}_{1/2}$	$2a_\mu^2$	0.47
	$2P^{\mathrm{F}=1}_{3/2}$	a_μ^2	1.27
	$2P^{\mathrm{F}=2}_{3/2}$	$5a_\mu^2$	—

emission

$$A_a = \sum_{E_b<E_a} \frac{4}{3}\frac{e^2\omega^3}{\hbar c^3}|\langle b|\mathbf{r}|a\rangle|^2 \ . \tag{E.17}$$

If one adds the intensities of the transitions from a certain state $|n'F'M'\rangle$ to all sub–states $|nFM\rangle$ disregarding the direction of polarization of the emitted photon, one finds that the sum is independent of M':

$$\begin{aligned}\sum_{Mm} |\langle nFM|Q^1_m|n'F'M'\rangle|^2 &= |\langle nF||Q^1||n'F'\rangle|^2 \sum_{Mm} \begin{pmatrix} F & 1 & F' \\ -M & m & M' \end{pmatrix}^2 \\ &= |\langle nF||Q^1||n'F'\rangle|^2 \ \frac{1}{2F'+1}\end{aligned} \tag{E.18}$$

where we made use of the Wigner–Eckard theorem and the orthogonality properties of the $3j$–symbols.

We consider in the following spontaneous decay from the initial state with $F'=2$. Since $A_{ab}\sim\omega_{ab}^3$, the spontaneous transition rate from the $2P$ state to the $2S$ state is negligible compared to a transition rate from the $2P$ state to the ground state. The selection rules $\Delta F=0,\pm1$, $\Delta M=0,\pm1$ (with $F+F'\geqslant 1$) predict that starting from $F'=2$ only decays to states with $F=1$ are allowed. Combining Eq. (E.13) with Eq. (E.18), calculating the reduced element in L–basis and inserting the numerical values related to the the $2P^{\mathrm{F}=2}_{3/2}-1S^{\mathrm{F}=1}_{1/2}$ transition, results in

$$\sum_{Mm} |\epsilon_m \ \langle n=1,F=1,M|r_m|n'=2,F'=2,M'\rangle|^2 = \frac{1}{3}(R^{10}_{21})^2 = \frac{1.67}{3}\ a_\mu^2 \tag{E.19}$$

where $(R^{nl}_{n'l'})^2 = (\int dr\ R_{nl}R_{n'l'}\,r^3)^2$ [154] is the integral over the radial component of the Schrödinger wave function. Note that this result is equivalent if fine and hyperfine structure would have been neglected. The total transition probability of Eq. (E.17) for the $2P^{\mathrm{F}=2}_{3/2}$ state is then

$$A_{2P} = \frac{4}{3}\frac{\alpha\omega^3}{c^2}\frac{1.67}{3}\ a_\mu^2 \simeq 117\times10^9\ \mathrm{s}^{-1} \ . \tag{E.20}$$

This corresponds to a $2P$ lifetime τ_{2P} and a linewidth Γ_ν at FWHM of

$$\tau_{2P} \ \simeq \ 8.5\times10^{-12}\ \mathrm{s} \tag{E.21}$$

$$\Gamma_\nu \ = \ \frac{A_{2P}}{2\pi} \simeq 18.6\ \mathrm{GHz} \tag{E.22}$$

The spontaneous transition rate of $1.5\times10^3\ \mathrm{s}^{-1}$ [155] from the $2S$ state is negligible since it can decay only via a two–photon decay. For comparison the $2P$ state in hydrogen has a linewidth of 99.8 MHz.

E.3 Laser intensity

In this section the required laser intensity is calculated. The transition rate (transition probability per unit time) is given by Eq. (E.5) where the matrix element for the $2S^{\mathrm{F}=1}_{1/2} - 2P^{\mathrm{F}=2}_{3/2}$ transition is $|\langle b|\epsilon\cdot\mathbf{r}|a\rangle|^2 = 5\,a_\mu^2$ (see Table E.1) and $\Gamma = 2\pi\Gamma_\nu = 117\times10^9\ \mathrm{s}^{-1}$. On resonance the transition rate is then

$$W_{ab} = \frac{40\pi}{\hbar}\alpha\frac{I}{\Gamma}a_\mu^2\,. \tag{E.23}$$

For $\Gamma \gg W_{ab}$ (no Rabi oscillations), and short laser illumination time compared with the $2S$ lifetime, the probability that after an illumination time t the transition already occurred ($w_{ab}(t)$) is given by the following differential equation

$$\frac{dw_{ab}(t)}{dt} = W_{ab}\big(1 - w_{ab}(t)\big) \tag{E.24}$$

with initial condition $w_{ab}(0) = 0$, since we assume that we start with one atom in the initial state. For a constant laser intensity I of time duration T

$$w_{ab}(T) = 1 - e^{-W_{ab}\,T}\,. \tag{E.25}$$

It is of practical use to introduce the laser fluence defined as

$$F = \frac{E}{A} = \int_0^T I(\omega,t)\,dt \tag{E.26}$$

where A is the beam surface and E the laser energy. The transition probability may be expressed as function of the fluence as

$$w_{ab}(T) = 1 - e^{F/F_s} \tag{E.27}$$

with

$$F_s = \frac{\hbar}{8\pi\alpha}\frac{\Gamma}{5a_\mu^2} = 16.5\ \mathrm{mJ/cm^2}\,. \tag{E.28}$$

The required fluence to induce a transition with a probability of $w_{ab} = 1 - e^{-1} \simeq 63\%$ is given by F_s. In this work we call F_s the saturation fluence.

The saturation energy which is inversely proportional to the transition strength depends on the mass of the orbiting particle m of the atomic system as

$$F_s \sim \frac{\Gamma}{a_\mu^2} \sim \frac{m}{1/m^2} = m^3\,. \tag{E.29}$$

The muonic transition is hence a factor 10^7 weaker than the corresponding transition in hydrogen.

E.4 Two–level system

The starting point for the calculation of the transition probability in §E.1 was given by the golden rule. In this section we start from the time–dependent Schrödinger equation which allows us to follow the evolution of both the $2S$ and $2P$ states as function of time. Rabi oscillations as well as lifetimes of the concerned levels are taken into account in this

model. In the rotating wave approximation (terms with $e^{\omega_0+\omega}$ are neglected, see below) the solution of the time dependent Schrödinger equation leads to the two following differential equations for the amplitudes a and b [156]

$$\begin{aligned}\dot{a} &= -\frac{1}{2}\gamma_a a + \frac{V^*}{\hbar i}e^{i\Omega t}b \\ \dot{b} &= -\frac{1}{2}\gamma_b b + \frac{V}{\hbar i}e^{-i\Omega t}a\end{aligned} \tag{E.30}$$

with

$$\begin{aligned}\omega_0 &= \omega_b - \omega_a = (E_b - E_a)/\hbar \\ \Omega &= \omega - \omega_0 \\ V &= \langle b|H_{\text{int}}(0)|a\rangle \\ &= -i\sqrt{2\pi\hbar\alpha I_0}\langle b|\epsilon\cdot\mathbf{r}|a\rangle\end{aligned}$$

where V is the matrix element, γ_a and γ_b the decay constants of the states $|a\rangle$ and $|b\rangle$, respectively. The measured laser bandwidth of 0.7 GHz (cf. §4.8) is small compared to the atomic linewidth. The assumption of monochromatic laser light assumed in Eq. (E.30) is therefore justified. These are the basic equations which have to be solved to obtain the population amplitudes $a(t)$ and $b(t)$. The probability to find an atom after the time t in state $|a\rangle$ or $|b\rangle$ is then $|a(t)|^2$ or $|b(t)|^2$, respectively.

Equations (E.30) have been numerically integrated for a fully occupied $2S$ state at time $t = 0$, *i.e.*, for initial conditions $a(0) = 1$, $b(0) = 0$. The intensity of the laser light is assumed to have an exponential decay time $\tau = 140$ ns. As shown in §4.11 this roughly corresponds to the intensity time distribution of the light which illuminates the muonic atom. The observation of the 1.9 keV photon which corresponds to the $2P-1S$ transition is considered in the analysis as laser–induced x ray only if it occurs within a given time window termed "laser time window" (cf. §6.2). Figure E.1 (Left) shows the probability that the laser light induces a $2S-2P-1S$ transition as function of the laser detuning for a laser

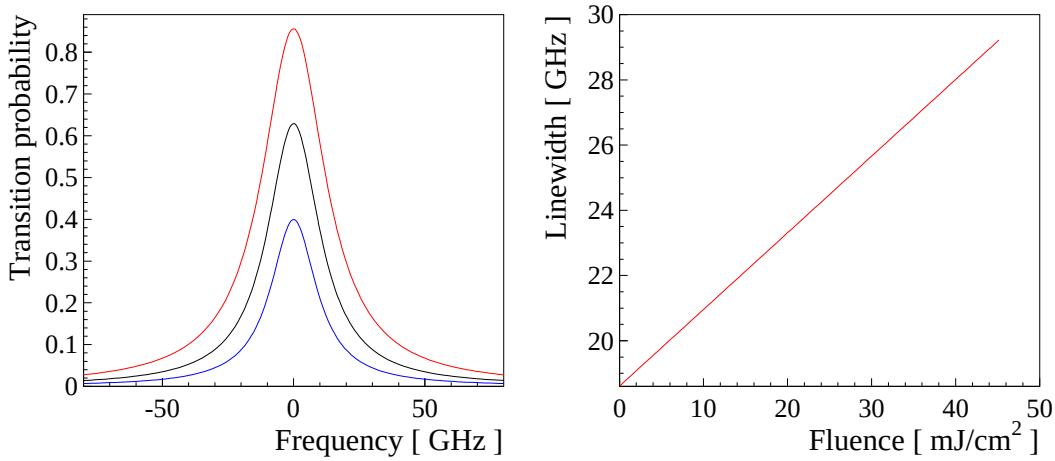

Figure E.1: (Left): $2S-2P$ resonance curve. The transition probability is plotted versus laser detuning for various laser fluences (top to bottom: 45.6 mJ/cm^2, 22.8 mJ/cm^2 and 11.4 mJ/cm^2) and a laser time window of 200 ns. (Right): $2S-2P$ linewidth for various fluences and for a laser time window of 200 ns.

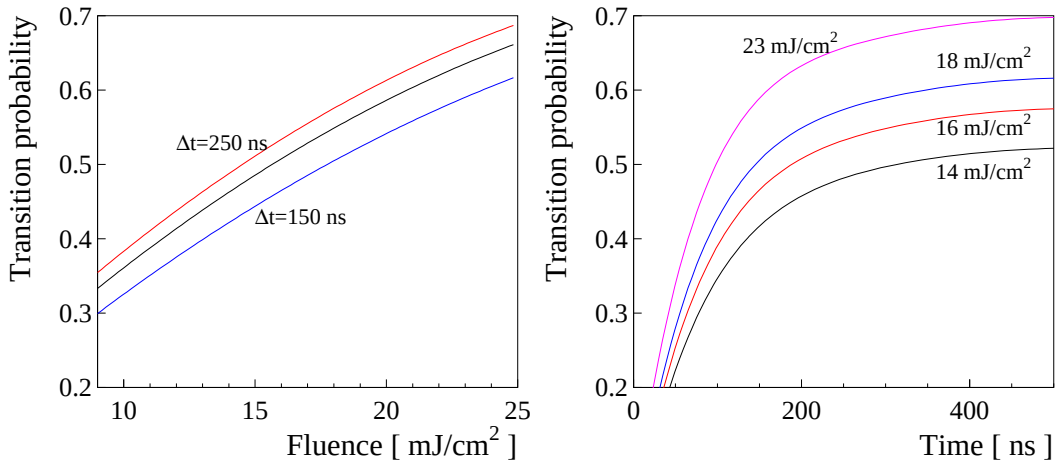

Figure E.2: (Left): $2S-2P$ transition probability as a function of the laser fluence for three different illumination times, 150, 200 and 250 ns, for zero detuning. (Right): $2S-2P$ transition probability as a function of the observation time for four different laser fluences and zero detuning.

time window of 200 ns and for various fluences. Figure E.1 (Right) shows the saturation broadening, *i.e.,* the width of the $2S-2P$ resonance as a function of the laser light fluence. With decreasing fluence the linewidth is approaching the natural linewidth of 18.6 GHz. In Fig. E.2 (Left) the $2S-2P$ transition probability is plotted as a function of the laser fluence for various laser time windows. The laser is assumed to be on resonance. The right side of Fig. E.2 shows the complementary, *i.e.,* the probability for the $2S-2P$ excitation versus the laser time window for various fluences. The numerical results which account for the intensity time distribution of the light (exponential with $\tau = 140$ ns) and the 2 keV observation time (laser time window of 200 ns) predict that 52% of the $2S$ atoms are excited to the $2P$ state when the laser fluence is 16.5 mJ/cm^2. The laser intensity and the laser time window needed to optimize the determination of the $2S-2P$ line position has to take into account the increase of line broadening with increasing fluence and laser time window, the increase of background for increasing laser time window, and the increase of signal with increasing laser intensity and laser time window.

E.5 Summary

In Table E.2 some properties of the $2S_{1/2}^{F=1} - 2P_{3/2}^{F=2}$ transition are summarized. The transition with maximum initial population (initial state is a triplet state) and with the

Table E.2: Spectroscopic properties of the $2S_{1/2}^{F=1} - 2P_{3/2}^{F=2}$ transition.

$2S$ lifetime (0.6 hPa)	1.3×10^{-6} s
$2P$ lifetime	8.5×10^{-12} s
$\lvert\langle b\rvert\mathbf{r}\lvert a\rangle\rvert^2$	$5a_\mu^2$
transition frequency/wavelength	50 THz / 6 μm
linewidth (FWHM)	18.6 GHz
saturation fluence	16.5 mJ/cm^2

largest matrix element was chosen. The population of the triplet state is 3 times larger than that of the singlet state assuming the $2S$ state to be statistically populated. All $2S-2P$ transitions have the same sensitivity to finite size effects but the transition with $F+1$ initial state is a factor of 3 less sensitive to the uncertainty of the $2S$ hyperfine splitting. The chosen transition is also free from complications by state–mixing as for the $2P_J^{\mathrm{F}=1}$ states.
The fluence required to induce a transition with $(1-e^{-1})$ probability is $F_s = 16.5$ mJ/cm^2. The transition width of 18.6 GHz (FWHM) is given by the $2P$ lifetime. The laser bandwidth has to be small compared to the transition width, *i.e.,* no more than $1-2$ GHz. The measured laser width of 0.7 GHz (cf. §4.8) fulfills this requirement.

Appendix F

$2S - 2P$ transition systematics

In this Appendix possible systematic effects which shift or broaden our $2S - 2P$ transition line are studied. Doppler and Zeeman effect, and pressure shift are considered since μp atoms are formed in H_2 gas at 0.6 hPa at room temperature and in a 5 T magnetic field. Generally speaking, muonic hydrogen atoms are quite insensitive to these effects due to their small size, and the resulting shift turns out to be totally negligible whereas the corresponding broadening is still much smaller than the natural linewidth.

F.1 Doppler broadening

The Doppler effect is causing a broadening of the $2S - 2P$ transition of 0.5 GHz (FWHM) if the μp_{2S} atoms would be thermalized. However the μp_{2S} atoms may not be fully thermalized at the time of the laser transition. The measured lifetime of the short–lived $2S$ component of 150 ns [16] shows that 150 ns after the formation of the $2S$ state, the μp atoms have an average kinetic energy smaller than 0.31 eV, *i.e.,* are below the threshold energy for radiative quenching. When the laser transition takes places (1.6 μs after the μp formation) the thermal energy of the μp atoms is therefore below 0.3 eV. A Monte Carlo simulation which traces the slowing down of the μp atoms in the hydrogen gas predicts that at laser time the average kinetic energy of the μp atoms is below 0.1 eV [157]. This simulation considers the energy–dependent elastic and inelastic cross sections for $\mu p(2S) + H_2$ collisions calculated by T. Jensen. In conclusion a Doppler broadening of approximately 1 GHz is expected which is small compared to the natural linewidth of 18.6 GHz.

F.2 Zeeman effect

A 5 T magnetic field is used to keep the size of the muon stop volume small. The μp atoms can thus be effectively illuminated by the laser pulse. The effect of this rather high magnetic field on the $2S - 2P$ energy difference is treated in this section. First the relevance of the quadratic Zeeman effect compared to the linear term is considered. The effect of the magnetic field on the $2S$ level is then calculated in first order perturbation theory (Zeeman effect) and compared to the exact Breit–Rabi solution. The $2P$ Zeeman shift is calculated in first order perturbation theory. The observable effect of the magnetic field on the $2S - 2P$ transition is given by the different Zeeman corrections for the upper and the lower levels of the transition.

F.2.1 Linear versus quadratic Zeeman effect

Consider the Hamiltonian H of a charged particle with mass m, charge e and spin $\mathbf{S}$ in an external constant magnetic field $\mathbf{B}$:

$$\begin{aligned} H &= \frac{1}{2m}\left(\mathbf{p} - \frac{e}{c}\mathbf{A}\right)^2 - \frac{e}{mc}\mathbf{S}\cdot\mathbf{B} \\ \mathbf{A} &= \frac{1}{2}\mathbf{r}\times\mathbf{B}\,. \end{aligned} \tag{F.1}$$

The first term accounts for the interaction between charge and electromagnetic field, and the second one represents the interaction of the particle magnetic moment with the magnetic field. Inserting the definition of the field $\mathbf{A}$ and that of the angular momentum $\mathbf{L} = \mathbf{p}\times\mathbf{r}$ gives

$$\begin{aligned} H &= \frac{\mathbf{p}^2}{2m} - \frac{e}{mc}\left(\mathbf{p}\cdot\mathbf{A} + \mathbf{S}\cdot\mathbf{B}\right) + \frac{1}{2m}\frac{e^2}{c^2}\mathbf{A^2} \\ &= \frac{p^2}{2m} - \frac{e}{mc}\left(\frac{1}{2}\mathbf{L}\cdot\mathbf{B} + \mathbf{S}\cdot\mathbf{B}\right) + \frac{p^2}{2m}\frac{e^2}{c^2}\frac{1}{4}(\mathbf{r}\times\mathbf{B})^2 \\ &= \frac{p^2}{2m} - \frac{e\hbar}{2mc}\left(l_z + 2s_z\right)B + \frac{e^2}{8mc^2}r^2B^2\sin^2\theta \end{aligned} \tag{F.2}$$

where $\hbar l_z$ and $\hbar s_z$ are the eigenvalues of the operator L_z and S_z, respectively. The ratio of the quadratic to the linear term in the 5 T magnetic field turns out to be of the order of 10^{-10} and consequently the quadratic term may be neglected. Thus the magnetic field dependent part of the Hamiltonian takes the simplified form

$$H_B = \frac{e\hbar}{2mc}(L_z + 2S_z)B\,. \tag{F.3}$$

F.2.2 Orbital and spin magnetic moments

The atomic interaction with an external magnetic field $\mathbf{B}$ can be described by the Hamilton operator of Eq. (F.3) applied to both particles forming the atomic system

$$\begin{aligned} H_B &= \left(g_L^\mu\,\mu_B^\mu\,\mathbf{L} + g_L^p\,\mu_B^p\,\mathbf{L} + g_S^\mu\,\mu_B^\mu\,\mathbf{S} + g_I\,\mu_B^p\,\mathbf{I}\right)\cdot\frac{\mathbf{B}}{\hbar} \\ &= \left(g_L^\mu\,L_z + g_L^p\,\frac{\mu_B^p}{\mu_B^\mu}\,L_z + g_S^\mu\,S_z + g_I\,\frac{\mu_B^p}{\mu_B^\mu}\,I_z\right)\mu_B^\mu\,B\,. \end{aligned} \tag{F.4}$$

where g_L^μ, g_L^p, g_S^μ and g_I are respectively the muon orbital, the nuclear orbital, the muon spin, and nuclear "g-factors". $\mathbf{L}$ stands for the orbital momentum of the orbiting particle which is the same as the orbital momentum of the nucleus, $\mathbf{S}$ the muon spin and $\mathbf{I}$ the nucleus spin.

The muon magnetic moment is defined as $\mu_B^\mu = \frac{e\hbar}{2mc}$ where m is the muon mass, and the proton magnetic moment is $\mu_B^p = \frac{e\hbar}{2Mc}$ where M is the proton mass. The magnetic field is assumed to be in z-direction. The source of the orbital magnetic moment is given by the orbital angular momentum of the moving particle. A fraction $m/(m+M)$ of the total orbital momentum of an atom is contributed by the motion of the nucleus and the fraction $M/(m+M)$ by the orbiting particle. The muon's contribution to the orbital angular momentum, and hence to the orbital gyromagnetic factor, is reduced by the factor $M/(m+M)$ to

$$g_L^\mu = 1\cdot\frac{M}{m+M} \simeq 0.90\,. \tag{F.5}$$

The motion of the nucleus gives rise to an orbital g-factor of

$$g_L^p = 1 \cdot \frac{m}{m+M} \simeq 0.10 \tag{F.6}$$

which is negligible since $g_L^p \, \mu_B^p \simeq \frac{m^2}{M^2} \, g_L^\mu \, \mu_B^\mu$. The spin component of the muon magnetic moment for a free muon is given by the Dirac value, corrected for small QED contributions

$$g_S^\mu = 2\,(1 + \frac{\alpha}{2\pi} + \cdots) \simeq 2\,(1 + 0.001) \simeq 2\,. \tag{F.7}$$

Additional corrections to the muon g-factor are known which account for the fact that the muon is in a bound system and not a free particle. These corrections which are mainly of kinematic origin affect the g-value below the 10 ppm level [29] and are therefore negligible. The measured proton gyromagnetic factor is $g_I \simeq -5.58$.

Compared to hydrogen, muonic hydrogen shows a decrease of the spin and orbital magnetic moments of the orbiting particle by a factor of about 200 due to the mass ratio of the orbiting particles.

F.2.3 Zeeman effect of the hyperfine levels

If the energy shift due to the magnetic field is small compared to the fine–structure splitting, then J ($\mathbf{J} = \mathbf{L} + \mathbf{S}$) is a good quantum number (hyperfine interaction neglected) and the Hamiltonian can be written as

$$H_B = \left(g_J J_z + g_I \frac{\mu_B^p}{\mu_B^\mu} I_z \right) \mu_B^\mu \, B \tag{F.8}$$

where

$$g_J = g_L \frac{J(J+1) - S(S+1) + L(L+1)}{2J(J+1)} + g_S \frac{J(J+1) + S(S+1) - L(L+1)}{2J(J+1)} \tag{F.9}$$

The small orbital component of the proton magnetic moment is neglected. Similarly if the energy shift due to the external magnetic field is small compared to the hyperfine splitting then F ($\mathbf{F} = \mathbf{J} + \mathbf{I}$) is a good quantum number and the interaction Hamiltonian H_B becomes

$$H_B = g_F \, \mu_B^\mu \, B \frac{F_z}{\hbar} \tag{F.10}$$

where the hyperfine Landé g-factor is

$$g_F = g_J \frac{F(F+1) - I(I+1) + J(J+1)}{2F(F+1)} + g_I \frac{\mu_B^p}{\mu_B^\mu} \frac{F(F+1) + I(I+1) - J(J+1)}{2F(F+1)} \tag{F.11}$$

For weak magnetic fields the interaction Hamiltonian H_B perturbs the zero–field eigenstates of $H_{\rm hfs}$. To lowest order the levels split linearly according to

$$\Delta E_B = g_F \, \mu_B^\mu \, m_F \, B \tag{F.12}$$

where the g_F values are given by combining Eq. (F.11) with Eq. (F.9) and $\hbar m_F$ is the eigenvalue of F_z. Inserting the gyromagnetic values of §F.2.2 with $g_L = g_L^\mu$ gives

$$\begin{aligned} g_F &= 0.99 \quad \text{for } 2S_{1/2}^{\mathrm{F}=1} \text{ states} \\ g_F &= 0.94 \quad \text{for } 2P_{3/2}^{\mathrm{F}=2} \text{ states}\,. \end{aligned} \tag{F.13}$$

Table F.1: Zeeman shift in a 5 T magnetic field for the three allowed $2S^{\mathrm{F}=1}_{1/2} - 2P^{\mathrm{F}=2}_{3/2}$ transitions in muonic hydrogen for light linear polarized along the magnetic field.

$2S^{\mathrm{F}=1}_{1/2} \to 2P^{\mathrm{F}=2}_{3/2}$	Energy shift [meV]	Frequency shift [MHz]
$m_F = 1$	-0.8×10^{-4}	-20
$m_F = 0$	0	0
$m_F = -1$	0.8×10^{-4}	20

For a 5 T magnetic field the g-values for the lower and upper states cause a Zeeman shift of

$$\begin{aligned} \Delta E_B &= 1.40 \times 10^{-6}\, m_F \quad \text{(eV)} \qquad \text{for } 2S^{\mathrm{F}=1}_{1/2} \text{ states} \\ \Delta E_B &= 1.32 \times 10^{-6}\, m_F \quad \text{(eV)} \qquad \text{for } 2P^{\mathrm{F}=2}_{3/2} \text{ states .} \end{aligned} \tag{F.14}$$

Since the laser light inducing the transition is linearly polarized parallel the B-field (atomic quantization axis) only transitions with $\Delta m_F = 0$ are allowed by selection rules. This reduces the effect of the magnetic field on the transition frequency since only the difference between the upper and lower level shift is observed which is an order of magnitude than the shifts themselves. Table F.1 shows the energy shifts for the 3 allowed transitions between the triplet $2S$ state and the $2P$ state with $F = 2$. The average shift resulting in the 5 T magnetic field is zero because the Zeeman shift is opposite for the $m_F = \pm 1$ transitions and zero for the $m_F = 0$ transition (the m_z sublevels are equally populated). However these Zeeman shifts cause, in principle, a broadening of our resonance line of order 40 MHz/18.6 GHz $\sim 0.25\%$ (relative to the natural linewidth), which is negligible.

F.2.4 Anomalous Zeeman effect versus Breit–Rabi solution

An exact solution of the magnetic field effect on the atomic levels is given by finding the energy eigenvalues of the Hamiltonian:

$$H = \frac{\Delta E_{\mathrm{hfs}}}{2\hbar^2}\, \mathbf{I}\cdot\mathbf{J} + \left(g_J \mathbf{J} + g_I \frac{\mu_B^p}{\mu_B^\mu} \mathbf{I} \right) \cdot \frac{\mu_B^\mu}{\hbar}\, \mathbf{B} \,. \tag{F.15}$$

The $\mathbf{I}\cdot\mathbf{J}$ coupling (hyperfine) has to be taken into account because the external field is affecting the coupling within the various atomic magnetic moments. Contrary to the perturbative approach of the previous section, this approach (Breit–Rabi) is valid regardless of the magnetic field amplitude. Using the relation $J_\pm = J_x \pm J_y$ and $I_\pm = I_x \pm I_y$ the Hamiltonian H may be written as

$$H = \frac{\Delta E_{\mathrm{hfs}}}{2\hbar^2}\, (I_+ J_- + I_+ J_- + I_z J_z) + \left(g_J\, J_z + g_I\, \frac{\mu_B^p}{\mu_B^\mu}\, I_z \right) \frac{\mu_B^\mu}{\hbar}\, B_z \tag{F.16}$$

For S states ($L = 0$), the elements of the Hamiltonian may be easily calculated using the relations

$$\begin{aligned} J_\pm |J, J_z\rangle &= \hbar \sqrt{J(J+1) - J_z(J_z \pm 1)} \quad |J, J_z \pm 1\rangle \\ I_\pm |I, I_z\rangle &= \hbar \sqrt{I(I+1) - I_z(I_z \pm 1)} \quad |I, I_z \pm 1\rangle \end{aligned} \tag{F.17}$$

Since $[H, F_z] = 0$, m_F is a good quantum number. It is therefore justified to consider only the subspace spanned by

$$\left\{ |m_I = m_F - 1/2, m_J = 1/2\rangle, |m_I = m_F + 1/2, m_J = -1/2\rangle \right\} \tag{F.18}$$

The Hamiltonian in this basis is expressed as the following 2×2 matrix ($m \equiv m_F$):

$$\begin{pmatrix} \frac{\Delta E_{\rm hfs}}{2}\left(m-\frac{1}{2}\right)+\left[\frac{g_J}{2}-g_I\frac{\mu_B^p}{\mu_B^\mu}\left(m-\frac{1}{2}\right)\right]\frac{\mu_B^\mu}{\hbar}B & \frac{\Delta E_{\rm hfs}}{2}\sqrt{I(I+1)-\left(m-\frac{1}{2}\right)\left(m-\frac{1}{2}\right)} \\ \frac{\Delta E_{\rm hfs}}{2}\sqrt{I(I+1)-\left(m-\frac{1}{2}\right)\left(m-\frac{1}{2}\right)} & \frac{-\Delta E_{\rm hfs}}{2}\left(m+\frac{1}{2}\right)+\left[\frac{-g_J}{2}-g_I\frac{\mu_B^p}{\mu_B^\mu}\left(m+\frac{1}{2}\right)\right]\frac{\mu_B^\mu}{\hbar}B \end{pmatrix}$$

Diagonalizing this matrix leads to the eigenvalues and hence the energy levels

$$E_m^{\pm} = -\frac{\Delta E_{\rm hfs}}{4} - g_I\,\mu_B^p\,mB \pm \frac{\Delta E_{\rm hfs}}{2}\sqrt{1+4mx+x^2} \tag{F.19}$$

whit

$$x = \frac{\left(g_J^\mu + g_I\frac{\mu_B^p}{\mu_B^\mu}\right)\,\mu_B^\mu\,B}{\Delta E_{\rm hfs}}\,. \tag{F.20}$$

This formula describes exactly the effect of the magnetic field. For $B = 0$ the usual hyperfine structure of the S states is found, with the triplet states shifted upward by $1/4\,\Delta E_{\rm hfs}$ and the singlet state shifted downward by $-3/4\,\Delta E_{\rm hfs}$.

It turns out that for a 5 T magnetic field the perturbative results of Eq. (F.14) are equivalent to the Breit–Rabi solution. Linearizing the Breit–Rabi equation as a function of the magnetic field gives the first order perturbation Zeeman shift. Linearizing is a legitimate approximation for $x \ll 1$, which is equivalent to low magnetic fields. For the $2S_{1/2}$ state $x \sim 10^{-4}$, and for the $2P_{3/2}$ state $x \sim 10^{-3}$, which means that the perturbation theory is a good approximation of the exact solution and therefore the level shifts caused by the magnetic field are the ones shown in Table F.1.

F.3 Collisional shift and broadening

Since muonic hydrogen is formed in hydrogen gas the effect of collisions with the surrounding hydrogen gas has to be considered. An estimate for collisional–induced line shift and broadening is presented in this section. A simple model was developed in the impact theory framework, which takes into account the effects of the H_2 molecular properties.

F.3.1 Model

Let us consider an atomic oscillator moving in a gas. The frequency of its emitted or absorbed radiation changes gradually when a surrounding gas molecule is approached. We consider only adiabatic perturbations, neglecting transitions between different states of the atom. Let $V(r)$ be the transition energy shift (interaction potential) caused by the colliding hydrogen molecule, then the time evolution of the oscillator can be expressed in the form [158]

$$\begin{aligned} f(t) &= \exp\left(-i\omega_0 t + i\eta(t)\right) \\ \eta(t) &= \int_{-\infty}^{t} dt'\; V(r(t'))/\hbar\,, \end{aligned} \tag{F.21}$$

where ω_0 is the unperturbed transition frequency, $\eta(t)$ the phase of the oscillator caused by the interaction, and $r(t)$ the trajectory of the oscillator in the hydrogen gas. Since inelastic channels are neglected the phase η is a real number. The power spectrum of the

emitted and absorbed radiation is given by the Fourier transform of the function $f(t)$. It can be derived that [158]

$$\Delta\nu_{\text{broadening}} = n\bar{v}\int_0^\infty 2\pi b\,db\,[1-\cos(\eta)] \tag{F.22}$$

$$\Delta\nu_{\text{shift}} = n\bar{v}\int_0^\infty 2\pi b\,db\,\sin(\eta) \tag{F.23}$$

$$\eta = \int_{-\infty}^{\infty} dt\,V\left(\sqrt{b^2+\bar{v}^2t^2}\right) \tag{F.24}$$

where $\Delta\nu_{\text{broadening}}$ is the collisional broadening, $\Delta\nu_{\text{shift}}$ the collisional line shift, and b the impact parameter. A precise derivation of this formula requires the introduction of the correlation function, its expansion at low density and several averaging procedures. It assumes a spherically symmetric interaction and an average over all possible classical rectilinear atomic trajectories supposing that each atom is not deflected by the collision ($\mathbf{r}(t)=\mathbf{r_0}+\mathbf{v}t$). Moreover only the mean velocity $\bar{v}$ is used instead of the detailed velocity distribution. The phase of Eq. (F.24) is computed for a collision with a single molecule at a fixed impact parameter. Equations (F.22) and (F.23) are an average over all possibles trajectories.

The validity conditions for these impact approximations are considered here. We define τ_c as a representative duration of collision, and τ_{cc} as a mean time between collisions. The impact approximation is valid when $\tau_c \ll \tau_{cc}$, implying that the total absorbed energy comes from the interval between collisions. $\tau_c \simeq b/\bar{v}$ and $\tau_{cc} \simeq 1/n\bar{v}\pi a^2$, where n is the density of hydrogen molecules and a (Weisskopf radius) the impact parameter for which the collisional phase shift is one radian. We estimate a to be near $2.5a_0$ and taking $b \simeq 2a$ we have $\tau_c/\tau_{cc} = 2\pi a^3 n = n/(0.7\times10^{23}\ \text{cm}^{-3})$. Note that 1 hPa corresponds to $n \simeq 2.8\times10^{16}\ \text{cm}^{-3}$ and therefore this model is applicable for our experimental conditions.

F.3.2 $2S-2P$ energy shift

The energy levels of the μp $n=2$ manifold are affected by the Stark effect where the related electric field originates from the colliding molecules. Let's consider the effect of an electric field on the four–level system with $n=2$ in the $|nL_m\rangle$ notation (fine and hyperfine structure neglected):

$$|2S_0\rangle,\quad |2P_1\rangle,\quad |2P_{-1}\rangle,\quad |2P_0\rangle\ . \tag{F.25}$$

The $|2P_m\rangle$ states are degenerate, and lie 0.2 eV above the $|2S_0\rangle$ state. The perturbation Hamiltonian for an electric field $\mathbf{E}$ in z-direction is:

$$H_1 = eEz \tag{F.26}$$

where e is the electric charge and z the space operator in z-direction. The energy eigenvalues of the perturbed system are

$$E_\pm = \frac{1}{2}\left[(E_S+E_P)\pm\sqrt{(E_P-E_S)^2+4|H_{SP}|^2}\right] \tag{F.27}$$

$$H_{SP} = 3ea_\mu\,|\vec{E}| \tag{F.28}$$

where E_S, E_P are the energy eigenvalues of the unperturbed $2S$ and $2P$ states, respectively, and $a_\mu = \hbar^2/m_\mu e^2$ is the Bohr radius for μp atoms. For vanishing perturbation ($H_1 \to 0$), E_+ reduces to E_P and E_- to E_S.

The interaction potential which describes the transition energy shift during the collision is then given by

$$\begin{aligned} V(r) &= (E_+ - E_-) - (E_P - E_S) \\ &= \sqrt{(E_P - E_S)^2 + 4\,|H_{SP}|^2} - (E_P - E_S) \ . \end{aligned} \tag{F.29}$$

Therefore the interaction potential can be computed if the external electric field is known.

F.3.3 Electric field and interatomic potential

The electrostatic potential Φ of a charge distribution can be expanded in multi–pole moments:

$$\Phi = \frac{q}{r} + d_\alpha \frac{r_\alpha}{r^3} + \frac{\Theta_{\alpha\beta}}{3r^5}\left(3r_\alpha r_\beta - r^2\delta_{\alpha\beta}\right) + \ldots \tag{F.30}$$

where $q = \sum_i e_i$ is the total charge, $d_\alpha = \sum_i e_i r_{i\alpha}$ the dipole moment, and $\Theta_{\alpha\beta} = \frac{1}{2}\sum e_i(3r_{i\alpha}r_{i\beta} - r_i^2\delta_{\alpha\beta})$ the quadrupole moment.

The charge distribution of the hydrogen molecule is not affected, in the lowest order, by the colliding μp atom, since the μp atom is small and neutral. The μp_{2S} atom does become polarized, but because of the smallness of the induced electric dipole moment, its effect may be neglected even when it is well inside the molecular orbital. Since the hydrogen molecule is neutral ($q = 0$) and does not have a permanent dipole moment ($d_\alpha = 0$), the relevant potential is given by the quadrupole term

$$\Phi = \frac{\Theta_{\alpha\beta}}{3r^5}\left(3r_\alpha r_\beta - r^2\delta_{\alpha\beta}\right) \ . \tag{F.31}$$

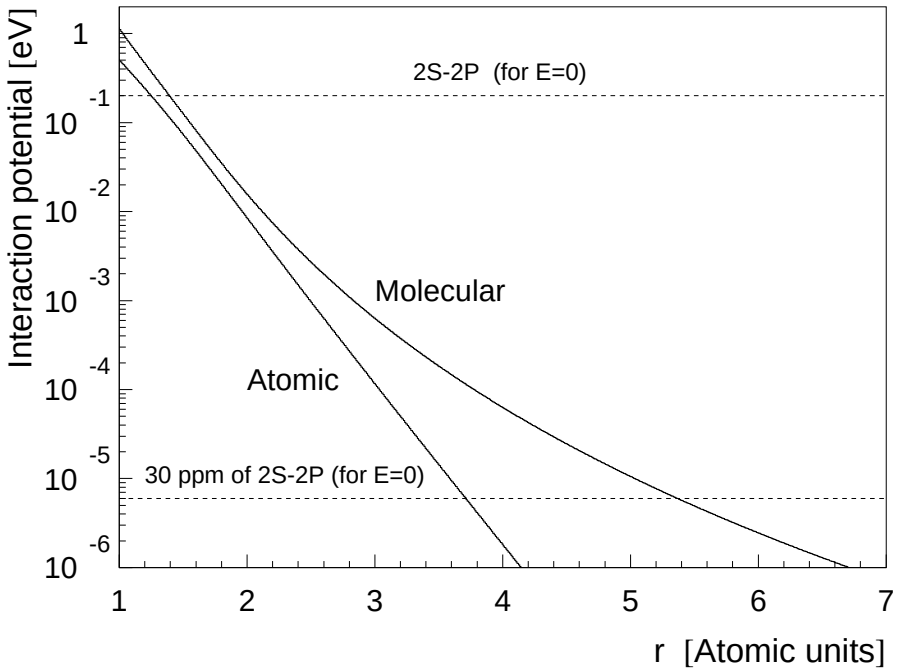

Figure F.1: Interaction potentials as a function of the distance r between the μp atom and hydrogen molecule for two different electric field models: the one generated by the electrostatic quadrupole moment of the hydrogen molecule, and that caused by a single hydrogen atom. The higher lying dashed curve represents the unperturbed transition energy, and the one at the bottom represents the aimed precision (30 ppm).

$\Theta_{\alpha\beta}$ is a tensor having 9 components, but by a proper choice of the axes of reference, all off–diagonal elements ($\Theta_{\alpha\beta}(\alpha \neq \beta)$) can be made to vanish. Thus three principal axes x, y, and z are obtained with the relative quadrupole components:

$$\begin{aligned}\Theta_{xx} &= \frac{1}{2}\sum_i e_i\left(3x_i^2 - r_i^2\right)\\ \Theta_{yy} &= \frac{1}{2}\sum_i e_i\left(3y_i^2 - r_i^2\right)\\ \Theta_{zz} &= \frac{1}{2}\sum_i e_i\left(3z_i^2 - r_i^2\right)\end{aligned} \tag{F.32}$$

These are the principal quadrupole moments of the molecule. The sum of the above quadrupole moments per definition gives

$$\Theta_{xx} + \Theta_{yy} + \Theta_{zz} = 0\ , \tag{F.33}$$

so that only two of them are independent. Because the charge distribution of the hydrogen molecule is symmetric around, say, the z-axis, there is:

$$\Theta = \Theta_{xx} = \Theta_{yy} = -\frac{1}{2}\Theta_{zz}\ . \tag{F.34}$$

It can be shown that the spatially averaged electric field caused by the quadrupole moment of the hydrogen molecule is approximately

$$\left|E^{\mathrm{Avg}}\right| \simeq \frac{3\Theta}{r^4} \tag{F.35}$$

where $\Theta = 0.6 \times 10^{-26}$ esu cm^2 [159].

At short distances ($r < a_0$) the hydrogen molecule can be treated as two independent hydrogen atoms. The spherically symmetric Coulomb potential generated by the hydrogen atom in the region $r < a_0$ is expanded in r. The first non–vanishing contribution gives [160]:

$$|E(r)| = r^{-2}\left(1 + 2r + 2r^2\right)\ e^{-2r}\frac{e}{a_0^2} \tag{F.36}$$

where r is expressed in atomic units. Both the molecular quadrupole potential and the atomic potential are calculated with Eq. (F.29) and shown for comparison in Fig. F.1. The potential at large distances is dominated by the quadrupole term. At short distances ($r \lesssim 2a_0$) the atomic transition is so far shifted from its unperturbed value that the exact knowledge of the potential is unnecessary for the calculation of the pressure shift. As will be shown below only collisions with impact parameter $b \gtrsim 2$ plays a role in the determination of the collisional line shift.

F.3.4 Numerical results

Equations (F.22 – F.24) combined with Eqs. (F.27 – F.29), and (F.35) give the pressure shift and broadening. The phase shift η for a complete collision has to be computed for every impact parameter b. The functions $b\sin(\eta)$ and $b[1-\cos(\eta)]$ are plotted in Fig. F.2 versus the impact parameter b. The integrals of these two curves are proportional to the pressure shift and broadening (see Eqs. (F.23) and (F.22)). This illustrates which impact parameter region is relevant for the shift and the broadening. The line shift, proportional

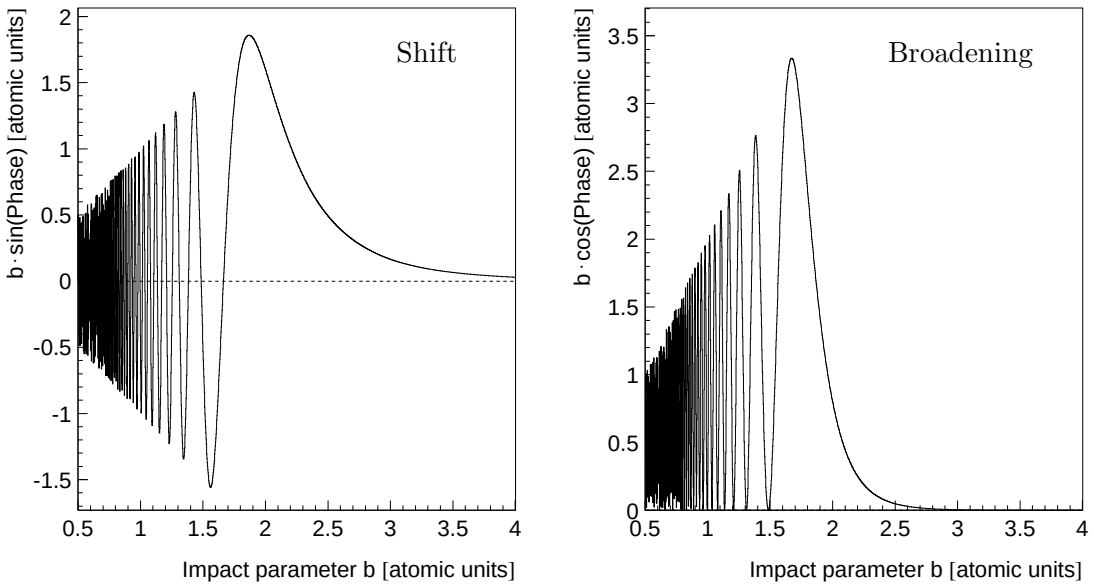

Figure F.2: Plotted are functions whose integral is proportional to the pressure shift (left) and broadening (right). It shows that only soft collisions ($b \gtrsim 2$) contribute to the shift and predominantly hard collisions ($b \lesssim 2$) contribute to the broadening.

to the integral of the function in Fig. F.2 (left), turns out to be determined only by collisions with impact parameter greater than $\sim 2a_0$. Therefore a precise knowledge of the interatomic potential for distances smaller than $\sim 2a_0$ is not required for the computation of the line shift. At larger distances the long–range quadrupole potential turns out to be correct and it is the relevant potential causing the pressure shift. Only soft collisions contribute to the line shift, whereas the broadening is given by harder collisions with impact parameters $b \lesssim 2a_0$. At these short distances the multi–pole expansion leading to the quadrupole potential is not valid. Hence the pressure broadening value computed using the quadrupole potential is only qualitatively correct.

A pressure shift and broadening of

$$\begin{aligned} \Delta\nu_{\text{shift}} &= 1.3 \text{ MHz} \times p \text{ [hPa]} \\ \Delta\nu_{\text{broadening}} &= 2.4 \text{ MHz} \times p \text{ [hPa]} \end{aligned} \tag{F.37}$$

are expected. This is three orders of magnitude smaller than the accuracy in the determination of the $2S - 2P$ centroid position we are aiming at (1.5 GHz), and therefore completely negligible.

Appendix G

Population and lifetime of the $2S$ state

The feasibility of our experiment relies crucially on a sizable fraction of muonic hydrogen atoms in the $2S$ state with sufficiently long lifetime. This Appendix is devoted to the description of the muonic hydrogen formation in highly excited states and subsequent deexcitation mechanisms (cascade). Focus is given to the fraction of formed μp which reach the $2S$ state, to the distinction between "long–lived" and "short–lived" $2S$ states and to the lifetime of the "long–lived" $2S$ state which corresponds to the initial state relevant for the laser experiment.

G.1 Muonic hydrogen formation and cascade processes

A negatively charged muon introduced into H_2 gas will slow down to a kinetic energy of about 15 eV and is then captured by a hydrogen molecule. The hydrogen molecule breaks up and muonic hydrogen is formed [161]. Deceleration of the muon is caused by inelastic processes, *i.e.,* by ionization and excitation of hydrogen molecules.

Based on measurements with μ^- [162] and $\bar{\text{p}}$ [163] the stopping power of μ^- in H_2 gas for μ^- energies between 1 and 5 keV ranges from $S = 2.4\times10^{-15}$ eV/cm^2 to $S = 3.7\times10^{-15}$ eV/cm^2, respectively. Knowing the stopping power of μ^-, it is possible to calculate its energy loss via $dE/dx = -nS$ where n is the atomic density. The resulting range and slowing down time until the μ^- is captured is respectively 20 cm and 300 ns for a 1 keV μ^-, and 60 cm and 500 ns for a 5 keV μ^- in 0.6 hPa H_2 gas at room temperature, assuming a capture energy of 15 eV [16].

As a rule of thumb, muonic hydrogen is formed in an orbit with similar energy and distance from the nucleus as the displaced electron, since then the overlap between electronic and muonic wave function is maximal. The corresponding principal quantum number of the initial state is then $n_i \sim \sqrt{m_r^{\mu p}/m_r^{ep}} \sim 14$ where $m_r^{\mu p}$ and m_r^{ep} are respectively the reduced masses of μp and H atoms.

After the formation of the μp atom in a highly excited state a number of different processes take place until the metastable $2S$ or the $1S$ ground state are reached: radiative transition, Auger emission, Coulomb deexcitation, Stark mixing and elastic collisions. Figure G.1 and Table G.1 give a summary of the processes included in the present cascade model of T. S. Jensen and V. Markushin [12, 164–169].

Table G.1: Processes involved in the deexcitation of μp after its formation at highly excited states.

Stark mixing:	$(\mu\mathrm{p})_{nl_i} + \mathrm{H}_2 \rightarrow (\mu\mathrm{p})_{nl_f} + \mathrm{H}_2$
External Auger effect:	$(\mu\mathrm{p})_i + \mathrm{H}_2 \rightarrow (\mu\mathrm{p})_f + \mathrm{H}_2^+ + e$
Coulomb deexcitation:	$(\mu\mathrm{p})_{n_i} + \mathrm{H}_2 \rightarrow (\mu\mathrm{p})_{n_f} + \mathrm{H}_2 \quad (n_f < n_i)$
Elastic collision:	$(\mu\mathrm{p})_{nl} + \mathrm{H}_2 \rightarrow (\mu\mathrm{p})_{nl} + \mathrm{H}_2$
Radiative transition:	$(\mu\mathrm{p})_{n_i l_i} \rightarrow (\mu\mathrm{p})_{n_f l_f} + \gamma$
Weak decay:	$\mu^- \rightarrow e^- \nu_\mu \bar{\nu}_e$
Nuclear capture:	$\mu^- + p \rightarrow n + \nu_\mu$

1. **Radiative transitions:** The radiative rates of muonic hydrogen are related to those of atomic hydrogen by $\Gamma^{\mathrm{rad}}_{n_i l_i \rightarrow n_f l_f}(\mu\mathrm{p}) = m_r^{\mu p}/m_r^{ep}\ \Gamma^{\mathrm{rad}}_{n_i l_i \rightarrow n_f l_f}(\mathrm{H})$ (as follows from Eq. (E.16)). Only electric dipole transitions are considered in the cascade model:

$$(\mu\mathrm{p})_{n_i l_i} \rightarrow (\mu\mathrm{p})_{n_f l_f} + \gamma \tag{G.1}$$

   with $l_f = l_i \pm 1$. This is the only cascade process which does not depend on density and kinetic energy. The radiative rates strongly increase with decreasing n due to the radiative rate dependence on the energy difference ($\Gamma^{\mathrm{rad}} \sim \Delta E^3_{nn'}$) and the wave–function overlap [154]. Hence below a specific density–dependent n value which increases with lower hydrogen density, the radiative transitions dominate the cascade. For the same reason ($\Gamma^{\mathrm{rad}} \sim \Delta E^3_{nn'}$), the population of the circular states $|n, l = n-1\rangle$ is strongly enhanced by $\Delta n \gg 1$ radiative dipole transitions since $\Delta l = \pm 1$. From such states the radiative decay can proceed exclusively via $\Delta n = 1$ dipole transitions. Therefore the circular transitions are the most important source feeding the $1S$ ground state. The $2S$ state is not fed via radiative transitions from these circular states since the $2P$ state "always" decays radiatively to the ground state (except at very high densities, *i.e.,* close to that of liquid hydrogen).

2. **Stark mixing:** Since muonic hydrogen is neutral and rather small in the atomic scale, it approaches closely the nuclei of neighboring atoms, experiencing their Coulomb field. Hence the corresponding cross section is given by the size of the hydrogen atom. The electric field experienced during a collision mixes the pure parity states $|nlm\rangle$ with states of different angular momentum (linear Stark effect):

$$(\mu\mathrm{p})_{nl_i} + \mathrm{H}_2 \rightarrow (\mu\mathrm{p})_{nl_f} + \mathrm{H}_2 \tag{G.2}$$

   The rates of this process increase with increasing kinetic energy and principal quantum number n. Radiative transitions preferably populate the circular states whereas Stark mixing is reestablishing a statistical distribution of the orbital angular momentum l. Since the radiative transition rates are pressure–independent and the Stark mixing rate depends linearly on the pressure, an increase of the pressure will lead to an increase of the fraction of μp atoms reaching the $2S$ state (see Fig. G.2).

3. **Coulomb deexcitation:** This process is important in the upper part of the cascade $n > 10$ (at 0.6 hPa) and is the only process which accelerates the μp atoms considerably,

$$(\mu\mathrm{p})_{n_i} + \mathrm{H}_2 \rightarrow (\mu\mathrm{p})_{n_f} + \mathrm{H}_2 + \text{kin. energy} \tag{G.3}$$

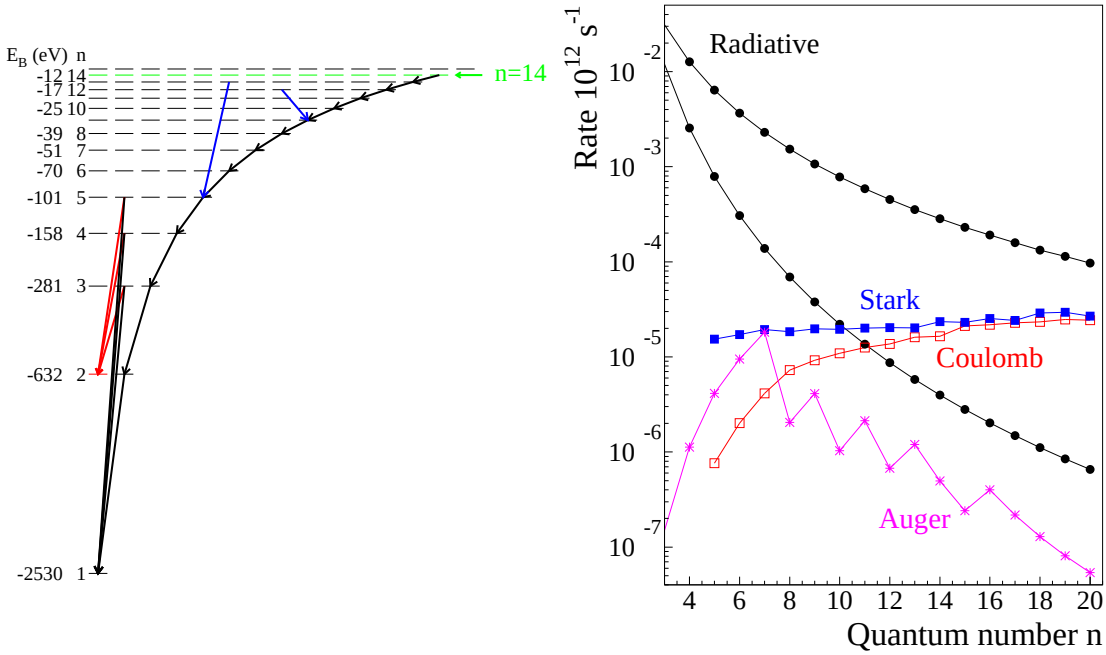

Figure G.1: (Left): Schematic view of the atomic cascade in μp. The μp atom is formed in a highly excited state with principal quantum number $n \sim 14$. At ~ 1 hPa pressure the most important deexcitation mechanism in the upper part of the cascade is Coulomb deexcitation with large jumps $\Delta n = 1 - 4$. Below $n \sim 10$ the radiative transitions are the dominant deexcitation mechanism. (Right): The l-average rates at 1 eV kinetic energy for 1 hPa pressure: Coulomb deexcitation (empty red squares), Stark mixing (full blue squares), Auger transitions (magenta stars) and radiative deexcitation (black full circles). The two extreme cases of radiative rates are shown: $np \longrightarrow 1s$ and the circular $n(n-1) \longrightarrow (n-1)(n-2)$. These cross sections have been computed by T. Jensen.

where $n_f < n_i$. The transition energy is shared between the colliding particles, *i.e.*, the released energy $\Delta E_{nn'}$ is partially converted into kinetic energy of the μp atom producing exotic atoms with energies $E \gg 1$ eV [10].

4. **External Auger deexcitation:** This is a deexcitation which occurs via ionization of the H_2 molecule in a collision:

$$(\mu p)_i + H_2 \ \rightarrow (\mu p)_f + H_2^+ + e \ . \tag{G.4}$$

In contrast to the Coulomb deexcitation, nearly all the transition energy is carried away by the released electron, so that the recoil energy of the μp atom is rather small. The Auger rate has its maximum at a critical level $n_c = 7$ above which only $\Delta n > 1$ transitions are energetically possible (to be compared with the H_2 ionization potential of 15.4 eV). Above n_c therefore the cross section decreases. Below n_c, $\Delta n = 1$ transitions are possible but the probability of electron emission decreases rapidly with n since the size of the neutral μp atoms decreases much below the size of the electron wave–function.

5. **Elastic scattering:** Elastic scattering describes the collision of μp atoms with the H_2 molecule:
$$(\mu\mathrm{p})_{nl} + \mathrm{H}_2 \;\rightarrow (\mu\mathrm{p})_{nl} + \mathrm{H}_2 \tag{G.5}$$
in which the quantum state is not changed. Together with Stark mixing (inelastic scattering), elastic scattering is decelerating the μp atoms, counteracting the acceleration caused by the Coulomb deexcitation. However elastic scattering does not dominate the evolution of the energy distribution, and when the μp atoms reach the ground state or the $2S$ metastable state they are far from being thermalized. However this process is responsible for the thermalization of the $2S$ state which is of fundamental importance for the laser experiment (cf. §G.3).

The cascade model developed by Jensen and Markushin accounts also for the time evolution of the kinetic energy of the μp atoms during the cascade. The present cascade model reproduces well the measured x-ray yields [14] and kinetic energy distributions [10] whereas it gives too long values for the cascade time [16]. The measured cascade time at 0.6 hPa is (30 ± 7) ns [16].

G.2 Population of the $2S$ state

The fraction of formed μp atoms reaching the $2S$ state can be determined experimentally by measuring the Lyman–series (K_α, K_β, ...) x-ray yields [14],

$$\varepsilon_{2S} = 0.134\, Y_{K\beta} + 0.144\, Y_{K\mathrm{rest}} \tag{G.6}$$

where it was made use of the calculated radiative branching ratios $\Gamma^{\mathrm{rad}}(3P \rightarrow 2S)/\Gamma^{\mathrm{rad}}(3P \rightarrow 1S) = 0.134$ and $\Gamma^{\mathrm{rad}}(n > 3 \rightarrow 2S)/\Gamma^{\mathrm{rad}}(n > 3 \rightarrow 1S) = 0.144$. The above expression assumes that only radiative transitions are the processes feeding the $2S$ and the $1S$ states, which is justified at our conditions. It will be shown below how the yields Y_{Ki} are deduced from the measured relative x-ray intensity ratios $(Y_{Kj}/\sum_i Y_{Ki})$.

As will be further discussed below, there are two classes of $\mu\mathrm{p}_{2S}$ atoms: a component with a long lifetime termed "long–lived" ($\varepsilon_{2S}^{\mathrm{long}}$) and a component with a short lifetime termed "short–lived" ($\varepsilon_{2S}^{\mathrm{short}}$):
$$\varepsilon_{2S} = \varepsilon_{2S}^{\mathrm{long}} + \varepsilon_{2S}^{\mathrm{short}}\ . \tag{G.7}$$

At 0.6 hPa the short–lived component decays within 150 ns emitting a K_α x ray (after a collisional excitation to the $2P$ state), whereas the "long–lived" component decays nonradiatively to the ground state with a lifetime of 1.3 μs (cf. §G.4). The sum of all radiative K-yields is $Y_{\mathrm{tot}} = \sum_i Y_{Ki} = 1 - \varepsilon_{2S}^{\mathrm{long}}$, because the long–lived component does not contribute, whereas the short–lived component is practically included in the measured K_α x-ray intensity. For hPa gas pressures between 0.06 and 64 hPa, $\varepsilon_{2S}^{\mathrm{long}}$ was measured to be about 1% [10]. By multiplying the measured relative yields $Y_{k\beta}/Y_{\mathrm{tot}}$ and $Y_{K\mathrm{rest}}/Y_{\mathrm{tot}}$ with $Y_{\mathrm{tot}} \simeq 0.99$, the absolute yields needed in Eq. (G.6) are obtained.

At 0.6 hPa a value
$$\varepsilon_{2S} = (2.49 \pm 0.17)\ \% \tag{G.8}$$
can be interpolated from the data shown in Fig. G.2. The initial $2S$ population increases with pressure due to Stark mixing which diminishes the importance of the circular transitions, enhancing the probability that the $2S$ state is fed.

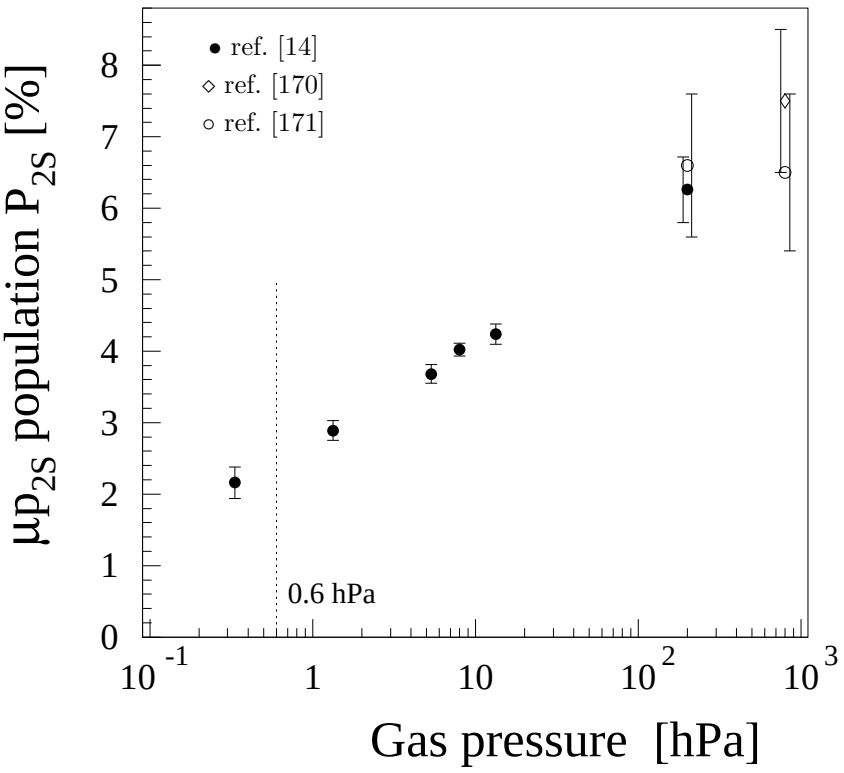

Figure G.2: Fraction ε_{2S} of muons reaching the 2S state versus gas pressure as obtained from measurements of muonic hydrogen K-series x-ray yields. The vertical dotted line represents the gas pressure used in the 2003 data taking period of the μp_{2S} Lamb shift experiment (Courtesy of R. Pohl and F. Kottmann).

G.3 Long and short–lived $2S$ components

In the absence of collisions the lifetime of a μp_{2S} atom is essentially given by the muon lifetime. Two–photon transitions to the ground state occur with a rate of 1.5×10^3 s^{-1} [155] which is negligibly small compared to the muon decay rate of $\lambda_\mu = 4.55 \times 10^5$ s^{-1} (corresponding to the inverse of the muon lifetime of 2.197 μs). However in a gaseous environment the interactions with the surrounding molecules have to be taken into account.

The cross section for collisional $2S$–quenching depends critically upon whether the kinetic energy is less or greater than the $2S - 2P$ splitting of 0.2 eV. μp_{2S} atoms with kinetic energy larger than 0.2 eV in the center–of–mass system, corresponding to 0.31 eV in the laboratory system, can undergo a Stark collision with excitation to the $2P$ state. Thus deexcitation to the ground state via emission of a K_α photon occurs (predominantly after the collision):

$$\mu p(2S) + H_2 \rightarrow \mu p(2P) + H_2 \rightarrow \mu p(1S) + H_2 + K_\alpha \; . \tag{G.9}$$

The μp_{2S} atoms quenched by this process belong to the short–lived component of the $2S$ state.

If the relative kinetic energy is smaller than the $2S-2P$ splitting, this inelastic process is energetically forbidden. However quenching may still occur during the collision since for this time the pure $2S$ state is mixed with the $2P$ state. An electric dipole transition

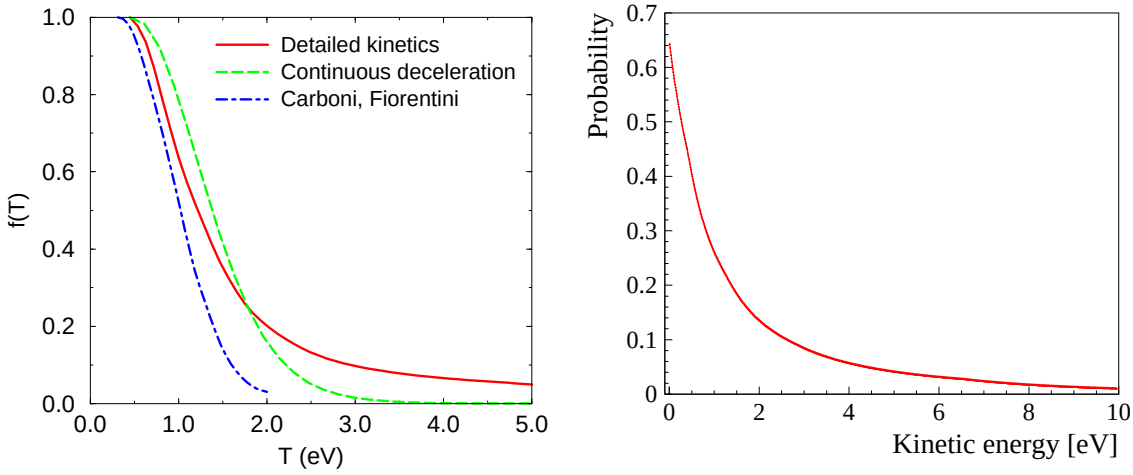

Figure G.3: (Left): Fraction of μp_{2S} atoms which are slowed below 0.31 eV in the laboratory system as a function of their initial kinetic energy T for different cascade models (Courtesy of T. Jensen). (Right): Initial (before thermalization occurs) kinetic energy distribution of the μp_{1S} atoms, interpolated for 0.6 hPa from measurements in Ref. [10].

may take place during the collision:

$$\mu\mathrm{p}(2S) + \mathrm{H}_2 \rightarrow \mu\mathrm{p}(\alpha|2S\rangle + \beta|2P\rangle) + \mathrm{H}_2 \begin{array}{ll} \nearrow \mu\mathrm{p}(2S) + \mathrm{H}_2 & (\text{elastic: } 2S \rightarrow 2S) \\ \searrow \mu\mathrm{p}(1S) + \mathrm{H}_2 + K_\alpha & (\text{deexc. during coll.}) \, . \end{array} \tag{G.10}$$

Collision times are typically of the order of $\tau_c \sim 10^{-14}$ s, quite short compared to the radiative lifetime of the $2P$ state of $\tau_{2P} \sim 10^{-11}$ s. Since this type of radiative transitions occurs only during the collision, the corresponding cross section is reduced by a factor $\tau_c/\tau_{2P} \sim 10^{-3}$ relative to the inelastic cross section of Eq. (G.9) which is of the order of the atomic size ($\sim 10^{-16}$ cm^2). The μp_{2S} atoms quenched by this weaker process (and other molecular processes which will be the subject of the next section) are termed long–lived $2S$ states.

The competition between fast quenching given by the inelastic process ($2S \rightarrow 2P$) and slowing down caused by the elastic process ($2S \rightarrow 2S$) determines the probability for a μp_{2S} atom to survive the process of slowing down and end up as a μp_{2S} with kinetic energy below the threshold energy for the inelastic collision. The long–lived $2S$ component corresponds to μp_{2S} atoms either formed with kinetic energies below 0.31 eV or formed at higher kinetic energies but slowed below this threshold due to elastic collisions.

At kinetic energies below 1 eV the elastic process which slows down the μp atoms starts to dominate over the inelastic process which quenches the $2S$ population. Starting from a kinetic energy T above threshold, every elastic collision $2S \rightarrow 2S$ decelerates the μp_{2S} atom, which reduces the probability for a subsequent inelastic collision. The fraction of μp_{2S} atoms with initial energy T which are slowed below threshold and thus belong to the long–lived component is given in Fig. G.3. Most of these long–lived atoms reach near thermal energies (< 0.1 eV) within a few hundreds ns [157, 172].

In the present high statistics experiment it was possible for the first time to deduce the fraction of the short–lived component (relative to all μp atoms) and its lifetime at 0.6 hPa

by measuring the time distribution of the K_α x rays [16]:

$$\begin{aligned} \varepsilon_{2S}^{\text{short}} &= (1.02 \pm 0.21)\,\% \\ \tau_{2S}^{\text{short}} &= (148 \pm 22)\ \text{ns} \end{aligned} \tag{G.11}$$

G.4 Lifetime of the $2S$ long–lived state

The long–lived component is the population which is relevant for the laser experiment since we need to distinguish between laser–induced K_α photons and "ordinary" K_α x rays from the muonic cascade. As will be described below the fraction of long–lived μp_{2S} is about 1% at 1 hPa, but experiments searching for delayed Lyman-α originated by radiative quenching during collisions as described by Eq. (G.10) were unsuccessful [170, 171, 173]. This implies a nonradiative deexcitation mechanism of the $2S$ state. Muonic hydrogen atoms with $\sim$ 900 eV kinetic energy have been found which are produced via resonant formation of excited muonic molecules with subsequent auto–dissociation

$$\mu\text{p}(2S) + H_2 \rightarrow \{[(\text{pp}\mu)^+]^*\text{p}ee\}^* \rightarrow \mu\text{p}(1S) + \text{p} + \text{kin. energy} + \dots\ . \tag{G.12}$$

The $2S-1S$ transition energy of 1.9 keV is shared as kinetic energy among the μp_{1S} atom and one proton. The resulting quenching rate was found to be [10, 11]

$$\lambda_{\text{quench}}^{2S} = 5.1^{+2.4}_{-2.1} \times 10^5\ \text{s}^{-1} \cdot p\ [\text{hPa}]\ . \tag{G.13}$$

This nonradiative deexcitation mechanism is found to be the dominant decay channel of the long–lived $2S$ component since its cross section is $\sigma \sim 10^{-16}$ cm^2 (per hydrogen molecule at thermal energies) whereas the cross section for radiative deexcitation during collisions is expected to be of the order $\sigma \sim 10^{-18}$ cm^2 [174]. The lifetime of the μp_{2S} state is therefore essentially given by this molecular quenching channel and the muon decay:

$$\tau_{2S}^{\text{long}} = \left(\lambda_{\text{quench}}^{2S} + \lambda_\mu\right)^{-1} \tag{G.14}$$

where λ_μ is the muon decay rate.

From the same data, not only the lifetime but also the population of the long–lived component can be inferred. The values resulting at 0.6 hPa for population and lifetime of the long–lived component are:

$$\begin{aligned} \varepsilon_{2S}^{\text{long}} &= (1.1 \pm 0.2)\,\% \\ \tau_{2S}^{\text{long}} &= (1.32 \pm 0.24)\ \mu\text{s}\ . \end{aligned} \tag{G.15}$$

Combined with the known total population of the $2S$ state of 2.49% [14] (relative to the number of μp atoms in the ground and $2S$ state), the new measurement of the short–lived component is also an indirect determination of the long–lived component [16]:

$$\varepsilon_{2S}^{\text{long}} = 2.49\,\% - 1.02\,\% = (1.47 \pm 0.27)\,\% \tag{G.16}$$

Both the indirect value (Eq. (G.16)) and the direct determination (Eq. (G.15)) of the long–lived μp_{2S} population are in agreement.

Appendix H

Background of the $2S - 2P$ resonance

It is of major importance — especially for future measurements — to understand the origin of the background, *i.e.,* 2 keV x rays in the laser time window which do not arise from laser–induced K_α transitions. The main background process which is muon transfer to the polypropylene foils in front of the LAAPDs, is presented in §H.1. Section H.2 summarizes all known possible background processes and gives an estimate of their relative intensity and time dependence. In §H.3 the expected theoretical time distribution of 2 keV x rays is compared with the measured one, confirming the validity and completeness of the background model presented in the previous sections.

The signature of a background event is per definition the same as that of a "good" laser–induced event:

- a muon triggers the laser and data acquisition system;
- no signals are detected in any LAAPD or electron detector in the time interval preceding the arrival of the laser light in the cavity;
- in the laser time window (when the laser light is illuminating the μp atoms) a signal is detected in the LAAPDs which is classified as a 2 keV *x ray*;
- in a delayed time window relative to the *x ray* detection, a signal is detected in the LAAPDs or electron detectors which is classified as *electron*.

In the following a brief overview of the various processes contributing to the background is given:

- μp_{1S} atoms formed in a region close to the target axis move in arbitrary direction through the hydrogen gas and hit within typically 1 μs the foils in front of the Li sheets. These foils are made of polypropylene ($\sim (CH_2)_n$). Muon transfer to carbon occurs ($\mu p + C \rightarrow (\mu C)^* + p$), and the $(\mu C)^*$ atoms deexcite emitting x rays of 4.9 keV and higher energies (see Table H.1). As explained in §3.2.1 the energy spectrum of each x ray shows a tail towards lower energies. The muon lifetime in μC is 2.0 μs [101]. Therefore the transfer process may fake laser–induced events since they have the same signature: *x-rays* signals of low energy (including 2 keV) at delayed time (time necessary to reach the foil), followed by a muon decay electron with approximately the same time distribution (2.0 μs lifetime instead of 2.2 μs). Both the DELE and the *second muon* cut clearly do not suppress this background, whereas the K_α energy cut strongly reduces it. The majority of the background events has to be attributed to this process. This background is fully correlated

Table H.1: Energies [175] and yields of radiative transitions after muon transfer from a μp to a μC atom. The yields are calculated [176] based on the cascade model and program given in Refs. [177,178], respectively.

Transition	Energy [keV]	Yield $n_{\rm ini} = 5$	Yield $n_{\rm ini} = 4$
$5 \rightarrow 4$	2.26	0.005	0
$4 \rightarrow 3$	4.89	0.035	0.039
$3 \rightarrow 2$	13.97	0.20	0.22
$2 \rightarrow 1$	75.25	0.41	0.44
$3 \rightarrow 1$	89.21	0.30	0.34

with the muon which entered the target since both *x ray* and *electron* signals are originated by this muon.

– It may occur that a 2 keV *x ray* signal is generated by the muon decay electron (cf. Fig. 5.2), whereas the signal classified as *electron* is uncorrelated, because it is caused by random noise signals in the electron paddle PMTs (cf. §5.5).

– Another source of background is given by a signal which is classified as 2 keV *x ray* but which is not correlated to the *first muon* opening the EVG, whereas the *electron* signal originates from the decay electron of the *first muon*. Even if these x rays are time–uncorrelated they appear to have a ~ 2 μs decay time because they have to precede the electron detection.

– The last and less important source of background has a flat time distribution which means that both *x ray* and *electron* signals are not correlated with the *first muon*. It may arise from *second muons* entering the gas target without being recorded in S_1. The deexcitation of the μp atom correlated to the *second muon* fakes a K_α x ray delayed with respect to the *first muon*, and the electron of the *second muon* decay fakes the electron of the *first muon* decay.

In the following the term "background events" is used to account for all events in the *xe* event class (K_α energy cut, *second muon* cut and DELE cut applied) with x ray times delayed relative to the "prompt" deexcitation, regardless if the *x ray* is detected or not in the laser time window. Background events are therefore termed all events which contribute to the tail towards larger times of Fig. 6.2.

H.1 Background from muon transfer to carbon

To disentangle the various contributions to the background at delayed times, a set of x-ray energy spectra for different time windows were studied. The time interval from 0.1 μs to 6 μs after the μp_{1S} formation is divided in 19 intervals and for each time window the corresponding x-ray energy spectrum was generated. Only the *xe* event class is considered with a delayed electron time interval from 0.1 μs to 5 μs after the x-ray detection. The *second muon* cut is not applied. Three out of 19 spectra are shown in Fig. H.1.

The number of delayed events (background) is decreasing as a function of time (see Fig. 6.2). A detailed investigation shows that the background is the sum of several components with different time dependence. The time evolution of the 4.9 keV and 2 keV peaks

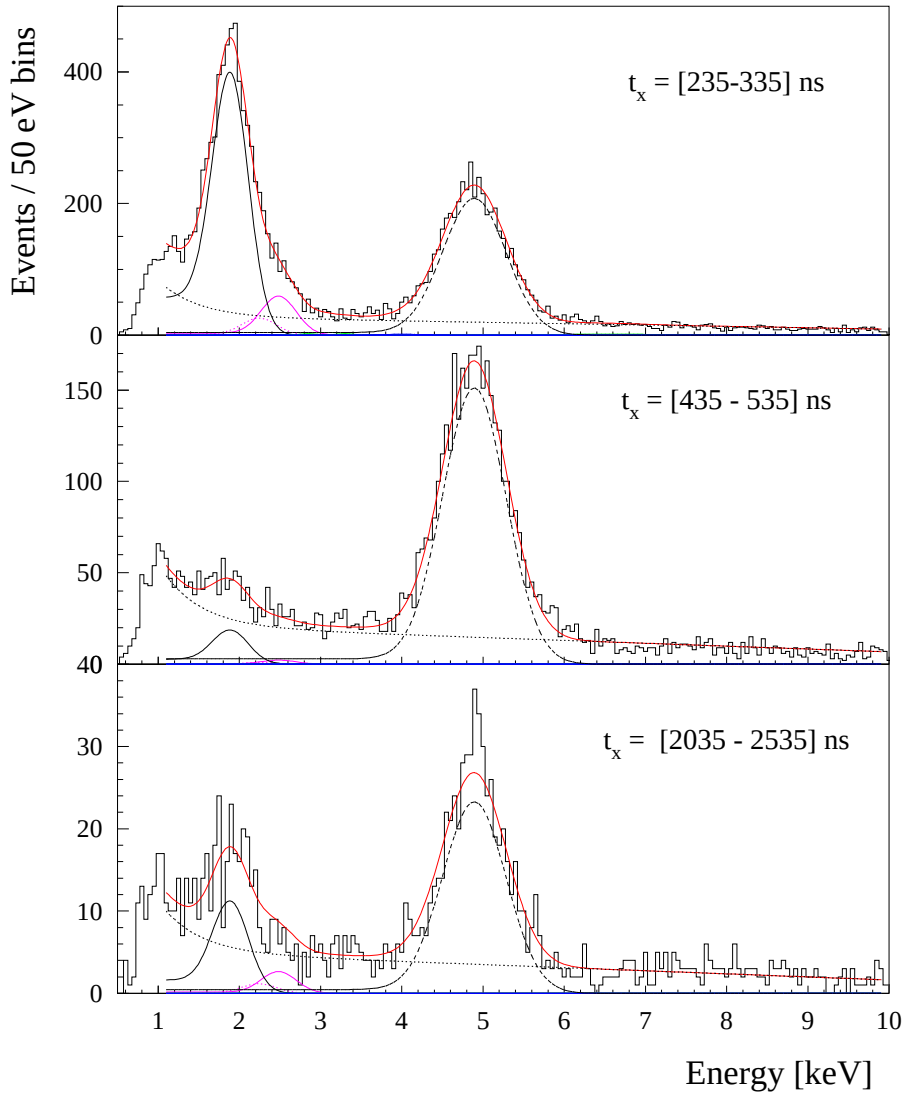

Figure H.1: X-ray energy spectra (3 out of 19) which were studied in order to deduce the shape of delayed background, i.e., the function $B(t, E_x)$ (dotted black lines) discussed in the text. The applied time cuts are indicated in the plots. The spectra are shown for the sum of LAAPDs with the best resolution. Only the xe event class is considered, but the second muon cut is not applied. The 2 keV peaks for the middle and bottom plot are mostly caused by K_α deexcitations of second muon μp atoms The peak at 4.9 keV is the $\mu C_{4\to3}$ transition (dashed black line), the black solid line represents μp K_α , while magenta lines K_β and $K_{\rm rest}$ transitions. The total fit function is shown in red (Courtesy L. Ludhova).

can be seen in Fig. H.1. At early–delayed times (top spectrum), the 2 keV peak is caused by the tail (in time) of the "prompt" μp cascade and radiative quenching of the short–lived $2S$ component (cf. §G.3). The peak at 4.9 keV energy is caused by μp atoms reaching the polypropylene foils in front of the LAAPDs where transfer to carbon occurs. The formed $(\mu C)^*$ atoms immediately deexcite and partially emit 4.9 keV x rays which may be detected by the LAAPDs. At intermediate times (central spectrum), the 2 keV peak has drastically decreased since collisional quenching of the short–lived $2S$ component (which is the slowest process of the "prompt" deexcitation) has an exponential decay time of only

$\sim$150 ns [16]. The 4.9 keV peak, on the contrary, is still present because the μp drift time has a broad time distribution due to the wide distribution of the μp kinetic energy and the various trajectories of μp atoms in the target. At later times (bottom) the 4.9 keV peak decreases since the majority of the μp atoms has already decayed or reached the walls where muon transfer with immediate deexcitation occurs. With decreasing intensity of the total background at late time, a small 2 keV peak becomes visible which has to be attributed to "prompt" deexcitations of *second muon* μp atoms (cf. §5.4). This process has a flat distribution in time whereas all other processes decrease with time. Note that the *second muon* cut was not applied here and compare these spectra with the spectrum of Fig. 5.5 which shows the effectiveness of the *second muon* cut.

As explained previously in §3.2.1, the measured energy spectrum of an x-ray transition is composed of a Gaussian peak and a "flat" tail towards lower energies, starting from the Gaussian peak. Compare the spectra of Fig. H.1 with the source spectrum. The tail at energies below 4 keV has therefore to be attributed partially to 4.9 keV x rays. In addition there is also a quasi–flat background at energies above 6 keV which did not show up in the source spectrum of Fig. 3.9. This background corresponds to the low energy tail of higher lying transitions which have been identified to be μC transitions: $\mu C_{3\to 2}$, $\mu C_{2\to 1}$ and $\mu C_{3\to 1}$ (Table H.1). This identification is confirmed by the fact that the 4.9 keV peak and the intensity of the flat background have similar time distributions, as will be discussed below.

A simultaneous fit of all 19 energy spectra has lead to an empirical parametrization of the continuous background as [16]

$$B(t, E_x) = P(t) \cdot \exp\Big(- \frac{E_x}{0.47}\Big) + R(t) \cdot (14.3 - E_x) \tag{H.1}$$

where E_x is the x-ray energy in keV–units and R, P two time–dependent free fit parameters shown in Fig. H.2. This parametrization does not have any physical meaning and is valid only up to 10 keV. However it may be used to compare the time evolution of the background with that of the 4.9 keV peak intensity, *i.e.,* the time evolution of the transfer process to carbon. For times between 0.3 and 1.5 μs the parameters R, P and the 4.9 keV peak intensity have similar time dependences indicating that the main contribution to background at these times has to be attributed to muon transfer to carbon. At times larger than $\sim$ 1.5 μs, deviations between these dependences are visible indicating that there is an additional background contribution not related to the transfer to carbon.

The arrival time distribution of the μp_{1S} atoms reaching the polypropylene foils in front of the LAAPDs has been computed using a Monte Carlo (MC) simulation. This MC traces the path of the μp_{1S} atoms from the muon stop volume to the walls. Their kinetic energy distribution is taken from previous time–of–flight measurements [10] (see Fig. G.3) and their formation time distribution is the measured time distribution of the K_α peak. When μp_{1S} atoms impinge on the polypropylene foils they are either back–reflected with probability P_R, or muon transfer to the carbon atoms occurs. No theoretical prediction nor measurement of P_R exist, and therefore the simulation has some free parameters to describe the reflection probability which is assumed to depend on energy and incident angle. If transfer occurs, the MC program assumes that an x ray (yield=100%) is instantaneously emitted with isotropic distribution. This x ray is traced and if it hits an LAAPD the time when this happens is recorded.

Two arrival time spectra for different reflection probabilities P_R are plotted in Fig. H.3 together with the measured time distribution of the 4.9 keV peak . For the computation

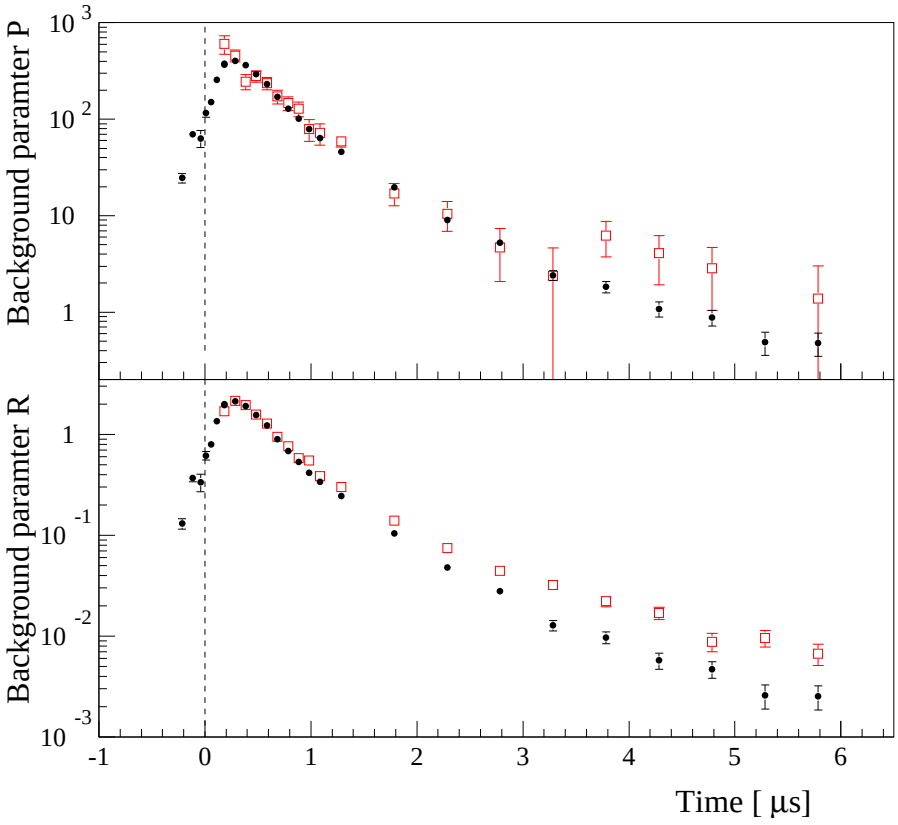

Figure H.2: Parameters P (top) and R (bottom) of the x-ray energy spectra background $B(t, E_x)$ as a function of time (red empty squares). The $\mu C_{4\to3}$ line intensity as a function of time is plotted for comparison on both diagrams (black full circles). It is normalized such that there is optimal superposition with the measured parameters P and R. The ordinate values refer only to the R and P parameters but has no meaning for the μC line intensity. The dashed vertical line indicates the average time of the μp K_α transitions.

of the curve in the left graph it is assumed that no reflection occurs ($P_R = 0$), whereas for the right graph a reflection probability is assumed which depends on the μp kinetic energy T and the incident angle Θ as

$$P_R(\Theta, T) = 0.8\, e^{-0.3T} \cdot (1 - 0.5 \cos\Theta) \tag{H.2}$$

where T is expressed in eV units. For $T = 1$ eV, *e.g.*, P_R varies between $\sim$ 30% and $\sim$ 60%. The reflection probability is chosen to approximately reproduce the data in the time interval between 0.5 and 1.5 μs while keeping the reflections probabilities at reasonable values, *i.e.*, well below 100%.

The simulations approximately reproduce the measured time dependence of the carbon peak intensity, confirming the assumption that the background originates from muon transfer at the polypropylene foils. At times above ~ 3 μs the measurements show a small additional tail compared with the simulations which may be attributed mainly to electrons detected as 5 keV *x rays* followed by an electron paddle noise signal.

The results of these simulations can be used to determine not only the relative but absolute number of delayed background events arising from the transfer process. From the background analysis shown in Fig. H.2 it follows that the 2 keV–background (in the K_α energy cut) is in the time interval 0.4 to 1 μs almost proportional to the 4.9 keV μC

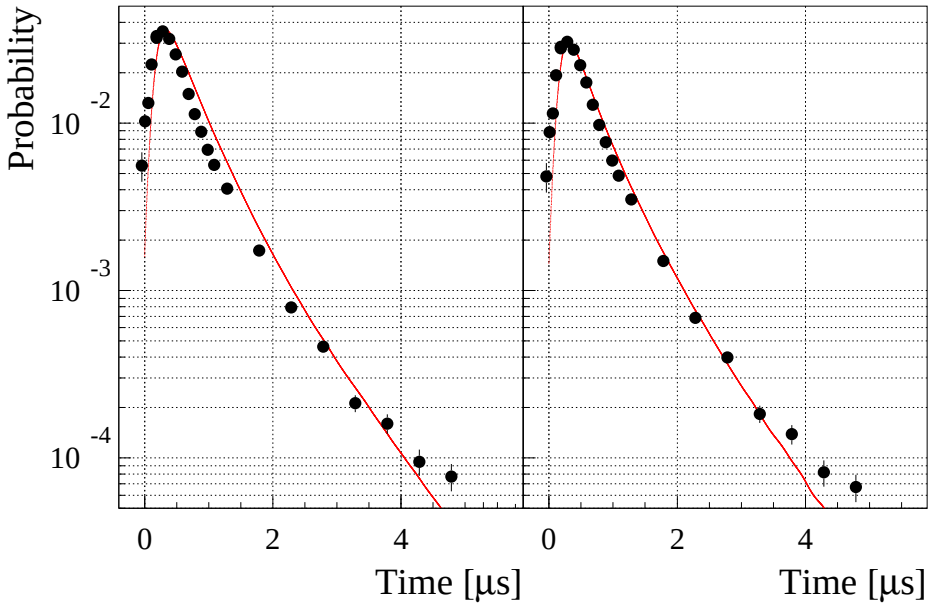

Figure H.3: Time spectra generated by a Monte Carlo simulation of the μC x rays from muon transfer to the polypropylene foils in front of the LAAPDs. When muon transfer occurs, it is assumed that an x ray is emitted, and that this x ray is detected if it hits an LAAPDs. The ordinate values correspond to the probability to detected such a x ray in a 200 ns time window at the abscissa value. The simulation accounts also for muon decay. The measured 4.9 keV peak intensities (black circles) are normalized in such a way that they have the same amplitude at maximum as the simulated curves. This normalization is slightly different for the two graphs. The simulated curve on the left assumes that the μp_{1S} atom is not reflected by the polypropylene foils whereas on the right the reflection probability is given by Eq. (H.2).

peak amplitude. The corresponding number of events for 2 keV–background relative to the 4.9 keV–amplitude is $R_{2-5\,\mathrm{keV}} \simeq 0.2$ (second muon cut applied), as can be seen, *e.g.*, in Fig. H.1 (middle).

To compute the absolute number of background events as a function of time caused by the muon transfer process, $B^{\mu\mathrm{C}}(t)$, the probability distribution extracted from the MC simulation $P^{MC}_{\mathrm{drift}}(t)$ which is shown in Fig. H.3 has to be scaled with the yield of $\mu\mathrm{C}_{4\to3}$ radiative transitions (Table H.1) and with the probability that these x rays are detected in the LAAPDs as a *x ray* within the K_α energy cut. Note that $R_{2-5\,\mathrm{keV}}$ includes all possible background events related to carbon, and consequently by normalizing the background at 2 keV to the 4.9 keV peak amplitude the tails from all higher energy μC transitions are automatically accounted for. The efficiency to detect a 4.9 keV x ray has to be considered (Fig. 5.10), but not the solid angle which is already included in $P^{MC}_{\mathrm{drift}}(t)$. Also the probability to detect a delayed electron has to be taken into account since for the laser experiment only the *xe* event class is accepted. Thus the number of delayed 2 keV–background caused by a transfer process to carbon is

$$B^{\mu\mathrm{C}}(t) = P^{MC}_{\mathrm{drift}}(t)\;\; Y_{\mu\mathrm{C}_{4\to3}}\; \varepsilon_{5\,\mathrm{keV}}\; R_{2-5\,\mathrm{keV}}\; \varepsilon_e^{\mathrm{foil}} \tag{H.3}$$

where $Y_{\mu\mathrm{C}_{4\to3}} = (0.039 \pm 0.005)$ is the calculated yield for the 4.9 keV μC transition (Table H.1), $\varepsilon_{5\,\mathrm{keV}} = (0.88 \pm 0.05)$ the detection efficiency for a 4.9 keV x ray, $R_{2-5\,\mathrm{keV}} = (0.20 \pm 0.05)$ the ratio between number of events in the K_α energy cut and number of events in the 4.9 keV peak, and $\varepsilon_e^{\mathrm{foil}} = (0.75 \pm 0.10)$ the electron detection efficiency for

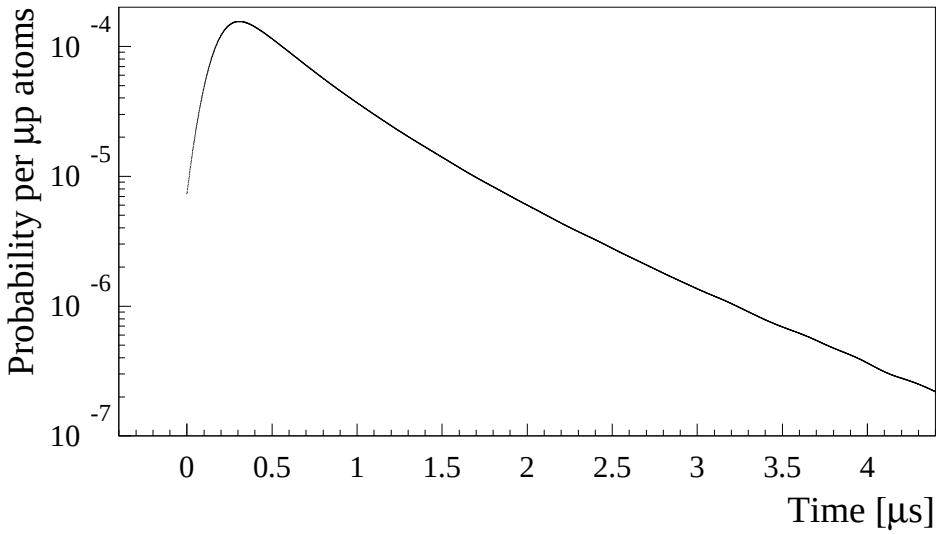

Figure H.4: 2 keV–background $B^{\mu C}(t)$ due to muon transfer from μp to C–atoms in the polypropylene foils in front of the LAAPDs. The ordinate value gives the probability (per formed μp atom) to detect a signal within the μp K_α energy cuts, and a time window of 200 ns at the abscissa value, followed by a delayed electron.

muons decaying on the polypropylene foils. Within the laser time window from 1.5 to 1.7 μs, the expected transfer–induced background events normalized to the number of formed μp atoms is therefore

$$B^{\mu C}(t \in \Delta t_{\text{laser}}) = (1.2 \pm 0.4) \times 10^{-5} \quad [\text{events}/\mu\text{p}] \; . \tag{H.4}$$

The μp reflection probability at polypropylene is assumed to be as given in Eq. (H.2).

The time evolution $B^{\mu C}(t)$ of the transfer–induced background is plotted in Fig. H.4. This transfer–induced background has to be compared with the total measured background in the laser time window. As previously anticipated (cf. §6.2) the measured ratio of delayed to "prompt" events in the laser time window corresponds to a background per formed μp atom of

$$B^{\text{meas}}(t \in \Delta t_{\text{laser}}) = (1.9 \pm 0.2) \times 10^{-5} \quad [\text{events}/\mu\text{p}] \tag{H.5}$$

when the x ray and electron detection efficiencies are taken into account. This number has to be compared with the predicted number of events caused by the transfer process given in Eq. (H.4). In the laser time window, $B^{\mu C}$ turns out to be approximately 65% of the total measured background B^{meas}. The difference between the predicted μC transfer background and the measured total background has to be attributed to other background processes.

H.2 Uncorrelated background

In this section, probabilities and time dependences of other types of background events are investigated. Most of them can be denoted as "uncorrelated" background corresponding to a signal identified as a delayed 2 keV *x ray* followed by a signal identified as an *electron*, in which at least one of the measured signals is not correlated to the *first muon*. The following categories of events are considered:

- *Paddles noise:* A muon opens the EVG and a μp atom is formed. The 2 keV K-line x ray is not detected. However the muon decay electron induces a signal in one of the LAAPDs which corresponds to a 2 keV *x ray* and no signal in any other LAAPD or electron detector. Therefore this signal is identified as a delayed 2 keV *x ray*. A following random noise signal from the electron paddles PMTs fakes an *electron* signal (cf. §5.5). The probability that such an event occurs is given by the product of the following terms:

  - the probability that the "prompt" deexcitation of the formed μp atom is not detected ($1 - \eta_{2\text{ keV}} \simeq 0.9$)
  - the probability that the electron is detected only in one LAAPD and not in any other LAAPD or electron paddle (0.1)
  - the probability that the electron measured in a LAAPD has an energy in the μp K_α energy cut (0.025)
  - the probability that the paddle's–PMTs deliver a noise signal in the DELE time window. This is the product of the measured paddle–PMTs noise rate (9×10^3 s^{-1}) with the width of the DELE time window of 7 μs.

  The probability to detect such an event per formed μp atom is therefore

$$B^{\text{paddles}}(t \in \text{EVG}) = 0.9 \times 0.1 \times 0.025 \times (9 \times 10^3) \times (7 \times 10^{-6}) \simeq 1.4 \times 10^{-4} \quad \text{(H.6)}$$

  The time distribution of these background events follows the time distribution of the probability to detect the muon decay electron. The random signal from the paddles has no influence on the *x ray* time. Knowing the number of background events in the whole EVG (Eq. (H.6)) and its time distribution which correspond to time spectrum of Fig. 5.8, it is possible to calculate the number of background events as a function of time. The probability that a muon decays in the laser time window compared to the total integral number is $\sim 5\%$. Hence the number of events in the laser time window caused by this background class is expected to be

$$B^{\text{paddles}}(t \in \Delta t_{\text{laser}}) = (7 \pm 2) \times 10^{-6} \; . \quad \text{(H.7)}$$

  This represents about 35% of the measured total background (Eq. (H.5)). The sum of this background and the transfer–induced one, $B^{\text{paddles}}(t \in \Delta t_{\text{laser}}) + B^{\mu\text{C}}(t \in \Delta t_{\text{laser}}) = (1.9 \pm 0.5) \times 10^{-5}$, approximately equals the total measured background.

- *Second muon (1.2×10^{-7}):* A *first muon* opens the EVG but neither the "prompt" x ray nor the decay electron are detected. A *second muon* enters the target during the EVG. Both the 2 keV x ray and the electron of the *second* formed μp atom are detected. If the *second muon* is not detected in S_1, the signals caused by the *second muon* are not eliminated by the *second muon* cut and are erroneously attributed to the *first muon*. The x ray of the *second muon* μp atom thus fakes a delayed 2 keV event. The probability that such an event occurs in the laser time window is given by the product of the following factors:

  - the probability that the Lyman–series x ray related the *first muon* is not detected (0.9)
  - the probability that the electron from the decay of the *first muon* is not detected (0.3)

- the probability to detect the Lyman–series x ray related to the *second muon* (0.11)
- the probability to detect the electron from *second muon* decay (0.65)
- the probability that a *second muon* enters the target without being detected by S_1 and its "prompt" deexcitation occurs in the laser time window $\Delta t_{\rm laser}$. This probability is the product of the muon stop rate ($\sim 200\ {\rm s}^{-1}$), and $\Delta t_{\rm laser}$, times the probability that the muon is not seen in S_1 which is 15%. Note that the muon stop rate considered here does not include the S_1 and S_2 detection efficiencies of 85% and 42%, respectively.

Since both detected signals are caused by *second muons* entering the target at random times, this background is time independent. In a time window of 200 ns a background of $0.9 \times 0.3 \times 0.11 \times 0.65 \times 200 \times (200 \times 10^{-9}) \times 0.15 \simeq 1.2 \times 10^{-7}$ events per formed μp atoms is expected. In the laser time window this background class is completely negligible but it becomes visible at times larger than 8 μs after the *first muon* entry (see Fig. H.5).

- *Radiative quenching of short–lived* $2S$ *component (*3×10^{-8}*):* About 1% of the μp atoms populate the short–lived $2S$ component (cf. §G.3) which deexcites to the ground state via emission of a delayed K_α x ray. The corresponding time distribution is proportional to $\exp(-t/\tau_{2S}^{\rm short})$ where $\tau_{2S}^{\rm short} \simeq 150$ ns is the measured lifetime of the short–lived $2S$ component [16]. This gives rise to a background of about 3×10^{-8} events in the laser time window per formed μp atom, which is negligible compared to the main background classes.

- *Uncorrelated signals in the LAAPDs, supposedly neutrons (*2×10^{-7}*):* A muon enters and opens an EVG. The related "prompt" μp deexcitation is not observed, but the muon decay electron is detected. In the time interval between muon entry and decay, a random signal is seen in the LAAPDs as a 2 keV *x ray*. Its origin may be attributed to neutrons from the muon beam line.

  The rate of *neutron*–induced signals can be estimated by considering the x-ray energy spectra at very late times. The LAAPDs energy spectra of late events have a shape compatible with the shape of an electron spectrum, besides a small contribution peaking at low energy (~ 1 keV) which may be attributed to neutrons. During the whole measuring time about 2000 such *neutron* signals have been detected in total in the LAAPDs at late times from 7 to 12 μs in the μp K_α cut interval. Only signals which are not in time coincidence with any other in LAAPDs or electron paddles have been accepted. Since the total number of EVGs is approximately 10^8 it follows that the *neutron* rate is about 4 ${\rm s}^{-1}$.

  Therefore the probability to detect such a background event in the 200 ns long laser time window is given by the product of the following factors:

  - the probability that the 2 keV x ray correlated to the *first muon* is not seen (0.9)
  - the probability that a *neutron* is seen in the LAAPDs in a 200 ns time window ($4 \times 200 \times 10^{-9}$)
  - the probability that the muon did not decay before the laser time window occurs, when the neutron is detected (0.45)

Table H.2: Summary of the various contributions to the background in the laser time window $t \in [1.5 - 1.7\ \mu s]$ and their time dependencies. The number of background events is normalized per formed μp atoms, and t is expressed in μs.

Contribution	$B(t \in \Delta t_{\rm laser})$ [events/μp atoms]	Time dependency at laser time
μC transfer at LAAPD windows	12×10^{-6}	$\sim e^{-t/0.5}$ (Fig. H.4)
2 keV correlated to μ^- decay,	7×10^{-6}	$\sim e^{-t/1.6}$ (Fig. 5.8)
electron from paddle noise		none
2 keV from *second muon*,	1×10^{-7}	none
electron from *second muon*,		none
2 keV from *neutron* (uncorrelated)	2×10^{-7}	(none)
electron from *first muon* decay		$\sim e^{-t/1.6}$ (Fig. 5.8)
short–lived $2S$ deexcitation	3×10^{-8}	$\sim e^{-t/0.15}$ [16]
sum	1.9×10^{-5}	(Fig. H.5)

– the probability to detect the muon decay electron (0.65)

In the laser time window the expected background from this class of events is therefore $0.9 \times (800 \times 10^{-9}) \times 0.45 \times 0.65 \simeq 2 \times 10^{-7}$. It has the same time dependence as the background events caused by the noise in the paddle PMTs which is a factor of 35 larger. Hence the *neutron*–induced background is irrelevant at any time.

H.3 Total background

The results of the previous sections are summarized in Table H.2. The time evolution of the various expected background classes are known. The transfer–induced background events have a time dependence as shown in Fig. H.4. The background with the *x ray* signal caused by the correlated muon decay electron and the *electron* signal from an uncorrelated signal in the paddle–PMTs has a time distribution which follows the measured $t_e - t_x$ time spectrum of Fig. 5.8. The background caused entirely by the *second muon* (totally uncorrelated) has a flat distribution in time. The deexcitation of the short–lived $2S$ state may be described by an exponential with a lifetime of $\tau_{\rm 2S}^{\rm short} = 150$ ns [16].

The measured 2 keV background $B_{\rm tot}^{\rm exp}(t)$ shown in Fig. 6.2 is therefore fit with the following function

$$B_{\rm tot}^{\rm theory}(t) = k_1 \cdot B^{\mu{\rm C}}(t) + k_2 \cdot e^{-t/\tau_e} + c \cdot e^{-t/\tau_{2S}^{\rm short}} + d\,. \qquad \text{(H.8)}$$

The first term accounts for the transfer–induced background which is given in Fig. H.4 and Eq. (H.3). The parameter $k_1 \simeq 1$ is a free fit parameter. The second term describes the delayed events related to the paddle's noise. The parameter k_2 is also a free fit parameter. The electron time spectrum may be described locally with an exponential function. Its decay time "constant" is slightly varying with time: $\tau_e(t = 1.5\ \mu{\rm s}) = 1.5\ \mu$s, $\tau_e(t = 2.5\ \mu{\rm s}) = 1.9\ \mu$s and $\tau_e(t = 3.5\ \mu{\rm s}) = 2.0\ \mu$s. When the fit is performed τ_e follows the

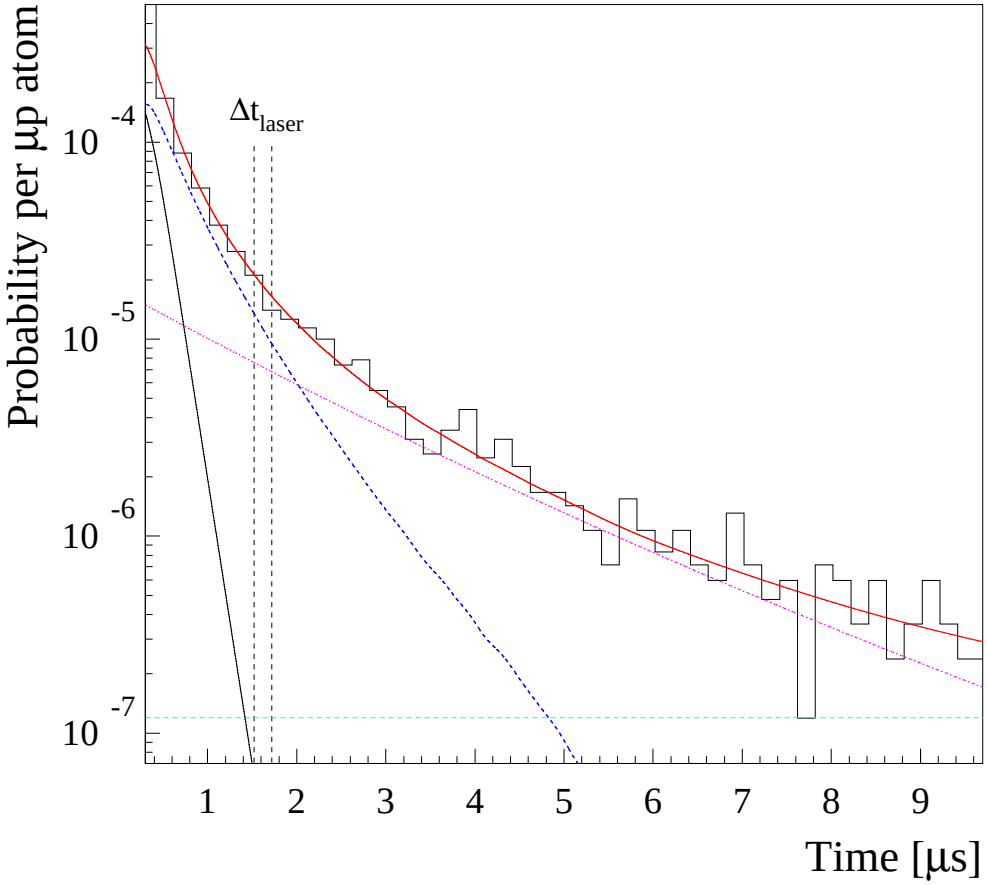

Figure H.5: Measured 2 keV–background x-ray time spectrum for the xe event class, with second muon cut. The bin width is 200 ns. The ordinate gives the measuring probability per formed μp atom. The total fit function (continuous red line) is a sum of four components (Eq. (H.8)) with fixed time dependencies: background related to muon transfer to carbon (dashed blue), background related to paddle's noise (dotted pink), flat background caused by undetected second muons (dashed–dotted cyan), and radiative deexcitation of the short–lived $2S$ component (solid black). The two vertical lines define the laser time window.

measured distribution until it reaches 2.0 μs (μC lifetime) as shown in Fig. 5.8. The third term describes the contribution from the deexcitation of the short–lived $2S$ component. It is relevant only at early delayed times. At such early times it is important to account also for the stopping time distribution, *i.e.,* the time distribution of the prompt K_α peak which is approximately described by a Gaussian with $\sigma = 80$ ns. The time spectrum of the short–lived $2S$ deexcitation results from a convolution of this Gaussian with an exponential function of 150 ns decay constant. Since the initial population of the short–lived $2S$ component is known (cf. §G.3), this background component is kept fix during the fit procedure. The last term in Eq. (H.8) describes the flat background. This background has been estimated in §H.2 to be $d = 1.2 \times 10^{-7}$ (per 200 ns).

Note that in Eq. (H.8) only k_1 and k_2 are free parameters since the other two amplitudes can be predicted reliably. The fit reproduces the measured data quite well as shown in Fig. H.5. At early times the background mainly arises from transfer process to carbon until approximately 2 μs where the background related to paddles noise starts to dominate. The uncorrelated background is negligibly small.

The numbers of delayed background events (per formed μp atom) in the laser time window deduced from the values resulting for the free parameters k_1 and k_2 are

$$\begin{aligned} B_{\text{fit}}^{\mu\text{C}}(t \in \Delta t_{\text{laser}}) &= (1.18 \pm 0.15) \times 10^{-5} \quad [\text{events}/\mu\text{p}] \\ B_{\text{fit}}^{\text{paddles}}(t \in \Delta t_{\text{laser}}) &= (0.72 \pm 0.07) \times 10^{-5} \quad [\text{events}/\mu\text{p}] \end{aligned} \tag{H.9}$$

which are in agreement with the estimated values given in Eq. (H.4) and Eq. (H.7). The good quality of the fit gives confidence in our simple background model.

In summary a satisfactory model was developed which describes the measured background time spectrum of delayed 2 keV *x rays* valid for a time interval between 0.3 μs and 10 μs after μp formation for a hydrogen gas pressure of 0.6 hPa. Besides the small $2S$ component all contributions are almost pressure–independent. 63% of the background events in the laser time window ($t \in [1.5 - 1.7\mu\text{s}]$) are correlated to the transfer process of the muon to carbon when the the μp_{1S} atoms hit the polypropylene foils in front of the LAAPDs. The remaining 37% has to be attributed to the random signals in the electron paddles. The identification of these main background components opens the way to reduce the background for the future measurements (cf. §7.4).

References

[1] P. J. Mohr and B. N. Taylor. *CODATA recommended values of the fundamental physical constants: 2002.* Rev. Mod. Phys. **77** (2005), 1–107.

[2] K. Pachucki and U. D. Jentschura. *Two-loop Bethe-logarithm correction in hydrogenlike atoms.* Phys. Rev. Lett. **91** (2003), 113005.

[3] U. D. Jentschura. *Extrapolation of $Z\alpha$ expansion and two-loop bound-state energy shifts.* Phys. Lett. B **564** (2003), 225–230.

[4] V. A. Yerokhin, P. Indelicato, and V. M. Shabaev. *Two-loop self-energy correction in high-Z hydrogenlike ions.* Phys. Rev. Lett. **91** (2003), 073001.

[5] B. de Beauvoir et al. *Metrology of the hydrogen and deuterium atoms: Determination of the Rydberg constant and Lamb shifts.* Eur. Phys. J. D **12** (2000), 61–93.

[6] I. Sick. *On the rms–radius of the proton.* Phys. Lett. B **576** (2003), 62–67.

[7] M. Niering et al. *Measurement of the hydrogen 1S-2S transition frequency by phase coherent comparison with a microwave cesium fountain clock.* Phys. Rev. Lett. **84** (2000), 5496–5499.

[8] P. Mohr. Private communication.

[9] D. B. Leinweber and T. D. Cohen. *Chiral corrections to lattice calculations of charge radii.* Phys. Rev. D **47** (1993), 2147–2150.

[10] R. Pohl. *Investigation of the long–lived metastable 2S state in muonic hydrogen.* PhD thesis, Swiss Federal Institute of Technology (ETHZ), Switzerland, 2001. URL `http://e-collection.ethbib.ethz.ch/index\_e.html`.

[11] R. Pohl et al. *Observation of the molecular quenching of $\mu p(2S)$ atoms.* Hyp. Interact. **138** (2001), 35–40.

[12] T. S. Jensen and V. E. Markushin. *Collisional quenching of the 2S state of muonic hydrogen.* Preprint nucl–ph **0001009** (2000).

[13] T. S. Jensen. *Atomic cascade in light exotic atoms.* PhD thesis, University of Zurich, Switzerland, 2002. (unpublished).

[14] H. Anderhub et al. *Measurement of the K–line intensity ratios in muonic hydrogen between 0.25 and 150 torr gas pressures.* Phys. Lett. B **143** (1984), 65–68.

[15] L. M. P. Fernandes. *Characterization of large area avalanche photodiodes for detection of x rays, vacuum ultraviolet and visible light.* PhD thesis, University of Coimbra (Portugal), 2005. (unpublished).

[16] L. Ludhova. *The muonic hydrogen Lamb shift experiment: lifetime and population of the $\mu p(2S)$ state.* PhD thesis, University of Fribourg (Switzerland), 2005. (unpublished).

[17] K. Pachucki. *Theory of the Lamb shift in muonic hydrogen.* Phys. Rev. A **53** (1996), 2092–2100.

[18] K. Pachucki. *Proton structure effects in muonic hydrogen.* Phys. Rev. A **60** (1999), 3593–3598.

[19] M. I. Eides, H. Grotch, and V. A. Shelyuto. *Theory of light hydrogenlike atoms.* Phys. Rep. **342** (2001), 63–261.

[20] P. Indelicato et al. *Aspects of QED in the framework of exotic atoms.* In P. Kienle et al., editors, *Proceedings of the Int. Workshop on Exotic Atoms (EXA02)*, pages 61–70. Austrian Acad. of Science, Vienna, 2003.

[21] E. Borie. *Lamb shift in muonic hydrogen.* Phys. Rev. A **71** (2005), 032508.

[22] E. Borie and G. A. Rinker. *The energy levels of muonic atoms.* Rev. Mod. Phys. **54** (1982), 67–118.

[23] A. Pineda. *Chiral structure of the Lamb shift and the definition of the proton radius.* Phys. Rev. C **71** (2005), 065205.

[24] T. Kinoshita and M. Nio. *Sixth-order vacuum-polarization contribution to the Lamb shift of the muonic hydrogen.* Phys. Rev. Lett. **82** (1999), 3240–3243.

[25] E. Borie. Private communication.

[26] J. L. Friar, J. Martorell, and D. W. L. Sprung. *Hadronic vacuum polarization and the Lamb shift.* Phys. Rev. A **59** (1999), 4061–4063.

[27] E. Borie. *Hadronic vacuum polarization correction in muonic atoms.* Z. Phys. A **302** (1981), 187–189.

[28] A. Czarnecki. Private communication.

[29] S. G. Karshenboim. Private communication.

[30] K. Pachucki. Private communication.

[31] R. Barbieri, M. Caffo, and E. Remiddi. *Fourth-order charge radius of the muon and its contribution to the Lamb shift.* Lett. Nuovo Cimento Soc. Ital. Fis. **7** (1973), 60.

[32] J. L. Friar. *Nuclear finite-size effects in light muonic atoms.* Ann. Phys. (NY) **122** (1979), 151–196.

[33] R. Rosenfelder. *Proton polarization shifts in electronic and muonic hydrogen.* Phys. Lett. B **463** (1999), 317–322.

[34] E. V. Cherednikova, R. N. Faustov, and A. P. Martynenko. *Proton polarizability contribution to the hyperfine splitting in muonic hydrogen.* Nucl. Phys. A **703** (2002), 365–377.

[35] R. N. Faustov and A. P. Martynenko. *Proton polarizability and the Lamb shift in muonic hydrogen.* nucl–ph preprint **9904362** (1999).

[36] R. Rosenfelder. Private communication.

[37] A. Pineda. Private communication.

[38] J. R. Sapirstein and D. R. Yennie. *Theory of hydrogenic bound states.* In T. Kinoshita, editor, *Quantum electrodynamics*, volume 7, pages 560–672. World Scientific, Singapore, 1990.

[39] A. Veitia and K. Pachucki. *Nuclear recoil effects in antiprotonic and muonic atoms.* Phys. Rev. A **69** (2004), 042501.

[40] A. Czarnecki and K. Melnikow. *Expansion of bound-state energies in powers of m/M.* Phys. Rev. Lett. **87** (2001), 013001.

[41] I. Blokland, A. Czarnecki, and K. Melnikow. *Expansion of bound-state energies in powers of m/M and $(1 - m/M)$.* Phys. Rev. D **65** (2001), 073015.

[42] A.P. Martynenko. *2S hyperfine splitting of muonic hydrogen.* Phys. Rev. A **71** (2005), 022506.

[43] E. H. Barker and N. M. Glover. *Reduction of relativistic two-particle wave equations to approximate forms.* Phys. Rev. **99** (1955), 317–324.

[44] E. Morenzoni et al. *Generation of very slow polarized positive muons.* Phys. Rev. Lett. **72** (1994), 2793–2796.

[45] L. M. Simons. *Die Zyklotronfalle.* Phys. Bl. **48** (1992), 261.

[46] L. M. Simons. *Recent results on antiprotonic atoms using a cyclotron trap at LEAR.* Phys. Scripta **T22** (1988), 90–95.

[47] P. deCecco et al. *A new method to produce a negative muon beam of keV energies.* Nucl. Instrum. Methods A **394** (1997), 287–294.

[48] J. D. Jackson. *Klassische Electrodynamik.* Walter de Gruyter, Berlin, Germany, 1982.

[49] M. Mühlbauer et al. *Frictional cooling: experimental results.* Hyperf. Int. **119** (1999), 305.

[50] *Advanced Photonix Inc.* 1240 Avenida Acaso, Camarillo, CA 93012, USA.

[51] *Radiation Monitoring Devices, Inc.* 44 Hunt Street, Watertown, MA 02472, USA.

[52] L. Ludhova et al. *Planar LAAPDs: temperature dependence, performance, and application in low–energy x-ray spectroscopy.* Nucl. Instrum. Methods A **540** (2005), 169–179.

[53] L. M. P. Fernandes et al. *LAAPD low temperature performance in X-ray and visible-light detection.* IEEE Trans. Nucl. Sci. **51** (2004), 1575–1580.

[54] L. M. P. Fernandes et al. *Application of large-area avalanche photodiodes to X-ray spectrometry of muonic atoms.* Spectro. Acta B **58** (2003), 2255–2260.

[55] L. M. P. Fernandes et al. *Behaviour of large-area avalanche photodiodes under intense magnetic field for VUV- visible and x-ray photon detection.* Nucl. Instrum. Methods A **498** (2003), 362–368.

[56] L. M. P. Fernandes, J. A. M. Lopes, J. M. F. dos Santos, and C. A. N. Conde. *Application of large-area avalanche photodiodes to energy-dispersive x-ray fluorescence analysis.* X–Ray Spectr. **30** (2001), 164–169.

[57] K. Kirch et al. *Muonic cascades in isolated low-Z atoms and molecules.* Phys. Rev. A **59** (1999), 3375–3385.

[58] H. Gassel, K.-Th. Brinkmann, H. Freiesleben, and J. Kiesewetter. *Production of extremely thin plastic films of large area for gas filled detectors.* Nucl. Instrum. Methods A **295** (1990), 377–383.

[59] `http://midas.psi.ch/`.

[60] A. Antognini et al. *Powerful fast triggerable 6 μm laser for the muonic Lamb shift experiment.* Opt. Com. **253** (2005), 362–374.

[61] K. L. Vodopyanov et al. *$AgGaS_2$ optical parametric oscillator continuously tunable from 3.9 to 11.3 μm.* Appl. Phys. Lett. **74** (1999), 1204–1206.

[62] K. Kato. *High-power difference-frequency generation at 5-11 μm in $AgGaS_2$.* IEEE J. Quantum Electron. **20** (1984), 698–699.

[63] *Lambda Physik GMBH.* D-3400 Goettingen, Germany.

[64] D. J. Brink and C. J. van der Hoeven. *Excimer-pumped dye laser with high beam quality.* Rev. Sci. Instrum. **55** (1984), 1948–1951.

[65] *Radiant Dyes Laser Accessories.* D-42929 Wermelskirchen, Germany.

[66] P. F. Moulton. *Spectroscopic and laser characteristics of $Ti:Al_2O_3$.* J. Opt. Soc. Am. B **3** (1986), 125–133.

[67] S. Bourzeix, M. D. Plimmer, L. Julien F. Nez, and F. Biraben. *Efficient frequency doubling of a continuous wave titanium:sapphire laser in an external enhancement cavity.* Opt. Com. **99** (1993), 89–94.

[68] F. Biraben and P. Labastie. *Balayage d'un laser a colorant continu monomode sur 150 GHz.* Opt. Com. **41** (1982), 1.

[69] *The Roditi International Corp.* London, England W1B 5SE.

[70] P. Bakule. *A chirp-compensated, injection-seeded alexandrite laser.* App. Phys. B **71** (2000), 11.

[71] N. Melikechi, S. Gangopadhyay, and E. E. Eyler. *Phase dynamics in nanosecond pulsed dye laser amplification.* J. Opt. Soc. Am. B. **11** (1994), 2402–2411.

[72] K. F. Wall et al. *Optically induced nonresonant changes in the refractive index of* $Ti{:}Al_2O_3$. Optics Letters **14** (1989), 180–182.

[73] A. E. Siegman. *Lasers*. University Science Books, Sausalito, California, 1986. Chapter 24, Laser dynamics: the laser cavity equation.

[74] S. Gerstenkorn and P. Luc. *Atlas du spectre d'absorption de la molecule de l'iode entre 14000-15600* cm^{-1}. Ed. CNRS II, 91405 Orsay, France (1978).

[75] P. Rabinowitz, B. Perry, and N. Levinos. *A continuously tunable sequential Stokes Raman laser*. IEEE J. Quantum Electron. **QE-22** (1986), 797.

[76] W. R. Trutna and R. L. Byer. *Multiple-pass Raman gain cell*. App. Opt. **19** (1980), 301.

[77] B. N. Perry et al. *Controllable pulse compression in a multiple-pass-cell Raman laser*. Opt. Lett. **5** (1980), 288.

[78] I. P. Kaminow G. D. Boyd, W. D. Johnston. *Optimization of stimulated Raman scattering threshold*. IEEE J. Quantum Electron. **QE-5** (1969), 203.

[79] D. Herriott, H. Kogelnik, and R. Kompfner. *Off-axis paths in spherical mirror interferometers*. App. Opt. **3** (1964), 523.

[80] *SPAWR Optical Research Inc.* Lake Havasu City, AZ 86403, USA.

[81] B. N. Perry et al. *Stimulated Raman scattering with a tightly focused pump beam*. Opt. Lett. **10** (1985), 146–148.

[82] R. L. Byer and W. R. Trutna. *16* μm *generation by* CO_2*-pumped rotational Raman scattering in* H_2. Opt. Lett. **3** (1978), 144–146.

[83] R. L. Carman, F. Shimizu, C. S. Wang, and N. Bloembergen. *Theory of Stokes pulse shapes in transient stimulated Raman scattering*. Phys. Rev. A **2** (1970), 60–72.

[84] Y. K.Park W. R. Trutna and R. L. Byer. *The dependence of Raman gain on pump laser bandwidth*. IEEE J. Quantum Electron. **QE-15** (1979), 648–655.

[85] B. N. Perry, P. Rabinowitz, and M. Newstein. *Wave propagation in media with focused gain*. Phys. Rev. A **27** (1983), 1989.

[86] W. K. Bischel and M. J. Dyer. *Temperature dependence of the Raman linewidth and line shift for the Q(1) and Q(0) transition in normal and para-*H_2. Phys. Rev. A **33** (1986), 3113.

[87] D. E. Jennings, A. Weber, and J. W. Brault. *Raman spectroscopy of gases with Fourier transform spectrometer: the spectrum of* D_2. App. Opt. **25** (1986), 284.

[88] E. C. Looi, J. C. Stryland, and H. L. Welsh. *Pressure shifts in the vibrational Raman spectra of hydrogen and deuterium, 315-85 K*. Can. J. Phys. **56** (1978), 1102.

[89] J. R. Murray and A. Javan. *Effects of collisions on Raman line profiles of hydrogen and deuterium gas*. J. Mol. Spectrosc. **42** (1972), 1.

[90] J. C. Lewis and J. Van Kranendonk. *Theory of intercollisional interference effects. Induced absorption in a Lorentz gas.* Can. J. Phys. **50** (1972), 352.

[91] L. S. Rothman. *The HITRAN molecular spectroscopy database: edition of 2000 including updates through 2001.* J. of Quantitative Spectroscopy & Radiative Transfer **82** (2003), 5–44.

[92] R. A. Toth. *Water vapor measurements between 590 and 2582 cm^{-1}: line positions and strengths.* J. of Mol. Spect. **190** (1998), 379–396.

[93] R. Battesti et al. *Bloch oscillations of ultracold atoms: A tool for a metrological determination of h/m_{Rb}.* Phys. Rev. Lett. **92** (2004), 253001.

[94] R. Battesti. *Accélération d'atomes ultra froids; mesure de h/M.* PhD thesis, Université P. et M. Curie, Paris, 2003. URL `http://tel.ccsd.cnrs.fr/`.

[95] F. Nez. Private communication.

[96] *LENS-Optics.* D-85391 Allershausen, Germany.

[97] *LohnStar Optics.* Escondido, CA 92029, USA.

[98] *VIGO System.* PL-01-318 Warsaw, Poland.

[99] M. Bregant et al. *Measurement of the K X–ray intensity ratios in muonic hydrogen at low gas densities.* Phys. Lett. A **241** (1998), 344–350.

[100] B. Lauss et al. *X-ray emission during the muonic cascade in hydrogen.* Phys. Rev. Lett. **80** (1998), 3041–3044.

[101] T. Suzuki, D. F. Measday, and J. P. Koalsvig. *Total nuclear capture rates for negative muons.* Phys. Rev. C **35** (1987), 2212–2224.

[102] P. Hauser, K. Kirch, F. Kottmann, and L. M. Simons. *Absolute x–ray yields of light muonic atoms.* Nucl. Instrum. Methods A **411** (1998), 389–395.

[103] `http://www.cxro.lbl.gov/optical_constants/atten2.html`.

[104] S. V. Romanov. *On the photoexcitation of the 2S→2P transition in light muonic atoms.* Z. Phys. D **33** (1995), 17–26.

[105] A. Giesen et al. *Scalable concepet for diode–pumped high–power solid–state lasers.* Appl. Phys. B **58** (1994), 365.

[106] C. Stewen et al. *A 1-kW cw thin–disk laser.* IEEE Journal of Selected Topics in Quantum Electronics **6** (2000), 650–657.

[107] K. Contag et al. *Theoretical modelling and experimental investigation of the diode–pumped thin–disk Yb:YAG laser.* Quantum Electronics **29** (1999), 697–703.

[108] U. Brauch, A. Giesen, A. Voss, and K. Witting. *Laserverstärkersysteme.* Europäische Patentenmeldung 0632551A1 (1994).

[109] U. Brauch, A. Giesen, A. Voss, and K. Witting. *Laser amplifying system.* United State patent 5553088 (1993).

[110] `http://www.ifsw.uni-stuttgart.de`.

[111] L. Bracci and G. Fiorentini. *Meson transfer to atoms and molecules.* Nuovo Cimento A **50** (1979), 373–392.

[112] W. Leidenmann and R. Rosenfelder. *Deuteron nuclear polarization shifts with realistic potentials.* Phys. Rev. C **51** (1995), 427–430.

[113] A. Huber et al. *Hydrogen-deuterium 1S-2S isotope shift and structure of the deuteron.* Phys. Rev. Lett. **80** (1998), 468–471.

[114] C. Gohle et al. *A frequency comb in the extreme ultraviolet.* Nature **436** (2005), 234–237.

[115] P. Hauser et al. *Search for the 2S–2P energy difference in muonic ^{4}He ions.* Phys. Rev. A **46** (1992), 2363–2377.

[116] H. P. von Arb et al. *Measurement of the lifetime and quenching rate of metastable 2S muonic helium ions*[*1]. Phys. Lett. B **136** (1984), 232–236.

[117] J. D. Bjorken and S. D. Drell. *Relativistic quantum mechanics.* Plenum, NY, 1977.

[118] E. E. Salpeter and H. A. Bethe. *A relativistic equation for bound-state problems.* Phys. Rev. **84** (1951), 1232–1242.

[119] H. Grotch and D. R. Yennie. *Effective potential model for calculating nuclear corrections to the energy levels of hydrogen.* Rev. Mod. Phys. **41** (1969), 350–374.

[120] M. Niering. *Doppler-freie Zweiphotonen–Spektroskopie an atomarem Wasserstoff.* PhD thesis, Max-Planck-Institut für Quantenoptik, 2000. URL `ftp://ftp.ipp-garching.mpg.de/pub/mpq/`.

[121] G. G. Simon, Ch. Schmitt, F. Borkowski, and V. H. Walther. *Absolute electron–proton cross sections at low momentum transfer measured with a high pressure gas target system.* Nucl. Phys. A **333** (1980), 381–391.

[122] U. D. Jentschura. *Theory of the Lamb shift in hydrogenlike systems.* PhD thesis, Ludwig-Maximilians-University, Munich, 1996. (unpublished).

[123] S. Mallampalli and J. Sapirstein. *Fourth-order self-energy contribution to the Lamb shift.* Phys. Rev. A **57** (1998), 1548–1564.

[124] K. Pachucki. *Complete two–loop binding correction to the Lamb shift.* Phys. Rev. Lett. **72** (1994), 3154–3157.

[125] V. A. Yerokhin and M. V. Shabaev. *Two-loop self-energy correction in H-like ions.* Phys. Rev. A **64** (2001), 062507.

[126] K. Pachucki. *Logarithmic two-loop corrections to the Lamb shift in hydrogen.* Phys. Rev. A **63** (2001), 042503.

[127] U. D. Jentschura and K. Pachucki. *Higher-order binding corrections to the Lamb shift of 2P states.* Phys. Rev. A **54** (1996), 1853–1861.

[128] E.-O. Le Bigot et al. *Perturbation approach to the self-energy of non-S hydrogenic states.* Phys. Rev. A **68** (2003), 042101.

[129] U. D. Jentschura, P. Mohr, and G. Soff. *Calculation of the electron self-energy for low nuclear charge.* Phys. Rev. Lett. **82** (1999), 53–56.

[130] V. A. Yerokhin, P. Indelicato, and V. M. Shabaev. *Two-loop self-energy contribution to the Lamb shift in H-like ions.* Phys. Rev. A **71** (2005), 040101.

[131] U. D. Jentschura, P. Mohr, and G. Soff. *Electron self-energy for the K and L shells at low nuclear charge.* Phys. Rev. A **63** (2001), 042512.

[132] P. J. Mohr. *Lamb shift in a strong Coulomb potential.* Phys. Rev. Lett. **34** (1975), 1050–1052.

[133] U. D. Jentschura. *Radiative energy shifts induced by local potentials.* J. Phys. A **36** (2003), 229–236.

[134] S. G. Karshenboim. *New logarithmic contributions in muonium and positronium.* JETP **76** (1993), 541.

[135] M. I. Eides and V. A. Shelyuto. *Corrections of order $\alpha^2(Z\alpha)^5$ to the hyperfine splitting and the Lamb shift.* Phys. Rev. A **52** (1995), 954–961.

[136] J. L. Friar. *The structure of light nuclei and its effect on precise atomic measurements.* arXiv:nucl-th/ **0211064 v1** (2002).

[137] J. L. Friar and G. L. Payne. *Higher-order nuclear-size corrections in atomic hydrogen.* Phys. Rev. A **56** (1997), 5173–5175.

[138] I. B. Khriplovich and R. A. Senkov. *Comment on "proton polarization shifts in electronic and muonic hydrogen":[Phys. Lett. B 463 (1999) 317–322].* Phys. Lett. B **481** (2000), 447–449.

[139] P. J. Mohr, G. Plunien, and G. Soff. *QED corrections in heavy atoms.* Phys. Rep. **293** (1998), 227–369.

[140] L. Essen et al. *Frequency of hydrogen maser.* Nature **229** (1975), 110–111.

[141] S. G. Karshenboim. *The Lamb shift of excited S-levels in hydrogen and deuterium atoms.* Z. Phys. D **39** (1997), 109.

[142] B. R. Taylor. Private communication.

[143] R. G. Sachs. *High-energy behavior of nucleon electromagnatic form factors.* Phys. Rev. **126** (1962), 2256–2260.

[144] Y. S. Tsai. *Radiative corrections to electron-proton scattering.* Phys. Rev. **122** (1961), 1898–1907.

[145] L. Andivahis et al. *Measurements of the electric and magnetic form factors of the proton from $q^2 = 1.75$ to 8.83 $(\mathrm{GeV/c})^2$.* Phys. Rev. D **50** (1994), 5491–5517.

[146] L. W. Mo and Y. S. Tsai. *Radiative corrections to elastic and inelastic ep and μp scattering.* Rev. Mod. Phys. **41** (1969), 205–235.

[147] F. Mandl and G. Shaw. *Quantum field theory.* AULA-Verlag, Wiesbaden, 1993.

[148] R. Rosenfelder. *Coulomb corrections to elastic electron-proton scattering and the proton charge radius.* Phys. Lett. B **479** (2000), 381–386.

[149] C. N. Hand, D. J. Miller, and R. Wilson. *Electric and magnetic form factors of the nucleon.* Rev. Mod. Phys. **35** (1963), 335–349.

[150] B. Dudelzak, G. Sauvage, and P. Lehmann. *Measurements of the form factors of the proton at momentum transfers $q^2 \leq 2$ fermi^{-2}.* Nuovo Cimento **28** (1963), 18.

[151] J. J. Murphy et al. *Proton form factor from 0.15 to 0.79 fm^{-2}.* Phys. Rev. C **9** (1974), 2125–2129.

[152] J. L. Friar, J. Martorell, and D. W. Sprung. *Nuclear size and isotope shift.* Phys. Rev. A **56** (1997), 4579.

[153] D. R. Yennie, M. M. Lévy, and D. G. Ravenhall. *Electromagnetic structure of nucleus.* Rev. Mod. Phys. **29** (1957), 144–157.

[154] H. A. Bethe and E. E. Salpeter. *Quantum mechanics of one- and two- electron atoms.* Springer-Verlag, Berlin, 1957.

[155] J. Shapiro and G. Breit. *Metastability of 2S states of hydrogenic atoms.* Phys. Rev. **113** (1959), 179–181.

[156] W. Demtröder. *Laser spectroscopy.* Springer-Verlag, Berlin, 2002.

[157] D. Taqqu. Private communication.

[158] N. Allard and J. Kielkopf. *The effect of neutral nonresonant collision on atomic spectral lines.* Rev. Mod. Phys. **54** (1982), 1103–1182.

[159] K. V. Prakash. *Evaluation of molecular quadrupole moments.* Rev. Mod. Phys. **38** (1966), 690–709.

[160] R. O. Mueller, V. W. Hughes, H. Rosenthal, and C. S. Wu. *Collisional quenching of the metastable 2S state of muonic hydrogen and the muonic helium ion.* Phys. Rev. A **11** (1975), 1175–1186.

[161] J. S. Cohen. *Capture of negative exotic particles by atoms, ions and molecules.* Rep. Prog. Phys. **67** (2004), 1769.

[162] P. Hauser, F. Kottmann, C. Lüchinger, and R. Schaeren. *Slowing down of negative muons in gaseous H_2 and determination of the stopping power.* In L. A. Schaller and C. Petitjean, editors, *Muonic Atoms and Molecules*, pages 235–241. Birkhäuser Verlag, Basel, 1993. [Proceedings of the Int. Workshop on Muonic Atoms and Molecules, Ascona].

[163] M. Agnello et al. *Antiproton slowing down in H_2 and He and evidence of nuclear stopping power.* Phys. Rev. Lett. **74** (1995), 371–374.

[164] V. E. Markushin. *Cascade in muonic and pionic atoms with Z=1.* Hyp. Interact. **119** (1999), 11–21.

[165] V. E. Markushin and T. S. Jensen. *Kinetic of atomic cascade in ligth exotic atoms.* Hyp. Interact. **138** (2001), 71–76.

[166] T. S. Jensen and V. E. Markushin. *Scattering of light exotic atoms in excited states.* Hyp. Interact. **138** (2001), 113–116.

[167] T. S. Jensen and V. E. Markushin. *Scattering of light exotic atoms in excited states.* Eur. Phys. J. D **19** (2002), 165–181.

[168] T. S. Jensen and V. E. Markushin. *Collisional deexcitation of exotic hydrogen atoms in highly excited states I. Cross-sections.* Eur. Phys. J. D **21** (2002), 261–270.

[169] T. S. Jensen and V. E. Markushin. *Collisional deexcitation of exotic hydrogen atoms in highly excited states II. Cascade calculations.* Eur. Phys. J. D **21** (2002), 271–283.

[170] P. O. Egan et al. *Search for long–lived 2S muonic hydrogen in H_2 gas.* Phys. Rev. A **23** (1981), 1152–1163.

[171] H. Anderhub et al. *Search for the metastable 2S state in muonic hydrogen.* Phys. Lett. B **71** (1977), 443–445.

[172] T. S. Jensen. Private communication.

[173] J. A. Böcklin. *Suche nach dem metastabilen 2S-Zustand im myonischen Wasserstoff bei tiefen Gasdrucken.* PhD thesis, ETHZ, Switzerland, 1982. (unpublished).

[174] J. S. Cohen and J. N. Bardsley. *Radiative collisional quenching of metastable muonic hydrogen μp_{2S} and the metastable muonic helium ion ($\alpha\mu_{2S}$).* Phys. Rev. A **23** (1981), 46–51.

[175] R. Engfer, H. Schneuwly, J. L. Vuilleumier, H. K. Walter, and A. Zehnder. *Charge-distribution parameters, isotope shifts, isomer shifts, and magnetic hyperfine constants from muonic atoms.* At. Data and Nucl. Data Tables **14** (1974), 509–597.

[176] F. Mulhauser. Private communication.

[177] G. Holzwarth and H. J. Pfeiffer. *The muonic X–ray cascade in fluorine following the μ^- transfer from hydrogen.* Z. Phys. A **272** (1975), 311–313.

[178] V. R. Akylas and P. Vogel. *Muonic atom cascade program.* Comp. Phys. Comm. **15** (1978), 291–302.

Acknowledgments

I would like to thank

- Prof. Theodor Hänsch for giving me the opportunity to join the μp($2S$) Lamb shift collaboration, for his constant support of our experiment, and for the wonderful meetings in the Ringberg castle which have opened my mind to a large field of physics.
- Dr. Franz Kottmann for his guidance. In comparison the guidance that Dante received from Virgil in the "Divine comedy" was ridiculous. His precision and capability of approaching every problem and situation was, and still is, a great lesson that exceeds the border of physics.
- Dr. David Taqqu for having transmitted to me the pleasure of doing physics, and to have introduced me to many concepts. If you miss some ideas go to him, I assure you that he will have soon plenty of them.
- Dr. Randolf Pohl for having helped me a lot with programming and for his excellent guidance. It is impossible not to be influenced by his strength and his very methodological approach. Next run Randolf, we will try to work three days continuously! Two days was too easy for us!
- Dr. Françoise Mulhauser (the Madame) for the life and the dynamics she is bringing in our group. Special thanks for continuous support and for editing the final version of this thesis. She is also the best organizer you can imagine.
- Dr. Paul Knowles for his explanations about electronics and detectors, and especially for the hyper–patient English corrections of my non–Shakespearianslike writings.
- Dr. Andreas Dax and Dr. François Nez, "les Monsieuuuurrs" of the laser hut, two laser foxes with whom I have shared a crazy and enriching time. Special thanks to monsieur Dax to have done the most boring work of our experiment, that is, the refilling of the Cyclotron Trap.
- Dr. Dr. Livia Ludhova for being a very pleasant co–graduate student always ready to help me and to enjoy life.
- Prof. Lucile Julien (Maman), Prof. François Biraben (Papa) and Dr. Catherine Schwob for their help and support.
- Prof. Paul Indelicato, Dr. Eric–Olivier Le Bigot, Dr. Roland Rosenfelder and Prof. Edith Borie for discussion about QED.
- Prof. Lukas Schaller for his continuous support and nice discussions.
- The Coimbra University group for their help especially during the data taking periods, and for the very pleasant time shared: Prof. Joaquim dos Santos, Dr. João Veloso, Cristina Monteiro, Daniel Covita, Dr. Luis Fernandes, Prof. Carlos Conde and Dr. João Cardoso.
- A special thanks goes to Fernando Amaro, with whom I shared the mixing of 1000 ℓ of beautiful toxic dye during the 2003 beam period. Maybe we have the record Fernando!
- Prof. Paul Rabinowitz and Prof. Bruce Perry for providing us the Raman laser and for their very kind support and important suggestions about the Raman process.
- Olivier Huot for his help with the electronics.
- Dr. Satish Dhawan for the newly developed wave–form–digitizers.
- Dr. Leo Simons for his help with the Cyclotron Trap and its constant support for our experiment.

- Dr. Valery Markushin for his very kind and fast help with Linux problems.
- Dr. Thomas Jensen for providing the results of his cascade calculations adjusted to our experimental conditions and for his kindness in advising me on several atomic processes.
- Prof. Savely Karshenboim for exhausting but beautiful discussions about his favorite theme, *i.e.,* QED.
- Bruno Leoni and Zdenek Hochman for technical support.
- The accelerator group for providing us with an excellent beam, the PSI-workshop for the excellent work, and the Hallendienst for helping us to put everything together and to take it apart again.
- Dres. Thomas Gerber, Rolf Bombach, Peter Radi and Gregor Knopp for providing us laser components and helpful advice.
- Prof. H.-J. Kluge and W. Nörthershäuser of GSI Darmstadt for providing us with dye pumps, excimer and Ar^+ lasers.
- Prof. R. Zenobi and A. Renn of the Department of Chemistry at ETH Zurich for a dye pump and an Ar^+ laser; and H. van Den Bergh of EPFL Lausanne for an excimer laser.
- Michael Horisberger for the sputtering of thin polypropylene foils and Claudio Vanoni for measuring their thickness.
- Prof. Ingo Sick and Prof. Antonio Pineda for an informative correspondence.
- Gabriele Gschwendtner and Rosemarie Lechner for their kindness shown to me.